

**MODELLING, ANALYSIS AND VALIDATION OF
MICROWAVE TECHNIQUES FOR THE
CHARACTERISATION OF METALLIC
NANOPARTICLES**

**A thesis submitted to Cardiff University
In candidature for the degree of**

Doctor of Philosophy

By

Aslam Sulaimalebbe, BEng (Hons)

Division of Electrical and Electronic Engineering
School of Engineering
&
School of Chemistry
Cardiff University
United Kingdom

November 2009

UMI Number: U585293

All rights reserved

INFORMATION TO ALL USERS

The quality of this reproduction is dependent upon the quality of the copy submitted.

In the unlikely event that the author did not send a complete manuscript and there are missing pages, these will be noted. Also, if material had to be removed, a note will indicate the deletion.



UMI U585293

Published by ProQuest LLC 2013. Copyright in the Dissertation held by the Author.
Microform Edition © ProQuest LLC.

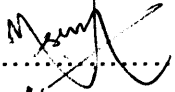
All rights reserved. This work is protected against
unauthorized copying under Title 17, United States Code.



ProQuest LLC
789 East Eisenhower Parkway
P.O. Box 1346
Ann Arbor, MI 48106-1346

DECLARATION

This work has not previously been accepted in substance for any degree and is not concurrently submitted in candidature for any degree.

Signed  (Candidate)

Date 7/12/2009

STATEMENT 1

This thesis is being submitted in partial fulfilment of the requirements for the degree of PhD.

Signed  (Candidate)

Date 7/12/2009

STATEMENT 2

This thesis is the result of my own independent work/investigation, except where otherwise stated. Other sources are acknowledged by explicit references.

Signed  (Candidate)

Date 7/12/2009

STATEMENT 3

I hereby give consent for my thesis, if accepted, to be available for photocopying and for inter-library loan, and for the title and summary to be made available to outside organisations.

Signed  (Candidate)

Date 7/12/2009

STATEMENT 4

I hereby give consent for my thesis, if accepted, to be available for photocopying and for inter-library loans after expiry of a bar on access approved by the Graduate Development Committee.

Signed  (Candidate)

Date 7/12/2009

ABSTRACT

In the last decade, the study of nanoparticle (NP) systems has become a large and interesting research area due to their novel properties and functionalities, which are different from those of the bulk materials, and also their potential applications in different fields. It is vital to understand the behaviour and properties of nano-materials aiming at implementing nanotechnology, controlling their behaviour and designing new material systems with superior performance. Physical characterisation of NPs falls into two main categories, property and structure analysis, where the properties of the NPs cannot be studied without the knowledge of size and structure. The direct measurement of the electrical properties of metal NPs presents a key challenge and necessitates the use of innovative experimental techniques. There have been numerous reports of two/four point resistance measurements of NPs films and also electrical conductivity of NPs films using the interdigitated microarray (IDA) electrode. However, using microwave techniques such as open ended coaxial probe (OCP) and microwave dielectric resonator (DR) for electrical characterisation of metallic NPs are much more accurate and effective compared to other traditional techniques. This is because they are inexpensive, convenient, non-destructive, contactless, hazardless (i.e. at low power) and require no special sample preparation.

This research is the first attempt to determine the microwave properties of Pt and Au NP films, which were appealing materials for nano-scale electronics, using the aforementioned microwave techniques. The ease of synthesis, relatively cheap, unique catalytic activities and control over the size and the shape were the main considerations in choosing Pt and Au NPs for the present study. The initial phase of this research was to implement and validate the aperture admittance model for the OCP measurement through experiments and 3D full wave simulation using the commercially available Ansoft High Frequency Structure Simulator (HFSS), followed by the electrical characterisation of synthesised Pt NP films using the novel miniature fabricated OCP technique. The results obtained from this technique provided the inspiration to synthesise and evaluate the microwave properties of Au NPs. The findings from this technique provided the motivation to characterise both the Pt and Au NP films using the DR technique. Unlike the OCP technique, the DR method is highly sensitive but the achievable measurement accuracy is limited since this technique does not have broadband frequency capability like the OCP method. The results obtained from the DR technique show a good agreement with the theoretical prediction. In the last phase of this research, a further validation of the aperture admittance models on different types OCP (i.e. RG-405 and RG-402 cables and SMA connector) have been carried out on the developed 3D full wave models using HFSS software, followed by the development of *universal models* for the aforementioned OCPs based on the same 3D full wave models.

ACKNOWLEDGEMENT

I would like to thank my supervisors Prof. Adrian Porch and Prof. Gary Attard for giving me the opportunity to study this interdisciplinary degree jointly with Cardiff School of Engineering and Chemistry. I am enormously grateful to both of them for their unwavering support, esteemed guidance, invaluable help, fruitful suggestions and friendly affection during the last three years, made me possible to endure this task. I have benefited deeply from Prof. Porch's expertise in the area of microwave engineering while Prof. Attard has skilfully guided me through the background of electrochemistry. I am also sincerely thankful to Dr. Francisco José Vidal Iglesias, University of Alicante, Spain, for his esteemed guidance, invaluable help and useful suggestions in the synthesis and electrochemical characterisation of nanoparticles. I also sincerely thank Prof. David Barrow, Cardiff School of Engineering, in providing his laboratory facilities and encouragement during the course of my PhD. I acknowledge the Cardiff School of Engineering and Chemistry, for the financial support provided through the Richard Wipp Studentship for the work undertaken in this thesis.

I acknowledge Dr. Alison Crossley and Dr. Martin Owen Jones, University of Oxford, for their experimental assistance in structural characterisation of the synthesised nanoparticles. I also acknowledge Mr. Ravi Mitha, Cardiff School of Engineering, for his invaluable assistance in the structural characterisation of the nanoparticles. I also appreciate the cooperation of Dr. Jonathan Lees and my fellow PhD students, namely Simon Woodington and Nilaped Russamee, for helping me out with the development of the IGOR Pro software code used for carrying out resonator experiments. I must also mention here Adnan Masood, Mohammad Shabi Hashmi and Ahmed Izzidien, who became my closest friends during my time at Cardiff University provided me with valuable help in different facets of my research. I would also like to thank my fellow PhD students Sharon Huxter, Mujib Ahmed and Adam Teer from School of Chemistry, for their invaluable help during the course of my PhD.

I owe a debt of gratitude to my parents and sisters in Sri Lanka, whose prayers and encouragement have been the biggest source of motivation and support for me during the course of my PhD. My brother Amjed Sulaimalebbe, who is doing his undergraduate degree at Cardiff University, deserves a special word of appreciation for his persistent moral support and invaluable help in the last three years. Finally, I would like to take this opportunity to thank everybody who has contributed directly and indirectly towards this project.

LIST OF PUBLICATIONS

Publications and Conference Papers

1. **Aslam Sulaimalebbe**, A. Porch, F.J. Vidal-Iglesias and G. Attard, “Microwave Properties of Platinum Nanoparticles Films”, *IEEE MTT-S International Microwave Symposium Digest*, pp. 1585 – 1588, June, 2008.

Conference Poster Presentations

1. IEEE MTT-S International Microwave Symposium Digest, Atlanta, USA, 15th- 20th June 2008.
“*Microwave Properties of Platinum Nanoparticles Films*”
2. Great Western Electrochemistry Meeting, University of Bath, Bath, 10th July 2008.
“*Electronic Properties of Platinum Nanoparticles Films*”
3. 2nd Annual Nanoscience Network Meeting, Cardiff University, Cardiff, 8th Nov 2007.
“*Microwave Conductivity Studies of Gold and Platinum Nanoparticles*”

LIST OF ACRONYMS

NPs – Nanoparticles
Pt – Platinum
Au – Gold
TEM – Transmission Electron Microscopy
SEM – Scanning Electron Microscopy
XRD – X-ray Diffraction
AFM – Atomic Force Microscopy
STM – Scanning Tunnelling Microscopy
RF – Radio Frequencies
MF – Microwave Frequencies
IDA – Interdigitated Array
DC – Direct Current
SDR – Sapphire Dielectric Resonator
TEM – Transverse Electro Magnetic
DR – Dielectric Resonator
TE – Transverse Electric
TM – Transverse Magnetic
HEM – Hybrid Electromagnetic Mode
IL – Insertion Loss
VNA – Vector Network Analyser
OCP – Open Ended Coaxial Probe
GPB – General Purpose Interface Bus
DMF – Dimethylformamide
RMSE – Root Mean Squared Error
HFSS – High Frequency Structure Simulator
CV – Cyclic Voltammogram
DMM – Digital Multi-Meter
PTFE – Polytetrafluoroethylene
PC – Personal Computer
EM – Electromagnetic
3D – Three Dimensional
FEM – Finite Element Method
CPU – Central Processing Unit

TABLE OF CONTENTS

CHAPTER 1	INTRODUCTION AND THESIS SUMMARY	1
	1.1 Introduction	1
	1.2 Thesis Synopsis	2
	1.3 Interdisciplinary Applications of Pt and Au Nanoparticles	4
	1.4 References	6
CHAPTER 2	MICROWAVE TECHNIQUES FOR ELECTRICAL CHARACTERISATION OF METALLIC NANOPARTICLES	7
	2.1 Introduction	7
	2.2 Historical Development	8
	2.3 Methods of Nanoparticles Synthesis	9
	2.4 Characterisation of Nanoparticles	10
	2.5 Fundamental Aspects of the Interaction of Microwaves with Materials ..	11
	2.6 The Main Microwave Techniques for Electrical Characterisation	11
	2.7 Alternative Approaches for Electrical Characterisation of Metallic NPs..	14
	2.8 Resonator Perturbation Analysis	17
	2.9 Application of Resonator Perturbation Theory	19
	2.8.1 Magnetic Dipole Adsorption in Non-Magnetic Samples	19
	2.10 References	23
CHAPTER 3	MICROWAVE THEORY FOR MATERIAL CHARACTERISATION	28
	3.1 Introduction	28
	3.2 Overview of Microwave Techniques for Material Characterisation	28
	3.3 “Why Microwaves?” for Material Characterisation	29
	3.4 Non-Resonant Methods	29
	3.4.1 Reflection Methods	30
	3.4.2 Open Reflection Method	30
	3.4.3 Open Ended Coaxial Reflectance Probe	31
	3.5 Resonant Methods	32
	3.5.1 Basic Parameters of Dielectric Resonator	32
	3.5.2 Transmission Mode Measurements with Resonators	34

3.5.3 Resonator Spectral Response in Transmission Mode	34
3.5.4 Two-port Resonator Analysis with Symmetrical Coupling	35
3.5.5 Theoretical Calculations of Dielectric Resonators Parameters	40
3.5.6 Resonant Perturbation Technique	44
3.6 Modelling of the Open Ended Coaxial Probe	45
3.6.1 Capacitive Model	46
3.6.2 Variational Model	48
3.7 Validation of the Above Models Using Debye Liquids of Known Permittivity	52
3.8 Concept of Microwave Network	53
3.8.1 Scattering Parameters	54
3.8.2 Why Scattering Parameters?	55
3.8.3 Basics of the Vector Network Analyser (VNA)	55
3.9 References	57

CHAPTER 4 PREPARATION, PHYSICAL, ELECTROCHEMICAL AND MICROWAVE CHARACTERISATION OF METALLIC NANOPARTICLES	60
4.1 Introduction	60
4.2 Synthesis of Pt NPs of Different Sizes	61
4.2.1 “Why Chemical Methods are Used?” for the Synthesis of Metallic NPs	61
4.2.2 Reagents	61
4.2.3 Micellar Method	61
4.2.4 Synthesis of Spherical 6.9 nm Nanoparticles	63
4.2.5 Colloidal Method	64
4.3 Transmission Electron Microscopy (TEM) Characterization	65
4.3.1 TEM Sample Preparation	66
4.4 Preparation of Electrode and Electrochemical Measurements	69
4.4.1 Experiment Details	69
4.4.2 Apparatus	69
4.4.3 Electrochemical measurements	71
4.4.4 Preparation of electrode	71
4.4.5 Cleaning and Characterisation Method for Pt NPs	72

4.5 Synthesise of Spherical Au NPs of Different Sizes	77
4.5.1 Reagents and Instrumentation	77
4.5.2 Synthesis of Au NPs of Different Size by the Frens Method	77
4.6 Chapter Summary	81
4.7 References	82

CHAPTER 5	3D ELECTROMAGNETIC SIMULATION OF COAXIAL PROBE AND SAPPHIRE DIELECTRIC RESONATOR	84
5.1	Introduction	84
5.2	Background	84
5.3	Modelling of the OCP and SDR	86
5.3.1	The Process (Flow Chart)	86
5.3.2	Main Strategies of Model Development	87
5.4	A Typical Model Set-Up	87
5.5	Performing a Simulation	88
5.6	Construction of K-connector Open Ended Coaxial Probe	89
5.6.1	Modelling the Actual K-Connector OCP	90
5.6.2	Excitations	92
5.6.3	Boundary Conditions	93
5.6.4	Material Properties	94
5.6.5	Generating the Solution	94
5.6.6	Meshing the structure	96
5.6.7	Post Processing and Simulation Results	97
5.6.8	Simulation Results of K-Connector OCP	100
5.6.9	Error Analysis	105
5.7	Modelling of Different Types of Open Ended Coaxial Probes (OCPs) ...	105
5.7.1	Simulation Results of Different Types of OCPs	107
5.8.	Modelling and Boundary Conditions of Sapphire Dielectric Resonator ..	111
5.8.1	Construction of Sapphire Dielectric Resonator	111
5.8.2	Modelling Methods in HFSS	112
5.8.3	Boundary Conditions and Mesh Seeding of SDR	112
5.8.4	Assigning Materials	114
5.8.5	Generating Solution	114
5.8.6	Post Processing	115

5.8.7 Calculations of SDR Parameters Using HFSS	118
5.8.8 HFSS Field Calculator	119
5.9 Parametric Analysis	120
5.9.1 Limitation of the Coaxial Probe System	120
5.9.2 Penetration Depth of the Coaxial Probe System	127
5.9.3 SDR System	128
5.9.4 Analysis of Results	130
5.10 Chapter Summary	132
5.11 References	134

CHAPTER 6 MICROWAVE CHARACTERISATION OF METALLIC NANOPARTICLES	135
6.1 Introduction	135
6.2 Validation of the Coaxial Probe Models	136
6.2.1 Instrumentation	136
6.2.2 Coaxial Probe Technique	136
6.2.3 Fabrication Process of K-Connector Coaxial Probe	137
6.2.4 Microwave Calibration Procedure	139
6.2.5 Modelling the Aperture Admittance of the Probe	140
6.2.6 Capacitive Model	140
6.2.7 Calibration of the Probe Using Polar Liquids of Known Permittivity	141
6.2.8 Variational Model	146
6.3 Coaxial Probe System for the Characterisation of Pt and Au NP	148
6.3.1 Microwave Measurement	148
6.3.2 Analysis and Discussion	153
6.3.3 DC Measurement	162
6.3.4 Analysis of Results	164
6.4 SDR System for the Characterisation of Pt and Au NPs	166
6.4.1 Construction of SDR	166
6.4.2 Superfish Analysis of SDR	167
6.4.3 Calculation of Unloaded Q Using MathCAD Program	169
6.4.4 SDR Experiment	171
6.4.5 Analysis of Results	174

6.5 Hydrogen Adsorption on Pt NP Films	179
6.5.1 Introduction	179
6.5.2 Experimental setup	180
6.5.3 Analysis of Results	184
6.6 Random Network Circuit Construction	188
6.6.1 Typical Response of the R-C Network	190
6.6.2 Typical Response of R-L Network	192
6.7 Chapter Summary	193
6.8 References	195
 CHAPTER 7	
CHAPTER 7: CONCLUSIONS AND RECOMMENDATIONS	197
7.1 Conclusions	197
7.2 Recommendations	199

APPENDIX A	Two-Port Resonator Analysis with Asymmetrical and Symmetrical Coupling	204
APPENDIX B	Detailed Derivation to Obtain the Locus of $\varepsilon(\omega)$ in the Debye Model ..	208
APPENDIX C	Detailed Procedure of Synthesis of Pt NPs (3.0 nm)	210
APPENDIX D	Periodic Table	216
APPENDIX E	Detailed Procedure of Synthesis of Spherical Pt NPs (6.9 nm)	217
APPENDIX F	Detailed Procedure of Synthesis of Pt cubic NPs (8.6 nm)	221
APPENDIX G	Detailed Procedure of Preparation of 0.5 M H₂SO₄ (Electrolyte)	225
APPENDIX H	Cyclic Voltammetry Profile of Spherical Pt NPs (6.9 nm)	227
APPENDIX I	Cyclic Voltammetry Profile of Spherical Pt NPs (3.0 nm)	230
APPENDIX J	Detailed Procedure for the Synthesis of Au NPs (8.2, 16.5, & 24.8 nm)	234
APPENDIX K	Determination of Complex Permittivity of Unknown Materials Using Capacitive Model.....	237
APPENDIX L	Fringing Field Capacitances Obtained From the HFSS Simulation for Different Types of OCPs	239
APPENDIX M	First Order Approximation of Aperture Admittance Using Variational Method	246
APPENDIX N	Necessary Polynomial Coefficients for the Calculation of $E(m)$	247
APPENDIX O	HFSS Field Calculator Code for Calculation of SDR Unloaded Q	248
APPENDIX P	MathCAD for Calculation of Unloaded and Loaded Quality Factor of SDR (e.g. Superfish model, HFSS model)	249
APPENDIX Q	Limitation of RG-405, RG-402 and SMA Open Ended Coaxial Probe	254
APPENDIX R	Anritsu K- Connector (Machining Dimension)	262
APPENDIX S	Determination of Complex Permittivity of Unknown Materials Using Variational Model	263
APPENDIX T	Coaxial Probe Analysis of Metal Oxide Nanoparticles	265
APPENDIX U	Input Text File for the Superfish Analysis of SDR	269
APPENDIX V	Coaxial Probe Analysis of Pure Metal Nanoparticles	270
APPENDIX W	Detailed Derivation to Obtain the Internal Inductance of Porous Conducting Layer	275
APPENDIX X	The Components Values Chosen for the R-C and R-L Network Models	277
APPENDIX Y	MATLAB Script for Random Network Circuits	279

Key Original Contributions Made

- The implementation and validation of a full aperture admittance model (i.e. capacitive model) for the open ended coaxial probe (OCP), by carrying out experiments on several different dielectric materials including low, medium and high permittivity materials.
- Synthesis of platinum (Pt) and gold (Au) nanoparticles (NPs) of various sizes, with electrochemical structural characterisation of those synthesised NPs using cyclic voltammetry (CV).
- Fabrication of a novel miniaturised K-connector OCP for the characterisation of metallic NP films.
- Development of three dimensional (3D) full wave K-connector OCP using the commercially available Ansoft High Frequency Structure Simulator (HFSS) software, which further validated the aforementioned capacitive model. This model is also novel in the sense that it is the smallest probe in the literature and nobody has developed the actual K-connector OCP so far.
- Development of 3D full wave model of a sapphire dielectric resonator (SDR) using the HFSS software. Also the development of SDR model using the freely available Superfish software and post processing to extract the microwave parameters of interest by suitable MathCAD programs.
- Extremely sensitive electrical characterisation of synthesised Pt and Au NPs films by means of OCP and SDR microwave techniques. These measurements are novel and are first attempts to characterise NPs films using OCP and SDR techniques. The results of these experiments show good agreement with theory.
- Microwave properties of synthesised Pt NPs by means of hydrogen (H_2) adsorption using the OCP technique. This experiment itself is novel since no systematic work has been reported on the microwave properties of Pt NPs by means of H_2 adsorption.
- Development of *universal models* for different types of OCPs (i.e. K and SMA connectors, RG-405 and RG-401 cables) based on the developed 3D full wave OCP models using HFSS software by mapping the complex admittance (Y_L) of the probe obtained from the 3D full wave OCP onto a complex permittivity (ϵ_1 and ϵ_2) plane.

CHAPTER 1

INTRODUCTION AND THESIS SUMMARY

1.1 Introduction

In the last decade synthesis, characterisation and understanding of a material with very small particle size have become the most interesting research area due to their novel properties and potential applications in different fields. Metal nanoparticles (NPs) offer enormous promise as functional units for the development of sensors, photo-electrochemical cell and general nanoelectronic devices due to their ease of synthesis and stability [1]. However, they exhibit unconventional properties and functionalities which differ significantly from those of the bulk parent metals. The properties of the NPs cannot be studied without the knowledge of size and structure (or shape) [2]. Experimental studies on the electrical properties of nanoparticles are limited [3]. Measuring the electrical conductivity of such metal NPs represents a challenging and key experiment and necessitates the use of innovative experimental techniques. In the context of this thesis, the focus will be solely on the electrical characterisation of metallic NPs using a novel approach, applicable to a wide range of materials for which direct electrical contact is unfeasible: namely, contactless microwave measurements using a coaxial probe and dielectric resonator (DR) techniques.

This research is the first attempt to determine the electrical properties of Pt and Au NP films using microwave techniques. The ease of preparation of these NPs was one of the main considerations in choosing them for the present study. Initially the experiments were carried out on Pt NPs using the coaxial probe technique, since this technique is relatively cheap, non-destructive, broad bandwidth and no special sample preparation is needed. The Pt was selected due to its ease of synthesis and its unique catalytic [4, 5] properties. The results obtained from this technique provided the motivation to evaluate the electrical properties of Au NPs, selected because it is relatively cheap and can be synthesised in various sizes [6]. The results obtained from this technique provided the motivation to characterise both the Pt and Au NPs using the DR technique. Unlike the coaxial probe technique, the DR method is highly sensitive but the achievable measurement accuracy is limited since this technique does not have swept frequency capability like the coaxial probe method. The results obtained from

the DR technique show a good agreement with theoretical predictions. There are many advantages of using these microwave techniques (i.e. coaxial probe and DR) over other methods. The main advantages with such microwave sensors are their capability to measure non-destructively and contactlessly, using penetrating waves without any health hazards to personnel and also being fast [7]. This chapter consists mainly of an overview of the structure of this thesis followed by the interdisciplinary applications of Pt and Au NPs.

1.2 Thesis Synopsis

- **Microwave Techniques for Electrical Characterisation of Metallic Nanoparticles (Chapter 2)**

This chapter will cover the reviews of historical development of nanotechnology, the existing various NP synthesis methods, characterisation techniques of NPs that are in use currently, the main microwave techniques for the electrical characterisation of NPs and also the existing alternative approaches for the electrical characterisation of NPs, followed by the relevant resonator perturbation theory.

- **Microwave Theory for Material Characterisation (Chapter 3)**

The two main microwave techniques (i.e. non-resonant and resonant methods) for the material characterisation are explained. Existing aperture admittance models (i.e. capacitive and variational model) for the open ended coaxial probe (OCP), the transmission mode measurement with microwave resonator along with derivation of expression of their resonant frequency and unloaded quality factor are detailed. The concept of microwave networks, scattering parameters and Debye theory for dielectric response are described.

- **Preparation, Physical and Electrochemical Characterisation of Metallic Nanoparticles (Chapter 4)**

The various chemical methods carried out in the synthesis of various sizes of metallic (i.e. Pt and Au) NPs, ranging from 3 nm, 6.9 nm, 8.6 nm (i.e. Pt) and 8.2 nm, 16.5 nm, 24.8 nm (i.e. Au) are explained. Secondly, the cleanliness, structure and the size of those synthesised NPs (i.e. Pt) were validated electrochemically using the cyclic voltammetry (CV). Thirdly, in-depth structural characterisations of those particles (i.e. Pt and Au) were performed using

transmission electron microscopy (TEM). Finally, this chapter discusses the relevant experimental details and all of the obtained results.

- **3D Electromagnetic Simulation of Coaxial Probe and Sapphire DR (Chapter 5)**

This chapter provides a full account of the development and validation of the 3D full wave models of the OCP (i.e. K and SMA connectors, and using RG-405, RG-402, RG-401 cables) and sapphire DR. Development of the 3D full wave OCP model enabled validation of the capacitive model by simulation. Moreover, later sections in this chapter describe the limitation of the capacitive model of the OCPs by mapping the complex admittance (Y_L) values onto the complex permittivity (ϵ_1 and ϵ_2) plane obtained from the developed 3D full wave models of OCPs. Such mappings provide a visual representation of how the complex admittance, Y_L , varies with ϵ_1 and ϵ_2 at a fixed frequency and give an indication of the sensitivity of the parameters (i.e. C_0 and C_1) of the capacitor model. In the last phase of this chapter, the experimental results obtained from microwave studies for the Pt oxide and Au NP films were supported with a relevant 3D full wave sapphire DR model, which closely resembled and predicted the correct signature. Finally, this chapter discusses the relevant simulation details and the results obtained.

- **Microwave Characterisation of Metallic Nanoparticles (Chapter 6)**

There are several essential parts of this research which are covered in this chapter. Firstly, fabrication of K-connector OCP, and implementation and validation of aforementioned aperture admittance models (i.e. capacitive and variational models) were described, by carrying out experiments on several different dielectric materials including low, medium and high permittivity materials. Secondly, microwave electrical characterisations of those NP films were carried out using the OCP (i.e. with the established capacitive model) and sapphire DR. Thirdly, the DC and microwave electrical characterisation of the Pt and Au NP films are compared. Fourthly, the surface modifications of the Pt NPs were carried out by means of hydrogen adsorption using the OCP technique. Fifthly, the results obtained from the microwave experimental studies for the Pt oxide, pure Pt and Au NP films were theoretically supported with a simple modelling based on random R-C and R-L network arrangements, which closely resembled and predicted the correct signature. Finally, this chapter discusses the relevant experimental details and all of the obtained results.

- **Conclusions and Recommendations (Chapter 7)**

A brief summary of the work carried out so far and suggestions for future studies are discussed.

1.3 Interdisciplinary Applications of Pt and Au Nanoparticles

Recent advances in the production and measurement on nano-scale systems have revitalized the study of Pt and Au metallic particles due to their ease of synthesis, stability, unconventional properties and functionalities which differ significantly from those of the bulk metals. Applications of NPs for catalysis and biological sensors (among others), are now receiving enormous attention due to their distinctive physical properties (e.g. high surface area to volume ratio, adsorption and scattering behaviour).

- **Widely Used as Catalysis [8]**

Chemical catalysis benefits especially from Pt and Au NPs due to their large surface to volume ratio. The application potential of NPs in catalysis ranges from fuel cell to catalytic converters and photo catalytic devices. Catalysis is also important for the production of chemicals. Pt NPs are now being considered in the next generation of automotive catalytic converters because the very high surface area of nanoparticles could reduce the amount of Pt required.

- **Protein Detection [9]**

Understanding the functionalities of proteins is extremely important for further progress in human well-being. Au NPs are widely used in immunohistochemistry to identify protein-protein interactions. However, the multiple simultaneous detection capabilities of this technique are limited. Surface enhanced Raman scattering spectroscopy is a well-established method for detection and identification of single dye molecules. By combining both techniques in a single NP probe one can drastically improve the multiplexing capabilities of protein probe.

- **Application in Cancer Cell Diagnostics [10]**

Au NPs act as excellent sensors and novel contrast agents for optical detection due to their enhanced adsorption and scattering. Using the surface plasmon resonance (SPR) scattering images and SPR adsorption spectroscopy generated from antibody conjugated Au NPs can be useful in molecular biosensor techniques for the diagnosis and investigation of oral living cancer cells in vivo and in vitro.

- **Nitric Oxide (NO) sensor [11]**

Pt NPs can be electrodeposited directly on the surface of multi-walled carbon nanotubes (MWNTs) by using a cyclic potential scanning technique to form a novel nano-Pt/MWNT modified electrode. The Pt/MWNT modified electrode can be used as a sensor to directly determine the Nitric Oxide concentration in aqueous solution.

1.4 References

1. H.S.P. Wong, "Nanoelectronics-Opportunities and challenges", *International Journal of High Speed Electronics and Systems*, pp. 83-94, Vol. 16, 2006.
2. C.N.R. Rao, G.U. Kulkarni, P.J. Thomas and P.P. Edwards, "Size-Dependent Chemistry: Properties of Nanocrystals", *Chemistry-A European Journal*, Vol. 8, No. 1, pp. 28-35, 2002.
3. J.H. Liu, C.L. Chen, H.T. Lue and J.T. Lue, "Measurement of Dielectric Constant of Metallic Nanoparticles by a Microwave Dielectric Resonator", *Measurement Science and Technology*, Vol. 13, pp. 2032-2037, 2002.
4. S. Park, S.A. Wasileski and M.J. Weaver, "Electrochemical Infrared Characterization of Carbon-Supported Platinum Nanoparticles: A Benchmark Structural Comparison with Single-Crystal Electrodes and High-Nuclearity Carbonyl Clusters", *Journal of Physical Chemistry B*, Vol. 105, No. 40, pp. 9719-9725, September 2001.
5. P. Marquardt, L. Borngen, H.R. Kunz and G.A. Gruver, "The Catalytic Activity of Platinum Supported on Carbon for Electrochemical Oxygen Reduction in Phosphoric Acid", *Journal of Electrochemical Society*, Vol. 122, No. 10, pp. 1279-1287, 1975.
6. S. Panigrahi, S. Basu, A. Praharaj, A. Pande, S. Jana, A. Pal, S.K. Ghosh and T. Pal, "Synthesis and size-selective Catalysis by Supported Gold Nanoparticles: study on Heterogeneous and Homogeneous Catalytic Process", *Journal of Physical Chemistry*, Vol. 111, pp. 4596-4605, December 2007.
7. A.P. Gregory and R.N. Clarke, "A Review of RF and Microwave Techniques for Dielectric Measurements on Polar Liquids", *IEEE Transactions on Dielectrics and Electrical Insulation*, Vol. 13, No. 4, August 2006.
8. Z. Liu, L.M. Gan, L. Hong, W. Chen, J.Y. Lee, "Carbon-supported Pt nanoparticles as catalysts for proton exchange membrane fuel cells", *Journal of Power Sources*, Vol. 139, No. 1-2, pp. 73-78, 2005.
9. Y.C. Cao, R. Jin, J.M. Nam, C.S. Thaxton, and, C.A. Mirkin, "Raman Dye-Labeled Nanoparticle Probes for Proteins", *Journal of the American Chemical Society*, Vol. 125, No. 48, pp. 14676-14677, 2003.
10. I.H. El-Sayed, X. Huang and M.A. El-Sayed, "Surface Plasmon Resonance Scattering and Adsorption of anti-EGFR Antibody Conjugated Gold Nanoparticles in Cancer Diagnostics: Applications in Oral Cancer", *Nano Letters*, Vol. 5, No. 5, pp. 829-834, 2005.
11. L. Zhang, Z. Fang, G.C. Zhao and X.W. Wei, "Electrodeposited Platinum Nanoparticles on the Multi-Walled Carbon Nanotubes and its Electrocatalytic for Nitric Oxide", *International Journal of Electrochemical Science*, Vol. 3, pp. 746-754, 2008.

CHAPTER 2

MICROWAVE TECHNIQUES FOR ELECTRICAL CHARACTERISATION OF METALLIC NANOPARTICLES

2.1 Introduction

The synthesis and characterisation of metal nanoparticles (NPs) have attracted intense research interest in the area of nanoscience, molecular chemistry and microwave engineering due to their unconventional properties and functionalities, which are different from those of the bulk metals. When a metal particle with bulk properties is reduced to a size of a few hundred atoms, the density of states in the conduction band decreases to such an extent that the electronic properties change dramatically. NP based materials are of interest because of their unique electrical and chemical properties. Specifically, platinum (Pt) and gold (Au) NPs have attracted much interest due to their ease of synthesis and their unique catalytic [1, 2, 3] activities, stability and potential importance as functional units for the construction of sensing [4], photo-electrochemical cell, and micro-electronic devices [5]. The properties of the NPs cannot be studied without the knowledge of size and structure [5]. Transmission electron microscopy (TEM), scanning electron microscopy (SEM), X-ray diffraction (XRD) and cyclic voltammetry (CV) are generally used to characterise the size and structure of NPs. Detailed description of these techniques can be found in the following section. Experimental studies on the electrical properties of nanoparticles are limited [6]. Although the electrical characterisation in bulk samples constructed by NPs has been investigated [7, 8], such studies of bare NPs and NPs stabilised by organic molecules are lacking. Measuring the electrical conductivity of such metal NPs represents a challenging and key experiment and necessitates the use of innovative experimental techniques. It would be interesting to explore the electrical properties of NPs stabilised by organic molecules and without those organic molecules (i.e. bare NPs). However, to the best of the author's knowledge there have been very few reports of investigation on the electrical properties of Pt and Au NP films [9]. Among those investigations, the direct contact measurement of the current-voltage characteristics of individual particles represents one such approach, where most of the authors have used two/four point probe techniques. Here we highlight an alternative, novel approach, applicable to a wide range of materials, for which direct electrical contact is unfeasible: namely,

contactless microwave measurements using a coaxial probe and dielectric resonator techniques. This research is the first attempt to determine the electrical properties of Pt and Au NP films using microwave techniques. The main advantage with microwave sensors is the capability to measure non-destructively, using penetrating waves, without health hazards to personnel [10].

This chapter will consist mainly of a review of the historical development of nanotechnology, the existing NP synthesis methods, characterisation of NPs, the main microwave techniques for the electrical characterisation of NPs and also the existing alternative approaches for the electrical characterisation of NPs.

2.2 Historical Development

Colloid science started essentially in 1861, where the scientist Ostwald classified dispersed systems of particles with sizes 1-100 nm as colloids [11]. Recent studies on NPs began in 1962 with the work of Kubo [12]. He predicted that the physical property of small metal particles will be quite different from those of bulk. The concept of atomic precision was first suggested in 1959 by the Physics Nobel Laureate Richard Feynman in a celebrated lecture to the American Physical Society [13]. Research on small particles (including atomic and electronic structure determination using experimental studies and theoretical methods) commenced in 1970 [14]. In 1980, atom clusters with selected size ranges were produced and chemical and physical property studies began [15]. Cluster assembled nano-materials have been getting great attention during the last couple of years. Recently, carbon clusters including both fullerenes and nanotubes have been arousing much interest [16, 17].

The developments in microscopy technology have enabled us to visualise images of nanostructures and have largely dictated the development of nanotechnology. Nanotechnology is the collaboration of both the science and engineering of making materials, functional structures and devices on the nano-scale [13]. Nanotechnology has become an essential and active area of research which is rapidly developing in industrial sectors and spreading over to almost every field of science and engineering.

2.3 Methods of Nanoparticles Synthesis

Various methods have been reported by many researchers for the synthesis of NPs of materials of interest and of varying size range [18, 19]. The reproducibility and control of the size and the shape of particles are the prime important factors in the synthesis of NPs. The synthesis of NPs generally falls into two main synthetic techniques, namely, physical and chemical methods [18]. The most widespread physical method is using inert gas evaporation [20], which is used for metals which are consolidated under vacuum conditions. There are other techniques such as Joule heated ovens, sputtering, etc. [20]. In-depth details of the synthesis of NPs using the physical techniques are not covered in this section since it is beyond the scope of this thesis. This thesis mainly focuses on the chemical synthesis* method, since this method is more advantageous due to its resulting chemical homogeneity owing to mixing of the constituents at a molecular level. NPs synthesis can be summarised as shown in fig. 2.1.

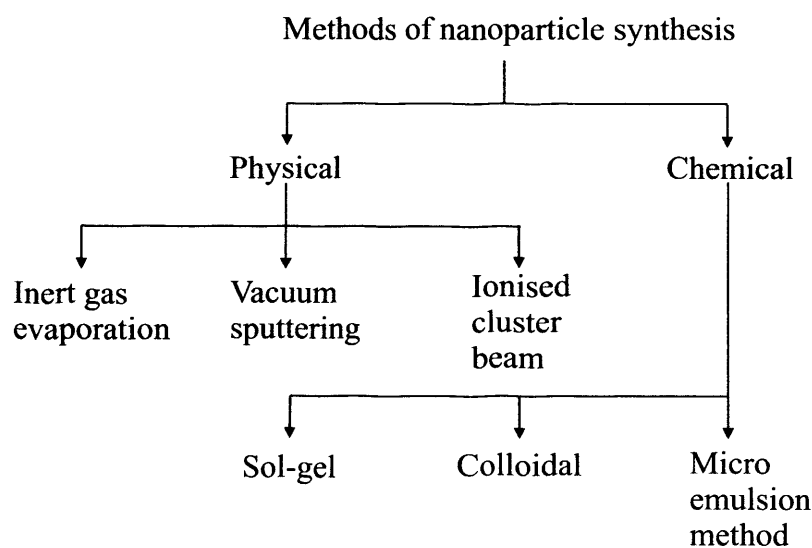


Figure 2.1 The main synthesis methods of NPs.

Sol-gel techniques can be used to produce ceramic materials through the processes of gelation, precipitation and hydro-treatment [21, 22]. The advantages of this technique are high mechanical strength and high thermal stability of the NPs. Metal NPs are also prepared by colloidal methods, for example cubic Pt NPs (of size ~ 9 nm) can be synthesised by this method. The micro-emulsion method has been used to produce metallic, semi-conducting, superconducting as well as alloy NPs [23]. For example, Pt NPs of size ~ 3 nm can be made

* For more reasons for the usage of chemical synthesis of NPs, please refer to section 4.2.1.

by this method. The main advantages of colloidal and micro-emulsion methods are that they allow synthesis of NPs of different sizes, are a relatively easy method, and (most importantly) allow the precipitated NPs to be cleaned very easily by removing the chemicals present due to the synthesis process.

2.4 Characterisation of Nanoparticles

Physical characterisation of NPs is vital to understand the behaviour and properties of nano-materials aiming at implementing nanotechnology, thus controlling their behaviour and designing new material systems with super performance. Characterisation falls into two main categories, property measurement and structural analysis.

Structural analysis is carried out by a variety of microscopy and spectroscopy techniques. Direct imaging of the NPs is possible using transmission electron microscopy (TEM) and scanning electron microscopy (SEM) [24] [i.e. both scanning tunnelling microscopy (STM) and atomic force microscopy (AFM)]. TEM imaging (in conjunction with selected area electron diffraction) is valuable for the analysis of crystalline samples. The greatest advantage of TEM is its ability to measure the size, shape and structure of the NPs. Both STM and AFM are used for surface analysis of NPs. Apart from these instruments, there are other techniques like X-ray diffraction (XRD) which provides information about the structure by diffraction and interference effects of photons or electrons, and Raman spectroscopy [25] as an aid to study the optical properties of the NPs. But cyclic voltammetry (CV) is a potential-controlled electrochemical technique, where the current that flows through the working electrode is registered versus the applied potential. This technique provides much information about the condition of surface of the working electrode or about the test solution. However, all these techniques except the CV, are expensive, require several preparatory steps as well as prior digestion of samples. For these reasons, the CV has been found to be relatively cheap, versatile, and sensitive enough without needing several conditioning steps before analytical measurements are taken [26], from which the cleanliness, structure, and the size of the NPs can be analysed (i.e. from the resulting CV profile) [27].

Electrical and electrochemical analyses of NPs are useful for the fabrication of sensors, photo electrochemical and general nano-electronic devices [28]. The measurement of electrical conductivity and permittivity gives valuable information about the electronic, ionic, different

relaxation processes, and different polarisation mechanisms in nano-structured material [29]. Impedance spectroscopy has also emerged as a powerful experimental tool for the characterisation of electrical properties of nano-structured materials [30].

2.5 Fundamental Aspects of the Interaction of Microwaves with Materials

When microwaves are directed towards a material, part of the microwave energy is reflected, part is transmitted through the surface and part of it is adsorbed. The proportions of energy which falls into these three categories have been defined in terms of the dielectric properties. The essential electrical property through which the interactions are described is the complex permittivity of the material (ϵ) and is a complex quantity expressed as follows [31]:

$$\epsilon = \epsilon_1 - j\epsilon_2 \quad (2.1)$$

where the real part of the permittivity (ϵ_1) is a measure of how much energy from an external electric field is stored in a material. The imaginary part of the permittivity (ϵ_2) is called the loss factor and is a measure of how dissipative or lossy a material is to an electric field and $j = \sqrt{-1}$. ϵ_2 is always greater than zero and is usually much smaller than ϵ_1 . The loss factor includes the effects of both dielectric loss and conductivity. Loss is commonly expressed in terms of the loss tangent (or dissipation factor), $\tan\delta = \epsilon_2/\epsilon_1$. In some areas (e.g. thin metallic films, biomedical measurements), it is common practice to express loss in terms of an equivalent conductivity, σ , measured in S/m, where $\sigma = 2\pi f\epsilon_2\epsilon_0$, where f is the measurement frequency and ϵ_0 is the permittivity of free space. Electrical conductivity exists because of the presence of conduction electrons that are free to move inside the material.

2.6 The Main Microwave Techniques for Electrical Characterisation

Utilizing a material for a specific application necessitates understanding the properties of the material. From the electromagnetic point of view, materials can be identified by their complex permittivities and permeabilities. There are various approaches for identifying these parameters, which generally fall into non-resonant and resonant methods. The first category (i.e. non-resonance method) includes reflection methods [32] and transmission/reflection methods [33, 34]. These techniques usually have the swept frequency ability for the measured frequency range. In reflection methods, the electromagnetic waves are directed towards a sample and the properties of the material sample are deduced from the reflection coefficient

(i.e. based on the broadband scattering parameters (S-parameters)) at a defined reference plane. This method can only measure either permittivity or permeability of the material under test. In a transmission/reflection method, the sample is inserted in a piece of transmission line, and the properties of the sample under test are deduced on the basis of the reflection from the sample and the transmission through the sample. This is a widespread method in the measurement of the permittivity and permeability of low conductivity material. The second category (i.e. resonant method) [35] generally includes the resonant perturbation method, which is based on resonant perturbation theory. Unlike the reflection and transmission/reflection techniques, resonant techniques do not have the broadband frequency capabilities. Only a single or certain frequency points can be measured. For a resonator with given electromagnetic boundaries, when part of the electromagnetic boundary condition is changed by introducing a sample, its resonant frequency (f_0) and quality factor (Q) will also be changed, from which the properties of the sample can be derived (i.e. depending on whether the sample is introduced into the electric field or magnetic field, the permittivity or permeability of the sample is being measured).

To the best of the author's knowledge, there have been very few reports of investigation on the electrical properties of NPs, the most of these being low frequency electrical characterisation of nano-composite materials [35, 36] (e.g. sol-gel derived metal NPs [37], metallic composite and semi-metallic thin films [38, 39, 40], metal-carbon covalent bond [41, 42]) and NPs suspensions [9] using various measurement techniques. Most of these have used the two/four point measurement technique. Numerous techniques have been widely adopted for the measurements of dielectric properties of the materials over radio frequencies (RF) and microwave frequencies (MF) [43, 44]. The number of such techniques and variations that exist is, however, so great that it be virtually impossible to discuss all of these in this chapter. The most widely used techniques are those based on measurement of either reflection coefficient or resonant cavities. In the cavity perturbation technique, which was widely adopted for microwave dielectric properties measurements [45, 46], the size of the sample under test must be much smaller than the cavity size. This measurement method is highly sensitive but the achievable measurement accuracy is limited since this technique does not have swept frequency capability. The reflectance method is the most widespread non-resonant technique currently in use because of the popularity of the coaxial sensors, also known as coaxial probe, coaxial reflectance probe, coaxial-line probe or open-ended coaxial probe. Coaxial lines are used as sensors for in-situ measurement of electrical properties of

various types of materials [10]. It is to be noted that the coaxial probe has several advantages over other sensors based on open-ended waveguide [47, 48], the most important being its simplicity, its high speed, versatility, low cost and non-destructive nature over a broad frequency band. From the stand point of this research, however, the most relevant and suitable methods are those based on such a coaxial probe and a cavity resonator. Vector Network Analysers (VNAs) are usually employed in all modern non-resonance and resonance techniques for measuring the scattering parameters (S-parameters – i.e. S_{11} and S_{21}) from which the material properties can be extracted.

The coaxial probe technique has been established over the last 20 years as a standard tool for evaluating electrical properties in the microwave frequency range. It involves termination of a short length of flanged coaxial transmission line with the material under test, followed by measurement of the reflection coefficient ρ at the material interface. Recently, Hussain *et al.* [49] proposed a different method for determining the electromagnetic properties of nanoparticles colloids using two different experimental techniques in order to cover a broadband frequency range. A Novocontrol Spectrometer and a dielectric probe kit together with a vector network analyzer was used for low and high frequencies measurements, respectively, to calculate the complex permittivity of the sample.

Lee and Collier [38] have used microwave transmission technique to measure the sheet resistance of thin metallic NiCr and Al films as shown in fig. 2.2. Liu *et al.* [6] have used a dielectric resonator to measure the dielectric constants of metallic nanoparticles. Similarly, Yeh *et al.* [50] have carried out measurement of the dielectric constant of metallic NPs embedded in a paraffin rod at microwave frequencies using a dielectric resonator. Recently, Krupka *et al.* [51] have reported a dielectric resonator technique for the measurement of conductivity and surface resistance of thin metal aluminium films deposited on a dielectric substrate. Similarly, Jarvis *et al.* [52] have used dielectric resonator for measuring the electrical conductivity of carbon nanotubes at microwaves to millimetre frequencies.

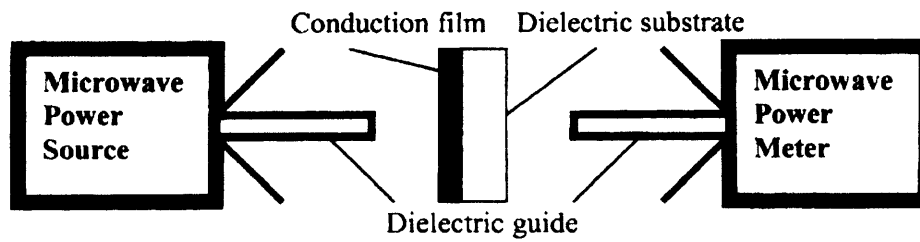


Figure 2.2 Shows the measurement set-up of thin films mounted on a dielectric substrate using a transmission technique [38].

Alternatively, Coors *et al.* [53] have measured the conductivity of yttrium barium cerate, in the frequency range of 20 Hz – 6 MHz, using impedance spectroscopy over the temperature range of 100⁰ – 900 ⁰C. Similarly, Ma *et al.* [54] have obtained the highest conductivity for the same material at 900 ⁰C in the frequency range of 1 Hz – 1 MHz, also using most powerful and accurate impedance spectroscopy (i.e. Solartron 1260 analyser provides spanning of 10 μ Hz – 32 MHz). Impedance spectroscopy is a non-destructive method to study the electrical properties of solids by measuring both the resistive (real part) and reactive (imaginary part) of complex impedance spectroscopic parameters by using an L-C-R meter.

2.7 Alternative Approaches for Electrical Characterisation of Metallic NPs

Given the very rare employment of microwave techniques for the electrical characterisation of NPs, it is sensible to mention other pertinent methods. A survey of the literature has divulged very few non-microwave electrical characterisation techniques; examples include the four point probe measurement and interdigitated microarray (IDA) electrode along with potentiostat (or electrometer). There have been numerous reports of four point resistance measurements of nanoparticles films at low frequencies [55]. Fang and Zang [9] proposed different methods for determining the electrical conductivity of gold nanoparticles in chloroform and toluene suspensions. The resistance of the gold nanoparticles was measured by a parallel Pt electrode from which the DC conductivity of the gold nanoparticle suspension was calculated using an Agilent electrometer in V/I mode. Fugita *et al.* [56] reported the measurement of DC resistivity of samples containing metal NPs by a conventional four probe method as early as 1969. Since then the four point probe measurement has been consistently employed by most of the researchers in the investigation of DC electrical resistivity of small

NPs. For example, Chatterjee and Chakravorty [37] have used the four point probe technique for the DC resistivity measurement of sol-gel derived metal NPs over the temperature range 80-300 K. Similarly, Lee and Collier [38] have used this technique to measure the sheet resistance of thin metallic NiCr and Al films. Recent employment of four point probe technique has been by Mallick *et al.* [57] and Yang *et al.* [58], who have measured the electrical conductivity of copper NPs composite materials and conducting polymer poly (3, 4-ethylenedioxythiophene) (PEDOT) NPs, respectively. Regarding the use of four point probe technique, Gorzny *et al.* [59], have measured the resistivity of tobacco mosaic virus (TMV)-based nanostructure using four independently controlled scanning tunnelling microscopes (STM) as a four point probe as shown in fig. 2.3. Using STM as a four point probe has advantages over other methods since it is possible to change the tip position and separation on the investigated nano-object. In the four point probe set up using an additional pair of sensing tips (i.e. compared to the two-point probe), there is no current flow through the high impedance voltmeter, so effects associated with the tip/nanowire (or material under test) interface are eliminated.

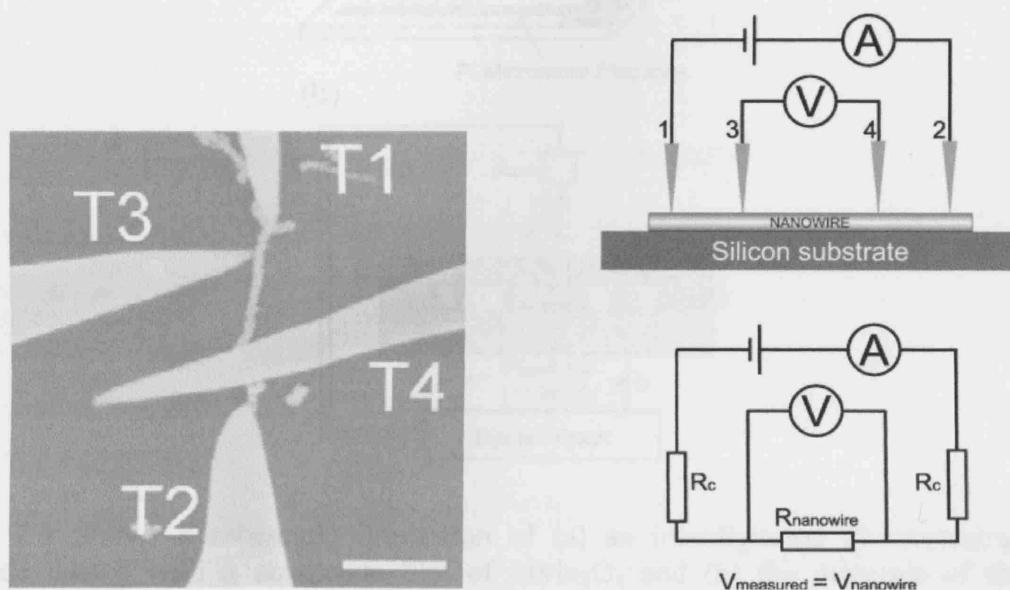


Figure 2.3 Left: shows the SEM images of a four point probe measurement on Pt covered tobacco mosaic virus (TMV) head to tail aggregation (scale bar is 500 nm). Top right: schematic of a four probe measurement. Tips T1 and T2 source a current, while the potential difference is measured across the tips T3 and T4. Bottom right: electrical representation of four probe measurement [59].

Very recently, Ghosh *et al.* [41] have studied the conductivity of palladium NPs, passivated by metal-carbon covalent bonds (Pd-C), using by electrochemical measurements with a

dropcast thick film of the particles on an interdigitated array (IDA) electrode. The same authors [42, 60] have reported measurement of conductivity of Ti-C and Ru-C using the same IDA electrode. Similarly, Nishizawa *et al.* [61] have measured the electrical conductivity of LiMn_2O_4 by means of an interdigitated micro-array electrode coated with a uniform dense film of LiMn_2O_4 as shown in fig. 2.4. The electronic conductivity was determined by measuring the resistance of the sample using an electrometer in the V/I mode, where the resistance (R) is measured from the slope of the current-voltage characteristics. The dc electrical conductivity (σ) of the deposited film is calculated by $\sigma = (1/R \cdot d)(w/l)$, where w/l is the IDA electrode geometrical factor (l is the total length of the electrode width and w is the electrode distance) and d is the film thickness.

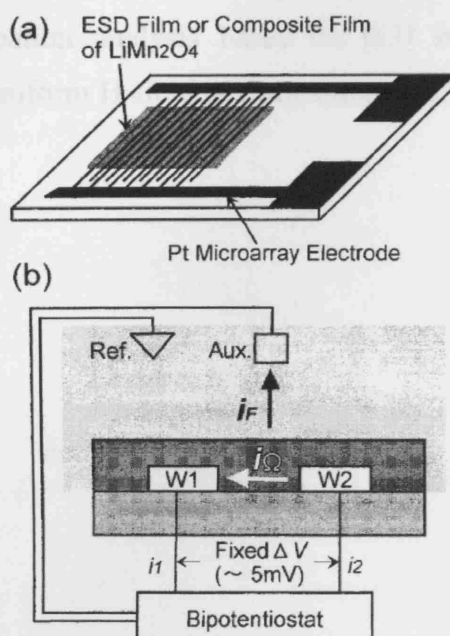


Figure 2.4 Shows a schematic illustration of (a) an interdigitated Pt microarray (IDA) electrode coated with a composite film of LiMn_2O_4 and (b) the principle of the in-situ conductivity measurement [56].

A detailed description of each of the non-microwave techniques mentioned above is beyond the scope of this thesis. These techniques have their relative strengths and weaknesses. The main limitation of these techniques over the microwave techniques is the use of electrical contact, except for the IDA electrode technique, which is an in-situ (or contactless) two point probe method. The IDA electrode has a major limitation in that they are not easy to construct, which limits their availability. Another limitation of the non-microwave techniques is the

surface damage they produce; even though the damage is not very severe, it is sufficient to result in non-reproducible results. These techniques require a large specimen of material which sometimes is not accessible. The main strengths, especially of the four point probe method, lies in its established use and the fact that it is an absolute measurement without the need to recourse to calibrated standards.

2.8 Resonator Perturbation Analysis

Introducing a sample in the high magnetic field (H-field) region in a dielectric resonator will change both the frequency (f_0) and the quality factor (Q) owing to sample magnetisation. The expressions for resulting change Δf_0 and $\Delta (1/Q)$ have been derived in various texts mostly using Maxwell's equations which involve complicated mathematics (e.g. [62]). Here, a simplified resonator perturbation analysis based on [63] is presented, considering the placement of a sample in a uniform H-field in a resonator. The equivalent circuit is shown in fig. 2.5.

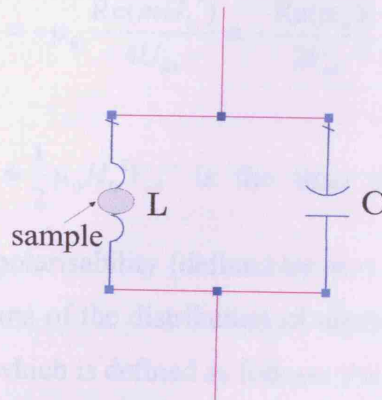


Figure 2.5 The equivalent resonator circuit for a sample placed in a uniform H-field (i.e. fixed applied current $i(t) = I_0 e^{j\omega t}$).

The fractional change in energy (ΔU) on inserting the sample is

$$\frac{\Delta U}{U_{tot}} = \frac{\frac{1}{2} \Delta L i^2}{\frac{1}{2} L i^2} = \frac{\Delta L}{L} \quad (2.1)$$

where L is the inductance of the resonator equivalent circuit and ΔL the inductance change.

The resonant frequency for the circuit of fig. 2.5 is $f_0 = \frac{1}{2\pi\sqrt{LC}}$ which can be used to derive

the fractional frequency shift, Δf , from the following expression [63]:

$$\frac{\Delta f_0}{f_0} = -\frac{1}{2} \frac{\Delta L}{L} = -\frac{1}{2} \frac{\Delta U}{U_{tot}} \quad (2.2)$$

If the sample is placed in high H-field magnitude (i.e. H_0) and gains a magnetic dipole moment m , then

$$\Delta U = \frac{1}{2} \mu_0 \text{Re}(mH_0^*) \quad (2.3)$$

where Re represents the real part. Combining both Eqs. (2.2) and (2.3) yields the expression below for the fractional change in resonant frequency:

$$\frac{\Delta f_0}{f_0} = -\mu_0 \frac{\text{Re}(mH_0^*)}{4U_{tot}} = -\frac{\text{Re}(\alpha_m)}{2V_{eff}} \quad (2.4)$$

where $U_{tot} = \frac{1}{2} \mu_0 \int_{resonator} H^2 dv \approx \frac{1}{2} \mu_0 H_0^2 V_{eff}$ is the time averaged stored energy in the

resonator, α_m is the sample's polarisability (defined by $m = \alpha_m V_s H_0$) and V_{eff} is the effective volume of the resonator in terms of the distribution of electrical energy [63]. Now, consider the resonator quality factor Q which is defined as follows [62]

$$Q = \omega_0 \frac{\text{time-averaged stored energy}}{\text{time-averaged power dissipated}} = \omega_0 \frac{U_{tot}}{\langle P \rangle} \quad (2.5)$$

Therefore Eq. (2.5) can be written as

$$\Delta \left(\frac{1}{Q} \right) = \frac{1}{\omega_0 U_{tot}} \Delta \langle P \rangle \quad (2.6)$$

which can be combined with the relation for power dissipated energy

$\left(\text{i.e. } \langle P \rangle = -\frac{1}{2} \omega_0 \mu_0 \text{Im}(mH_0^*) \right)$ to give

$$\Delta\left(\frac{1}{Q}\right) \approx -\mu_0 \frac{\text{Im}(mH_0^*)}{2U_{\text{tot}}} \equiv -\frac{\text{Im}(\alpha_m)}{V_{\text{eff}}} \quad (2.7)$$

Other way of representing Eq. (2.7) is

$$\frac{\Delta f_B}{f_0} \approx -\mu_0 \frac{\text{Im}(mH_0^*)}{2U_{\text{tot}}} \equiv -\frac{\text{Im}(\alpha_m)}{V_{\text{eff}}} \quad (2.8)$$

where Δf_B is the change on bandwidth of the resonator due to the presence of the sample. Eqs. (2.4) – (2.8) are the standard resonator perturbation results for the H-field, which will be used in the next section to establish the variation of f_0 and Q for a small conducting spherical particle placed in a high H-field.

2.9 Application of Resonator Perturbation Theory

In this research, a sapphire dielectric resonator (SDR) has been used to characterise the electrical properties of Pt and Au NP films. The films were deposited on the sapphire puck in a region where the magnetic field is maximum and perpendicular to the plane of the films. Resonator perturbation theory is applied to the scenario where the sample is considered to be spherical (not a thin film) to determine the expected results for $\Delta f_0/f_0$ and $\Delta f_B/f_0$; for this reason, we keep this analysis to be semi-quantitative.

2.9.1 Magnetic Dipole Adsorption in Non-Magnetic Samples

Consider a spherical shape object to which a magnetic field H_0 is applied, as shown in fig. 2.6.

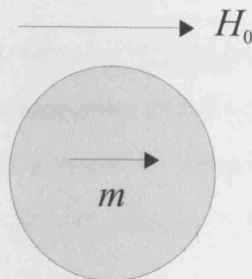


Figure 2.6 The applied magnetic field H_0 and developed magnetic dipole moment (due to the applied H_0) in a spherical sample.

A conducting sphere will develop magnetic dipole moment (m) in response to a uniform, applied magnetic field H_0 which is proportional to the volume of the sample (V_s) and the applied H_0 . Therefore m can be written as [63]

$$m = \alpha_m V_s H_0 \quad (2.9)$$

where α_m is the sample's polarisability, dependent on the sample geometry and a function of the conductivity (σ), frequency (ω) and the radius (a) of the sample ($\alpha_m(\sigma, \omega, a)$). The analytic solutions for m (i.e. $m = \alpha_m V_s H_0$) for a small conducting particle (i.e. of particle radii much less than the wavelength of the incident radiation) in this limit can be written as [63]

$$m = 2\pi a^3 H_0 \left(\frac{(\mu + 2)(1 - ka \cot ka) - \mu (ka)^2}{(\mu - 1)(1 - ka \cot ka) - \mu (ka)^2} \right) \quad (2.10)$$

Now Eq. (2.10) is in the form of Eq. (2.9), where α_m can be written as follows [63]:

$$\alpha_m = - \frac{(\mu + 2)(1 - ka \cot ka) - \mu (ka)^2}{(\mu - 1)(1 - ka \cot ka) - \mu (ka)^2} \quad (2.11)$$

where $k = \omega \sqrt{\epsilon \mu} / c$ is the wave number within the particle, $\epsilon = \epsilon_1 - j\epsilon_2$ is the complex permittivity, $\mu = \mu_1 - j\mu_2$ is the complex permeability of the particle and $c = 1 / \sqrt{\mu_0 \epsilon_0}$ is the velocity of light in free space. The time averaged power dissipated energy per unit volume $\langle P \rangle$ associated with magnetic dipole adsorption of a spherical conducting particle is then [63]

$$\langle P \rangle = \frac{1}{2} \omega \mu_0 \frac{\text{Im}(m H_0^*)}{\frac{4}{3} \pi a^3} = \frac{3}{4} \omega \mu_0 H_0^2 \text{Im} \left(\frac{(\mu + 2)(1 - ka \cot ka) - \mu (ka)^2}{(\mu - 1)(1 - ka \cot ka) - \mu (ka)^2} \right) \quad (2.12)$$

where H_0 is the amplitude (i.e. peak value) of the applied magnetic field. The origin of this dissipation is associated with electromagnetic induction by the changing applied magnetic field, so one would expect it to be a sensitive function of the particle size. For a non-magnetic, conducting particle $\epsilon = 1 - j\sigma / \omega \epsilon_0$ and $\mu_1 = 1$, so that Eq. (2.12) reduces to [63]

$$\langle P \rangle = \frac{3}{4} \omega \mu_0 H_0^2 \text{Im} \left(1 + \frac{3 \cot ka}{ka} - \frac{3}{(ka)^2} \right) \quad (2.13)$$

There are again two limiting forms for the magnetic dipole absorption set by the ratio a/δ . In the large skin depth limit (i.e. $a/\delta \ll 1$, appropriate for small particles of low conductivity at low frequency), Eq. (2.13) reduces to [63]

$$\lim_{a/\delta \rightarrow 0} \langle P \rangle = \frac{1}{20} \omega^2 \mu_0^2 a^2 \sigma H_0^2 \propto \omega^2 a^2 \sigma \quad (2.14)$$

which is that of a uniform applied internal magnetic field (in this case equal to the applied magnetic field since it is assumed that $\mu_1 = 1$). In the small skin depth limit (i.e. $a/\delta \gg 1$, appropriate for large particles of high conductivity at high frequency), Eq. (2.13) reduces to [63]

$$\lim_{a/\delta \rightarrow \infty} \langle P \rangle = \frac{9}{4} \frac{R_s}{a} H_0^2 \propto \frac{1}{a} \sqrt{\omega} \quad (2.15)$$

where $R_s = (\omega \mu_0 / 2\sigma)^{1/2}$ is the surface resistance of the conducting material.

Thus,

$$\frac{\Delta f_0}{f_0} = -\mu_0 \frac{\text{Re}(mH_0^*)}{4U_{tot}} \equiv -\frac{\mu_0 H_0^2}{4U_{tot}} \text{Re}(\alpha_m) \quad (2.16)$$

and

$$\frac{\Delta f_B}{f_0} = -\mu_0 \frac{\text{Im}(mH_0^*)}{2U_{tot}} \equiv -\frac{\mu_0 H_0^2}{2U_{tot}} \text{Im}(\alpha_m) \quad (2.17)$$

Using MathCAD, the variations f_0 and f_B have been plotted against the conductivity, for fixed values of ω , $\mu = 1$ (i.e. for non-magnetic sample) and a (i.e. $a = 1.5$ mm), as shown in fig. 2.7. In this instance, the value of ' a ' is the radius of the NP film deposited.

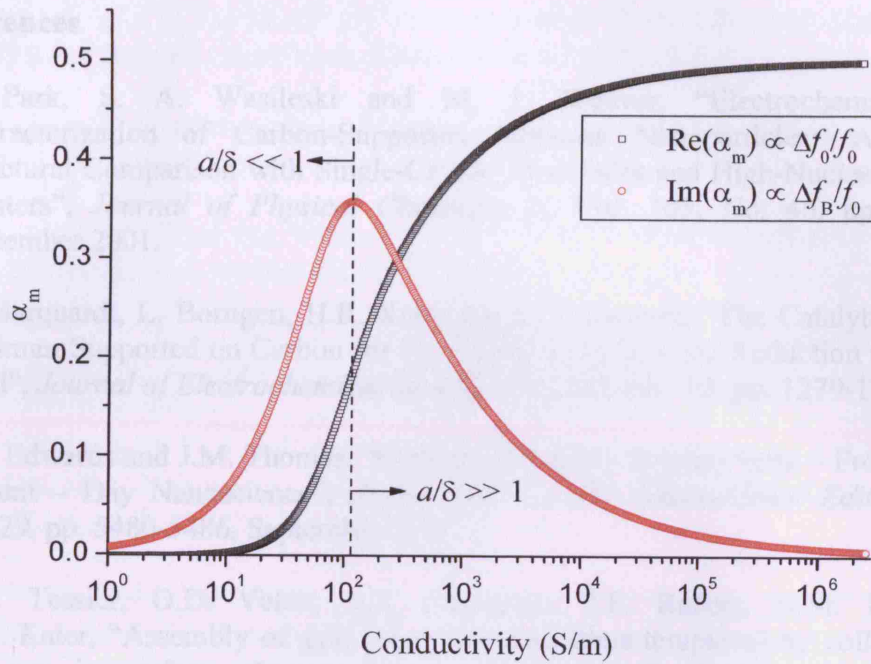


Figure 2.7 The variations of $\Delta f_0/f_0$ (screening) and $\Delta f_B/f_0$ (eddy current loss) with increasing conductivity of a sample in a resonator where the magnetic field is maximum.

Fig. 2.7 shows that $\Delta f_0/f_0$ increases due to the screening current within the sample. Correspondingly, the plot of $\Delta f_B/f_0$ can be split into 2 main regions since the magnetic dipole adsorption set by the ratio a/δ . In the large skin depth limit (i.e. $a/\delta \ll 1$, appropriate for a low conductivity sample), $\Delta f_B/f_0$ increases monotonically up to $a \approx \delta$ and then starts decreasing as the small skin depth limit is reached (i.e. $a/\delta \gg 1$, appropriate for high conductivity sample). This is a semi-quantitative theoretical model to support the results obtained from the SDR for different sizes of Pt oxide, pure Pt and Au NP films. Whereas Pt oxide is considered to be a low conductivity sample due to the insulating thin oxide layer, pure Pt and Au NPs films are considered to be highly conducting films. These statements will be qualified experimentally in chapters 5 and 6.

2.10 References

1. S. Park, S. A. Wasileski and M. J. Weaver, "Electrochemical Infrared Characterization of Carbon-Supported Platinum Nanoparticles: A Benchmark Structural Comparison with Single-Crystal Electrodes and High-Nuclearity Carbonyl Clusters", *Journal of Physical Chemistry B*, Vol. 105, No. 40, pp. 9719-9725, September 2001.
2. P. Marquardt, L. Borngen, H.R. Kunz and G.A. Gruver, "The Catalytic Activity of Platinum Supported on Carbon for Electrochemical Oxygen Reduction in Phosphoric Acid", *Journal of Electrochemical Society*, Vol. 122, No. 10, pp. 1279-1287, 1975.
3. P.P. Edwards and J.M. Thomas, "Gold in a Metallic Divided State – From Faraday to Present – Day Nanoscience", *Angewandte Chemie International Edition*, Vol. 46, No. 29, pp. 5480-5486, September 2007.
4. P.M. Tessier, O.D. Velez, A.T. Kalambur, J.F. Rabolt, A.M. Lenhoff, and E.W. Kaler, "Assembly of gold nanostructured films templated by colloidal crystals and use in surface-enhanced Raman spectroscopy", *Journal of the American Chemical Society*, Vol. 122, No. 39, pp. 9554–9555, 2000.
5. G. Schoen and U. Simon, "A fascinating new field in colloid science: Small ligand-stabilized metal clusters and possible application in microelectronics", *Colloid and Polymer Science*, Vol. 273, pp.101–117, 1995.
6. J.H. Liu, C.L. Chen, H.T. Lue and J.T. Lue, "Measurement of Dielectric Constant of Metallic Nanoparticles by a Microwave Dielectric Resonator", *Measurement Science and Technology*, Vol. 13, pp. 2032-2037, 2002.
7. P. Marquardt, L. Borngen, G. Nimtz and R. Sonnberger, "Microwave Adsorption by Small Metal Particles", *Physics Letter A*, Vol. 114, No. 1, pp. 39-42. 1986.
8. E. Kymakis, I. Alexandou and G.A.J. Amaratunga, "Single-Walled Carbon Nanotube-Polymer Composites: Electrical, Optical, and Structural Investigation", *Synthetic Metals*, Vol. 127, pp. 59-62. 2002.
9. F. Fang and Y.F. Zhang, "DC Electrical Conductivity of Au Nanoparticles/ Chloroform and Toluene Suspension", *Journal of Material Science*, Vol. 40, pp. 2979-2980, 2005.
10. A.P. Gregory and R.N. Clarke, "A Review of RF and Microwave Techniques for Dielectric Measurements on Polar Liquids", *IEEE Transactions on Dielectrics and Electrical Insulation*, Vol. 13, No. 4, August 2006.
11. T. Graham, "Liquid Diffusion Applied to Analysis", *Philosophical Transactions of the Royal Society*, Vol. 151, pp. 183-224, 1861.
12. R. Kubo, "Electronic Properties of Metallic NPs", *Journal of the Physical Society of Japan*, Vol. 17, pp.975-986, 1962.

13. H. Nalwa (Ed.), *Handbook of Nanostructured Materials and Nanotechnology*, Academic Press Inc., New York, 2000, ISBN 1-251-3760-5.
14. R.W. Siegel, *Physics of New Materials*, F.E Fujita (Ed.), Springer-Verlag, 1994, ISBN 0-387-56851-4.
15. R.W. Siegel, "Exploring Mesoscopia: The Bold New World of Nanostrutures" *Physics Today*, Vol. 46, No. 10, pp. 64-68, October 1993.
16. T. Belin and F. Epron, "Characterisation Methods of Carbon Nanotubes: A Review", *Materials Science and Engineering*, Vol. 119, No. 2, pp. 105-118, May 2005.
17. C.N.R. Rao, G.U. Kulkarni, A. Govindaraj, B.C. Satishkumar, and P.J. Thomas, "Metal Nanoparticles, Nanowires, and Carbon Nanotubes", *Pure and Applied Chemistry*, Vol. 72, No. 1-2, pp. 21-23, 2000.
18. H. Nalwa (Ed.), *Handbook of Nanostructured Materials and Nanotechnology*, Academic Press Inc., New York, 2000, ISBN 1-251-3760-5.
19. J. Turkevich, P.C. Stevenson and J. Hillier "A Study if the Nucleation and Growth Process in the Synthesis of Colloidal Gold", *Discussion of the Faraday Society*, Vol. 11, pp. 55-75, 1951.
20. R.W. Siegel, *Physics of New Materials*, E.E Fujita (Ed.), Springer-Verlag, 1994.
21. S. Datta, S.S. Mitra, D. Chakravorty, S. Ram and D. Bahadur, "Preparation of Glass-Metal Microcomposites by sol-gel route", *Journal of Materials Science Letters*, Vol. 5, No. 1, pp. 89-90, 1986.
22. A. Chatterjee and D. Chakravorty, "Glass-Metal Nanocomposite Synthesis by Metal Organic Route", *Journal of Physics D: Applied Physics*, Vol. 22, No. 9, pp. 1386-1392, 1989.
23. P. Somasundaran, *Encyclopaedia of Surface and Colloid Science, Volume 2*, 2006, ISBN 978-0849396076.
24. Z.L. Wang, *Characterisation of Nanophase Materials*, 1st edition, Wiley-VCH, 2000, ISBN 3-527-29837-1.
25. D.J. Gardiner, *Practical Raman Spectroscopy*. Springer – Verlag, 1989, ISBN 978-0387502540.
26. D.T. Sawyer, J.L. Roberts, *Experimental Electrochemistry for Chemists*, Wiley, 1974, ISBN 0-471-75560-5.
27. J. Solla-Gullon, A. Rodes, V. Montiel, A. Aldaz, and J. Clavilier, "Electrochemical characterisation of platinum-palladium nanoparticles prepared in a water-in-oil microemulsion", *Journal of Electroanalytical Chemistry*, Vol. 554-555, pp. 273-284, September 2003.

28. H-S.P. Wong, "Nanoelectronics – Opportunities and Challenges", *International Journal of High Speed Electronics and Systems*, Vol. 16, pp. 83-94, March 2006.
29. M. Thomas, S.K. Ghosh and K.C. George, "Characterisation of Nanostructured Silver Orthophosphate", *Materials Letters*, Vol. 56, No. 4, October 2002.
30. E. Barsoukov (Ed.) and J.R. Macdonald (Ed.), *Impedance Spectroscopy Theory, Experiment, and Applications*, 2nd edition, A John Wiley & Sons, Inc., ISBN 0-471-64749-7.
31. D.M. Pozar, *Microwave Engineering*, 3rd edition, John Wiley & Sons, Inc., 2005, ISBN 0-471-44878-8.
32. H. Zheng and C.E. Smith, "Permittivity Measurements Using a Short Open-Ended Line Probe", *IEEE Microwave and Guided Wave Letters*, Vol. 1, No. 11, pp. 337-339, November 1991.
33. W.B. Weir, "Automatic Measurement of Complex Dielectric Constant and Permeability at Microwave Frequencies", *Proceeding of the IEEE*, Vol. 62, pp. 33-36, 1974.
34. A.M. Nicolson and G.F. Rose, "Measurement of the Intrinsic Properties of Materials by Time Domain Techniques", *IEEE Transactions on Instrumentation and Measurement*, Vol. 19, pp. 377-382, 1970.
35. J. Krupka, R.G. Geyer, M. Kuhn and J.H. Hinden, "Dielectric Properties of Al_2O_3 , LaAlO_3 , SrTiO_3 , and MgO at Cryogenic Temperature", *IEEE Transactions on Microwave Theory and Techniques*, Vol. 42, pp. 1886-1890, 1994.
36. B. Thomas and M. Abdulkhadar, "Dielectric Properties of Nano-Particles of Zinc Sulphide", *Pramana – Journal of Physics*, Vol. 45, No. 5, pp. 431-438, November 1995.
37. A. Chatterjee and D. Ahakravorty, "Electrical Conductivity of Sol-Gel Derived Metal Nanoparticles", *Journal of Material Science*, Vol. 27, pp. 4115-4119, 1992.
38. M-H.J. Lee, and R.J. Collier, "The Sheet Resistance of Thin Metallic Films and Stripes at Both DC and 130 GHz", *Microelectronic Engineering*, Vol. 73-74, pp. 916-919, June 2004.
39. D.E. Steinhauer, C.P. Vlahacos, S.K. Dutta, B.J. Feenstra, F.C. Wellstood and S.M. Anlage, "Quantitative Imaging of Sheet Resistance with a Scanning Near-Field Microwave Microscope", *Applied Physics Letter*, Vol. 72, No. 7, pp. 861-863, February 1998.
40. A.J.A. El-Haija, "The DC Electrical Sheet Resistance of Semimetallic Sb Thin Films", *Physical Status Solid (a)*, Vol. 165, pp. 409-416, 1998.
41. D. Ghosh and S. Chen, "Palladium Nanoparticles Passivated by Metal-Carbon Covalent Linkages", *Journal of Material Chemistry*, Vol. 18, pp. 755-762, 2008.

42. D. Ghosh, S. Pradhan, W. Chen and S. Chen, "Titanium Nanoparticles Stabilized by Ti-C Covalent Bonds", *Chemistry of Materials*, Vol. 20, No. 4, pp. 1248-1250, January 2008.
43. H.E. Bussey, "Measurement of RF Properties of Materials a Survey", *Proceeding of the IEEE*, Vol. 55, No. 6, pp. 1046-1053, June 1967.
44. M.N. Afsar, and K.J. Button, "Millimeter-Wave Dielectric Measurement of Materials", *Proceeding of the IEEE*, Vol. 73, No. 1, pp. 131-153, January 1985.
45. J. Sheen, "Study of Microwave Dielectric Properties Measurements by Various Resonance Techniques", *Measurement*, Vol. 37, pp. 123–130, 2005.
46. L.F. Chen, C.K. Ong and B.T.G. Tan, "Amendment of Cavity Perturbation Method for Permittivity Measurement of Extremely Low-Loss Dielectrics", *IEEE Transactions on Instrumentations and Measurement*, Vol.48, pp. 1031–1037, 1999.
47. M.C. Decretton, M.S. Ramachandraiah, "Nondestructive Measurement of Complex Permittivity for Dielectric Slabs", *IEEE Transactions on Microwave Theory and Techniques*, Vol. 23, No.12, pp. 1077-1080, December 1975.
48. V. Teodoridis, T. Sphicopoulos, F.E. Gardiol, "The Reflection from an Open-Ended Rectangular Waveguide Terminated by a Layered Dielectric Medium", *IEEE Transactions on Microwave Theory and Techniques*, Vol.33, No.5, pp. 359-366, May 1985.
49. S. Hussain, I.J. Youngs and I.J. Ford, "The Electromagnetic Properties of Nanoparticle Colloids at Radio and Microwave Frequencies", *Journal of Physics D: Applied Physics*, Vol. 40, pp. 5331, September 2007.
50. Y.S. Yeh, J.T. Lue, and Z.R. Zheng, "Measurement of the Dielectric Constant of Metallic Nanoparticles Embedded in a Paraffin Rod at Microwave Frequencies", *IEEE Transactions on Microwave Theory and Techniques*, Vol. 53, No.5, pp. 1756-1760, May 2005.
51. J. Krupka, K. Derzakowski, T. Zychowicz, B.L. Givot, W.C Egbert and M.M. David, "Measurements of the Surface Resistance and Conductivity of Thin Conductive Films at Frequency About 1 GHz Employing Dielectric Resonator Technique", *Journal of European Ceramic Society*, Vol. 27, pp. 2823-2826, 2007.
52. J.B. Jarvis, M.D. Janezic, and J.H. Lehman, "Dielectric Resonator Method for Measuring the Electrical Conductivity of Carbon Nanotubes from Microwave to Millimeter Frequencies", *Journal of Nanomaterials*, 2007, doi:10.1155/2007/24242.
53. W.G. Coors, and D.W. Readey, "Proton Conductivity Measurement in Yttrium Barium Cerate By Impedance Spectroscopy", *Journal of the American Ceramic Society*, Vol. 85, No. 11, pp. 2637-2640, 2002.

54. G. Ma, T. Shimura, and H. Iwahara, "Simultaneous Doping with La^{3+} and Y^{3+} for Ba^{2+} and Ce^{4+} Sites in BaCeO_3 and Ionic Conduction," *Solid State Ionics*, Vol. 120, pp. 51–60, 1999.
55. J.B. Pelka, M. Brust, P. Gierlowski, W. Paszkowicz and N. Schell, "Structure and Conductivity of Self-Assembled Films of Gold Nanoparticles", *Applied Physics Letter*, Vol. 89, pp. 063110 (3pp), 2006, doi:10.1063/1.2245376.
56. T. Fujita, K. Ohshima and N. Wada, "D.C Electric Conductivity in Films of Aluminium Fine Particles Prepared by Evaporation in Helium Gas", *Journal of the Physical Society of Japan*, Vol. 27, pp. 1459-1462, 1969.
57. K. Mallick, M.J. Witcomb and M.S. Scurrrell, "In Situ Synthesis of copper Nanoparticles and Poly (*o*-toluidine): A Metal-Polymer Composite Material", *European Polymer Journal*, Vol. 42, No. 3, pp. 670-675, 2006.
58. Y. Yang, Y. Jiang, J. Xu and J. Yu, "Conducting Polymeric Nanoparticles Synthesised in Reverse Micelles and Their Gas Sensitivity Based on Quartz Crystal Microbalance", *Polymer*, Vol. 48, No. 15, pp. 4459-4465, July 2007.
59. M.L Gorzny, A.S. Walton, M. Wnek, P.G. Stockley and S.D. Evans, "Four-Probe Electrical Characterisation of Pt-Coated TMV-Based Nanostructures", *Nanotechnology*, Vol. 19, pp. 165704 (5pp), 2008.
60. D. Ghosh and S. Chen, "Solid-State Electronic Conductivity of Ruthenium Nanoparticles Passivated by Metal-Carbon Bonds", *Chemical Physics Letters*, Vol. 465, pp. 115-119, 2008.
61. M. Nishizawa, T. Ise, H. Koshika, T. Itoh, and I. Uchida, "Electrochemical In-Situ Conductivity Measurements for Thin Film of LiMn_2O_4 Spinel", *Chemistry of Materials*, Vol. 12, No. 5, pp. 1367-1371, April 2000.
62. D.M. Pozar, *Microwave Engineering*, 3rd edition, John Wiley & Sons, N.Y., 2005, ISBN 0-471-44878-8.
63. A. Porch, *Private Communications*, 2007-2009.

CHAPTER 3

MICROWAVE THEORY FOR MATERIAL CHARACTERISATION

3.1 Introduction

Microwaves refer to alternating signals within the frequency range of 300 MHz and 300 GHz. Since the relationship $\lambda = c/f$ shows that frequency (f) is related to electrical wavelength (λ), the corresponding λ values range between 1m and 1mm, respectively [1]. The majority of microwave technology applications are in radar systems, communication systems and medical systems. This chapter discusses the basic microwave theory and techniques for the electromagnetic materials characterisation. The techniques used for material properties characterisation generally fall into the two main categories of non-resonant methods and resonant methods [2]. Correspondingly, this chapter mainly discusses these two main microwave techniques. This is followed by a discussion on the existing models for the open ended coaxial probe, the concept of microwave network and also the parameters describing the microwave network.

3.2 Overview of Microwave Techniques for Material Characterisation

There have been many extensive review papers [3] on microwave methods for materials property characterisation. This section focuses on the basic principles for the measurement of complex permittivity of dielectric materials. The detailed structures of fixtures and detailed algorithms for the calculation of materials properties will be discussed in this chapter, as well as in chapters 5 and 6. As mentioned earlier, the microwave methods/ sensors for material characterisation generally fall into non-resonant methods and resonant methods, which will be discussed in the following sections. Non-resonant methods are often used to get a general knowledge of electromagnetic properties over a range of frequencies, while the resonant methods are used to get accurate knowledge of dielectric properties at single frequency or several discrete frequencies. In the following sections, the importance of the use of microwaves for material characterisation, and the working principles of various microwave measurement techniques will be discussed.

3.3 “Why Microwaves?” for Material Characterisation

The main reasons for using microwave stimuli are

- The use of microwaves is completely non-destructive at low power levels
- Microwaves penetrate all materials except for metals, so the measured result therefore represents the volume of the material, not only the surface.
- Microwave sensors do not need mechanical contact with the material.
- At the low power levels used for measurement with microwave sensors, microwaves are safe.

3.4 Non-Resonant Methods

Non-resonant methods mainly include reflection methods and transmission/ reflection methods. The material properties are deduced on the basis of the reflection from the sample in reflection methods, and in a transmission method, the material properties are calculated on the basis of the reflection from the sample and the transmission through the sample. Non-resonant methods require a means of directing the electromagnetic energy toward a material, and then collecting what is reflected from the materials, and/ or what is transmitted through the materials. This thesis focuses only on the reflection methods. In principle, all types of transmission lines can be used to carry the signal for non-resonant methods, such as coaxial line, planar transmission line, dielectric waveguide, etc [4, 5]. Among these, coaxial line is most widely used in the reflection method for material characterisation, since it is broadband and readily available in the form of commercial cables.

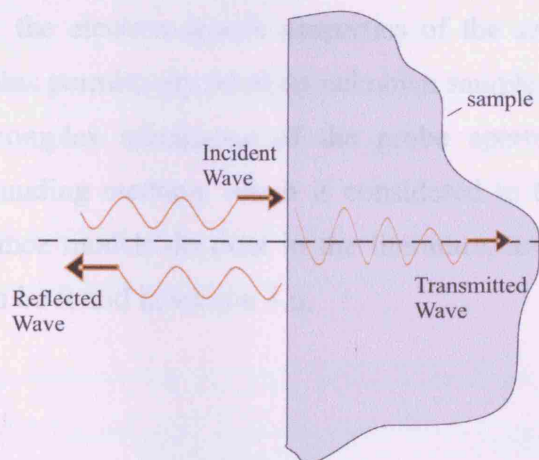


Figure 3.1 Material characterisation using non-resonant method.

3.4.1 Reflection Methods

In reflection methods, electromagnetic waves are directed to a sample under study, and the properties of the sample are deduced from the reflection coefficient due to the impedance discontinuity caused by the presence of the sample at the interface with the input line. Usually, a reflection method can only measure either permittivity or permeability of the sample under test. This chapter mainly focuses on the permittivity measurement. Open reflection method and shorted reflection method are the two most important methods used for material property characterisation. At an open circuit end, the main propagating TEM mode will only produce a finite E-field on reflection, so that's why we can only measure permittivity. As coaxial lines can cover broad band frequency, they are often used in developing measurement fixtures for reflection methods. Such fixtures are often called probe or sensors. Detailed discussions on open reflection methods can be found in the following section.

3.4.2 Open Reflection Method

Fig. 3.2 shows a schematic diagram of an open ended coaxial reflectance probe. It is a cut off section of a transmission line, with the optional extension of a ground plane, where the outer conductor at the open end is fabricated into a flange to provide suitable capacitance and ensure the repeatability of sample loading [2]. This method assumes that the materials under test are nonmagnetic, and require intimate contact between the probe and the sample [6]. The wave impedances either side of the resulting interface are different, so there is a reflection when an electromagnetic wave meets the interface. As the impedance of the side occupied by the sample is related to the electromagnetic properties of the sample, from the reflection coefficient (ρ), the complex permittivity (ϵ) of an unknown sample can be obtained through a model that gives the complex admittance of the probe aperture as a function of the permittivity of the surrounding medium, which is considered to be semi-infinite. A certain number of these admittance models do exist in the literature, and a detailed discussion of some of these models can be found in section 3.6.

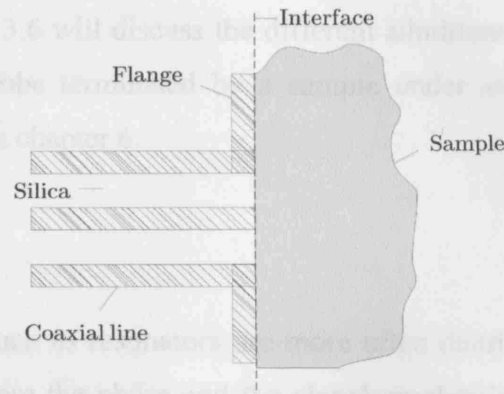


Figure 3.2 Schematic diagram of a coaxial reflectance probe.

3.4.3 Open Ended Coaxial Reflectance Probe

There are several advantages of a coaxial probe made from coaxial line over the ones made from other types of transmission lines, the most obvious one being its broadband frequency range. There are many outstanding papers on this technique published by several researchers, and many in-depth review papers on this subject [7, 8]. The coaxial probe technique has been established over the last 20 years as a standard tool for evaluating electrical properties in the microwave frequency range [6]. The attractiveness of the coaxial probe technique has arisen from its broadband measurement capabilities, non-destructive nature and the technique itself is deceptively simple. The technique involves terminating a length of flanged coaxial transmission line with the material under test and measuring the reflection coefficient (both amplitude and phase) of the coaxial aperture at the interface with the material. There are two non-trivial aspects of this problem which need to be addressed before the permittivity of the material can be evaluated:

- i. The system has to be carefully calibrated so that any stray reflections and additional path lengths are removed from the analysis routine.
- ii. An appropriate model for the admittance of the aperture as a function of the permittivity of the terminating material is required.

In the past, increasingly sophisticated models have been developed for determining the aperture admittance of open ended coaxial probe. Furthermore, in recent years, many efforts have been made in investigating the radiation of a coaxial probe into layered media [9, 10], and many variations in the conventional open ended reflection method have been made for

various purposes. Section 3.6 will discuss the different admittance/ capacitance models used in analysing a coaxial probe terminated by a sample under study and calibration of this system will be discussed in chapter 6.

3.5 Resonant Methods

Microwave components such as resonators are more often distributed structures rather than lumped element ones, where the phase and the signal amplitudes change significantly over the physical size of the device because the device dimensions are similar to the microwave wavelength. Since the wavelength is large at lower frequencies, there is an insignificant phase variation across the dimensions of the component [1], so it can be assumed to be lumped. Reducing the size of microwave circuits minimises cost. In this respect, microstrip and stripline have been vital in eliminating physically large waveguides and coaxial lines in a majority of the microwave applications. Dielectric resonators (DRs) are used to replace waveguide filters in such challenging applications as satellite communications, where the stripline or microstrip resonators cannot be used because they possess inherently high losses. Microwave resonators are mainly used as filters, but can also be utilized for the characterisation of materials and the production of high electromagnetic fields. In practical applications DRs are often modified by the introduction of small pieces of dielectric or metallic materials. Such resonant methods generally have higher sensitivities and accuracies than non-resonant methods owing to the high Q-factors of the host resonators. Resonant methods generally include the resonant perturbation and resonator methods. This chapter and the following chapters discuss the resonant perturbation method, which is based on resonant perturbation theory. For a resonator with given electromagnetic boundaries, when part of the electromagnetic boundary condition is changed by introducing a sample, its resonance frequency and quality factor will also be changed, from which the properties of the sample can be derived.

3.5.1 Basic Parameters of Dielectric Resonator

The Dielectric Resonator (DR) is an electromagnetic component that exhibits resonance over a narrow range of frequencies, generally in the microwave region [1]. To date, sapphire is the most popular among many dielectrics due to its extremely low loss tangent. It consists of a cylindrical puck of sapphire material. The resonant frequency depends on the overall

physical dimensions of the puck and the dielectric constant of the material. DRs are usually enclosed in an RF shield in order to prevent radiation. Quality factor (Q) is very useful in determining the qualitative behaviour of a resonant system. The Q quantifies the relationship between the time averaged stored energy $\langle U \rangle$ and the time averaged dissipated energy $\langle P \rangle$ in a resonant structure, which is defined as $Q = \omega_o \langle U \rangle / \langle P \rangle$. The other parameter is permittivity (ϵ), which is a measure of a material ability to resist the formation of an internal electric field. This is also known as dielectric constant or relative permittivity. Loss tangent ($\tan \delta$) is other parameter used in the specification of DRs, which is expressed as the ratio of the resistive component of the current to the capacitive component of current, and is equal to the tangent of the loss angle, also known as dissipation factor [1]. High Q-factor DRs are implemented with the advantage of high dielectric constant and low loss tangent to confine the electromagnetic field within the resonator, so that the conduction loss (Q_c) and radiation loss (Q_r) near the boundaries (cavity walls) are significantly reduced. The size of the DRs is considerably smaller than the size of an empty resonant cavity operating at the same frequency, provided the relative dielectric constant (ϵ_r) of the material is significantly larger than unity, in which case all dimensions are reduced by the factor $\approx \sqrt{\epsilon_r}$ (due to the $\lambda_d = \lambda / \sqrt{\epsilon_r}$, where λ_d is the wavelength in the dielectric). In general dielectric resonators are found in many different shapes, for instance short, solid cylinders, as well as spherical and tubular shapes [1]. The analysis and design of DR, specifically a sapphire DR, is discussed in detail in chapters 5 and 6. There are many possible resonant modes such as transverse electric (TE), transverse magnetic (TM), and hybrid electromagnetic modes (HEM), which can be excited in dielectric resonators [1]. TE modes have no electric field component in the direction of propagation (i.e. z-axis) while TM modes have no magnetic field component along the z-axis. A commonly used resonant mode in cylindrical DRs is denoted $TE_{01\delta}$. The subscript δ denotes the number of resonating waves in the longitudinal direction of the resonator (the lowest number is $\delta = 1$). The magnetic field and the electric field intensity for this mode are shown in fig. 3.3 (b) and (c) respectively, where it can be seen that the magnetic field intensity is solenoidal in nature, while the electric field lines are simply circles concentric with the axis of the cylinder. Microwave characterisation of materials using dielectric resonators is typically done in the $TE_{01\delta}$ mode (in cylindrical resonator), as this mode does not have a transverse electric field in the z-axis.

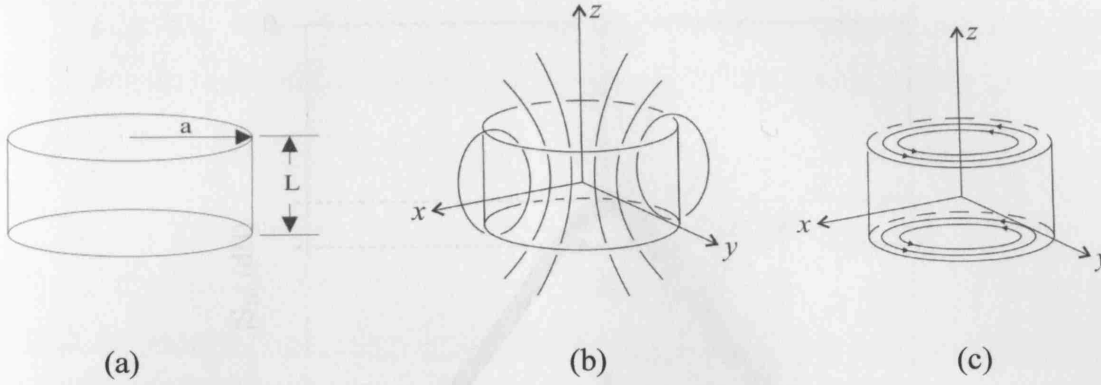


Figure 3.3 Prime mode (TE_{018}) of an isolated cylindrical DR. (a) Dimensions of the resonator (b) magnetic field distribution, and (c) electric field lines.

For a dielectric material with high relative dielectric constant (ϵ_r) and operating in the TE_{018} mode, most of the electrical energy and a significant part of the magnetic energy are located within the material. The remaining energy is stored in the space surrounding the resonator, decaying rapidly with distance away from the surface of the resonator.

3.5.2 Transmission Mode Measurements with Resonators

When resonators are measured in transmission mode, there are four parameters of interest related to the resonance: the resonant frequency (f_0), half-power (or 3dB) bandwidth (f_B), the insertion loss (IL) and the quality factor Q . Each of these will be dealt in detailed in the following sections.

3.5.3 Resonator Spectral Response in Transmission Mode

In transmission mode, a vector network analyser (VNA) is used to measure the magnitude of the voltage transmission coefficient S_{21} (i.e. $|S_{21}|$) of a resonator as a function of frequency. If $|S_{21}|$ is unity, it would imply perfect transmission through the resonator thereby meaning that it is completely lossless and doesn't absorb or reflect any power. On the other hand zero value of $|S_{21}|$ leads to total absorption or reflection of power by the resonator with no transmission at all. However, it is much more convenient to define the above mentioned resonator parameters if $|S_{21}|$ is expressed in logarithmic unit (i.e. dB) rather than linear magnitude. The characteristic spectral response of a resonator would then be as shown in fig. 3.4 [2].

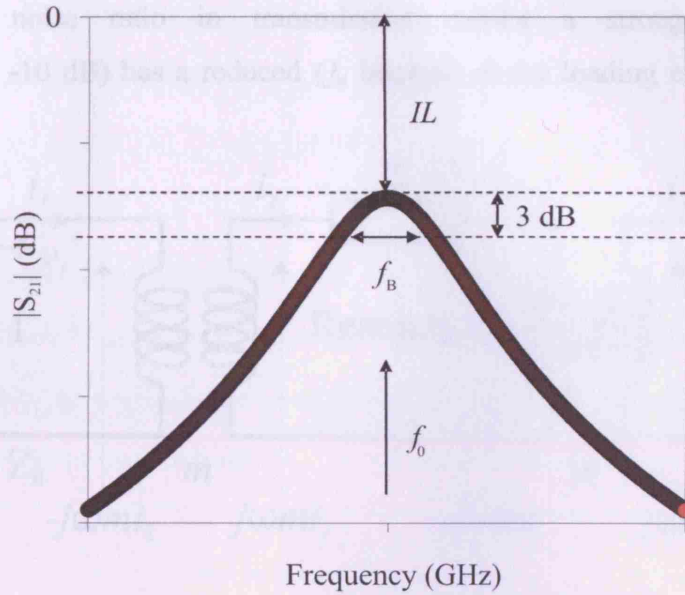


Figure 3.4. Idealised spectral response of a resonator in transmission mode [2].

In fig. 3.4, f_0 is the resonant frequency, f_B is the half-power bandwidth, and IL is the insertion loss at resonance, which is expressed in dB relative to the input power – typically 0 dBm (i.e. 1 mW rms) for the Agilent (HP) 8510C and 8753E VNA used in this research. The loaded quality factor can be evaluated from spectral response of fig. 3.4 (i.e. from f_0 and f_B) and the affects of resonator coupling are described later in this chapter.

3.5.4 Two-port Resonator Analysis with Symmetrical Coupling

Microwave resonators can be coupled either capacitively (using an open circuit transmission line, which couples to the resonator's electric field) or inductively (using a short circuit line, which couples to the magnetic field). The equivalent circuit of an inductively-coupled resonator is shown in fig. 3.5 (i.e. for symmetrical coupling). The input and output lines are terminated in coupling loops, forming a pair of mutual inductances m at both the ports 1 and 2, respectively, of the resonator. Each mutual inductance depends only on geometry, i.e. the loop area, its orientation and position relative to the resonator. In this research the coupling loops were made nearly identical to ensure symmetrical input/output couplings. In fig. 3.5 (and in the following analysis) we ignore the self-inductances of the loops, which is a usually a good approximation in practice. The insertion loss (IL), which is determined by the input and output coupling strength to the resonator, was kept in the range -40 to -10 dB. The reason for this is that a very weakly coupled resonator (i.e. $IL < -40$ dB) would suffer from a

low signal to noise ratio in transmission, whilst a strong coupled resonator (i.e. $0 \text{ dB} > IL > -10 \text{ dB}$) has a reduced Q_u because of the loading effects of the coupling circuitry [2].

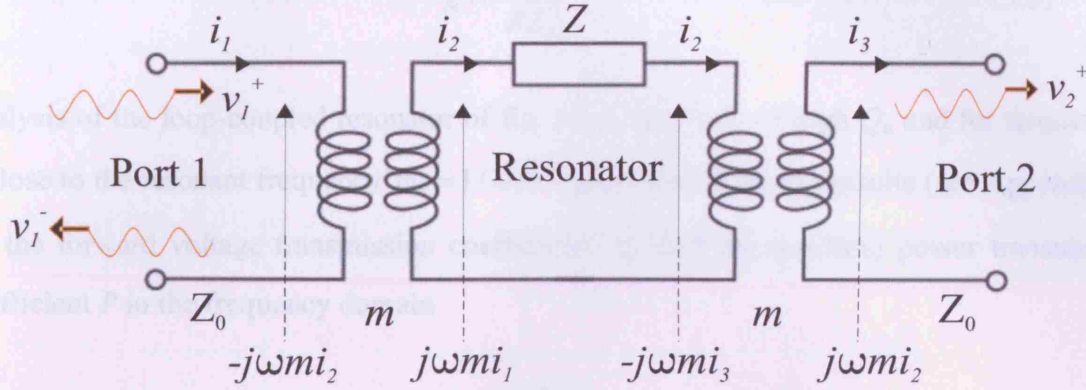


Figure 3.5 The equivalent circuit of a two port, loop-coupled resonator. The resonator is modelled as a series LRC circuit, of impedance Z [2].

The resonator is modelled as a series LRC circuit whose resonant frequency, impedance and (unloaded) quality factor are given by

$$\begin{aligned}\omega_0 &= \frac{1}{\sqrt{LC}} \\ Z &= R + j\omega L - j\frac{1}{\omega C} \\ Q_u &= \frac{\omega_0 L}{R}\end{aligned}\tag{3.1}$$

At resonance, the inductive and capacitive reactance cancel each other out and Z is purely real (i.e. $Z = R$). The input voltage v_1^+ is supplied by the VNA through of its ports, setting up current i_1 in the input circuit made up of the input coupling cable connected to the VNA. Current i_2 is induced in the resonator loop, which in turn induces current i_3 in the output circuit that is connected to the other port of the VNA through the output coupling cable. Depending on the strength of the input and the output couplings to the resonator, part of the input voltage is transmitted as v_2^+ to the output circuit whereas the residual (i.e. v_1^-) is reflected back into the input circuit. The detailed analysis of the resonator equivalent circuit at resonance is presented in appendix A, which provides the following expression for S_{21} as

$$S_{21} = -\frac{2g}{1+2g}\tag{3.2}$$

where g is the coupling coefficient (i.e. same for both the input and output coupling because of symmetric coupling) defined as

$$g = \frac{\omega^2 m^2}{RZ_0} \quad (3.3)$$

Analysis of the loop-coupled resonator of fig. 3.5 in the limit of high Q_u and for frequencies ω close to the resonant frequency $\omega_0 = 1/\sqrt{LC}$ gives the following results (see Appendix A) for the forward voltage transmission coefficient S_{21} and the resulting power transmission coefficient P in the frequency domain

$$S_{21} = \frac{-2g}{1 + 2g + 2jQ_u x} \quad (3.4)$$

$$\begin{aligned} \rightarrow P = |S_{21}|^2 &= \frac{4g^2}{(1 + 2g)^2 + 4Q_u^2 x^2} \\ &= \frac{4g^2}{(1 + 2g)^2} \quad (3.5) \\ &= \frac{4Q_u^2 x^2}{1 + \frac{4Q_u^2 x^2}{(1 + 2g)^2}} \end{aligned}$$

where $x = \Delta\omega/\omega_0 = (\omega - \omega_0)/\omega_0$ and dimensionless g is the coupling coefficient (i.e. same for input and output coupling because of symmetric coupling) defined by

$$g = \frac{\omega_0^2 m^2}{Z_0 R} = \frac{\omega_0 m^2 Q_u}{Z_0 L} \quad (3.6)$$

where Z_0 is the characteristic impedance of the input/output lines (usually 50 Ω). Note that $g \propto m^2 Q_u$, so that stronger coupling (and greater power transmission at resonance) is obtained by increasing m , by increasing Q_u , or by increasing both.

In Eq. (3.5), the term $\frac{Q_u^2}{(1 + 2g)^2}$ in the denominator is equal to Q_L^2 implying that

$$Q_L = \frac{Q_u}{1 + 2g} \quad (3.7)$$

Since Eq. (3.5) describes a Lorentzian curve, a curve fitting routine is used in this research to extract the microwaves parameters of interest from the $|S_{21}|^2$ data gathered from a VNA. In this research an automated data acquisition system was developed using IGOR Pro software, which is chosen because of its powerful built-in curve fitting routine. A typical curve fitted Lorentzian plot in IGOR Pro is illustrated in fig. 3.6.

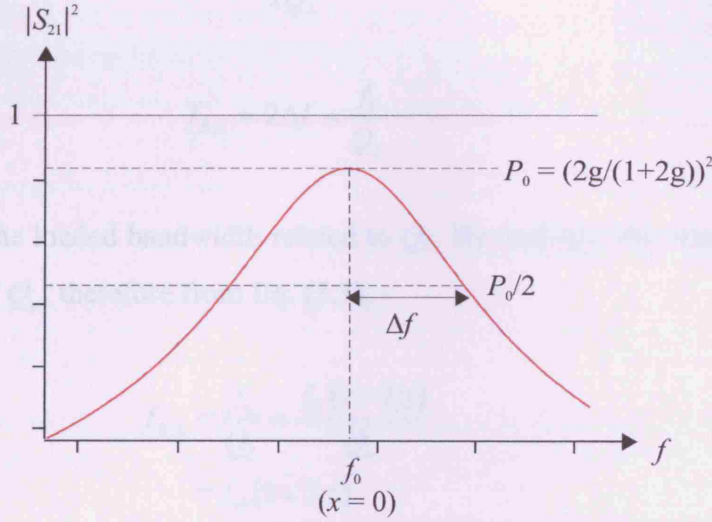


Figure 3.6 $|S_{21}|^2$ data acquired from 8510C VNA is curve fitted to lorentzian in IGOR Pro. The goodness of the fit is apparent that original curve (red) is almost hidden by the fitted curve (blue).

In fig. 3.6 at f_0 , where $x = 0$, $P_0 = \left(\frac{2g}{1+2g} \right)^2$, where P_0 is the peak power at resonance, then

Eq. (3.5) can be rewritten as

$$P = \frac{P_0}{1 + 4Q_L^2 \left(\frac{f - f_0}{f_0} \right)^2} \quad (3.8)$$

where x has been replaced by $\frac{\Delta f}{f_0} = \frac{f - f_0}{f_0}$, P_0 is the peak power at resonance and Q_L is called the *loaded quality factor*, which is smaller than Q_u due to the loading effects of the coupling.

To determine f_B (half power bandwidth), consider the again fig. 3.6. Since f_B is the half power bandwidth, it is equal to the span of the $|S_{21}|^2$ curve between those points where $|S_{21}|^2 = P_0/2$, as shown in fig. 3.6. therefore Eq. (3.8) becomes

$$\begin{aligned}
\frac{P_0}{2} &= \frac{P_0}{1 + 4Q_L^2 \left(\frac{\Delta f}{f_0} \right)^2} \\
\rightarrow 1 &= 4Q_L^2 \left(\frac{\Delta f}{f_0} \right)^2 \\
\rightarrow \Delta f &= \pm \frac{f_0}{2Q_L}
\end{aligned} \tag{3.9}$$

Consequently,

$$f_{B,L} = 2\Delta f = \frac{f_0}{Q_L} \tag{3.10}$$

where $f_{B,L}$ signifies the loaded bandwidth related to Q_L . By analogy, the relationship between f_B and Q_u is $f_B = f_0 / Q_u$, therefore from Eq. (3.7),

$$\begin{aligned}
f_{B,L} &= \frac{f_0}{Q_L} = \frac{f_0(1+2g)}{Q_u} \\
&= f_B(1+2g)
\end{aligned} \tag{3.11}$$

Hence, the loaded bandwidth ($f_{B,L}$) of the resonator is higher by a factor of $(1+2g)$ as compared to f_B ; as mentioned earlier this fact is quite intuitive given that Q_L is smaller than Q_u by the same factor. It is apparent from Eq. (3.7) that evaluation of Q_u requires not only the measured Q_L but also the value of coupling coefficient g , which is not directly quantifiable. Therefore, a practicable alternative method of estimating Q_u , that makes use of the IL (i.e. which can be directly read from the VNA), is described below:

The IL can be fixed by adjusting the input and the output coupling strength of the resonator. At resonance, let $|S_{21}|$ to be

$$\begin{aligned}
|S_{21}|_{x=0} &= \frac{2g}{1+2g} = 1 - \frac{1}{1+2g} \\
\rightarrow \frac{1}{1+2g} &= 1 - |S_{21}|_{x=0}
\end{aligned} \tag{3.12}$$

From the relationship between Q_L and Q_u , it follows that

$$Q_u = \frac{Q_L}{(1 - |S_{21}|_{x=0})} \tag{3.13}$$

and

$$f_B = f_{B,L} \left(1 - |S_{21}|_{x=0}\right) \quad (3.14)$$

If the transmitted power ratio (P) is in dB, then

$$P = 20 \log S_{21} \rightarrow S_{21} = 10^{P/20} \quad (3.15)$$

and therefore use of the IL results in

$$|S_{21}|_{x=0} = 10^{IL/20} \quad (3.16)$$

From Eqs. 3.13 and 3.16,

$$Q_u = \frac{Q_L}{(1 - 10^{IL/20})} \quad (3.17)$$

A simple through calibration of the VNA is sufficient here to determine an accurate value of IL . This allows a small correction due to cable loss (typically 0.2 dB per cable).

3.5.5 Theoretical Calculations of Dielectric Resonators Parameters

The two most important properties of a DRs are the quality factor (Q) and the resonant frequency (f_0). Resonance occurs due to exchange of electric and magnetic field energies at a set of resonant frequencies f_0 . Although the geometrical structure of dielectric resonators is very simple, it is much more complicated to obtain an exact solution of Maxwell's equations for them as compared with hollow metal cavities. For a given DR, the accurate resonant frequency of $TE_{01\delta}$ mode can be calculated only by complicated numerical procedures [11, 12, and 13]. For an appropriate estimation of the resonant frequency of the isolated DR (see fig. 3.3 (a)), the following simple formula can be used [1]:

$$f_0 (\text{GHz}) = \frac{34}{a\sqrt{\epsilon_r}} \left[\frac{a}{L} + 3.45 \right] \quad (3.18)$$

here, a and L are the radius and length of the dielectric resonator (in millimetres) respectively, and ϵ_r is the dielectric constant of the material. This formula is accurate to about 2% in the range $0.5 < a/L < 2$ and $30 < \epsilon_r < 50$ [1]. Eq. (3.18) is used to estimate the resonant frequency of the sapphire DR used in this research, which operates in $TE_{01\delta}$.

The quality factor quantifies the relationship between the mean stored EM energy and mean power loss in a resonant structure. The unloaded Q-factor (Q_u) of a cylindrical cavity is given by the fundamental relation:

$$Q_u = \omega_0 \frac{\langle U \rangle}{\langle P \rangle} \quad (3.19)$$

where $\langle U \rangle$ is the time averaged stored energy and $\langle P \rangle = \langle P \rangle_c + \langle P \rangle_d + \langle P \rangle_r$ is the time averaged dissipated energy [1, 2]. $\langle P \rangle_c$ is the conductor power loss, $\langle P \rangle_d$ is the power loss in dielectric and $\langle P \rangle_r$ is the power loss due to radiation of the fields. Q_u can thought of as comprising the sum of various constituent losses such as $\langle P \rangle_c$, $\langle P \rangle_d$ and $\langle P \rangle_r$. For a DR placed in a closed cavity with highly conductive walls, radiation is essentially non-existent and $\langle P \rangle_r = 0$. Thus $\langle P \rangle = \langle P \rangle_c + \langle P \rangle_d$ and

$$\frac{1}{Q_u} = \frac{\langle P \rangle_c}{\omega_0 \langle U \rangle} + \frac{\langle P \rangle_d}{\omega_0 \langle U \rangle} = \frac{1}{Q_c} + \frac{1}{Q_d} \quad (3.20)$$

At resonance the time averaged total stored energy $\langle U \rangle$ equals the time averaged maximum electric energy $\langle U \rangle_{e, \max}$ or time average maximum magnetic energy $\langle U \rangle_{m, \max}$:

$$\langle U \rangle = \langle U \rangle_{e, \max} = \frac{1}{2} \int_{\text{volume}} \epsilon_r \epsilon_0 |E|^2 dv = \frac{1}{2} \int_{\text{volume}} \mu_r \mu_0 |H|^2 dv = \langle U \rangle_{m, \max} \quad (3.21)$$

here, ϵ_r and μ_r are the relative permittivity and permeability of the medium in the resonator, E and H are the magnitudes of electric and magnetic energy, respectively. The above integration is made over the whole volume of the resonator.

If the material within the cavity is lossless then the energy dissipation $\langle P \rangle_c$ is caused by the cavity wall (curved, top and the bottom wall losses):

$$\langle P \rangle_c = \frac{R_{\text{surface}}}{2} \int_{\text{surface}} |H_{\text{surface}}|^2 ds \quad (3.22)$$

The above integration is made over the whole cavity wall surfaces. The surface resistance (R_{surface}) of the cavity wall in Eq. (3.22) is given by:

$$R_{surface} = \frac{\omega \mu_r \delta}{2} \quad (3.23)$$

here, μ_r is the permeability of the conductor (cavity wall), and δ is the skin depth of the conductor ($\delta = \sqrt{2 / \omega \mu \sigma}$, where $\mu = \mu_0 \mu_r$ is the permeability of the material in H/m and σ is the conductivity in S/m). According to Eqs. (3.18) – (3.23), the Q_u of a lossless hollow metallic resonator is:

$$Q_u = \frac{2}{\delta} \frac{\int_{volume} |H|^2 dv}{\int_{surface} |H_{surface}|^2 ds} \quad (3.24)$$

Inclusion of the dielectric loss of the medium in the cavity results in the value of Q_u being decreased:

$$Q_u = \omega_0 \frac{\langle U \rangle}{\langle P \rangle} = \frac{\omega_0 \langle U \rangle}{\langle P \rangle_c + \langle P \rangle_d} = \frac{1}{\frac{1}{Q_c} + \frac{1}{Q_d}} \quad (3.25)$$

where $\langle P \rangle_c$, $\langle P \rangle_d$ are the energy dissipation due to the conductor loss and dielectric loss, Q_u and Q_d are the quality factors when considering the conductor loss and dielectric loss, respectively. If the dielectric medium within the cavity is lossy, then

$$\langle P \rangle_d = \frac{1}{2} \epsilon_r \epsilon_0 \tan \delta \int_{in} |E|^2 dv \quad (3.26)$$

and since,

$$\langle U \rangle_{tot} = \langle U \rangle_d + \langle U \rangle_{air} = \frac{1}{2} \epsilon_r \epsilon_0 \int_{in} |E|^2 dv + \frac{1}{2} \epsilon_0 \int_{out} |E|^2 dv$$

this simplifies to:

$$Q_d = \omega_0 \frac{\langle U \rangle_{tot}}{\langle P \rangle_d} = \omega_0 \frac{\epsilon_r \int_{in} |E|^2 dv + \int_{out} |E|^2 dv}{\epsilon_r \tan \delta \int_{in} |E|^2 dv} \quad (3.27)$$

where, ϵ_r and $\tan \delta$ are the real permittivity and the loss tangent of the dielectric material (sapphire dielectric) respectively, $\langle U \rangle_{tot}$ is the time averaged total stored energy, which is the

combination of energy within the dielectric $\langle U \rangle_d$ and the air $\langle U \rangle_{air}$ region around. The subscripts *in* and *out* represent inside and outside the sapphire dielectric material and these are the volume integral.

Dividing the right hand side of the numerator and the denominator of the simplified Eq. (3.27) by $\epsilon_r \int_{in} |E|^2 dv$ yields

$$Q_d = \frac{1 + \left(\frac{\int_{out} |E|^2 dv}{\epsilon_r \int_{in} |E|^2 dv} \right)}{\tan \delta} = \frac{1+W}{\tan \delta} \quad (3.28)$$

where, the bracket term in the numerator of Eq. (3.28) is termed as W . i.e.

$$W \equiv \frac{\text{electrical energy outside dielectric}}{\text{electrical energy within dielectric}}$$

Therefore the overall unloaded quality factor (Q_{tot}) can be deduced as follows

$$Q_c = \omega_0 \frac{\langle U \rangle_{tot}}{\langle P \rangle_c} = \omega_0 \frac{\epsilon_r \epsilon_0 \int_{in} |E|^2 dv + \epsilon_0 \int_{out} |E|^2 dv}{R_{surface} \int_{surface} |H_t|^2 ds} \quad (3.29)$$

therefore,

$$\begin{aligned} \frac{1}{Q_{tot}} &= \frac{1}{Q_c} + \frac{1}{Q_d} \\ &= \frac{R_{surface} \int_{surface} |H_t|^2 ds}{\omega_0 \left(\epsilon_r \epsilon_0 \int_{in} |E|^2 dv + \epsilon_0 \int_{out} |E|^2 dv \right)} + \frac{\tan \delta}{1+W} \end{aligned} \quad (3.30)$$

For most practical DRs with $\epsilon_r \gg 1$, $W \ll 1$, therefore

$$Q_d = \frac{1+W}{\tan \delta} \approx \frac{1}{\tan \delta}$$

The Q_d can thus be very large, for instance if the loss tangent ($\tan \delta$) of the dielectric is 10^{-5} , then $Q_d \approx 1/10^{-5} = 100,000$ for a SDR. However, the overall Q-factor calculated using

Eq. (3.30) is reduced because of the contribution of Q_c , which is usually smaller than Q_d for SDRs. Eqs. (3.18) – (3.30) have been realised in the High Frequency Structure Simulator (HFSS) field calculator* (see chapter 5) to elaborate and compute the results obtained from the field data of HFSS solution. The detailed design of the sapphire dielectric resonator for material characterisation and the implementation of these equations can be found in chapter 6.

3.5.6 Resonant Perturbation Technique

When a sample is introduced into a resonator, the properties of the material are deduced from the changes of the resonant frequency and the quality factor. This cavity perturbation technique is one of the most popular methods for microwave material characterisation, also known as material perturbation methods [1]. Fig. 3.7 shows a cylindrical cavity (TM₀₁₀ mode) for measurement of material properties using resonant perturbation technique. If the sample under study is introduced into position A with maximum electric field and minimum magnetic field, the dielectric properties of the sample can be characterised; if the sample is inserted into place B with maximum magnetic field and minimum electric field, the magnetic properties of the sample can be characterised.

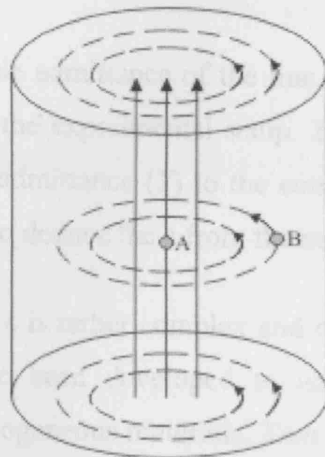


Figure 3.7 Cylindrical cavity (TM₀₁₀ mode) for material characterisation using resonant perturbation method. Position A and B are for permittivity and permeability measurement, respectively, as explained in the text.

* For the complete in-depth description of HFSS refer to chapter 5. The HFSS field calculator is one of the inbuilt tools, which is used to generate valuable information such as quality factor, resonance frequency, voltages and currents or any other quantity that can be viewed in a 3D environment for the modelled geometry.

3.6 Modelling of the Open Ended Coaxial Probe

Numerous papers have reported the use of open ended coaxial probe for complex permittivity measurement at microwave measurement [14-17]. The complex permittivity of an unknown material has generally been extracted from the reflection coefficient by modelling the fringing fields at the aperture of the probe as an equivalent lumped admittance [14]. In the case of an open ended coaxial probe the appropriate configuration is conductance (G) in parallel with a capacitive susceptance (B). Here, it is convenient to express its equivalent impedance in terms of its inverse, the admittance (Y), thus

$$Y = G + jB \quad (3.31)$$

where G and B are a factor of the propagation constant (γ) and the radial dimensions of the line. By the definition the complex reflection coefficient of the probe (ρ) is given in terms of this admittance as

$$\rho = \frac{\left(1 - \frac{Y}{Y_0}\right)}{\left(1 + \frac{Y}{Y_0}\right)} \quad (3.32)$$

where $Y_0 (= 1/Z_0)$ is the intrinsic admittance of the line. The complex reflection coefficient (ρ) is readily measurable from the experimental setup. The emphasis of the problem at this stage is the relationship of the admittance (Y) to the complex permittivity (ϵ) of the sample under study, which will enable to deduce the ϵ from the measured values of ρ or Y .

The relationship between ρ and ϵ is rather complex and rigorous analytical expression is not available. Certain models have been developed to analyse open ended coaxial probes terminated by semi-infinite homogeneous materials. Two different models have been studied in this chapter: the capacitive model [18] and the variational model [14]. In recent years, the full wave simulation method has also been used in analysing open ended coaxial lines [19]. The following sections present a brief description of capacitive and variational models.

3.6.1 Capacitive Model

Equivalent circuit for this model is presented in fig. 3.8 (b). The model is described in [18]. This lumped parameter model gives the capacitances as a function of frequency and dielectric constant. The probe discontinuity is modelled as a lumped admittance with fringing field capacitances originating from the dielectric material (silica) filling the line (C_0) and modelled capacitance of the material under test (C_1), as shown in fig. 3.8 (b). The reflection coefficient at the aperture of the coaxial probe is obtained by considering the complex admittance of the equivalent circuit shown.

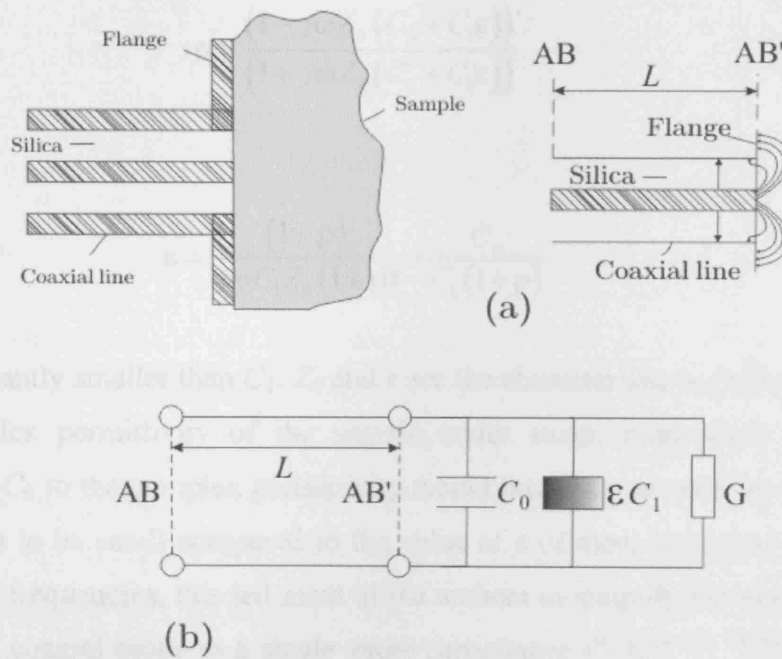


Figure 3.8 Schematic diagram and equivalent circuit of the coaxial probe. (a) Coaxial probe, (b) equivalent circuit (capacitive model).

The approach implemented in the first instance is to consider admittance (Y) in terms of its lumped equivalent circuit parameters. The susceptance (B) is capacitive and made up of internal and external fringing fields (see fig. 3.8 (b)).

$$Y = G + j\omega(C_0 + C_1(\epsilon_1 - j\epsilon_2)) \quad (3.33)$$

where ω is the angular frequency (rad/sec) and $\epsilon = \epsilon_1 - j\epsilon_2$ is the complex permittivity of the sample under test.

At the limit of low frequency $G = 0$ and C_0 and C_1 are constants that depend on the dimensions of the probe and the material under test, respectively. Assuming the probe is used at frequencies such that the wavelength of the propagating wave is significantly larger than the radial dimensions of the probe, a quasi-steady state would prevail. Therefore,

$$\rho = \frac{(1 - YZ_0)}{(1 + YZ_0)} \quad (3.34)$$

Substituting Eq. (3.33) into Eq. (3.34) yields:

$$\rho = \frac{(1 - j\omega Z_0 (C_0 + C_1 \epsilon))}{(1 + j\omega Z_0 (C_0 + C_1 \epsilon))} \quad (3.35)$$

and

$$\epsilon = \frac{(1 - \rho)}{j\omega C_1 Z_0 (1 + \rho)} - \frac{C_0}{C_1 (1 + \rho)} \quad (3.36)$$

with C_0 significantly smaller than C_1 . Z_0 and ϵ are the characteristic impedance of the coaxial line and complex permittivity of the sample under study, respectively. Neglecting the contribution of C_0 to the complex permittivity would introduce an error in ϵ . Since the error has been shown to be small compared to the value of ϵ of most biological samples at radio and microwave frequencies, this led most of the authors to simplify the equivalent circuit of the open ended coaxial probe to a single shunt capacitance C_1 [20, 21, 22]. In this case the reflection coefficient becomes

$$\rho = \frac{(1 - j\omega C_1 Z_0 \epsilon)}{(1 + j\omega C_1 Z_0 \epsilon)} \quad (3.37)$$

The accuracy of the capacitive model in measuring from low to high dielectric materials and their robustness are now investigated. To validate this technique, experimental measurements are carried out on several different dielectric materials, such as low, medium and high permittivity materials. The detailed investigation and the validation of this technique can be found in chapters 5 and 6.

3.6.2 Variational Model

In the cylindrical co-ordinate system $(\hat{\rho}, \varphi, z)$, fig. 3.9, assuming the radial electric field intensity over the aperture $E_{\hat{\rho}}$ is inversely proportional to $\hat{\rho}$, a simplified expression for aperture admittance (Y_L) can be obtained [14] and integrating the equation from $\hat{\rho} = a$ to $\hat{\rho} = b$ gives

$$Y_L = j \frac{k^2}{\pi k_c \ln\left(\frac{b}{a}\right)} \int_a^b \int_0^\pi \cos \varphi' \frac{\exp(-jkr)}{r} d\varphi' d\hat{\rho}' d\hat{\rho} \quad (3.38)$$

where:

$$k^2 = \omega^2 \mu_0 \epsilon$$

$$k_c^2 = \omega^2 \mu_0 \epsilon_c \epsilon_0$$

$$r^2 = \hat{\rho}^2 + \hat{\rho}'^2 - 2\hat{\rho}\hat{\rho}' \cos \varphi'$$

where a and b are correspondingly the inner and outer radii of the coaxial probe, ω is the angular frequency, k is the wavenumber in the material medium, ϵ_0 and μ_0 are the permittivity and permeability of free space, respectively, and ϵ_c is the dielectric permittivity of the material (silica) filling the probe. Prime and unprimed co-ordinates represent the source points and field points respectively. The dielectric window is assumed to be lossless of permittivity ϵ_c , and ϵ is the complex permittivity of a sample under test.

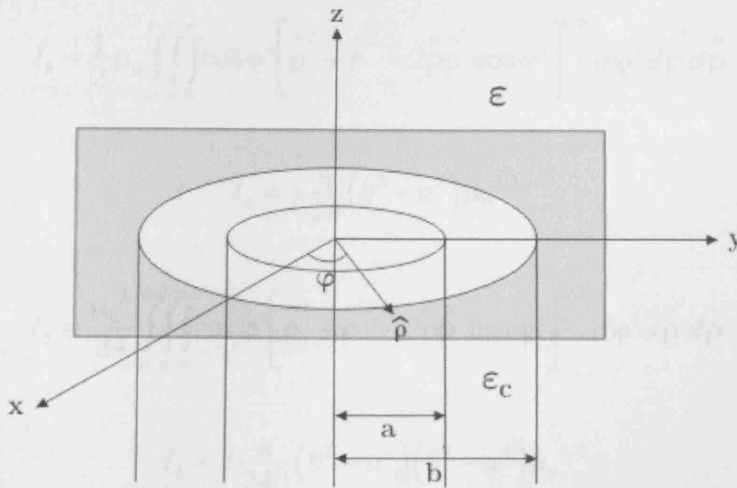


Figure 3.9 Geometry of an open ended coaxial probe in cylindrical co-ordinate system with an infinite flange. a and b are the inner and outer radii of the probe.

Misra [14] has shown that when the radial dimensions of the probe are much smaller than the propagating wavelength, Eq. (3.38) can be approximated by the first terms of the series expansion for the exponential term and then used to deduce ϵ , numerically, from measured values of Y_L . The characteristic admittance Y_0 of the coaxial line is

$$Y_0 = \frac{2\pi}{\left(\sqrt{\frac{\mu_0}{\epsilon_0 \epsilon_c}}\right) \ln\left(\frac{b}{a}\right)} \quad (3.39)$$

An expression for the admittance terminating the aperture can now be obtained as follows:

$$Y_L^a = I_0 \omega \left\{ \epsilon I_1 + \epsilon^2 I_3 \omega^2 + \epsilon^{5/2} I_4 \omega^3 + \epsilon^3 I_5 \omega^4 + \epsilon^{7/2} I_6 \omega^5 + \epsilon^4 I_7 \omega^6 \right. \\ \left. + \epsilon^{9/2} I_8 \omega^7 + \epsilon^5 I_9 \omega^8 + \epsilon^{11/2} I_{10} \omega^9 + \dots \right\} \quad (3.40)$$

where:

$$I_0 = j \frac{2}{\left(\ln\left(\frac{b}{a}\right)\right)^2}$$

$$I_1 = \int_a^b \int_a^b \int_0^\pi \frac{\cos \varphi'}{\left[\hat{\rho}^2 + \hat{\rho}'^2 - 2\hat{\rho}\hat{\rho}' \cos \varphi'\right]^{1/2}} d\varphi' d\hat{\rho}' d\hat{\rho}$$

$$I_3 = \frac{1}{2} \mu_0 \int_a^b \int_a^b \int_0^\pi \cos \varphi' \left[\hat{\rho}^2 + \hat{\rho}'^2 - 2\hat{\rho}\hat{\rho}' \cos \varphi'\right]^{1/2} d\varphi' d\hat{\rho}' d\hat{\rho}$$

$$I_4 = j \frac{\pi}{24} (b^2 - a^2) \mu_0^{3/2}$$

$$I_5 = \frac{\mu_0^2}{24} \int_a^b \int_a^b \int_0^\pi \cos \varphi' \left[\hat{\rho}^2 + \hat{\rho}'^2 - 2\hat{\rho}\hat{\rho}' \cos \varphi'\right]^{3/2} d\varphi' d\hat{\rho}' d\hat{\rho}$$

$$I_6 = j \frac{\pi}{240} (b^2 - a^2) (b^4 - a^4) \mu_0^{5/2}$$

$$I_7 = \frac{\mu_0^3}{720} \int_a^b \int_a^b \int_0^\pi \cos \varphi' \left[\hat{\rho}^2 + \hat{\rho}'^2 - 2\hat{\rho}\hat{\rho}' \cos \varphi' \right]^{5/2} d\varphi' d\hat{\rho}' d\hat{\rho}$$

$$I_8 = j \frac{\pi \mu_0^{7/2}}{3360} \left[\frac{(b^6 - a^6)(b^2 - a^2)}{3} + \frac{3}{8}(b^4 - a^4) \right]$$

$$I_9 = \frac{\mu_0^4}{40320} \int_a^b \int_a^b \int_0^\pi \cos \varphi' \left[\hat{\rho}^2 + \hat{\rho}'^2 - 2\hat{\rho}\hat{\rho}' \cos \varphi' \right]^{7/2} d\varphi' d\hat{\rho}' d\hat{\rho}$$

Prime and un-primed coordinates represent the source and the field points respectively. The second term (I_1) of the expression for Y_L^a goes to zero on integration over φ' . Since the integrand of I_1 is singular at $\hat{\rho} = \hat{\rho}'$ for $\varphi' = 0$, this can be avoided by introducing the elliptic integral of the first kind, which can be approximated by a polynomial [23]

$$I_1 = 4(a+b)[E(m)-1] \quad (3.41)$$

and

$$m = \frac{4ab}{(a+b)^2} \quad (3.42)$$

Since I_i , where $i = 0 \dots 10$, are only dependent on the physical dimensions of the aperture, these can be evaluated for a given coaxial line. The triple integrals are performed numerically by Simpson's three point rule.

Moreover, the integral with respect to φ' in Eq. (3.38) can be expressed in terms of Bessel functions, using an integral representation and Neumann formula. Interchanging the order of integration, yields [24]

$$Y^a = Y_0 \frac{jk_2}{\ln\left(\frac{b}{a}\right)} \int_0^\infty \frac{1}{\xi(\xi^2 - k_2^2)^{1/2}} [J_0(\xi a) - J_0(\xi b)]^2 d\xi \quad (3.43)$$

where

$$\arg(\xi^2 - k_2^2)^{1/2} = \begin{cases} 0, \xi^2 > k_2^2 \\ \frac{\pi}{2}, \xi^2 < k_2^2 \end{cases}$$

and k_2 is the wave number in the terminating dielectric of the coaxial line. The integral is considered separately over the ranges $0 > \xi > k_2$ and $k_2 < \xi < \infty$. The integrand changes from imaginary to real at $\xi = k_2$. Hence the integration over these two ranges gives the slot conductance (G) and suceptance (B) respectively. It follows that [24]

$$Y^a = G + jB \quad (3.44)$$

$$G = \frac{Y_0 \sqrt{\epsilon}}{\ln\left(\frac{b}{a}\right) \sqrt{\epsilon_c}} \int_0^\infty \frac{1}{\sin \theta} \left[J_0\left(k_0 \sqrt{\epsilon b \sin \theta}\right) - J_0\left(k_0 \sqrt{\epsilon a \sin \theta}\right) \right]^2 d\theta \quad (3.45)$$

$$B = \frac{Y_0 \sqrt{\epsilon}}{\pi \ln\left(\frac{b}{a}\right) \sqrt{\epsilon_c}} \int_0^\pi \left[\begin{array}{l} 2Si\left(k_0 \sqrt{\epsilon(a^2 + b^2 - 2ab \cos \theta)}\right) \\ -2Si\left(2k_0 \sqrt{\epsilon a \sin\left(\frac{\theta}{2}\right)}\right) \\ -2Si\left(2k_0 \sqrt{\epsilon b \sin\left(\frac{\theta}{2}\right)}\right) \end{array} \right] d\theta \quad (3.46)$$

where k_0 is the propagation constant in free space, J_0 is the Bessel function of zero order; Si is the sine integral, Y_0 is the characteristic impedance of the coaxial line; ϵ and ϵ_c are the complex permittivity of the sample under test and dielectric permittivity of the material filling the coaxial line, respectively.

Eqs. (3.45) and (3.46) represent an expression of the admittance of the probe (Y^a) as an integral over its aperture. This approximation was also studied by Levin and Papas [25], Xu *et al.* [26] and Misra *et al.* [27] and was derived by Misra [14] as Eq. (3.40). The derivations (Eqs. 3.40, 3.45 and 3.46) were obtained from a variational expression for the input admittance of a coaxial cable opening into an infinite ground plane. The variational expression was written in terms of an integral equation for the unknown electric field distribution in the aperture and was solved using the principal mode (TEM) of the coaxial line to represent the aperture field. Thus the solutions given by Eqs. (3.40), (3.45) and (3.46) do not take into account the excitation of the higher order modes at the aperture. The detailed implementations of these models (capacitive and variational models) are described in chapter 6.

3.7 Validation of the Above Models Using Debye Liquids of Known Permittivity

In order to validate the above techniques (sections 3.6.1 and 3.6.2), experimental measurements were carried out on standard polar liquids, which have been measured and compared to a full HFSS model of the probe which will be described in detail in chapters 5 and 6. The dielectric properties of polar liquids arise from the orientational response of permanent electric dipoles to an applied electric field. This behaviour is well-described by Debye theory [2], which are convenient as it enables complex permittivity to be calculated at any frequency. For a single relaxation time τ of each dipole, Debye theory predicts a frequency – dependent, complex permittivity of

$$\varepsilon(\omega) = \varepsilon_1(\omega) - j\varepsilon_2(\omega) = \varepsilon_\infty + \frac{\varepsilon_s - \varepsilon_\infty}{1 + j\omega\tau} \quad (3.47)$$

where ε is the complex permittivity ε_∞ and ε_s are the permittivity at infinite frequency ($\omega\tau \gg 1$) and static permittivity ($\omega\tau \ll 1$), respectively. The following equations have been obtained by separating real (ε_1) and imaginary (ε_2) parts; the detailed step by step procedures are shown below;

$$\begin{aligned} \varepsilon(\omega) &= \varepsilon_\infty + \frac{\varepsilon_s - \varepsilon_\infty}{1 + j\omega\tau} \\ &= \varepsilon_\infty + \frac{(\varepsilon_s - \varepsilon_\infty)(1 - j\omega\tau)}{(1 + j\omega\tau)(1 - j\omega\tau)} \\ &= \varepsilon_\infty + \frac{\varepsilon_s - j\varepsilon_s\omega\tau - \varepsilon_\infty + j\varepsilon_\infty\omega\tau}{1 + (\omega\tau)^2} \\ &= \varepsilon_\infty + \frac{(\varepsilon_s - \varepsilon_\infty) - j\omega\tau(\varepsilon_s - \varepsilon_\infty)}{1 + (\omega\tau)^2} \end{aligned}$$

which, therefore, simplifies to

$$\begin{aligned} \varepsilon_1(\omega) &= \text{Re}[\varepsilon(\omega)] = \varepsilon_\infty + \frac{\varepsilon_s - \varepsilon_\infty}{1 + \omega^2\tau^2} \\ \varepsilon_2(\omega) &= \text{Im}[\varepsilon(\omega)] = \frac{(\varepsilon_s - \varepsilon_\infty)\omega\tau}{1 + \omega^2\tau^2} \end{aligned} \quad (3.48)$$

The locus of $\epsilon(\omega)$ in the complex plane is a semicircle, as shown in fig. 3.10, where the plot $\epsilon_2 = -\text{Im}(\epsilon)$ vertically and $\epsilon_1 = \text{Re}(\epsilon)$ horizontally. The detailed derivation of the locus of $\epsilon(\omega)$ shown below can be found in appendix B.

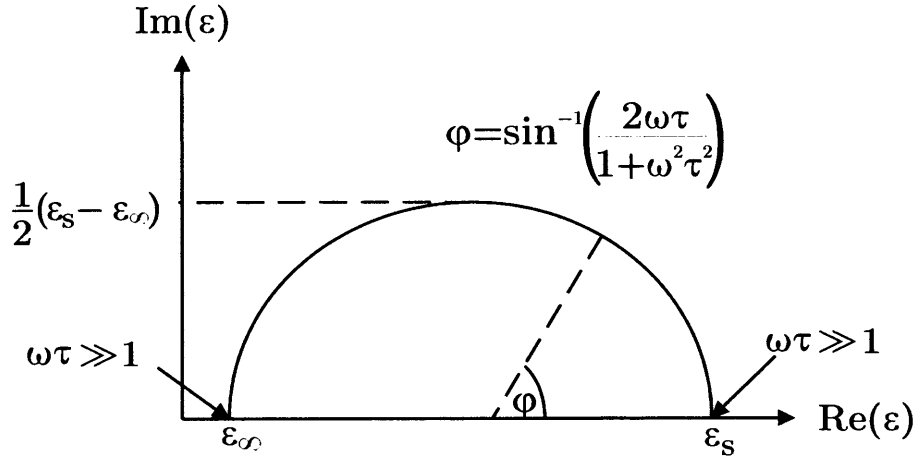


Figure 3.10 The locus of $\epsilon(\omega)$ in the complex plane. $\epsilon_2 = -\text{Im}(\epsilon)$ exhibits a relaxation peak when $\omega\tau = 1$.

3.8 Concept of Microwave Network

The concept of microwave network is developed from transmission line theory, and it is a powerful tool in microwave engineering. Microwave network methods uses the responses of a microwave structure to external signals, and it is a complement to the microwave field theory that analyses the field distribution inside the microwave structure. There are two sets of physical parameters often used in network analysis [4]. One set of parameters are voltage (V) and current (I), and the other set of parameters are the incident wave a (wave going into the network) and the reflected wave b (the wave coming out of the network). Different network parameters are used for different set of physical parameters. For instance, scattering parameters are used to describe the relationship between the incident and reflected waves, while impedance and admittance matrixes are used to describe the voltage and current [4]. The following sections mainly focus on the scattering parameters followed by principles of vector network analyser.

3.8.1 Scattering Parameters

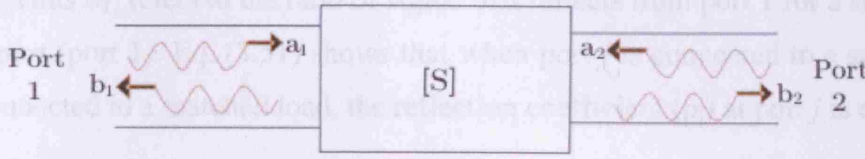


Figure 3.11 Schematic diagram of a two port network.

The scattering parameters (S-parameters) allow accurate description of the properties of incredibly complicated networks as a simple *black box*. The introduction of S-parameters arises naturally in microwave systems, due to lack of a unique definition for currents and voltages at these frequencies. The responses of a network to external circuits are described by the incident and reflected of the microwave signals. As shown in fig. 3.11, the incident signal at ports 1 and 2 are denoted as a_1 and a_2 respectively, and the reflected signals at ports 1 and 2 are denoted as b_1 and b_2 respectively [4]. These parameters (a_1 , a_2 , b_1 , and b_2) may be voltage (where the incident voltage denoted by ‘ a ’ while the voltage leaving the port is denoted by ‘ b ’) or current. The relationship between the input $[a]$ and output $[b]$ signals are often described by the scattering matrix $[S]$ where,

$$[b] = [S][a] \quad (3.49)$$

and

$$[a] = \begin{bmatrix} a_1 \\ a_2 \end{bmatrix} \quad [b] = \begin{bmatrix} b_1 \\ b_2 \end{bmatrix} \quad (3.50)$$

$$[S] = \begin{bmatrix} S_{11} & S_{12} \\ S_{21} & S_{22} \end{bmatrix}$$

For a scattering parameter S_{ij} , if $a_i = 0$ ($i \neq j$), from Eq. (3.49), yields

$$S_{jj} = \frac{b_j}{a_j} \quad (j = 1, 2) \quad (3.51)$$

$$S_{ij} = \frac{b_i}{a_j} \quad (i \neq j; i = 1, 2; j = 1, 2) \quad (3.52)$$

where the subscripts “ ij ”, are such that j is the port that is excited (input port) and i is the output port. Thus S_{11} refers to the ratio of signal that reflects from port 1 for a signal incident at the same port (port 1). Eq. (3.51) shows that when port j is connected to a source and the other port connected to a matched load, the reflection coefficient (ρ_j) at port j is equal to S_{jj} :

$$\rho_j = S_{jj} = \frac{b_j}{a_j} \quad (3.53)$$

Eq. (3.52) shows that when port j is connected to a source, and port i is connected to a matching load, the transmission coefficient ($T_{j \rightarrow i}$) from port j to port i equal to S_{ij} :

$$T_{j \rightarrow i} = S_{ij} = \frac{b_i}{a_j} \quad (3.54)$$

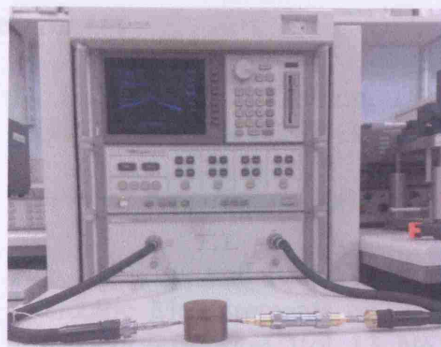
3.8.2 Why Scattering Parameters?

S-parameters are measured with resistive terminations and are determined by measuring incident and reflected signals. They are introduced because:

- At high frequencies, total voltage and current cannot be measured directly.

3.8.3 Basics of the Vector Network Analyser (VNA)

Network analysers are one of the most important tools for analysing analogue circuits. They are typically applied to measure small signal or linear characteristics of multi-port networks at frequencies ranging from lower frequencies (a few Hz), to higher frequencies. A measurement of the reflection from and/ or transmission through a material along with knowledge of its physical dimensions provides the information to characterise the permittivity and permeability of the material under test. In microwave engineering, network analysers are used to analyse a wide variety of materials, components, circuits and systems [4]. Photographs of the network analysers used in this research are shown in fig. 3.12. The implementation of the microwave techniques, which will be discussed in later chapters, for materials property characterisation, measurements are conducted by the network analyser, the detailed information about the network analysers can be found in [28].



(a)



(b)

Figure 3.12 Photograph of the Hewlett Packard VNA. (a) HP8510C and (b) HP 8753E. These test instruments are used to measure the S-parameters (magnitude and phase) of a one or two port microwave network from 45 MHz to 50 GHz and 30 kHz to 6 GHz, respectively.

4. D.M. Pozar, *Microwave Engineering*, 2nd edition, John Wiley & Sons, Inc., 2003.
5. M. Wu, J. Yang, and L. Zhang, "An Improved Coaxial Probe Technique for Measuring Microwave Permittivity of Thin Dielectric Materials", *Measurement Science and Technology*, Vol. 11, No. 11, pp. 1617-16, August 2000.
6. C.L. Pournazerian, and D.K. Mishra, "The Coaxial Aperture Electromagnetic Sensor and its Application to Material Characterization", *Measurement Science and Technology*, Vol. 8, No. 11, pp. 1195-1204, 1997.
7. M.A. Saeed, S.S. Saeed, "Coaxial Line Reflection Methods for Measuring Dielectric Properties of Biological Substrates at Radio and Microwave Frequencies - A Review", *IEEE Transactions on Instrumentation and Measurement*, Vol. 39, No. 3, pp. 176-180, 1990.
8. G. Choi, K. Li, and Z. Li, "Improved Dielectric Measurement with an Open-Ended Coaxial Probe", *IEEE Transactions on Microwave Theory and Techniques*, Vol. 42, No. 6, pp. 966-971, June 1994.
9. S. Akhtar, F. Ladouceur, and J. Naughton, "Variational Formulation of Open-Ended Coaxial Line in Contact with Layered Biological Medium", *IEEE Transactions on Biomedical Engineering*, Vol. 44, No. 10, pp. 1241-1248, June 1998.
10. A. Okaya and L.R. Benish, "The Dielectric Microwave Resistor", *Proceedings of the Institute of Radio Engineers*, Vol. 50, pp. 2081-2092, October 1962.
11. S.B. Cohn, "Microwave Bandpass Filters Containing High-Q Dielectric Resistor", *IEEE Transactions on Microwave Theory and Techniques*, Vol. MTT-16, No. 4, pp. 718-727, April 1968.
12. M.W. Popowicz, "Cylindrical Dielectric Resistor and Their Applications in TEM Line Microwave Circuits", *IEEE Transactions on Microwave Theory and Techniques*, Vol. MTT-27, No. 3, pp. 233-238, March 1979.

3.9 References

1. D. Kajfez, and P. Guillon, *Dielectric Resonators*, Noble Publishing Corporation, 1998, ISBN 1-884932-05-3.
2. A. Porch, *Private communication*, 2007-8.
3. A.P. Gregory, and R.N Clarke, "A Review of RF and Microwave Techniques for Dielectric Measurements on Polar Liquids", *IEEE Transaction on Dielectrics and Electrical Insulation*, Vol. 13, No. 4, August 2006.
4. D.M. Pozar, *Microwave Engineering*, 3rd edition, John Wiley & Sons, Inc., 2005, ISBN 0-471-44878-8.
5. B.C. Wadell, *Transmission Line Design Handbook*, Artech House Publishers, 1991, ISBN 0-89006-436-9.
6. M. Wu, X. Yao, and L. Zhang, "An Improved Coaxial Probe Technique for Measuring Microwave Permittivity of Thin Dielectric Materials". *Measurement Science and Technology*, Vol. 11, No. 11, pp. 1617–1622, August 2000.
7. C.L. Pournaropoulos, and D.K. Misra, "The Co-axial Aperture Electromagnetic Sensor and its Application in Material Characterisation", *Measurement Science and Technology*, Vol. 8, No. 11, pp. 1191-1202, 1997.
8. M.A. Stuchly, S.S. Stuchly, "Coaxial Line Reflection Methods for Measuring Dielectric Properties of Biological Substances at Radio and Microwave Frequencies - A Review", *IEEE Transaction on Instrumentation and Measurement*, Vol. 29, No. 3, pp. 176-183, 1980.
9. G. Chen, K. Li, and Z. Ji, "Bilayered Dielectric Measurement with an Open-Ended Coaxial Probe", *IEEE Transaction on Microwave Theory and Techniques*, Vol. 42, No. 6, pp. 966-971, June 1994.
10. E. Alanen, T. Lahtinen, and J. Nuutinen, "Variational Formulation of Open-Ended Coaxial Line in Contact with Layered Biological Medium", *IEEE Transaction on Biomedical Engineering*, Vol. 45, No. 10, pp. 1241-1248, June 1998.
11. A. Okaya and L.F. Barash, "The Dielectric Microwave Resonator", *Proceedings of the Institute of Radio Engineers*, Vol. 50, pp. 2081-2092, October 1962.
12. S.B. Cohn, "Microwave Bandpass Filters Containing High-Q Dielectric Resonators", *IEEE Transactions on Microwave Theory and Techniques*, Vol. MTT-16, No. 4, pp. 218-227, April 1968.
13. M.W. Pospieszalski, "Cylindrical Dielectric Resonators and Their Applications in TEM Line Microwave Circuits", *IEEE Transactions on Microwave Theory and Techniques*, Vol. MTT-27, No. 3, pp. 233-238, March 1979.

14. D.K. Misra, "A Quasistatic Analysis of Open-Ended Coaxial Lines", *IEEE Transaction on Microwave Theory and Techniques Society*, Vol. 35, No. 10, pp. 925-928, October 1987.
15. T. Marsland, and S. Evans, "Dielectric Measurement with an Open Ended Coaxial Probe", *IEE Proceedings*, Vol. 134, pp. 341-349, August 1987.
16. B.A. Shaw, "Measurement of the Permittivity of Organic Liquids Using Microwave Sensing Techniques", *Industrial Research Limited*, New Zealand, Rep. 108, 1993.
17. G. Gajda and S. Stuchly, "An Equivalent Circuit of an Open Ended Coaxial Line", *IEEE Transactions on Instrumentation and Measurement*, Vol. 32, No. 4, pp. 504-508, December 1983.
18. T.W. Athey, M.A. Stuchly, and S.S. Stuchly, "Measurement of Radio Frequency Permittivity of Biological Tissues with an Open-Ended Coaxial Line: Part 1 - Experimental Results". *IEEE Transaction on Microwave Theory and Techniques*, Vol. 30, No.1, pp. 82-86, January 1982.
19. C.L. Pournaropoulos, and D.K. Misra, "A Study on the Coaxial Aperture Electromagnetic Sensor and its Application in Material Characterisation" *IEEE Transactions on Instrumentation and Measurement*, Vol. 43, No. 2, pp. 111-115, April 1994.
20. E.C. Burdette, F.L. Cain, and J. Seals, "In Vivo Probe Measurement Technique for Determining Dielectric Properties at VHF through Microwave Frequencies," *IEEE Transactions on Microwave Theory and Techniques*, Vol.28, No.4, pp. 414-427, April 1980.
21. X. Dong, and Y.H. Wang, "Broadband Characterisations of Material Permittivity with a Small Sized Open Ended Coaxial Probe", *ASCE Proceedings*, pp.1-5, 2006.
22. M. Moukanda, F. Ndagijimana, J. Chilo, and P. Saguet, "A Coaxial Fixture Used for Extracting Complex Permittivity of Thin Layers", *IEEE Annual on Wireless and Microwave Technology Conference*, pp. 1-5, December 2006.
23. M. Abramowitz, and I.A. Stegun, *Handbook of Mathematical Function*, New York: Dove Publications, Inc., pp. 589-592, 1965, ISBN 0-486-61272-4.
24. N. Marcuvitz, *Wavelength Handbook*, New York: McGraw-Hill, pp. 213-216, 1951.
25. H.R. Levine, and C.H. Papas, "Theory of Circular Diffraction Antenna", *Journal of Applied Physics*, Vol. 22, pp. 29-43, 1951.
26. D. Xu, L. Li, and Z. Jiang, "Measurement of the Dielectric Properties of Biological Substances Using an Improved Open Ended Coaxial Line Resonator Method", *IEEE Transaction on Microwave Theory and Techniques*, Vol. 35, pp. 1424-1428, 1987.

27. D. Misra, M. Chhabra, B.R. Epstein, M. Mirotznik, and K.R Foster, “Noninvasive Electrical Characterisation of Materials at Microwave Frequencies Using an Open Ended Coaxial Line: Test of an Improved Calibration Technique”, *IEEE Transaction on Microwave Theory and Techniques*, Vol. 38, pp. 8-14, 1990.
28. D. Ballo, *Network Analyser Basics*, Hewlett Packard Company, Santa Rosa, CA, 1998.

CHAPTER 4

PREPARATION, PHYSICAL AND ELECTROCHEMICAL CHARACTERISATION OF METALLIC NANOPARTICLES

4.1 Introduction

Metal Nanoparticles (NPs) are particularly interesting nano-scale systems because of the ease with which they can be synthesised and modified chemically. A challenge in nanotechnology is to tailor the electrical and electronic properties of NPs by controlling their size and shape. Specially, both Pt and Au NPs have attracted much interest due to their ease of synthesis and their unique catalytic activities. Au NPs is an appealing material system for nanoscale electronics because it is relatively cheap and the NPs can be synthesised in various sizes [1]. Among the noble metals, Pt is attractive because of its superior catalytic activities [2]. However, Pt based applications have been limited by its high cost owing to the inherent high consumption. Reducing the size of the catalyst (i.e. Pt) to the nanoscale results in increasing the number of catalytic sites per unit mass, and here an attempt has been made to synthesise different sizes and shapes of Pt and Au NPs. Generally synthesis of NPs falls into two main categories, namely, chemical and physical methods. In this research, chemical methods have been chosen for the syntheses of Pt and Au NPs, since it has enormous advantages over the physical methods which are being discussed in section 4.2.1.

This chapter discusses simple chemical methods for the synthesis of different sizes of Pt and Au NPs with high control over particle size, chemical homogeneity and microstructure uniformity. This is followed by the in-depth structural characterisation of those synthesised NPs (i.e. Pt and Au NPs) using transmission electron microscopy (TEM) and cyclic voltammetry (CV).

4.2 Synthesis of Pt NPs of Different Sizes

4.2.1 Reasons for the Use of Chemical Methods for the Synthesis of Metallic NPs

Metallic NPs prepared by chemical methods offer the following advantages:

- The reaction process are simple
- The methods are low cost
- They result in high purity samples
- Particle size can be controlled accurately
- The resulting particles are monodispersed

4.2.2 Reagents

All chemicals used in this research were reagent^{*} or technically graded, and were used as received. Sodium borohydride (NaBH_4), n-heptane, polyethyleneglycol-dodecylether (Brij®30), sodium polyacrylate (NaPAA), and hydrazine (N_2H_4) were provided by Aldrich. Acetone and sodium hydroxide (NaOH) were purchased from Fisher Scientific. Potassium tetrachloroplatinate (K_2PtCl_4 – Pt content 46.67%) and hexachloroplatinic acid (H_2PtCl_6 - Pt content 24.95%) were obtained from Johnson Matthey, Royston, Hertfordshire, UK. All aqueous solutions were made with deionised (DI) water, which was further purified with a Milli-Q system (Millipore water, resistivity of $18.2 \text{ M}\Omega \text{ cm}^{-1}$).

4.2.3 Micellar Method

There are several techniques for the preparation of metallic NPs. The micellar is one of the most promising method known for the preparation of NPs. In our case, water-in-oil micro-emulsions have been prepared using the above-mentioned method. This method is the same one previously reported by Vidal-Iglesias et al. [3]. An emulsion is a dispersion of one liquid in another where each liquid is immiscible or poorly miscible in the other [4]. Water-in-oil micro-emulsions are isotropic and thermodynamically stable dispersions of two non-miscible liquids which are stabilised by a surfactant [5]. In this system, the aqueous phase is dispersed as nano-sized droplets surrounded by a single layer of surfactant molecules in a continuous apolar organic phase [6, 7].

^{*} A reagent or reactant is a substance or compound consumed during a chemical reaction.

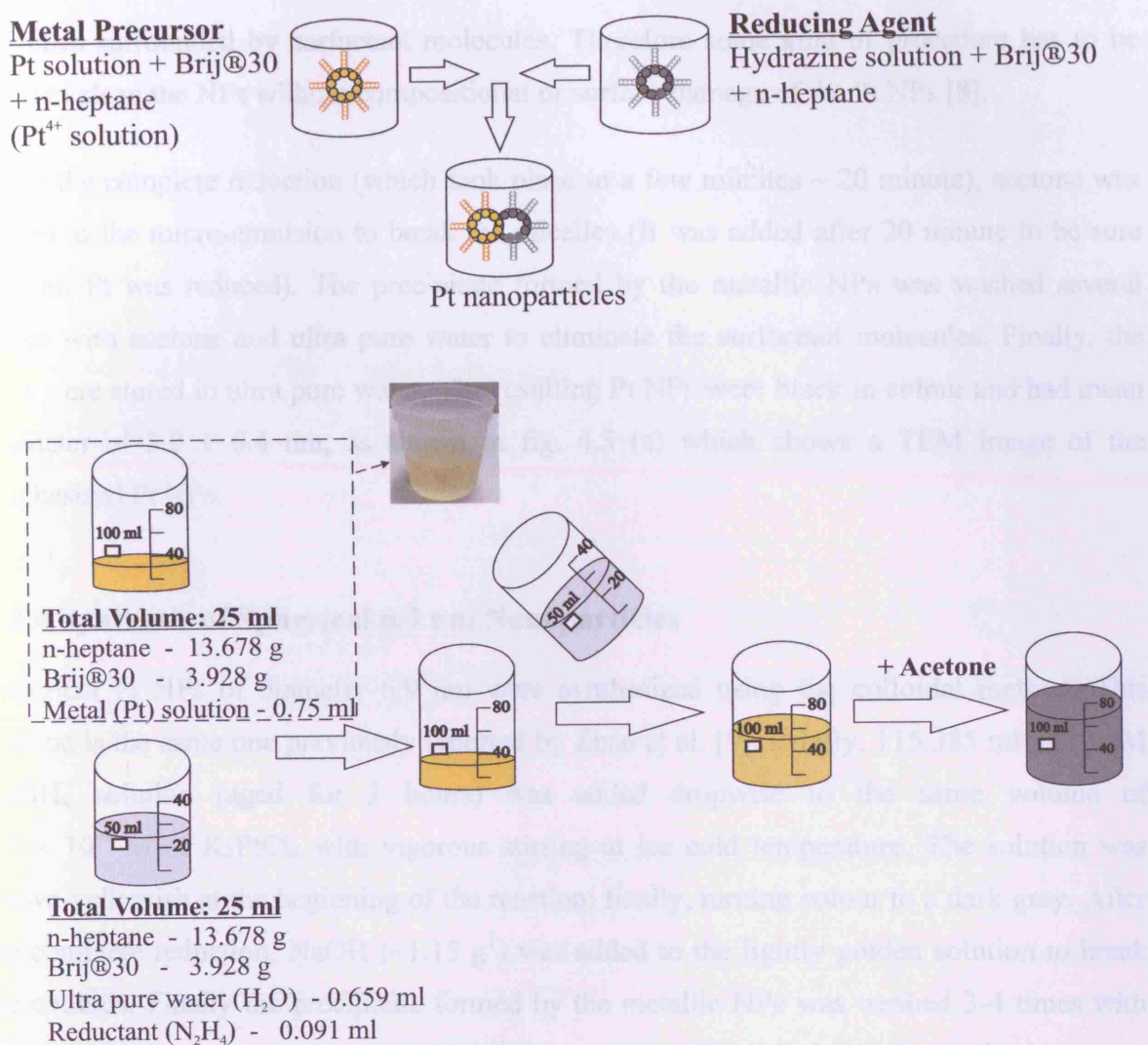


Figure 4.1 Synthesis scheme for the preparation of platinum metal NPs.

Platinum NPs (of diameter ~ 3 nm) were obtained by reduction of H_2PtCl_6 with hydrazine using water-in-oil micro-emulsions of water / polyethyleneglycol-dodecylether (Brij®30) / n-heptane. The synthesis was attained by mixing equal volumes of micro-emulsions that have the same water to surfactant molar ratio and the same surfactant concentration. One of the micro-emulsion solutions contains an aqueous solution of the metal precursors (Pt^{4+}) whereas the other contains an aqueous solution of hydrazine. Fig. 4.1 shows a scheme for the preparation of platinum metal NPs. The molar ratio of water to surfactant was the same in both solutions in order to have micelles with the same size. Once the micro-emulsions were prepared (one contains the metal precursor and the other the reducing agent) they were mixed and then the reducing agent reduces from Pt^{4+} to Pt^0 . Detailed procedures of synthesis of the Pt NPs can be found in Appendix C. The NPs prepared with this method are still inside the

micelles surrounded by surfactant molecules. Therefore some kind of procedure has to be used to clean the NPs without compositional or surface damage of the Pt NPs [8].

After the complete reduction (which took place in a few minutes ~ 20 minute), acetone was added to the micro-emulsion to break the micelles (It was added after 20 minute to be sure that all Pt was reduced). The precipitate formed by the metallic NPs was washed several times with acetone and ultra pure water to eliminate the surfactant molecules. Finally, the NPs were stored in ultra pure water. The resulting Pt NPs were black in colour and had mean diameter of 3.0 ± 0.4 nm, as shown in fig. 4.5 (a) which shows a TEM image of the synthesised Pt NPs.

4.2.4 Synthesis of Spherical 6.9 nm Nanoparticles

Spherical Pt NPs of diameter 6.9 nm were synthesized using the colloidal method. This method is the same one previously reported by Zhao et al. [9]. Briefly, 115.385 ml of 10^{-2} M NaBH_4 solution (aged for 3 hours) was added dropwise to the same volume of 6.5×10^{-4} M of K_2PtCl_4 with vigorous stirring at ice cold temperature. The solution was brown-yellowish at the beginning of the reaction; finally, turning colour to a dark grey. After the complete reduction, NaOH ($\sim 1.15 \text{ g}^\dagger$) was added to the lightly golden solution to break the colloids. Finally the precipitate formed by the metallic NPs was washed 3-4 times with ultra pure water and were then stored in ultra pure water. Fig. 4.2 shows the synthesis process for the preparation of spherical platinum metal NPs. The resulting Pt NPs had a mean diameter of 6.9 ± 0.9 nm. Fig. 4.5 (b) shows a TEM image of the synthesized NPs. The detailed procedure for the synthesis of these Pt NPs can be found in Appendix E.

[†] Add 0.5 g of NaOH for every 100 ml of solution [10]

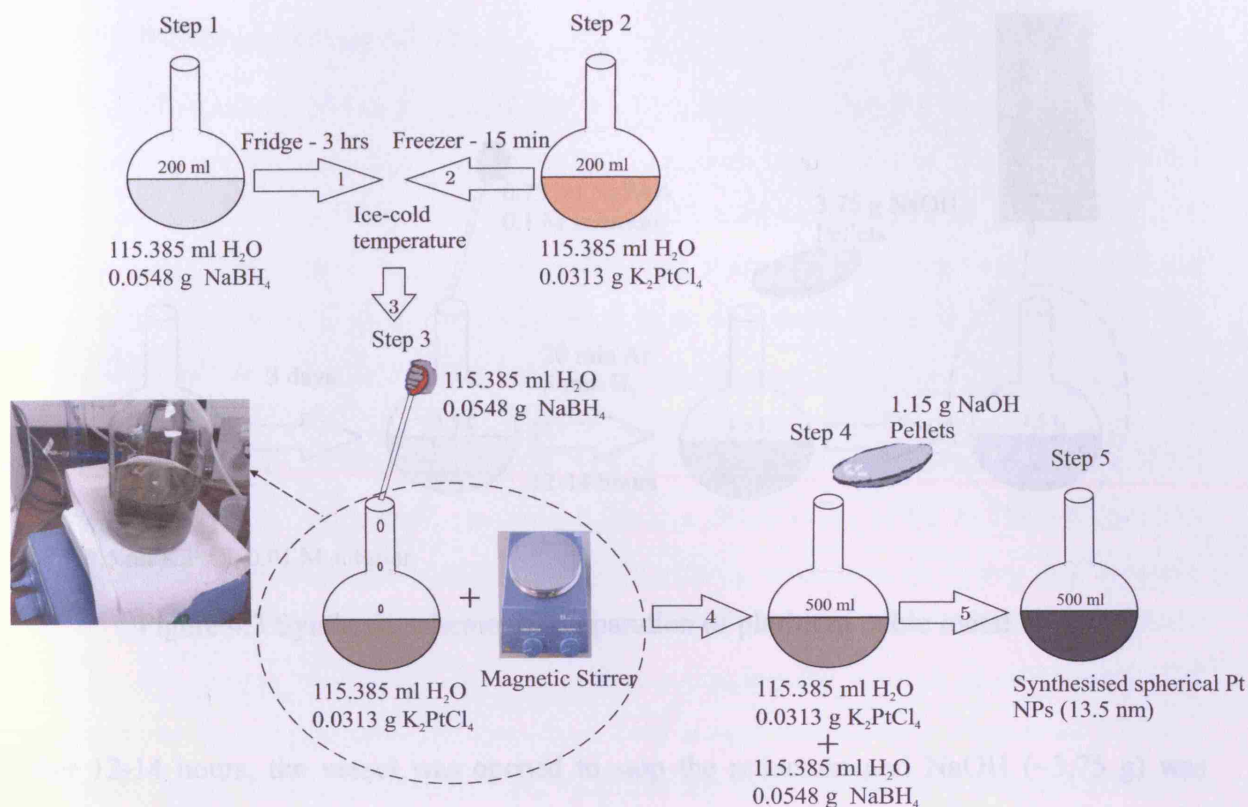


Figure 4.2 Synthesis scheme for the preparation of 6.9 nm metal NPs.

4.2.5 Colloidal Method

Cubic Pt NPs with an average size of 8.6 nm were prepared by the method of Rampino and Nord [11] and Henglein et al. [12]. Very briefly, a solution of 10^{-4} M K_2PtCl_4 was prepared in 750 ml of ultra pure water and aged for three days, to which 0.75 ml of 0.1 M sodium polyacrylate (NaPAA) was then added. After mixing, argon was bubbled through the solution for 20 minutes to deoxygenate the solution. The Pt ions were reduced by bubbling H_2 at a steady flow rate through the solution for 5 minutes. The reaction vessel was then completely sealed and covered with aluminium foil, and the solution was left overnight (for 14 h). During this time the solution turned lightly golden. NPs prepared by this method are surrounded by NaPAA molecules. Therefore some kind of procedure has to be used to clean the NPs without compositional and surface damage to the Pt NPs. Fig. 4.3 shows the synthesis scheme for the preparation of platinum cubic metal NPs. The detailed procedures of the synthesis of these Pt NPs can be found in Appendix F.

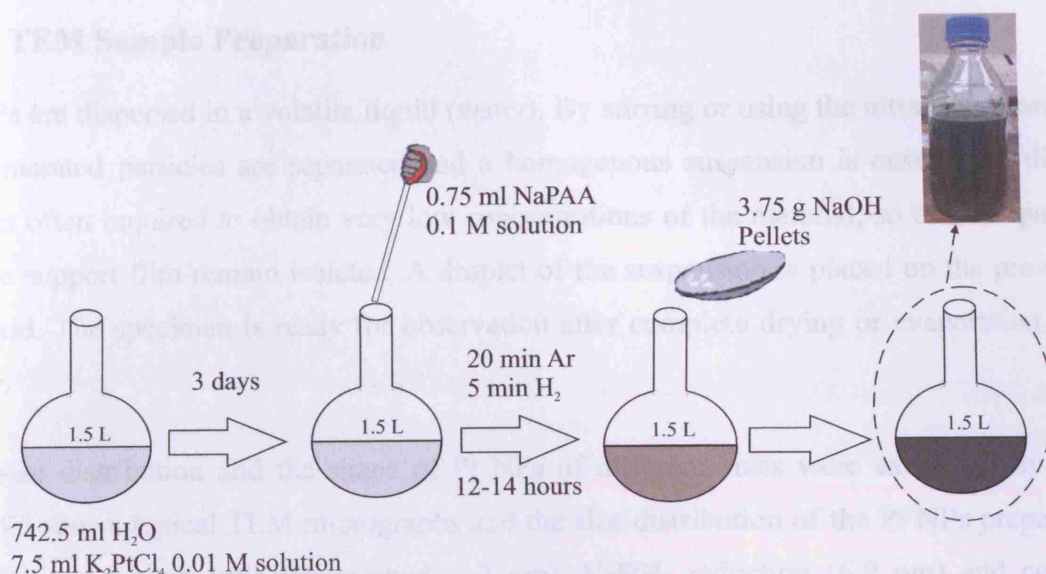


Figure 4.3 Synthesis scheme for preparation of platinum cubic metal NPs.

After 12-14 hours, the vessel was opened to stop the reduction and NaOH (~3.75 g) was added to the lightly golden solution to break the colloids. The precipitate formed by the metallic NPs was washed several times (3-4 times) with ultra pure water to eliminate the NaPAA and other residues from the surface of the Pt NPs. Finally, the NPs were stored in ultra pure water. The resulting Pt NPs had a mean size of 8.6 ± 1.1 nm and a preferentially {100} orientation, indicating the cubic structures as indicated by the TEM image shown in fig. 4.5 (c).

4.3 Transmission Electron Microscopy (TEM) Characterization

Transmission electron microscopic (TEM) analysis was performed in a FEI Tecnai T12 instrument, with an operating voltage range of 20 kV to 135 kV. The samples were prepared by placing a droplet of fresh diluted Pt solution bearing different sizes on 200 mesh Au grids pre-coated with formvar films (these grids were purchased from Agar Scientific Ltd., Essex, UK), followed by solvent evaporation by exposing the pre-coated Au grids to a flow of Argon. TEM has been one of the primary techniques used in the characterisation of NPs dimensions, surface morphology and crystalline structures. The greatest advantage that the TEM offers is the high magnification, ranging from 50 to 10^6 . Fig. 4.4 (a) shows the TEM instrument which has been used in this research.

4.3.1 TEM Sample Preparation

Pt NPs are dispersed in a volatile liquid (water). By stirring or using the ultra sound bath, the agglomerated particles are separated and a homogenous suspension is ensured. A dilution step is often required to obtain very low concentrations of the material, so that the particles on the support film remain isolated. A droplet of the suspension is placed on the pre-coated Au grid. The specimen is ready for observation after complete drying or evaporation of the water.

The size distribution and the shape of Pt NPs of different sizes were examined by TEM. Fig. 4.5 shows typical TEM micrographs and the size distribution of the Pt NPs prepared by hydrazine reduction (micellar method – 3 nm), NaBH₄ reduction (6.9 nm) and colloidal method (8.6 nm). The particle size distributions and the standard deviations were calculated for each NP sample by directly measuring and averaging the size of approximately 120 randomly chosen particles from the magnified TEM images using Adobe Photoshop CS3 (i.e. a graphics editing program developed and published by Adobe Systems) along with Origin 7 software (i.e. a data analysis and graphing software produced by OriginLab). The average particle sizes are summarised in table 4.1.

Synthesis method	Average size (nm)	NPs shape	Colloid color
Micellar method	3.0 ± 0.4	Spherical	Dark black
NaBH ₄ reduction	6.9 ± 0.9	Spherical	Dark grey
Colloidal method	8.6 ± 1.1	Cubic	Light golden

Table 4.1 Preparation conditions and experimental results of different sizes of Pt NPs

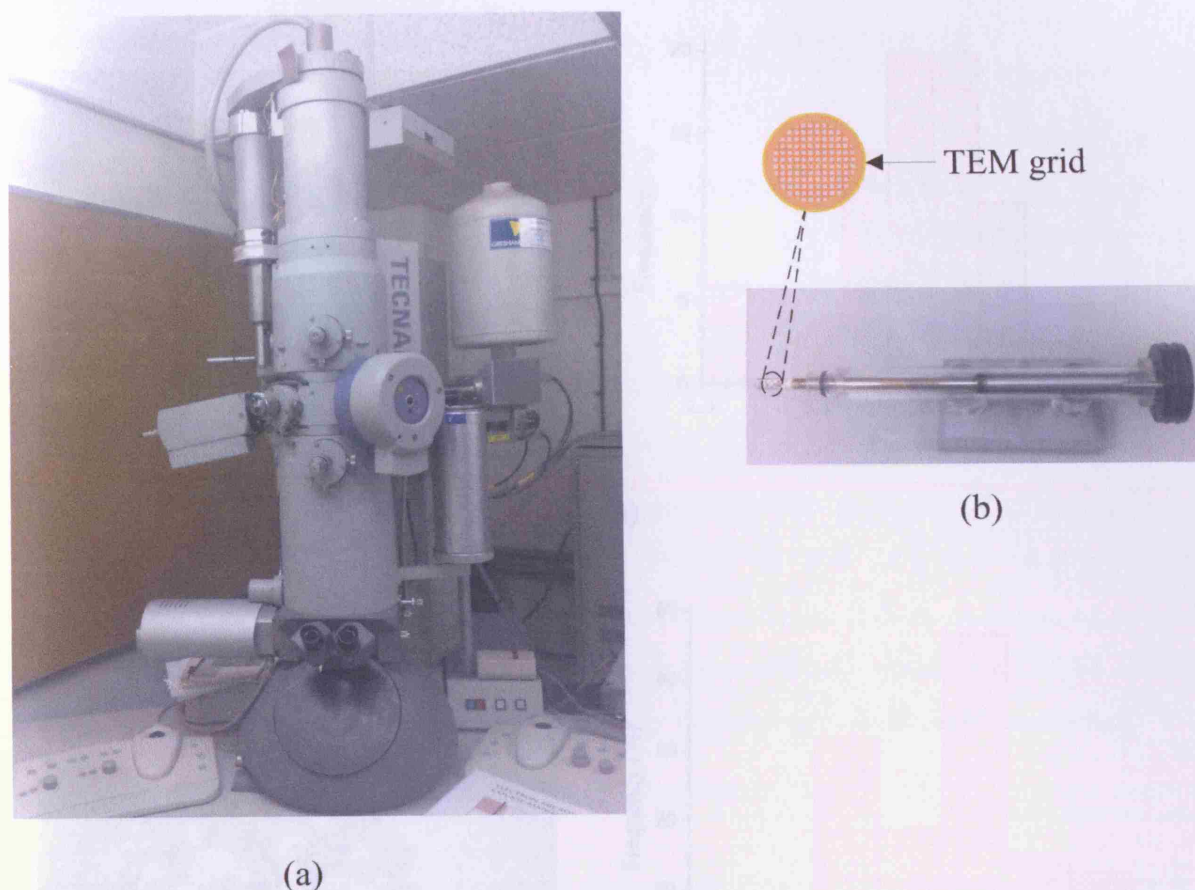
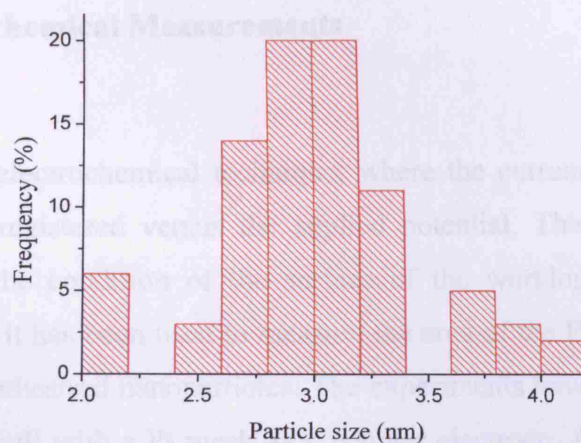
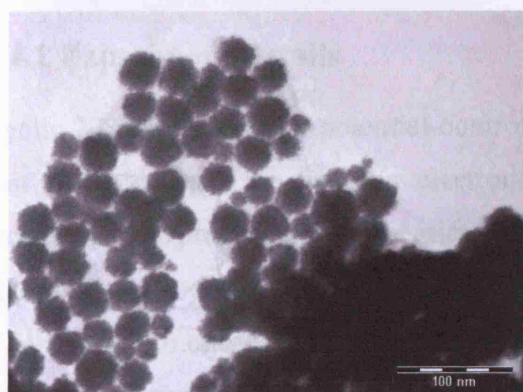
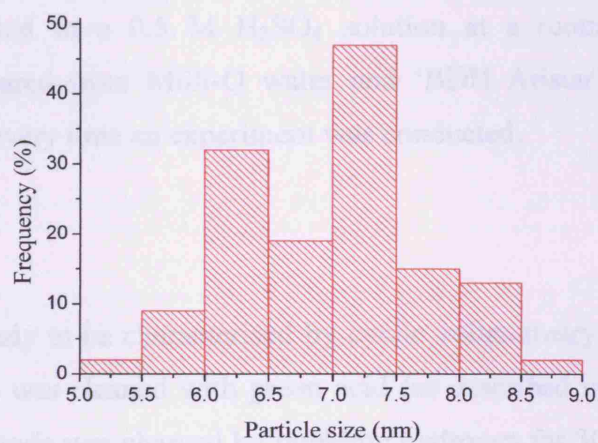
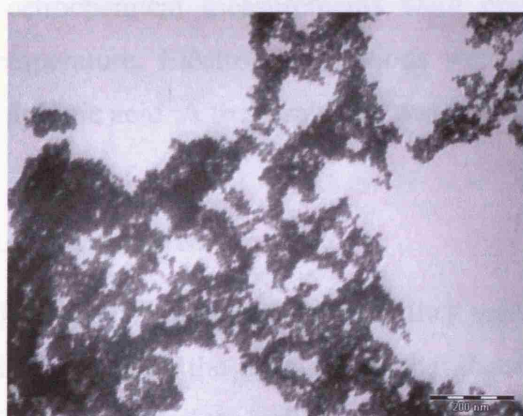


Figure 4.4 (a) Shows the Transmission Electron Microscopy (TEM) instrument used for the characterisation of NPs and (b) TEM sample holder.

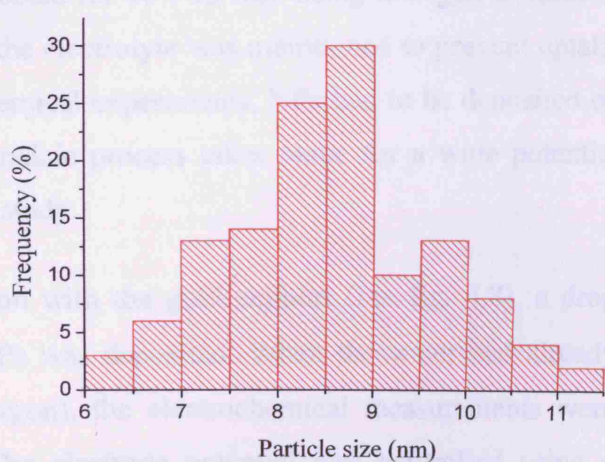
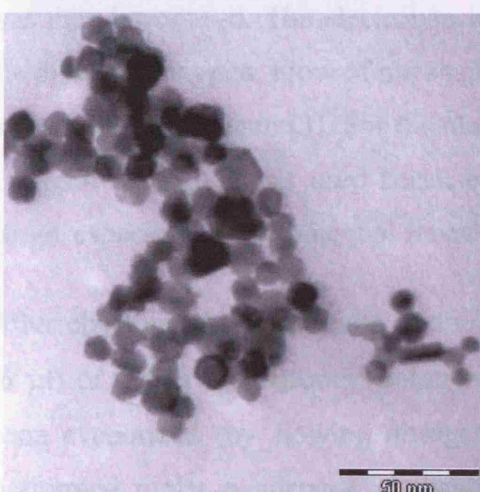
From the fig. 4.5, it can be seen that the particles aggregate, suggesting that there are no surfactant molecules or other residues on the surface of the NPs. Due to the fact that the conductance (G) of the NPs would decrease if there were adsorbed molecules on the surface after synthesis, the NPs had to be cleaned in the way that has been previously explained. To check the cleanliness before conductance measurements cyclic voltammetry was carried out in order to assure the cleanliness. The experimental conditions are the same reported previously [5]. The important thing to note in the syntheses of different sizes of Pt NPs is that the resulting particles have a metallic core surrounded by an oxide surface layer (experimental evidence for this statement can be found in section 6.3.1). Hence, the following experiments are on Pt NPs of different sizes (i.e. 3 nm, 6.9 nm, and 8.6 nm) surrounded by a surface oxide layer (PtO_2).



(a)



(b)



(c)

Figure 4.5 TEM micrographs and size distribution of Pt NPs.

4.4 Preparation of Electrode and Electrochemical Measurements

4.4.1 Experiment Details

Cyclic Voltammetry is a potential-controlled electrochemical technique, where the current that flows through the working electrode is registered versus the applied potential. This technique provides much information about the condition of the surface of the working electrode or about the test solution. In our case it has been used to measure the area of the Pt NPs in order to check the cleanliness of the synthesised nanoparticles. The experiments have been carried out in a classical three-electrode cell with a Pt mesh as a counter electrode. A Palladium (Pd) electrode was used as the reference electrode (Pd/H). All of the potentials shown in this research were indicated with respect to this reference electrode. All electrochemical measurements were performed in a 0.5 M H_2SO_4 solution at a room temperature. Electrolyte solutions were prepared from Milli-Q water and 'BDH Aristar' sulphuric acid. A fresh solution was prepared every time an experiment was conducted.

4.4.2 Apparatus

Once the NPs had been cleaned they were ready to be characterised by cyclic voltammetry. Before starting the experiment, the glassware was cleaned with green acid (as described in appendix G) and the palladium reference electrode was charged by bubbling hydrogen for 30 minutes allowing a constant reference potential for over 10 hours. After charging, the ultra pure water was decanted and the cell rinsed. A fresh solution of electrolyte (0.5 M H_2SO_4) was then introduced. The electrolyte was bubbled for 10 - 15 min using nitrogen to remove the dissolved oxygen. Flow of nitrogen over the electrolyte was maintained to prevent uptake of atmospheric oxygen [3]. For the electrochemical experiments, NPs had to be deposited on a support and gold was used because no faradaic process takes place for a wide potential range, especially in the potential range under study.

After checking the cleanliness of the solution with the gold support (see fig. 4.8), a drop (6 μl) of highly concentrated solution of NPs was deposited. When the water had already been evaporated (by flowing nitrogen or argon), the electrochemical measurements were performed under a nitrogen atmosphere. The electrode potential was controlled using a CH800 system. Fig. 4.6 shows the general arrangement of the apparatus. A diagram of the three-electrode cell can be seen in fig. 4.7.

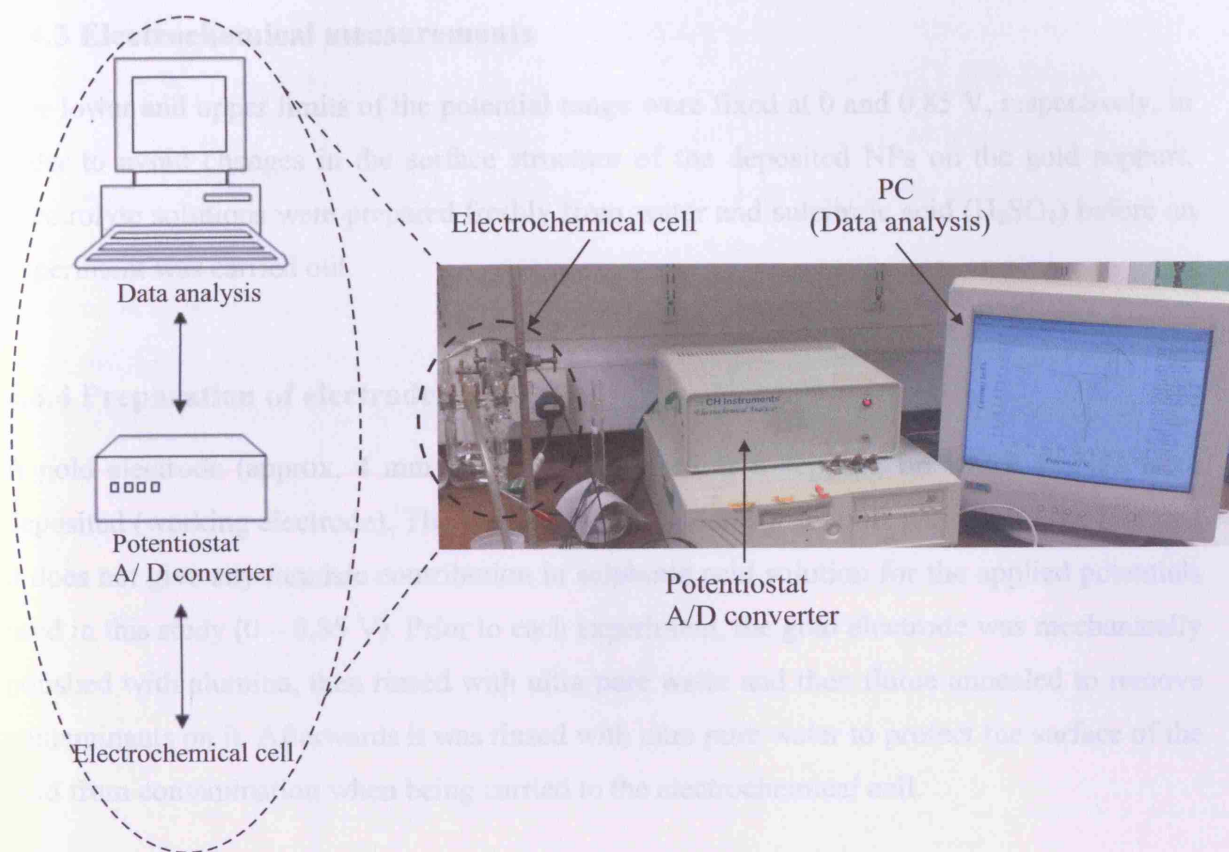


Figure 4.6 Schematic representation of the Cyclic Voltammetry systems – the electrochemical cell is shown in fig. 4.7.

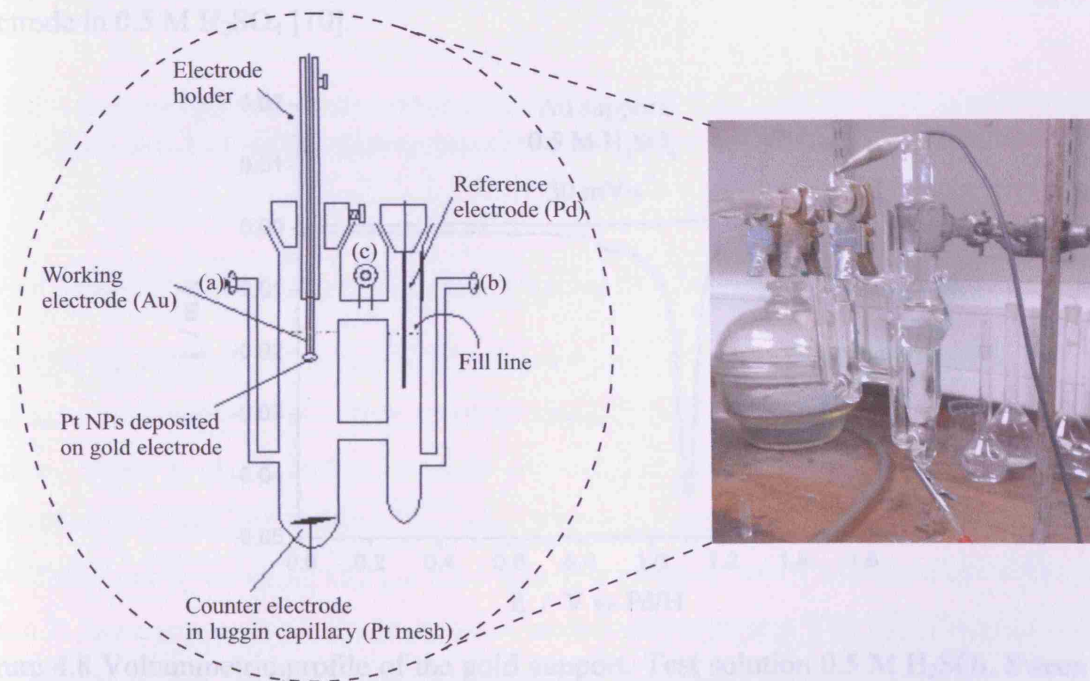


Figure 4.7 Electrochemical cell.

4.4.3 Electrochemical measurements

The lower and upper limits of the potential range were fixed at 0 and 0.85 V, respectively, in order to avoid changes in the surface structure of the deposited NPs on the gold support. Electrolyte solutions were prepared freshly from water and sulphuric acid (H_2SO_4) before an experiment was carried out.

4.4.4 Preparation of electrode

A gold electrode (approx. 4 mm diameter) was used as a support, on which Pt NPs were deposited (working electrode). The choice of using gold as a support was due to the fact that it does not give any faradaic contribution in sulphuric acid solution for the applied potentials used in this study (0 – 0.85 V). Prior to each experiment, the gold electrode was mechanically polished with alumina, then rinsed with ultra pure water and then flame annealed to remove contaminants on it. Afterwards it was rinsed with ultra pure water to protect the surface of the gold from contamination when being carried to the electrochemical cell.

To check the cleanliness of the solution and the surface of the gold electrode, a cyclic voltammetry in sulphuric acid was recorded from 0 to 1.65 V (this high potential is used to oxidise any possible contaminants). Fig. 4.8 shows the typical voltammetric profile of a gold electrode in 0.5 M H_2SO_4 [10].

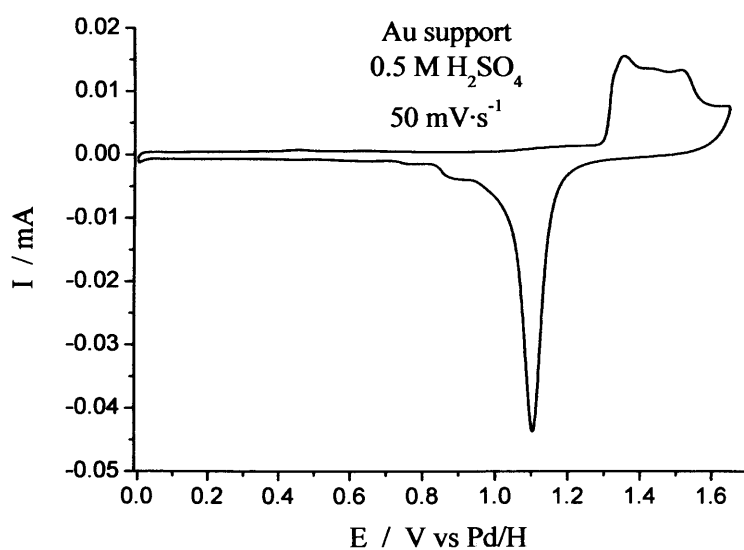


Figure 4.8 Voltammetric profile of the gold support. Test solution 0.5 M H_2SO_4 . Sweep rate: $50 \text{ mV}\cdot\text{s}^{-1}$.

After checking the cleanliness of the surface and the solution, Pt NPs were deposited on the gold electrode by depositing a drop of 6 μl of the water suspension of the NPs on the surface of the gold electrode. In order to evaporate the water and avoid contamination in the sample, the electrode was exposed to a flow of nitrogen or argon. For this deposit we used 6 μl as this amount was found to be appropriate for both the microwave studies and the electrochemical experiments. After the water evaporation the particles were strongly attached to the gold electrode. Fig. 4.9 shows the voltammetric profile of the platinum NPs and the gold electrode for sake of comparison, highlighting the fact that any contribution from gold is negligible.

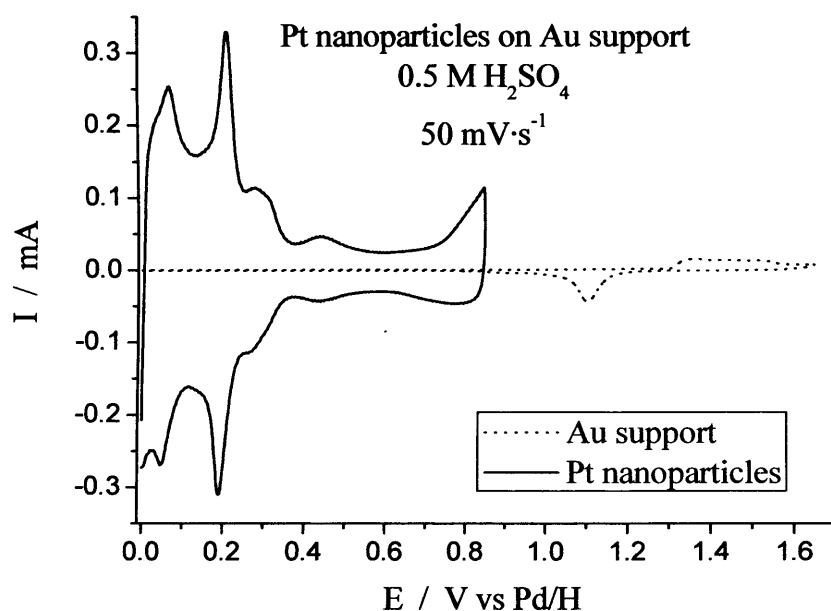


Figure 4.9 Voltammetric profile of platinum NPs (solid line) and the gold support electrode (dotted line) in 0.5 M H₂SO₄. Sweep rate: 50 mV·s⁻¹.

4.4.5 Cleaning and Characterisation Method for Pt NPs

Although the NPs have been chemically cleaned after their synthesis some small amounts of surfactant molecules or any other residues coming from the synthesis can still cover their surface. Then, it is necessary to carry out another cleaning procedure, here being an electrochemical step consisting of CO adsorption-oxidation. CO adsorption on the electrode was carried out by bubbling CO gas for 5 min in a bubbler, where CO adsorbs on the surface of the Pt and removes the contamination of surfactant molecules [10, 13]. The electrode was held just above the solution of the CO bubbler to make sure that the deposited Pt surface is not altered by bubbles during the process. After this, the electrode was removed and

transferred to the electrochemical cell with a drop of sulphuric acid solution on it to avoid contamination.

Once in the electrochemical cell, oxidation of the adsorbed CO was performed after checking that the surface was fully covered with CO. The following fig. 4.10 shows the CO monolayer oxidation.

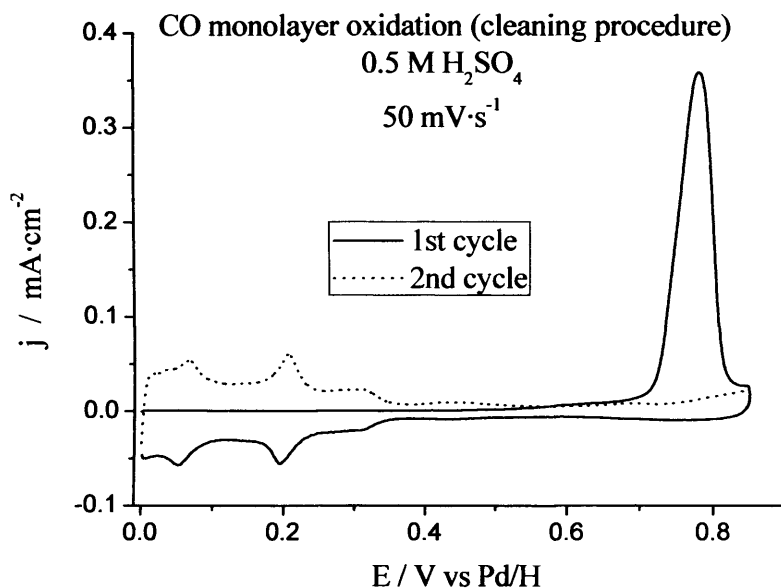


Figure 4.10 CO monolayer oxidation on Pt NPs. Test solution: 0.5 M H₂SO₄. Sweep rate: 50 mV·s⁻¹.

After the cleaning with the CO adsorption-oxidation process the voltammetric profile was obtained (see fig. 4.11). In platinum the different peaks are associated with hydrogen adsorption-desorption process as in different type of sites {(110), (100) and (111)}. No further explanation is given as this is not important for our study.

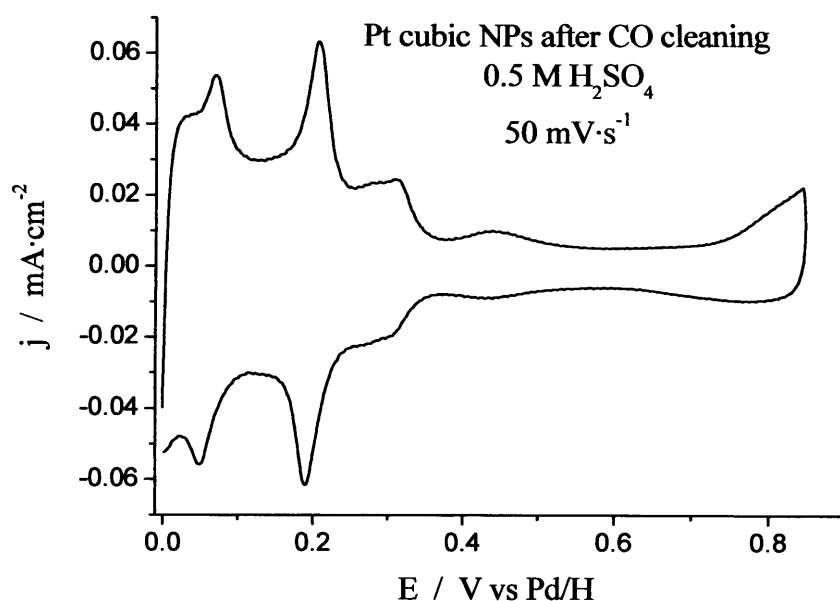


Figure 4.11 Voltammetric profile of platinum cubic NPs after CO cleaning in 0.5 M H₂SO₄. Sweep rate: 50 mV·s⁻¹.

As it is already has been well established [10, 14], for polycrystalline platinum surfaces, the occupation of all active sites of the surface with a complete monolayer of adsorbed hydrogen requires a charge of 210 $\mu\text{C}\cdot\text{cm}^{-2}$, so in this way the area of deposited platinum can be calculated. As the mean size of those NPs is known (8.6 nm approximately), the area of one NP can be calculated (assuming that they are cubic) and then the number of NPs deposited can be obtained. The accurate calculation of the number of NPs is actually a challenge because of the variations of the size and the size dispersity of the synthesised NPs.

For these NPs (e.g. cubic Pt), the hydrogen area (in the range 0-0.60 V) measured was $5.2383\cdot 10^{-5}$ A·V. Fig. 4.12 shows the calculations of the area of deposited platinum, removing the contribution from the double layer.

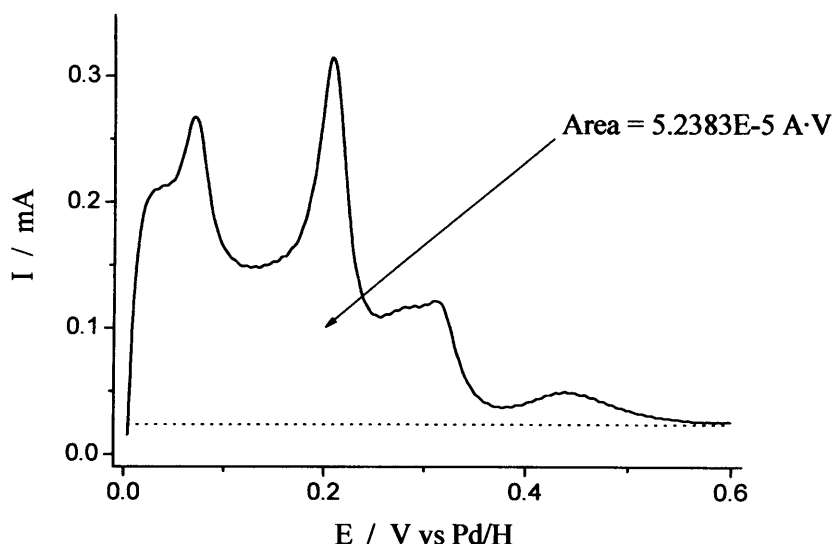


Figure 4.12 Area calculation of the deposited platinum.

(i) For the Pt cubic 8.6 nm Pt NPs

$$\text{Charge} = \frac{\text{Area}}{\text{Sweep rate}} \quad (4.1)$$

Therefore,

$$\begin{aligned} \text{Area} &= 5.2383 \cdot 10^{-5} \text{ A} \cdot \text{V} = 5.2383 \cdot 10^{-5} \frac{\text{C}}{\text{s}} \text{ V} = 52.383 \frac{\mu\text{C}}{\text{s}} \text{ V} \\ 52.383 \frac{\mu\text{C}}{\text{s}} \text{ V} \cdot \frac{1}{210 \frac{\mu\text{C}}{\text{cm}^2}} \cdot \frac{1}{0.05 \frac{\text{V}}{\text{s}}} &= \frac{52.383}{210 \cdot 0.05} \frac{\mu\text{C} \cdot \text{V}}{\text{s}} \frac{\text{cm}^2}{\mu\text{C}} \frac{\text{s}}{\text{V}} = 4.990 \text{ cm}^2 \end{aligned}$$

Since the sweep rate = 0.05 V/s (50 mV/s), therefore the amount of NPs in a droplet is;

$$4.99 \frac{\text{cm}^2}{6 \mu\text{l}} \cdot \frac{1 \text{ nanoparticle}}{6(8.6 \cdot 10^{-9})^2 \text{ m}^2} \cdot \frac{10^{-4} \text{ m}^2}{\text{cm}^2} = 1.244 \cdot 10^{12} \frac{\text{nanoparticles}}{6 \mu\text{l}}$$

(ii) Similarly for the 6.9 nm spherical Pt NPs (see appendix H)

$$\begin{aligned} 6.74254 \cdot 10^{-5} \text{ A} \cdot \text{V} &= 6.74254 \cdot 10^{-5} \frac{\text{C}}{\text{s}} \text{ V} = 67.4254 \frac{\mu\text{C}}{\text{s}} \text{ V} \\ 67.4254 \frac{\mu\text{C}}{\text{s}} \text{ V} \cdot \frac{1}{210 \frac{\mu\text{C}}{\text{cm}^2}} \cdot \frac{1}{0.05 \frac{\text{V}}{\text{s}}} &= \frac{67.4254}{210 \cdot 0.05} \frac{\mu\text{C} \cdot \text{V}}{\text{s}} \frac{\text{cm}^2}{\mu\text{C}} \frac{\text{s}}{\text{V}} = 6.421 \text{ cm}^2 \end{aligned}$$

$$6.421 \frac{\text{cm}^2}{6 \mu\text{l}} \cdot \frac{1 \text{ nanoparticle}}{4\pi \left(\frac{6.9 \cdot 10^{-9}}{2} \right)^2 \text{m}^2} \cdot \frac{10^{-4} \text{m}^2}{\text{cm}^2} = 4.293 \cdot 10^{12} \frac{\text{nanoparticles}}{6 \mu\text{l}}$$

(iii) Similarly for the 3.0 nm spherical Pt NPs (see appendix I)

$$\begin{aligned} 7.49698 \cdot 10^{-5} \text{A} \cdot \text{V} &= 7.49698 \cdot 10^{-5} \frac{\text{C}}{\text{s}} \text{V} = 74.9698 \frac{\mu\text{C}}{\text{s}} \text{V} \\ 74.9698 \frac{\mu\text{C}}{\text{s}} \text{V} \cdot \frac{1}{210 \frac{\mu\text{C}}{\text{cm}^2}} \cdot \frac{1}{0.05 \frac{\text{V}}{\text{s}}} &= \frac{74.9698 \mu\text{C} \cdot \text{V}}{210 \cdot 0.05} \frac{\text{cm}^2}{\mu\text{C}} \frac{\text{s}}{\text{V}} = 7.140 \text{ cm}^2 \\ 7.140 \frac{\text{cm}^2}{6 \mu\text{l}} \cdot \frac{1 \text{ nanoparticle}}{4\pi \left(\frac{3.0 \cdot 10^{-9}}{2} \right)^2 \text{m}^2} \cdot \frac{10^{-4} \text{m}^2}{\text{cm}^2} &= 2.525 \cdot 10^{13} \frac{\text{nanoparticles}}{6 \mu\text{l}} \end{aligned}$$

From the above calculation it could be concluded that there are 1.244×10^{12} platinum cubic NPs in a drop (6 μl). Similarly the hydrogen area measured for the 3 nm and 6.9 nm platinum NPs (assuming that they are spherical) were $7.49698 \times 10^{-5} \text{A} \cdot \text{V}$ and $6.7425 \times 10^{-5} \text{A} \cdot \text{V}$, respectively. Therefore it could be concluded that there are 2.525×10^{13} and 4.293×10^{12} Pt NPs, respectively, in a drop. Table 4.2 summarises the number of NPs available in a droplet.

Pt NPs	Hydrogen area (A·V)	Number of NPs per drop
8.6 nm	5.2383×10^{-5}	1.244×10^{12}
6.9 nm	6.7425×10^{-5}	4.293×10^{12}
3.0 nm	7.4969×10^{-5}	2.525×10^{13}

Table 4.2 Number of NPs in a drop of different sizes of Pt NPs.

Even though the structure of the Pt NPs were characterised by the TEM, it is apparent from the results obtained from the CV that the CV can be used to characterise the structure of the NPs.

4.5 Synthesis of Spherical Au NPs of Different Sizes

4.5.1 Reagents and Instrumentations

All the reagents were of AR[†] grade. Chloroauric acid (HAuCl₄ – Au content 41.29%) was obtained from Johnson Matthey, Royston, Hertfordshire, UK and trisodium citrate (usually referred as sodium citrate (99+%)) was purchased from Sigma/ Aldrich Chemical Co., and was used as received. Milli-Q water with a resistivity of 18.2 MΩcm⁻¹ was used as the solvent for all the syntheses of Au NPs. The centrifuge used was a Beckman Coulter Allegra 21R Centrifuge with F0850 rotor and the TEM was performed using the same instrument mentioned in section 4.3.

4.5.2 Synthesis of Au NPs of Different Size by the Frens Method

There are several methods used for the preparation of colloidal Au NPs [15]. Among these, the reduction of chloroaurate ions in the presence of sodium citrate is a classical technique that has been quoted frequently in literature [16]. Au NPs of variable size (8, 16, and 25 nm) were synthesised by a modification of the citrate reduction method of Frens [16]. Briefly [1], a 300 ml of aqueous solution of HAuCl₄ (7.5×10^{-5} moles) was heated to boiling, and then 12 ml of trisodium citrate dehydrate solution (1% by weight) was added to it under continuous stirring. After about 50 s of boiling a very faint blue tone appeared, gradually darkening over a period of about 5 minutes. The final color was deep wine red, indicating the formation of Au NPs. The reaction solution was boiled for another ~30 minutes for complete reduction of Au (III) ions. The solution was then gradually cooled to room temperature. Then the synthesised Au solution (300 ml) was transferred to six 50 ml centrifuging tubes, then centrifuged and concentrated to a final volume of 0.6 ml. The optimum conditions found experimentally for centrifuging were 2-3 hours at 20 °C and 10,000 rpm. These conditions were repeated 3-4 times for each size of Au NPs. By this procedure, Au NPs of 8.2 ± 0.7 nm size were obtained. By performing a similar procedure, particles of different sizes (16.5 ± 1.6 nm and 24.8 ± 3.2 nm) were also prepared by varying the amount of citrate solution. All the employed glassware was previously washed with aqua regia[§] (3 volume of HCl: 1 volume of

[†] AR stands for Analytical Reagent, it is of higher purity.

[§] Aqua regia (AR) is a high corrosive and toxic, fuming red solution; also known as nitro-hydrochloric acid. The mixture is formed by fresh mixing of concentrated hydrochloric acid (HCl) and concentrated nitric acid (HNO₃), in a volumetric ratio of 3:1, respectively. The used AR was decanted back into the AR flask, and the container then rinsed 3-4 times with ultra pure water in a fume cupboard followed by more thorough rinse outside the fume cupboard.

HNO₃) followed by washing them with ultra pure water for at least 12-15 times. Fig. 4.13 shows the synthesis process of Au NPs by the Frens method. The details of the size selective syntheses are given in table 4.3 (see appendix J). The particle sizes were determined from the TEM analysis.

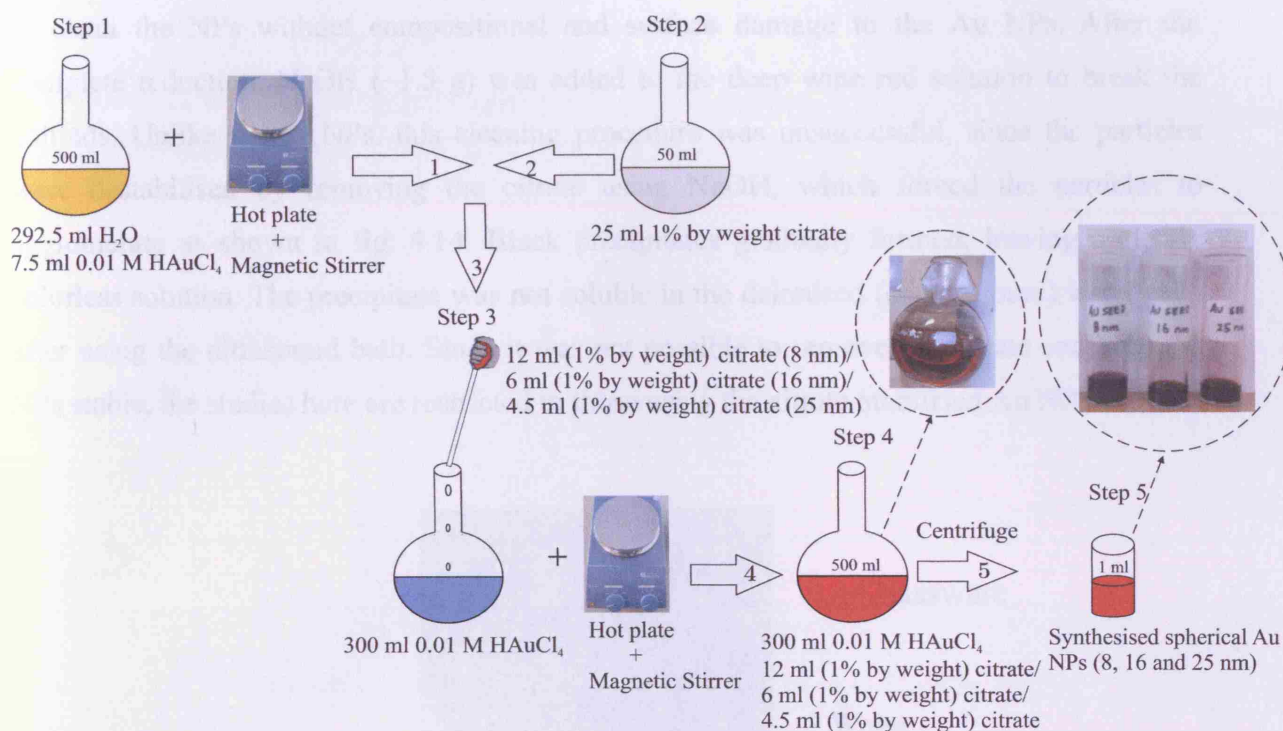


Figure 4.13 Synthesis scheme for preparation of 8.2, 16.5, and 24.8 nm Au metal NPs.

Particles Size (nm)	Total Volume of solution (ml)	Total Volume of HAuCl ₄ (0.01M) (ml)	Volume of citrate (1% by weight) (ml)
8.2 ± 0.7	300	7.5	12
16.5 ± 1.6	300	7.5	6
24.8 ± 3.2	300	7.5	4.5

Table 4.3 Details for the size selective synthesis of Au NPs by the Frens method.

The size distribution and the shape for the synthesised Au NPs of different sizes were examined by TEM using the same system previously mentioned in section 4.3. Fig. 4.15 shows typical TEM micrographs and particle size distribution of the Au NPs prepared by the citrate reduction method. Using Adobe Photoshop CS3 along with Origin 7, the particle size distributions were measured and summarised in table 4.4. It is observed the mean size is very close to the expected value.

Unlike the pure Pt NPs, the Au NPs prepared in this section using the Frens method are citrate-stabilised Au NPs. It is apparent from these TEM images that the particles are individually separated (i.e. with a gap/space between the particles) by ligands which are formed by citrate during the synthesis process to stabilise the NPs. NPs prepared by this method are surrounded by citrate molecules. Therefore some kind of procedure has to be used to clean the NPs without compositional and surface damage to the Au NPs. After the complete reduction, NaOH (~1.5 g) was added to the deep wine red solution to break the colloids. Unlike the Pt NPs, this cleaning procedure was unsuccessful, since the particles were destabilised by removing the citrate using NaOH, which forced the particles to agglomerate as shown in fig. 4.14. Black precipitates gradually formed, leaving a clearly colorless solution. The precipitate was not soluble in the deionised (or ultra pure) water even after using the ultrasound bath. Since it was not possible to remove the citrate and keep the NPs stable, the studies here are restricted to those using the citrate-stabilised Au NPs.

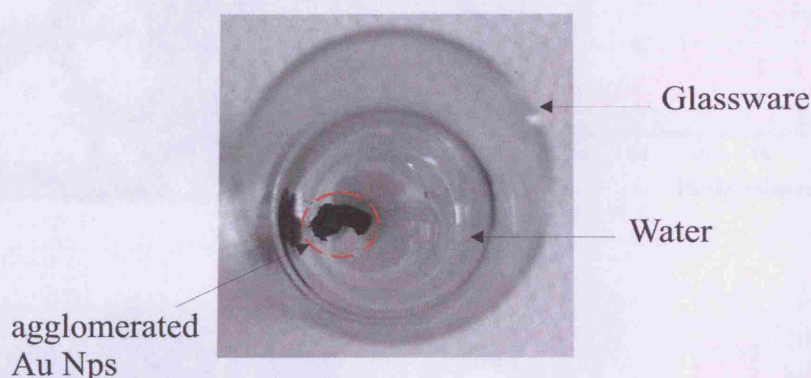
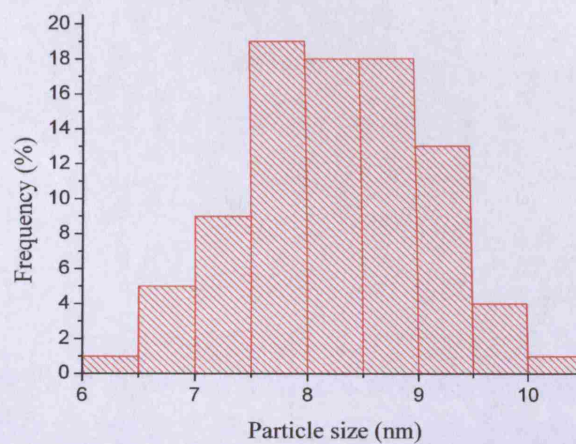
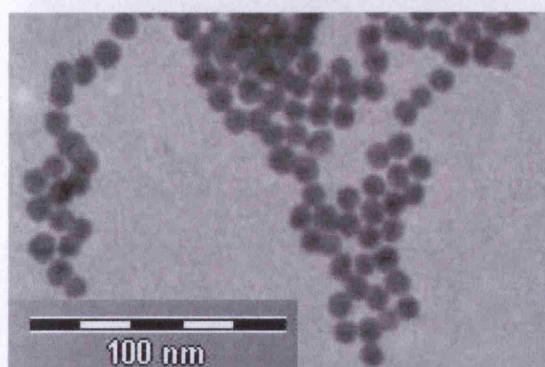


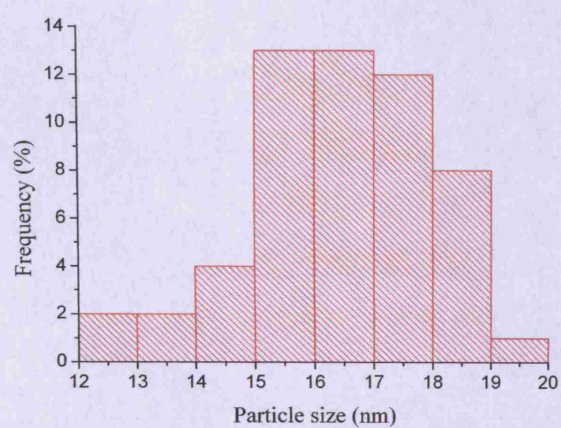
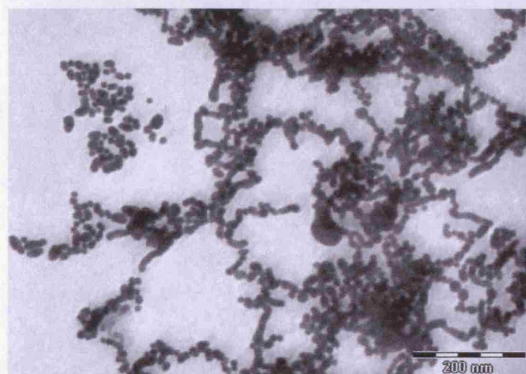
Figure 4.14 Photograph of the agglomeration of the Au NPs.

Average size (nm)	NPs shape	Colloid color
8.2 ± 0.7	Spherical	Deep wine red
16.5 ± 1.6	Spherical	Deep wine red
24.8 ± 3.2	Spherical	Deep wine red

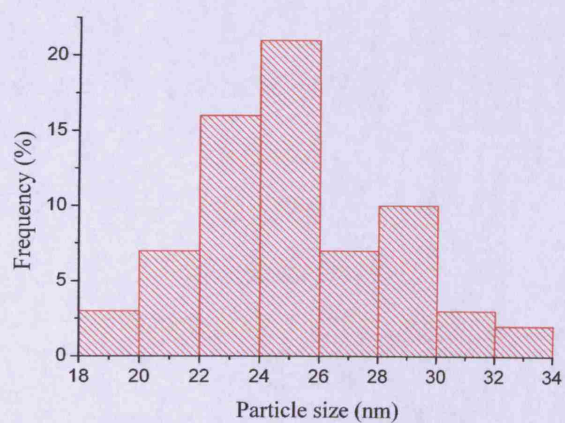
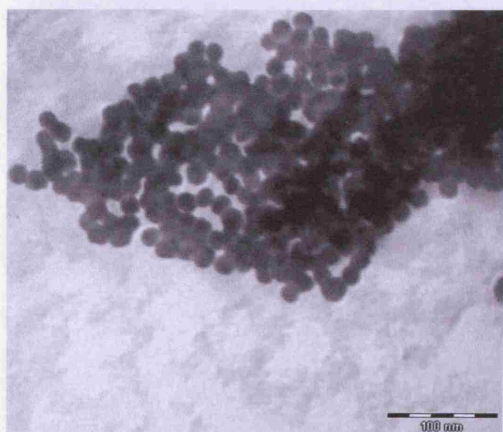
Table 4.4 Experimental results of different sizes of Au NPs.



(a)



(b)



(c)

Figure 4.15 TEM micrographs and size distribution of Au NPs (a) 8.2 ± 0.7 nm (b) 16.5 ± 1.6 nm, and (c) 24.8 ± 3.2 nm.

From the above fig. 4.15, it can be clearly seen in the case of 8.2 nm Au NPs that the particles are well dispersed on the Au grid, where the lack of particle aggregation suggests sufficient protection of the NPs cores by the citrate ligands. Practically we should have seen a similar TEM image for other sizes of Au NPs (i.e. 16.5 nm and 24.8 nm), but unfortunately this was not observed due to the agglomeration during the TEM sample preparation. As mentioned earlier in this section, a centrifuging technique has been used to concentrate (or condense) the NPs from a large volume (i.e. 300 ml) to a known final volume (i.e. 0.6 ml). A small volume (i.e. ~ 1 ml) of highly diluted (i.e. much lower concentration of NPs) sample should have been kept aside during this centrifuging process. A small amount of highly diluted Au NPs were kept aside for 8.2 nm but not for the other sizes, which was latter deposited directly onto the Au grid for TEM characterisation. For the other two sizes of Au NPs (i.e. 16.5 nm and 24.8 nm), the TEM sample preparations were made by diluting the highly concentrated Au NPs. In this process the Au NPs start to aggregate while adding deionised water to dilute the concentrated NPs, as shown in figs. 4.15 (b) and (c), where the aggregation depends on the amount of deionised water added.

4.6 Chapter Summary

This chapter presents the synthesis of Pt and Au NPs by chemical methods. The process is simple and highly reproducible. The surface cleanliness of the Pt NPs was confirmed by cyclic voltammetry profiles. The size and the crystal morphology of the formed particles were determined electrochemically using CV and also confirmed by the TEM imaging technique.

4.7 References

1. S. Panigrahi, S. Basu, A. Praharaj, A. Pande, S. Jana, A. Pal, S.K. Ghosh and T. Pal, "Synthesis and size-selective Catalysis by Supported Gold Nanoparticles: study on Heterogeneous and Homogeneous Catalytic Process", *Journal of Physical Chemistry*, Vol. 111, pp. 4596-4605, December 2007.
2. S. Park, S.A. Wasileski and M. J. Weaver, "Electrochemical Infrared Characterization of Carbon-Supported Platinum Nanoparticles: A Benchmark Structural Comparison with Single-Crystal Electrodes and High-Nuclearity Carbonyl Clusters", *Journal of Physical Chemistry B*, Vol. 105, No. 40, pp. 9719-9725, September 2001.
3. F.J. Vidal-Iglesias, J. Solla-Gullon, V. Montiel, J. M. Feliu, and A. Aldaz, "Screening of electrocatalysts for direct ammonia fuel cell: Ammonia oxidation on PtMe (Me: Ir, Rh, Pd, Ru) and preferentially oriented Pt (1 0 0) nanoparticles", *Journal of Power sources*, Vol. 171: pp. 448 – 456, 2007.
4. T.F. Tadros and B. Vincent, in: P. Becher (Ed.), *Encyclopedia of Emulsion Technology*, Dekker, New York, 1983.
5. J. Solla-Gullon, A. Rodes, V. Montiel, A. Aldaz, and J. Clavilier, "Electrochemical characterisation of platinum-palladium nanoparticles prepared in a water-in-oil microemulsion", *Journal of Electroanalytical Chemistry*, Vol. 554-555, pp. 273-284, September 2003.
6. K.A. Friedrich, A. Marmann, U. Stimming, W. Unkauf and R. Vogel, "Model electrodes with defined mesoscopic structure", *Journal of analytical Chemistry*, Vol. 358, No. 1-2, pp. 165-165, May 1997.
7. J. Solla-Gullon, V. Montiel, A. Aldaz, and J. Clavilier, "Synthesis and Electrochemical Decontamination of Platinum-Palladium Nanoparticles Prepared by Water-in-Oil Microemulsion", *Journal of Electrochemical Society*, Vol. 150, No. 2, pp. 104-109, January 2003.
8. K.A. Friedrich, F. Henglein, U. Stimming, and W. Unkauf, "Investigation of Pt Particles on Gold Substrates by IR Spectroscopy Particle Structure and Catalytic Activity", *Colloids and Surfaces A: Physicochemical and Engineering Aspects*, Vol. 134, pp. 193-206, March 1998.
9. S.Y. Zhao, S.H. Chen, S.Y. Wang, D.G. Li, and H.Y. Ma, "Preparation, Phase Transfer, and Self-Assembled Monolayers of Cubic Pt Nanoparticles", *Langmuir*, Vol. 18, pp. 3315-3318, November 2002.
10. F.J Vidal-Iglesias, *Private communication*, 2007-8.
11. L.D. Rampino, and F.F. Nord "Preparation of Palladium and Platinum Synthetic High Polymer Catalysts and the Relationship between Particle Size and Rate of Hydrogenation" *Journal of the American Chemical Society*, Vol. 63, No. 10, pp. 2745-2749, October 1941.

12. A. Henglein, B.G. Ershov, and M. Malow “Absorption Spectrum and Some Chemical Reactions of Colloidal Platinum in Aqueous Solution”, *The Journal of Physical Chemistry*, Vol. 99, No. 38, pp. 14129-14136, September 1995.
13. F.J. Vidal-Iglesias, J. Solla-Gullon, P. Rodriguez, E. Herrero, V. Montiel, J.M. feliu, and A. Aldaz, “Shape-dependent electrocatalysis: ammonia oxidation on platinum nanoparticles with preferential (100) surfaces”, *Electrochemistry Communications*, Vol. 6, No. 10, pp. 1080-1084, October 2004.
14. R. Woods, *Chemisorption at electrodes*, in: A.J. Bard (Ed.), *Electroanalytical Chemistry: a Series of Advances*, Marcel Dekker, Inc., New York, Vol.9, pp.1, 1976.
15. P.P. Edwards and J.M. Thomas, “Gold in a Metallic Divided State – From Faraday to Present –Day Nanoscience”, *Angewandte Chemie International Edition*, Vol. 38, No. 39, pp. 5480-5486, September 2007.
16. G. Fren, “Preparation of gold dispersions of varying particle size: Controlled nucleation for the regulation of the particle size in monodisperse gold suspensions”, *Nature: Physical Science*, Vol. 241, pp. 20–22, 1973.

CHAPTER 5

3D ELECTROMAGNETIC SIMULATION OF COAXIAL PROBE AND SAPPHIRE DIELECTRIC RESONATOR

5.1 Introduction

The theoretical analysis involved in the design of coaxial probes and dielectric resonators can become quite complex and in many cases an exact solution may not be possible. Advances in computational electromagnetic software have made it easier to analyse complex problems and design configuration. Ansoft High Frequency Structure Simulator (HFSS) is an interactive software package for electromagnetic (EM) modelling and analysing three dimensional (3D) structures. The following sections provide an insight into the various aspects involved in the process of modelling the real devices and running the simulation in HFSS version 11.

5.2 Background

HFSS uses the finite element method (FEM) for EM analysis on arbitrary 3D structures. FEM is a flexible numerical technique capable of being adapted to problems dealing with complex structures and material distributions. HFSS uses the FEM to divide the entire volume of the 3D structure into a large number of tetrahedral as shown in fig. 5.1. Each tetrahedron is composed of four equilateral triangles as shown in fig. 5.1. As described in fig. 5.1, the components of the field that are tangential to the three edges meeting at that vertex are stored. The other vector stored is the vector field at the midpoint of the selected edges, which is tangential to a face and normal to the edge. Using these stored values, HFSS estimates vector field quantities such as E-field and H-field inside each tetrahedron. Maxwell's equations are then formulated from those field quantities and are later transformed into matrix equations which can be solved by conventional numerical methods [1]. For more accurate results, a denser mesh with larger number of small finite elements is required. However, the density of the mesh is limited by the availability of the computer resources.

At the beginning of the solution process, the software produces an initial coarse mesh and finds an approximate field solution. The mesh is then optimised during several iterations carried out until the solution results converge to the defined level of accuracy or permitted number of iteration is reached. Using HFSS enables problem solving at single frequency or at several discrete frequencies, and permits the computation of basic electromagnetic field quantities, resonant frequencies of a structure, S-parameters, etc [1].

The following sections of this chapter contain the main strategies of model development and a brief description of modelling a 3D sapphire dielectric resonator (SDR) and different types of open ended coaxial probe (OCP) structures using HFSS software. It then describes the in-depth procedures involved in modelling and simulating the OCP and SDR as a major part of this chapter followed by the in-depth analysis of penetration depth of the OCP probe and also the development of *universal model* for different types of OCPs for the characterisation of material properties. Finally, a semi-quantitative SDR model was developed using the HFSS software to support the results observed from the microwave experiments for Pt oxide and pure Au NP films.

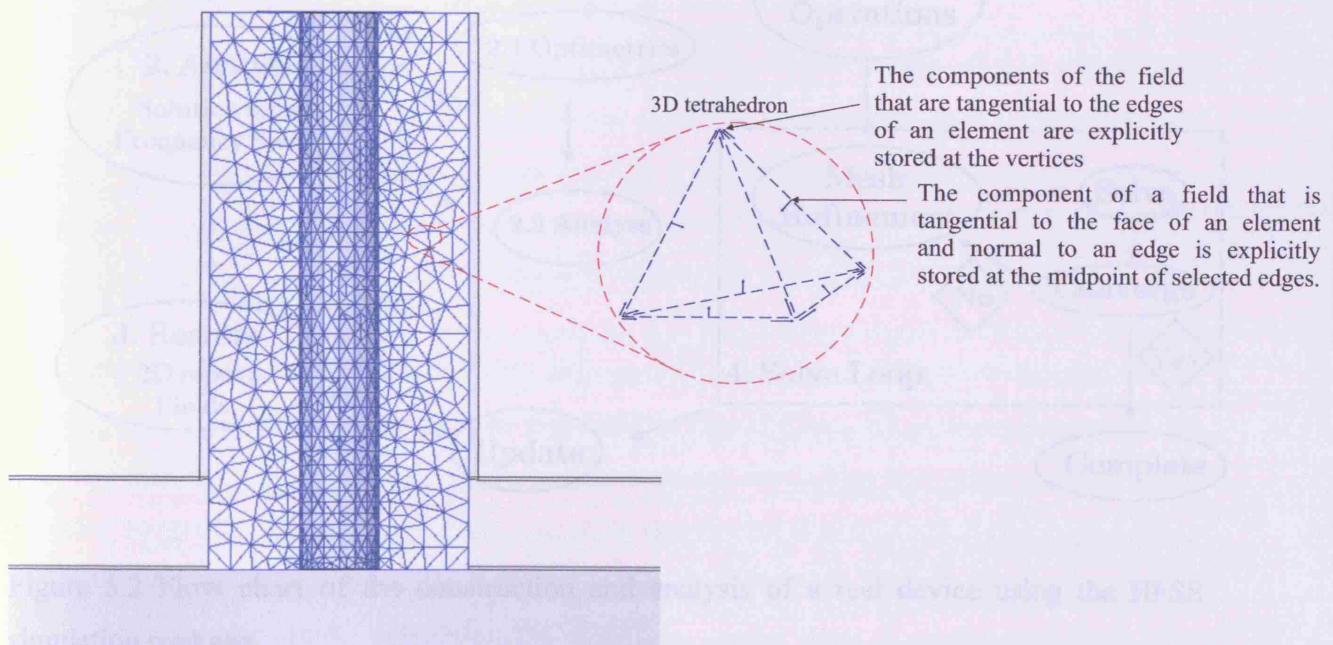


Figure 5.1 Finite Element Mesh on the cross section of the OCP.

5.3 Modelling of the OCP and SDR

5.3.1 The Process (Flow Chart)

This section gives the steps for constructing a geometric model and analysing its electromagnetic behaviour.

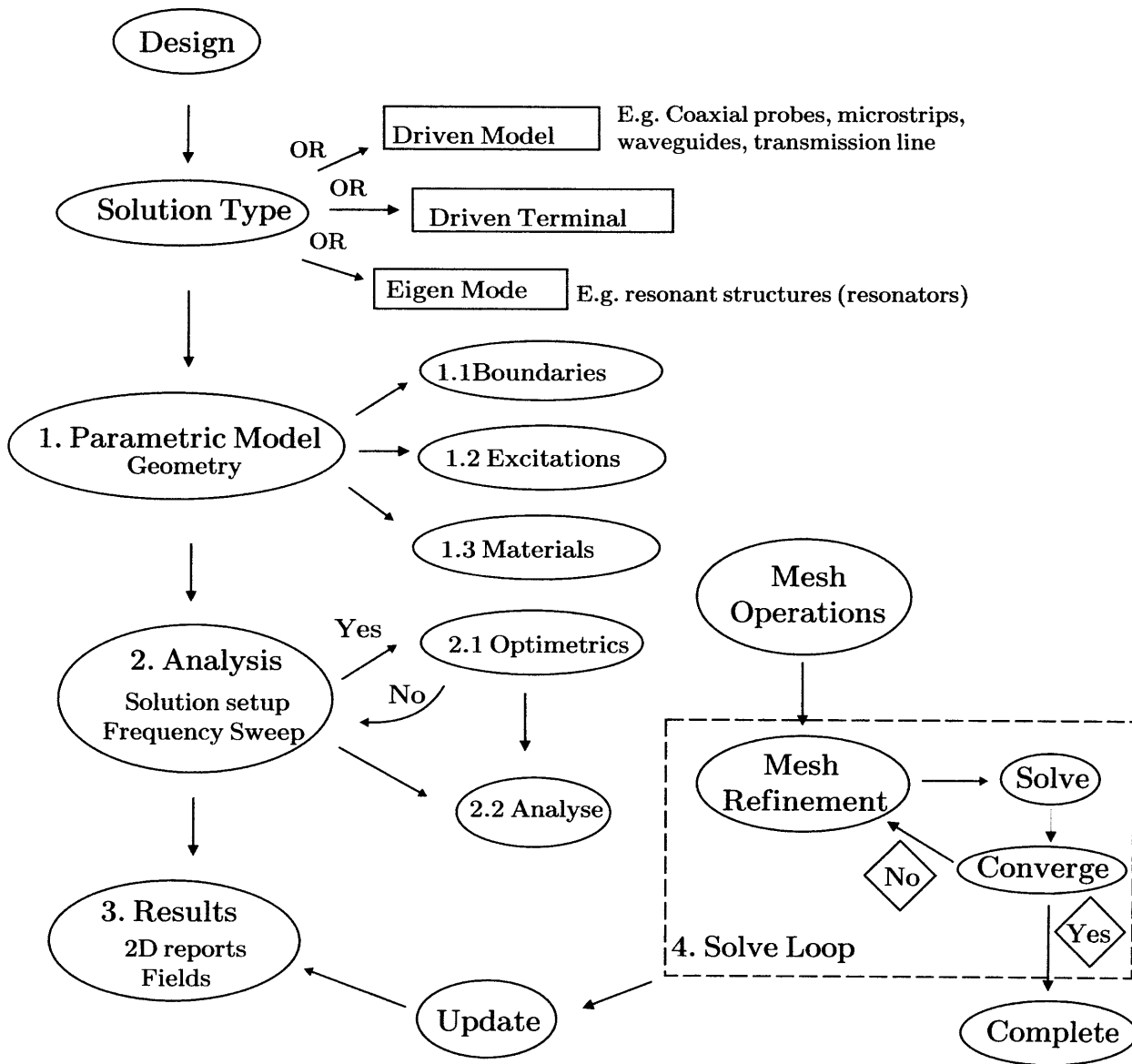


Figure 5.2 Flow chart of the construction and analysis of a real device using the HFSS simulation package.

5.3.2 Main Strategies of Model Development

Although the drawing tools in HFSS are flexible and make it possible to draw nearly any geometry, modelling problems must be realistic and within the scope of the software's analytical capabilities. There are certain things that need to be considered:

- When modelling open-region problems, designate the enclosure as a radiation boundary. Open-region problems, like the open ended coaxial probe, antenna and radiation problems, are solved by drawing an enclosure around the coaxial probe and the antenna and designating the enclosure as a radiation boundary.
- Structures must have at least one port.
- Structures should be kept electrically small. Since the simulator calculates the electromagnetic fields at every point in space as defined by the tetrahedral mesh, the structures must be kept to a reasonable size. To simulate electrically large structures, the geometry has to be split into subsections along the axis of the wave motion.
- The drawing of the structure as simple as possible. For an instance, rounded corners are much more complex and time-consuming to simulate than are square corners. If the rounded corners are not electrically important, they should be drawn as square corners to save time and computer memory.
- If the structure has electric or magnetic symmetry, take advantage of it by defining the symmetry plane or planes and solving only the symmetrical part of the structure. Exploiting symmetry reduces problem size and decreases solve time.

5.4 A Typical Model Set-Up

In setting up the models for real devices, such as OCP and SDR, there are several steps which are common to all simulation methods discussed in this chapter. All of them are susceptible to errors into the simulation, i.e. discrepancies between simulation and experimental results. Detailed modelling setups of an OCP and SDR are demonstrated in the following sections. Briefly, all the geometry needs to be created, either done by using the in-built modeller of the simulation software or by importing the geometry model from a mechanical CAD tool. Importing from a CAD tool is not that easy as the quality of the import filters varies significantly, but this is beyond the scope of this chapter. Here, the geometries were created using the in-built modeller. To compare the simulation model to an existing device, the exact same dimensions and material properties have to be used. Besides obvious errors, there are

always tolerances, and sometimes minute details are neglected, which are relevant at microwave frequencies.

Then the designer (or the user) has to choose the type of solver to be used to solve the modelled structure. For instance, as mentioned in the flow chart (see fig. 5.2), the user often uses a driven model solver to model a OCP to obtain scattering parameters* and similarly Eigenmode solver to model a completely enclosed resonator to obtain resonant frequencies and quality factors.

For an accurate simulation, knowledge of the exact material properties is essential, but which is not normally available. The computational effort for volume based methods depends on the volume size, and the simulation model must also be finite, even if in reality the device is placed in an infinite surrounding medium. In order to reduce size or the complexity of the design, boundary conditions need to be introduced which represent, symmetry, electric/magnetic walls, radiation walls. All of these boundary conditions are used in the modelling of the OCP as well as the SDR, which will be discussed in depth in the following sections. Finally, ports need to be defined to excite the structure and to monitor the simulation results such as the S-parameters.

5.5 Performing a Simulation

Having setup the geometrical representation of the real structure in the software environment, the next is to start the steps towards obtaining the final results. The first is the space discretization, i.e. the mesh setup, which is automated to a large extent in using modern commercial software such as HFSS. In spite of the high degree of automation, to obtain an accurate result, the proposed mesh might need to be checked or influenced manually. Then the software creates the system matrices based on the information of the geometry, and from this grid and method chosen for approximating Maxwell's equations. After all the required matrices are created and assembled, finally the solutions of the finite algebraic system are deduced. Here, the S-parameters for the OCP and resonant frequency (f_0) and the quality factor (Q) for the SDR are calculated, since they are the most often requested results for material characterisation. So far brief descriptions of modelling a real device have been discussed.

* Detailed description on S-parameters can be found in section 3.8.1 of chapter 3.

5.6 Construction of K-connector Open Ended Coaxial Probe

The OCPs considered in this chapter are assembled from different materials, such as glass (silica), brass, gold, dielectric bead, etc. The system that we modelled consisted of two main parts, i.e. the K-connector and its flange. In order to model the K-connector, its dimensions were measured using a Nikon Measuring Microscope MM-800 (Nikon Corp., Tokyo, Japan) and used together with the available catalogue data. This turned out to be enormously challenging, mainly due to the limited availability of the catalogue data (i.e. limited information regarding the dimensions and the materials properties of the K-connector). A perfect conductor is been assumed for the metals of the OCP, so there will be no field penetrating the conductor shielding. A schematic diagram of the K-connector coaxial probe used in this research is shown in fig. 5.3, based on the Anritsu K-connector (here K102F), which has an inherent bandwidth from DC up to 40 GHz. The connector's glass bead (silica) provides a convenient coaxial aperture, which can be ground flat to the plane of the brass flange. The following sections provide the detailed description of modelling the OCP. To obtain an accurate solution after the simulation, there are quite a few ingredients, such as model the reality correctly and ensure that the mesh is fine enough.

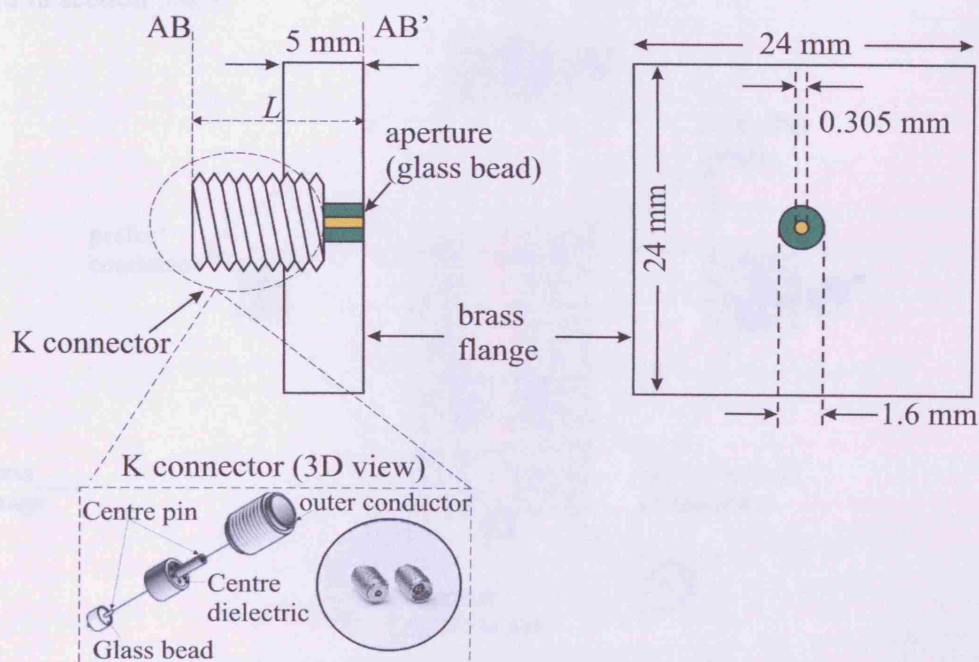
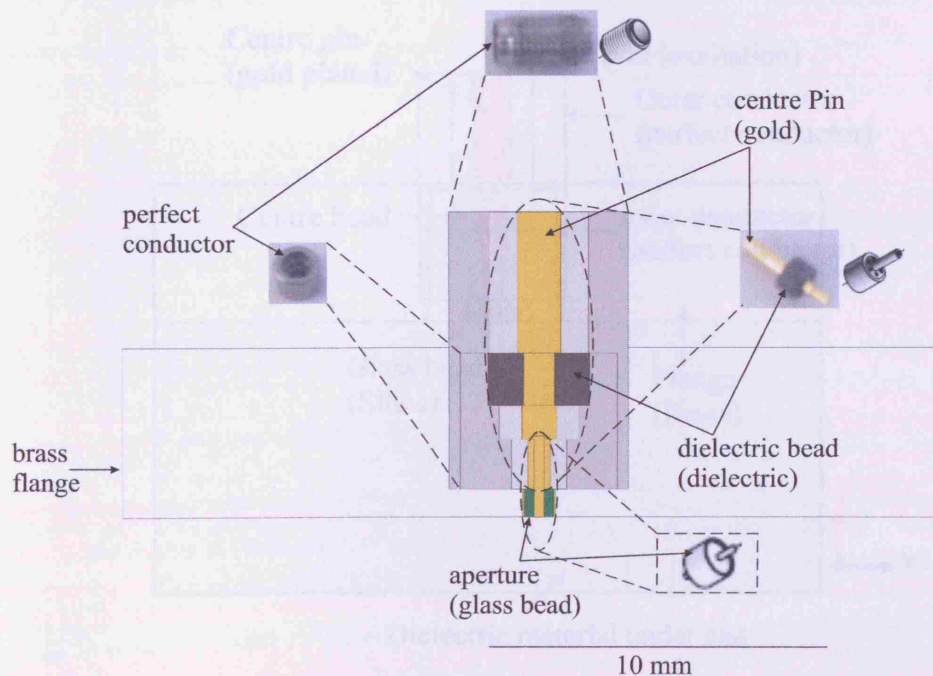


Figure 5.3 Schematic diagram of the K-connector coaxial probe.

5.6.1 Modelling the Actual K-Connector OCP

There are several important design parameters for an OCP. One of the most important among them is for an efficient transmission of incident and reflected signals between the VNA and probe head required that the impedance of the probe matched the $50\ \Omega$ impedance of the VNA and coaxial cable. This condition restricted the probe dimensions to fit commercially available connectors like K-connectors. As shown in fig. 5.4 (b), the K-connector OCP simulated in this section was assumed to have a glass bead (silica) of relative permittivity of 4 and loss tangent of 10^{-4} . The detailed dimensions of the OCP are shown in fig. 5.4 (a). The details of the material properties used in this simulation are listed in table 5.1. A driven model solver has been used in order to obtain S-parameters. The remedy for better accuracy and reduction of the complexity of the model and the simulation time is to utilise the geometrical symmetry to add one magnetic (H) wall boundary condition after cutting away the one-half of the object, as shown in fig. 5.6. Using the geometrical symmetry, this model can be even reduced to $1/4^{\text{th}}$ of the total object, but this alternative was not considered since the model with one-half of the object took less than 10 minutes and occupied less than 60 MB of memory, which is acceptable. The detailed implementations of the boundary conditions are discussed in section 5.6.3.



Note:

The above dimensions of the coaxial probe were measured by a Nikon Measuring Microscope MM-800 (Nikon Corp., Tokyo, Japan).

Figure 5.4 (a) Schematic diagram of the K-connector coaxial probe (the above figure is drawn to scale).

The area where the geometry model is defined is known as the 3D modeller. All the objects in the model are 3D objects. The unit of measurement is chosen to be millimetres (mm). *Global Co-ordinates* are chosen throughout the project and the entire model is centred at the origin. The first object created is the brass flange of dimensions $24 \times 24 \times 5 \text{ mm}^3$ using *Draw/Box* command in the drawing interface and is labelled as *brass flange*. Then the outer conductor of the K-connector (see fig. 5.4 (b)) is called the *outer conductor* and has a length of 8.35 mm and radius 2.65 mm. It is drawn using *Draw/Cylinder* command. HFSS does not allow any overlapping volume in the model. From the part of the model description above, it is seen that the *outer conductor* overlaps with the *brass flange*. Hence it becomes necessary to create a hole in the *brass flange* to accommodate the *outer conductor*. Thus, using the *Modeler/Boolean/ Subtract*, the *outer conductor* is subtracted from the *brass flange*. In the subtraction process, a copy of the *outer conductor* is made using the *Edit/Copy* and *Edit/Paste* commands. The copy *outer conductor1* is then subtracted from the *brass flange*. Then the inner conductor of the K-connector (see fig. 5.4 (b)) called the *inner conductor* (of a length of 4.1 mm and radius 2.32 mm) is drawn using the *Draw/Cylinder* command. The remaining objects of the K-connector are drawn following the same procedures as for the inner and outer conductors.

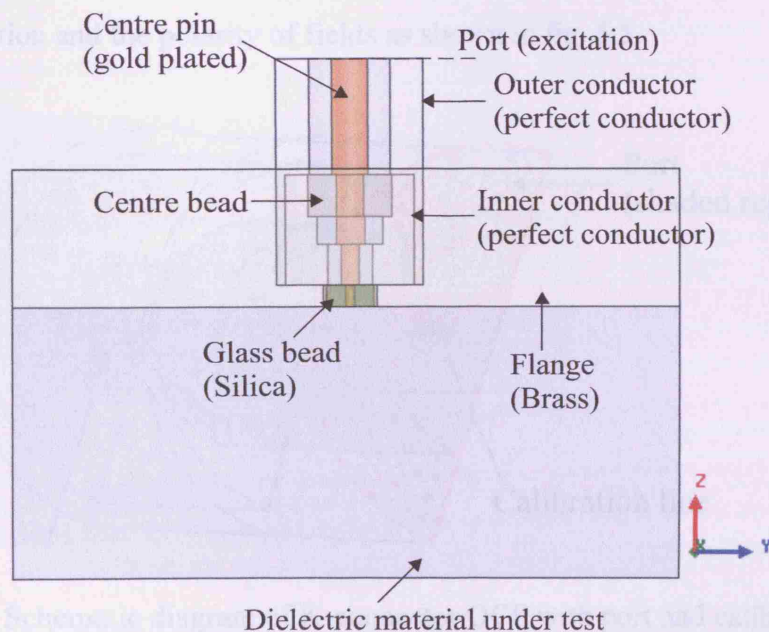


Figure 5.4 (b) Cross section of the K-connector coaxial probe.

In order to avoid overlapping of the objects, larger objects are constructed first followed by smaller objects. To mimic the reality of the empty K-connector coaxial probe, a virtual object

that is assigned the *radiation* boundary must be created in the boundary assignment stage which will be discussed in the later section. This object must be exposed to the background and it should be located at least one quarter wavelength away from the radiating source. The dimension of the radiation box for the simulation is chosen to be $24 \times 24 \times 15 \text{ mm}^3$. The box is created using *Draw/Box* and labelled as *radiation box*.

5.6.2 Excitations

The open ended coaxial probe has one port as shown in fig. 5.4 (b). Once the construction of the model is completed, then port needs to be defined at the location which, in reality, the sources (i.e. the VNA[†]) will be connected. This is usually at the same point along the transmission line shown in fig. 5.4 (b). Ports enable energy to flow into and out of a structure, which is necessary as a part of the simulation process. The port is defined using the *HFSS/Excitations/Assign* command. The port type is chosen to be *Wave Port*[‡] and labelled as *WavePort1*. By default, a structure is assumed to be completely encased in a conductive shield (or perfect E boundary[§]) with no energy propagation through it. Therefore ports need to be added to the structure to indicate the area where energy enters and exits the structure. After the assignments of the ports, next the ports must be calibrated. A calibration line determines direction and the polarity of fields as shown in fig. 5.5.

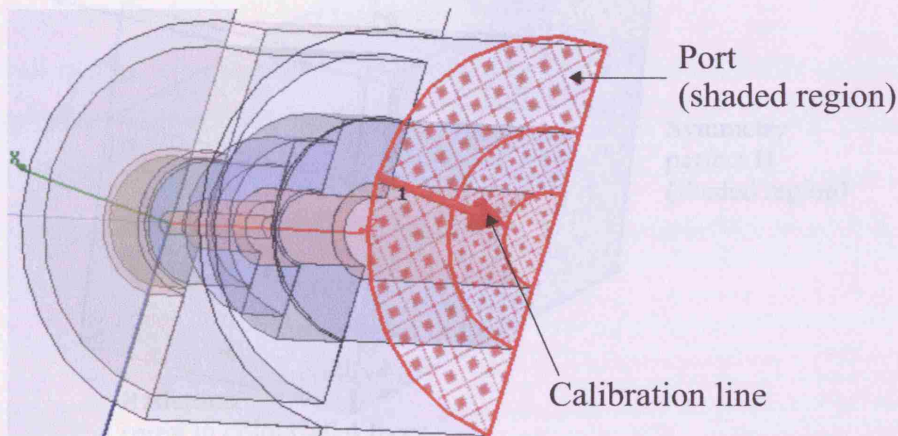


Figure 5.5 Schematic diagram of K-connector OCP with port and calibration line.

[†] VNA stands for vector network analyser, complete information can be found in section 3.8.3 of Chapter 3.

[‡] *Wave Port* is used to model *exterior* surfaces through which a signal enters or exits the geometry [6].

[§] A perfect E boundary is used to represent a perfectly conducting surface in a structure.

5.6.3 Boundary Conditions

As mentioned briefly in section 5.4, the simulation environment, infinite in reality, has to be truncated for the purpose of simulating the model on a computer. After the assignment of the excitation on the model, the next step is to introduce the boundary conditions on the model. At the boundary, special boundary conditions need to be imposed, depending on the real operating condition of the device. In order to assign boundary conditions to the objects in the model, the *HFSS/Boundaries/Assign* command is used. From the *Edit/Select/Faces*, all the faces of the air box are selected and assigned the *Radiation* boundary condition and similarly a *Symmetry Perfect H* boundary has been applied to the symmetrical plane of the OCP. The boundary conditions used in the HFSS simulation of an OCP are shown in fig. 5.6. Here, since the coaxial probe is placed in open space, then a so-called radiation boundary** condition needs to be imposed, which simulates the unperturbed propagation of EM waves through this boundary. A Symmetric perfect H boundary has been used to let the electromagnetic wave propagate smoothly from one material to other.

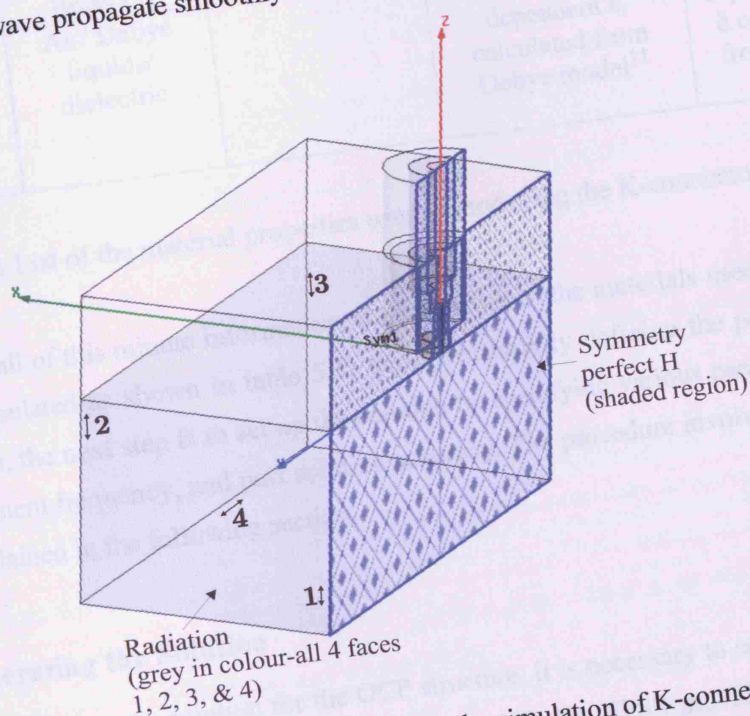


Figure 5.6 Boundary conditions used in the simulation of K-connector OCP.

** Radiation boundary is used to simulate an open problem that allows waves to radiate infinitely far into the space.

5.6.4 Material Properties

The permittivity and the conductivity values for all the materials present in the model naturally play an important role in the solution's accuracy. Often these values are frequency dependent (dispersive materials); the more accurately this frequency dependence is known, the more accurate the solution can be. None of the materials have a constant loss tangent from DC to several GHz [2].

Component name	Material	Conductivity (σ) S/m	Dielectric constant (ϵ_r)	Loss tangent ($\tan \delta$)
Centre conductor	Gold [3]	4.098×10^7	-	-
Centre bead	Dielectric [3]	-	2.07	10^{-4}
Glass bead	Silica [3]	-	4	10^{-4}
Outer/Inner conductor	Perfect conductor [1]	1×10^{30}	-	-
Flange	Brass [3]	2.564×10^7	-	-
Dielectric Material	Air/ Debye liquids/ dielectric	-	Frequency dependent ϵ_r calculated from Debye model ^{††}	Frequency dependent $\tan \delta$ calculated from Debye model

Table 5.1 List of the material properties used in modelling the K-connector OCP.

Allowing for all of this minute information, the properties of the materials used in this model have been tabulated as shown in table 5.1. After successfully defining the port, boundaries and materials, the next step is to set up the solution by specifying various parameters such as mesh refinement frequency, and port solution accuracy. The procedure involving the solution setup is explained in the following section.

5.6.5 Generating the Solution

In order to generate the solution for the OCP structure, it is necessary to specify the solution parameters. Fig. 5.7 shows a snapshot of the features that HFSS provides to generate the solutions for the OCP problem. The solution setup is the last pre-processing step that needs to

^{††} For more information regarding the Debye model refer to section 3.7 of Chapter 3.

be performed before a simulation can be started. The solution setup includes the mesh generation, ports solution, and a full solution over a frequency sweep.

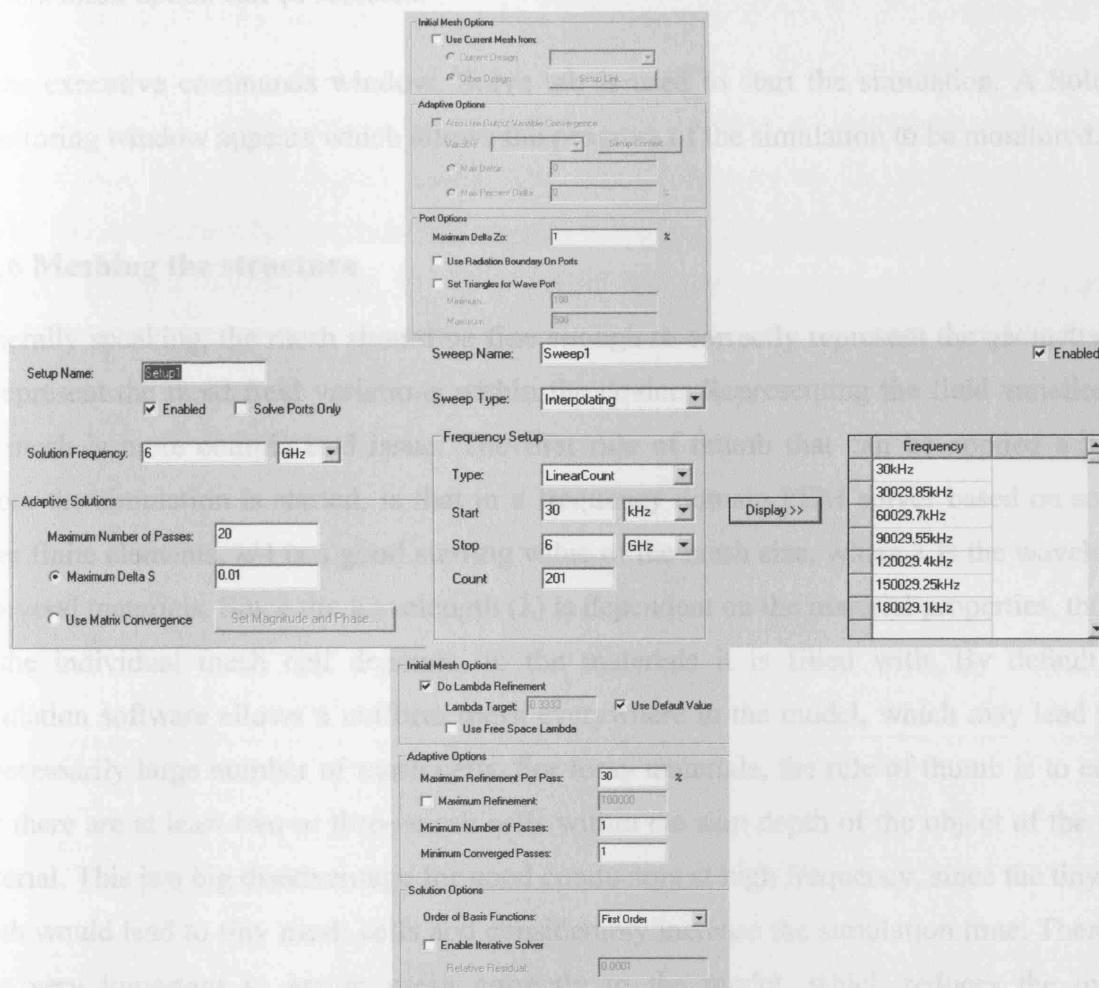


Figure 5.7 Solution Setup

For the OCP problem described in section 5.6, the solution is set at a frequency of 6 GHz and the number of adaptive passes is set to 20. It is necessary to specify the number of adaptive passes for which the error criterion can be met. The deviation or the error between the S-parameters for consecutive adaptive passes, *Max Delta S* is set to 0.01. This is necessary to achieve a higher degree of convergence.

The mesh refinement percentage, *Max Refinement Per Pass* is set to 30%. *Fast Sweep* is selected from 30 kHz to 6 GHz in order to calculate the frequency response using the mesh created by the adaptive refinement for a single frequency. Fast sweep is selected as it is a quick method of solving using a frequency sweep and it performs interpolation on the data

based on a small number of frequency values. *Initial mesh* is chosen if the simulation is being run for the first time. If the simulation has been run earlier for a few iterations then the *Current mesh* option can be selected.

In the executive commands window, Solve tab is used to start the simulation. A Solution Monitoring window appears which allows the progress of the simulation to be monitored.

5.6.6 Meshing the structure

Generally speaking, the mesh should be fine enough to correctly represent the geometry and to represent the rapid field variations within the device. Representing the field variations in the mesh is more complicated issue. The first rule of thumb that can be applied a priori, before the simulation is started, is that in a frequency domain FEM solver based on second order finite elements, $\lambda/4$ is a good starting value of the mesh size, where λ is the wavelength of several materials. Since the wavelength (λ) is dependent on the material properties, the size of the individual mesh cell depends on the materials it is filled with. By default, the simulation software allows a uniform mesh everywhere in the model, which may lead to an unnecessarily large number of mesh cells. For lossy materials, the rule of thumb is to ensure that there are at least two or three mesh cells within the skin depth of the object of the lossy material. This is a big disadvantage for good conductors at high frequency, since the tiny skin depth would lead to tiny mesh cells and considerably increase the simulation time. Therefore it is very important to assign mesh correctly to the model, which reduces the overall simulation time and increases the accuracy of the model.

In the case of meshing the OCP model, HFSS generates an initial mesh according to a minimal user input, then taking into account geometry, material properties, the user refines the mesh through an automatic adaptive meshing^{††}, until convergence is reached. Wherever rapid field variations occur, the mesh is refined and the simulation is restarted. This process is repeated until the results do not suffer further significant changes. With further increase in the number of mesh cells, the HFSS response can be improved at the expense of simulation time.

^{††} An adaptive analysis is a solution process in which the mesh is refined iteratively in regions where the error is high, which increases the solution's precision [6]

5.6.7 Post Processing and Simulation Results

The simulation of the K-connector OCP takes 12 minutes on a 3.4 GHz CPU and 2 GB RAM machine. HFSS provides three post processors for analysing the results of the simulation such as *Fields*, *Matrix Data*, and *Matrix Plot*. The *Fields* post processor provides many features such as 2D and 3D plots of fields, and animated plots of electric and magnetic fields. Fig. 5.8 shows contour plot of E-field magnitude at the cross-section of the air interface of the OCP, where the electric field values in HFSS are normalised to 1 V/m. *Matrix Data* post processor provides viewing and exporting of the matrices that are computed for the S-parameters, impedances and propagation constant during each adaptive solution. From the *Matrix Data* post processor, the characteristic impedance (Z_0) deduced at the port is 49.86 Ω , within an experimental error of 0.28%. This is close to the expected 50 Ω .

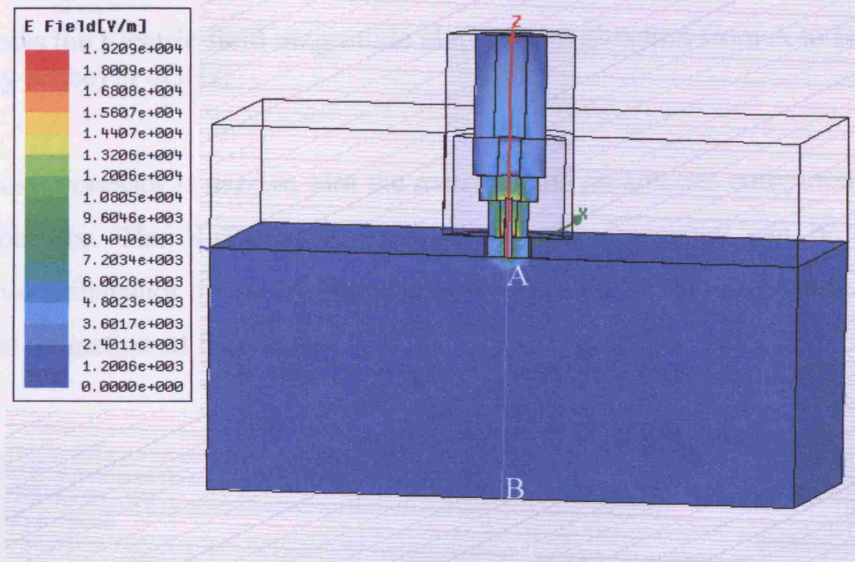


Figure 5.8 Contour plot of E-field magnitude at the cross-section of the air interface coaxial probe.

Fig. 5.9 shows the Electric field magnitude along the $-z$ direction from A to B as shown in fig. 5.8 for the empty probe. The maximum penetration depth (d) of E-field without the presence of the sample ($\epsilon_r = 1$) along A-B is around 0.2 mm as shown in fig. 5.9. For the complete understanding of the penetration depth as a function of material under test, further simulations have been carried out on different types of dielectric materials. In depth discussion on this issue can be found in section 5.9.2.

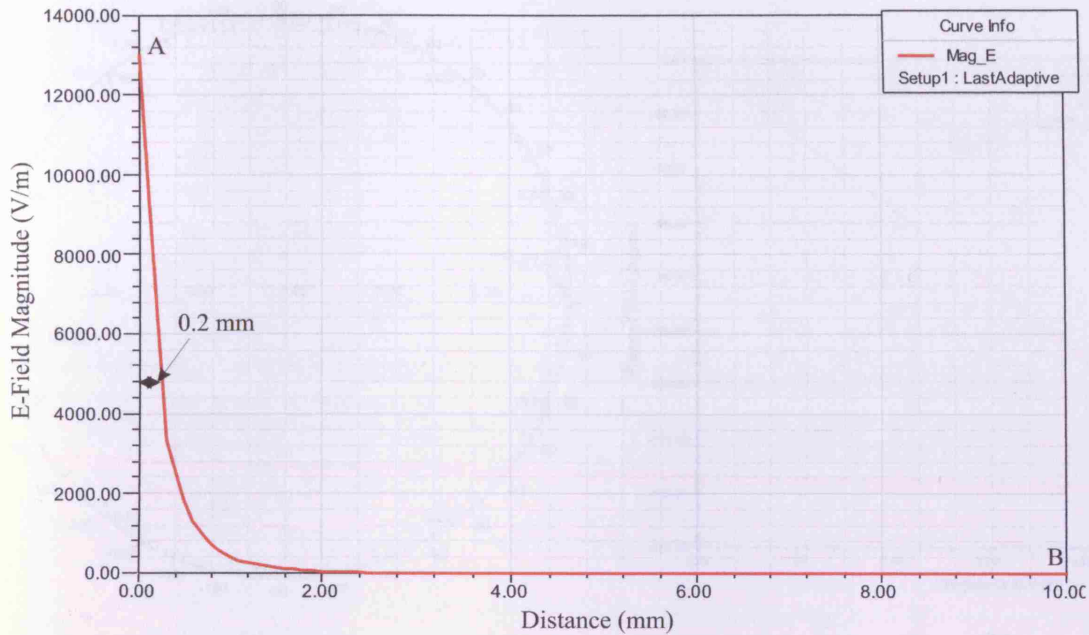


Figure 5.9 shows the Electric field magnitude along the $-z$ direction from A to B as shown in fig. 5.8 (empty probe) at 6GHz.

Matrix Plot post processor is used to plot the matrices and parameters computed in the matrix data post processor. The S-parameter (S_{11}) against the frequency can be plotted here. Fig. 5.10 shows a snapshot of the *Matrix Plot* post processor. It can be used to plot S_{11} on a Smith Chart as a function of frequency.

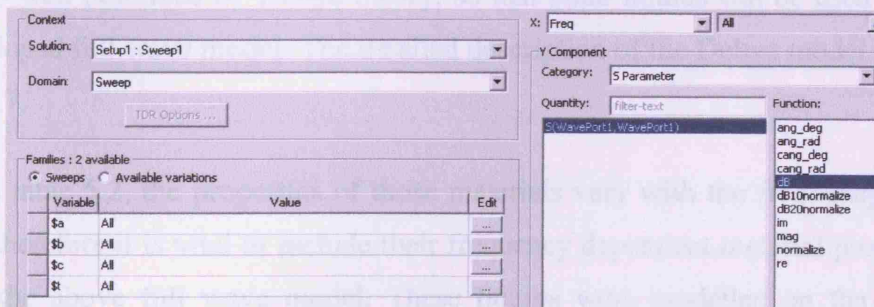


Figure 5.10 Matrix Plot post processor.

Fig. 5.11 (a) and (b) shows the plot of S_{11} -parameter on a Smith Chart and linear phase of S_{11} as a function of frequency (GHz) for an empty K-connector OCP described in section 5.6.

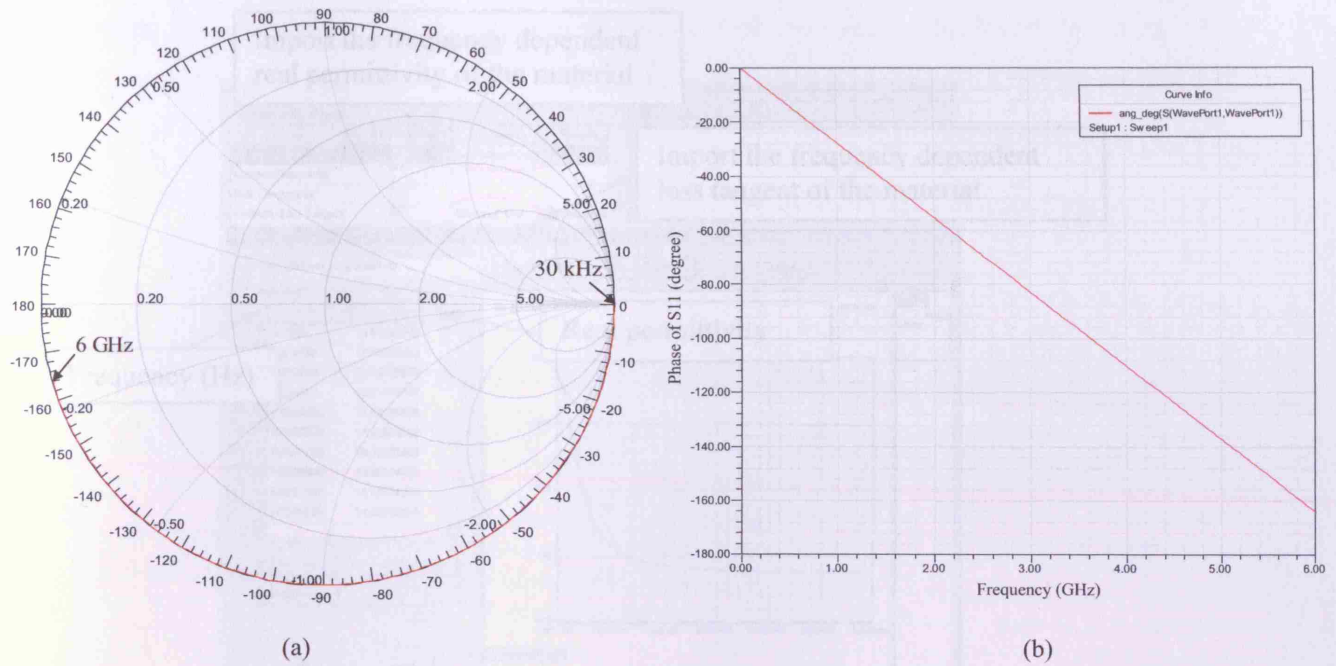


Figure 5.11 (a) S_{11} -parameter on a Smith Chart and (b) Phase of S_{11} -parameter as a function of frequency for an empty K-connector OCP, from 30 kHz - 6 GHz.

Further validation of the above full wave K-connector OCP model has been carried out by testing several different dielectric materials (e.g. polar liquids), including low, medium and high permittivity materials. The dielectric properties of polar liquids arise from the orientational response of permanent electric dipoles to an applied electric field. This behaviour is well described by Debye theory, so that polar liquids can be used to check the above developed full wave model. The detailed description of the Debye model can be found in section 3.7.

As listed in table 5.2, the properties of those materials vary with the frequency of the field excitation; therefore it is vital to include their frequency dependent material properties while simulating the above full wave model. These liquids were modelled on the basis of the available published data on Debye parameters as listed in table 5.2. To perform this in the HFSS simulation environment, the frequency dependent complex permittivity (i.e. real permittivity and loss tangent) of those materials need to be calculated for the entire frequency range (i.e. 30 kHz – 6 GHz) using the Debye model described in section 3.7. Then the calculated frequency dependent complex permittivity dataset was imported into the material library of the HFSS in *tab file format. Fig. 5.12 shows a snapshot of the *Enter Frequency Dependent Data Points*.

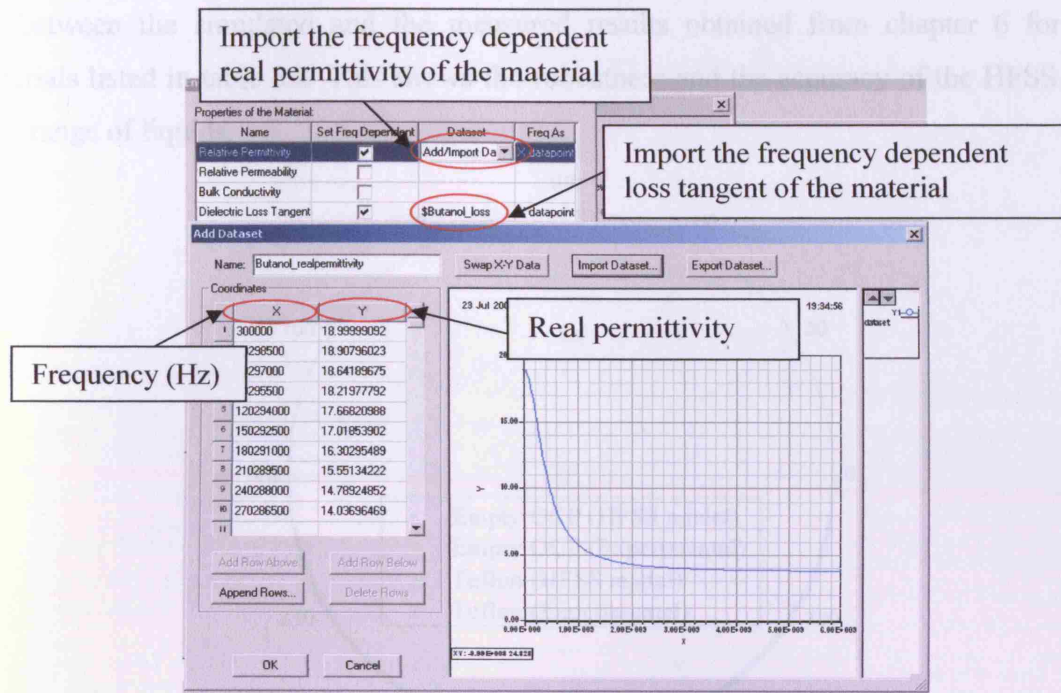


Figure 5.12 Enter Frequency Dependent Data Points.

The following table 5.2 shows the Debye parameters obtained from various literatures in order to validate the admittance model:

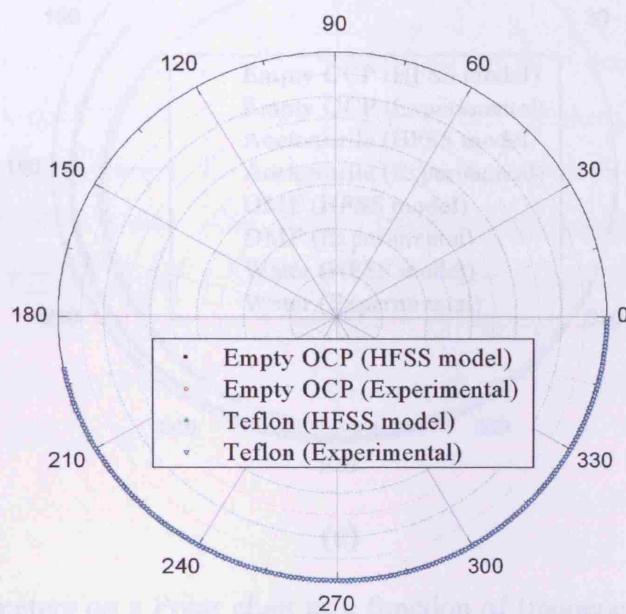
Solvents	ϵ_s Literature	ϵ_∞ Literature	τ (ps) Literature	ϵ_1	ϵ_2
Teflon [4]	-	-	-	2.08	0.0004
Butanol [5]	19	3.8	482	-	-
Propan-2ol [6]	20.8	3.8	327	-	-
Ethanol [5]	25.4	4.9	140	-	-
Methanol [7]	34.5	5.6	47	-	-
Acetonitrile [8]	37.5	2.26	3.2	-	-
Dimethylformamide (DMF) [5]	38.5	10	14.6	-	-
Water [9]	80.4	5.2	9.4	-	-

Table 5.2 Literature values of the Debye parameters of various liquids at 20-25 °C.

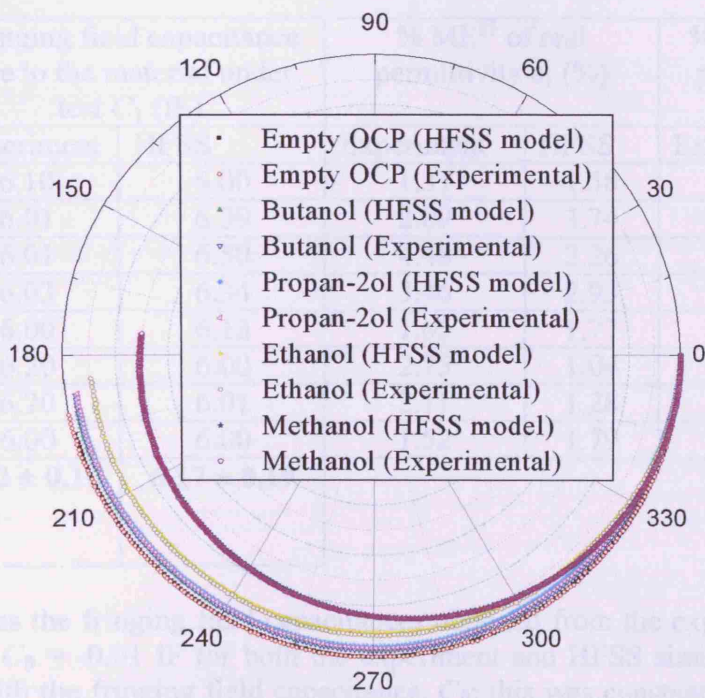
5.6.8 Simulation Results of K-Connector OCP

Once the individual frequency dependent material properties were imported into the material library, the simulation was repeated several times for those materials independently on the modelled full wave K-connector OCP (see table 5.2). Fig. 5.13 shows excellent agreement of

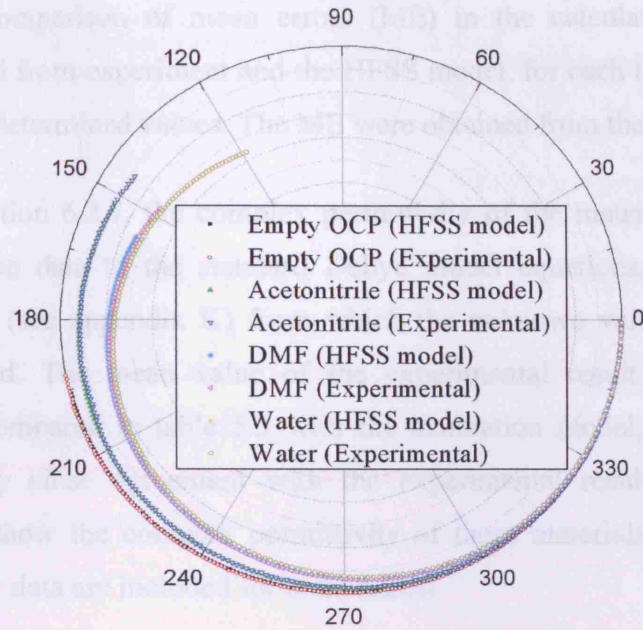
S_{11} between the simulated and the measured results obtained from chapter 6 for those materials listed in table 5.2. This shows the robustness and the accuracy of the HFSS model for a range of liquids.



(a)



(b)



(c)

Figure 5.13 S_{11} -parameters on a Polar chart as a function of frequency of different dielectric materials terminated at the end of the K-connector OCP (see fig. 5.4 (b)), including low (a), medium (b) and high permittivity (c) materials. The simulations were made in the frequency range from 30 kHz to 6 GHz.

Test Materials	Fringing field capacitance due to the material under test C_1 (fF)		% ME ^{§§} of real permittivity ϵ_1 (%)		% ME of imaginary permittivity ϵ_2 (%)	
	Experiment	HFSS	Experiment	HFSS	Experiment	HFSS
Teflon	6.10	6.00	1.37	1.58	9.87	7.55
Butanol	6.01	6.39	2.09	3.74	10.08	6.00
Propan-2ol	6.01	6.50	4.48	2.26	6.68	3.54
Ethanol	6.03	6.34	3.46	2.93	4.35	1.27
Methanol	6.00	6.13	1.65	1.77	1.19	2.31
DMF	6.20	6.00	2.75	1.04	6.91	2.26
Acetonitrile	6.20	6.01	2.11	1.28	7.67	6.64
Water	6.00	6.00	1.52	1.79	11.43	3.69
Fringing field capacitance	6.12 ± 0.16	6.17 ± 0.19				

Table 5.3 Compares the fringing field capacitances obtained from the experiment and HFSS simulation, where $C_0 = -0.01$ fF for both the experiment and HFSS simulation. There is no error associated with the fringing field capacitance, C_0 ; this was constant throughout for the wide range of permittivities.

^{§§} As defined in Eq. (5.1).

Table 5.3 shows comparison of mean errors (ME) in the calculations of the complex permittivity obtained from experiment and the HFSS model, for each test liquid compared to the standard Debye determined values. The ME were obtained from the Eq. (5.1).

As discussed in section 6.2.7, the complex permittivity of the materials were obtained by fitting the simulation data to the standard Debye model equations, using the developed MathCAD program (see appendix K) from which the unknown values of C_0 and C_1 (see table 5.3) are found. The mean value of the experimental result of the fringing field capacitance C_1 is compared in table 5.3 with the simulation model, where the simulation result shows a very close agreement with the experimental results within 0.3% error. Figs. 5.14 to 5.21 show the complex permittivity of these materials, where the measured complex permittivity data are included for comparison.

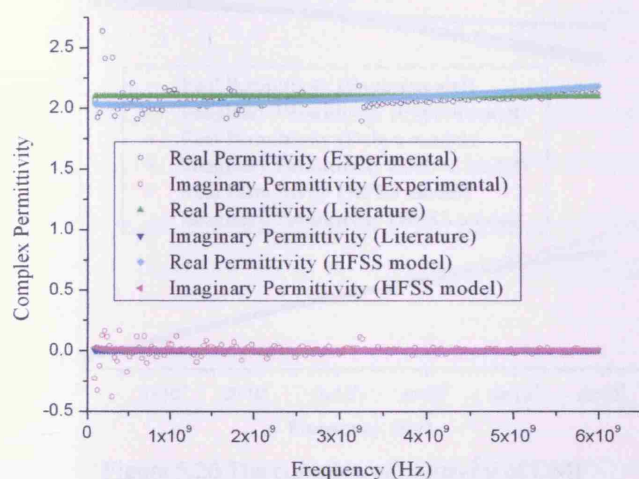


Figure 5.14 The complex permittivity of teflon as a function of frequency.

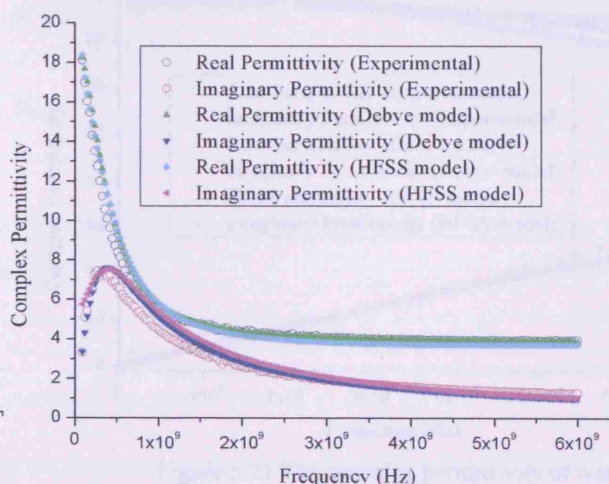


Figure 5.15 The complex permittivity of butanol as a function of frequency.

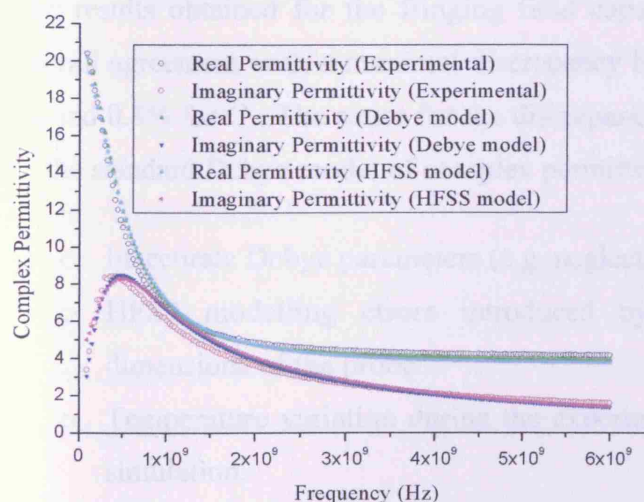


Figure 5.16 The complex permittivity of propan-2ol as a function of frequency.

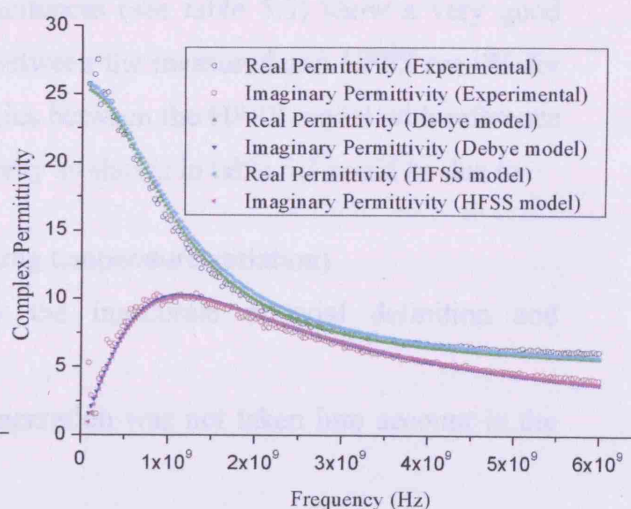


Figure 5.17 The complex permittivity of ethanol as a function of frequency.

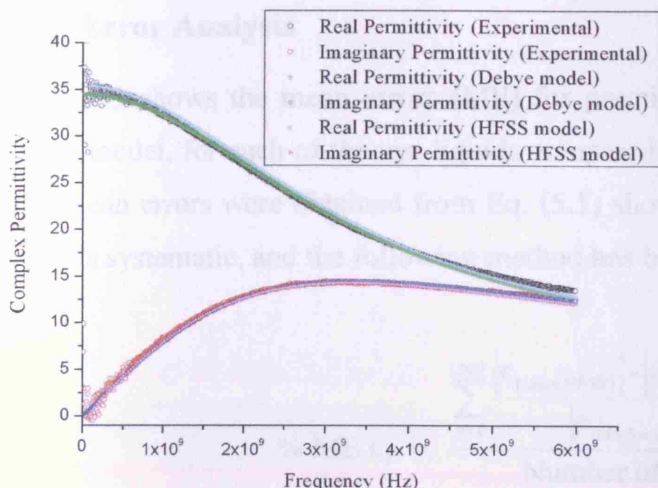


Figure 5.18 The complex permittivity of methanol as a function of frequency.

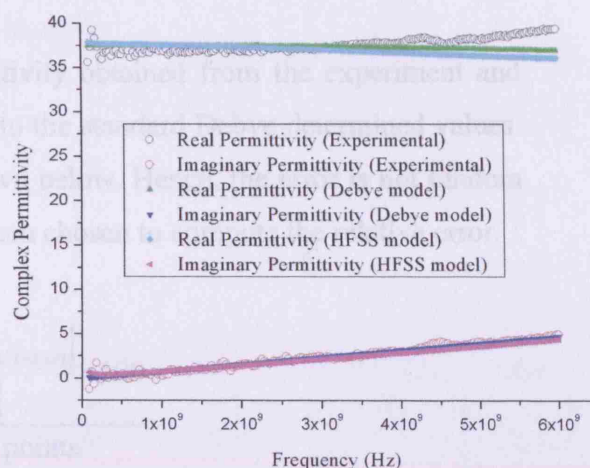


Figure 5.19 The complex permittivity of acetonitrile as a function of frequency.

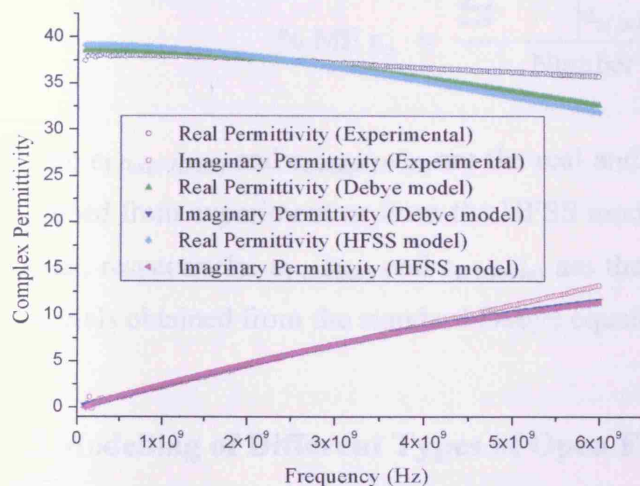


Figure 5.20 The complex permittivity of DMF as a function of frequency.

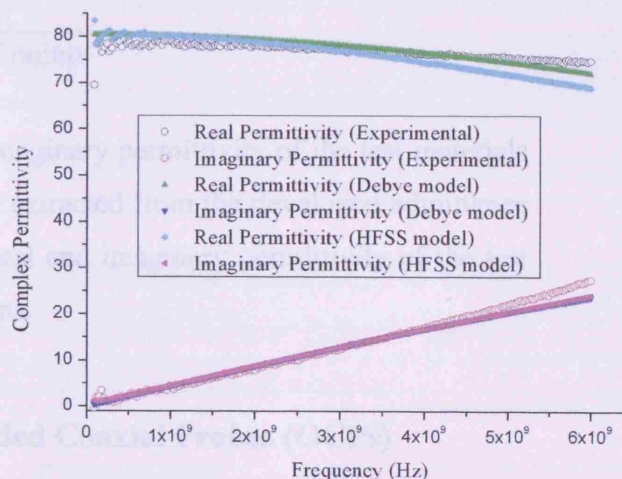


Figure 5.21 The complex permittivity of water as a function of frequency.

The results obtained for the fringing field capacitances (see table 5.3) show a very good overall agreement with a maximal discrepancy between the measured and HFSS are 0% for C_0 and 0.8% for C_1 . The cause for the discrepancies between the HFSS model with reference to the standard Debye model of complex permittivity as shown in table 5.3 could be due to

- Inaccurate Debye parameters (e.g. neglecting temperature variation).
- HFSS modelling errors introduced by the inaccurate material definition and dimensions of the probe.
- Temperature variation during the experimentation was not taken into account in the simulation.
- Purity, volatility and the freshness of the material is not considered in the simulation.

5.6.9 Error Analysis

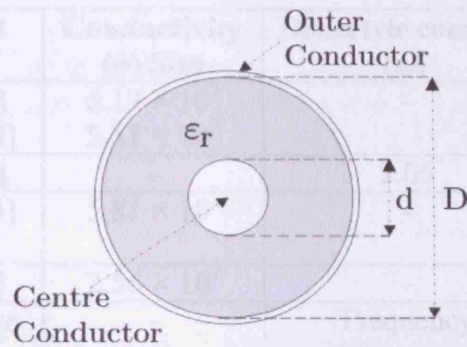
Table 5.3 shows the mean errors (ME) for permittivity obtained from the experiment and HFSS model, for each of the test liquids compared to the standard Debye determined values. The mean errors were obtained from Eq. (5.1) shown below. Hence, the error is not random but it is systematic, and the following method has been chosen to compute the relative error.

$$\begin{aligned} \% \text{ ME } \epsilon_1 &= \frac{\sum_{n=0}^{200} \frac{|\epsilon_{1(\text{exp/HFSS})}| - |\epsilon_{1(\text{Debye})}|}{|\epsilon_{1(\text{Debye})}|} \times 100}{\text{Number of points}} \\ &\quad (5.1) \\ \% \text{ ME } \epsilon_2 &= \frac{\sum_{n=0}^{200} \frac{|\epsilon_{2(\text{exp/HFSS})}| - |\epsilon_{2(\text{Debye})}|}{|\epsilon_{2(\text{Debye})}|} \times 100}{\text{Number of points}} \end{aligned}$$

where $\epsilon_1 (\text{exp/HFSS})$ and $\epsilon_2 (\text{exp/HFSS})$ are the real and imaginary permittivity of the test materials obtained from experiment or from the HFSS model extracted from the developed admittance model, respectively. $\epsilon_1 (\text{Debye})$ and $\epsilon_2 (\text{Debye})$ are the real and imaginary permittivity of the test materials obtained from the standard Debye equations.

5.7 Modelling of Different Types of Open Ended Coaxial Probes (OCPs)

Apart from the K-connector OCP, different types of OCP have been modelled using HFSS simulation package to validate the admittance models (see sections 3.6.1 and 3.6.2). The coaxial probes considered in this section have different aperture sizes and are assembled from different sizes of standard 50 Ω PTFE-filled semi-rigid coaxial cables, namely RG-405, RG-401, etc., terminated with a brass flange. The detailed dimensions of these cables are listed in table 5.4. These probes are assembled from different materials, like polytetrafluoroethylene (PTFE), silver, copper, and brass. The model structures of these probes are similar to the K-connector OCP, but consist of different sizes of semi-rigid coaxial cables and a SMA connector terminated to a brass flange (see fig. 5.22). Fig. 5.22 shows a cross-section of a modelled OCP using RG-402 semi-rigid coaxial cable. The properties of the materials used in modelling these OCP are listed in table 5.5.



Semi-rigid coaxial cables	d (mm)	D (mm)	Centre conductor material	Outer conductor material	ϵ_r
RG-405 [11]	0.51	1.68	Silver	Copper	2.06
RG-402 [11]	0.92	2.98	Silver	Copper	2.06
SMA [11]	1.275	4.2165	Copper	Brass	2.06
RG-401 [11]	1.63	5.31	Silver	Copper	2.06

Table 5.4 The dimensions of different semi-rigid coaxial cables used for modelling of OCP, where “silver” = silver plated.

Different types of OCP are modelled exactly following the same procedures as for the K-connector OCP, mentioned in section of 5.6. The simulations of these different types of OCP take around less than 15 minutes on a 3.4 GHz CPU and 2 GB RAM machine.

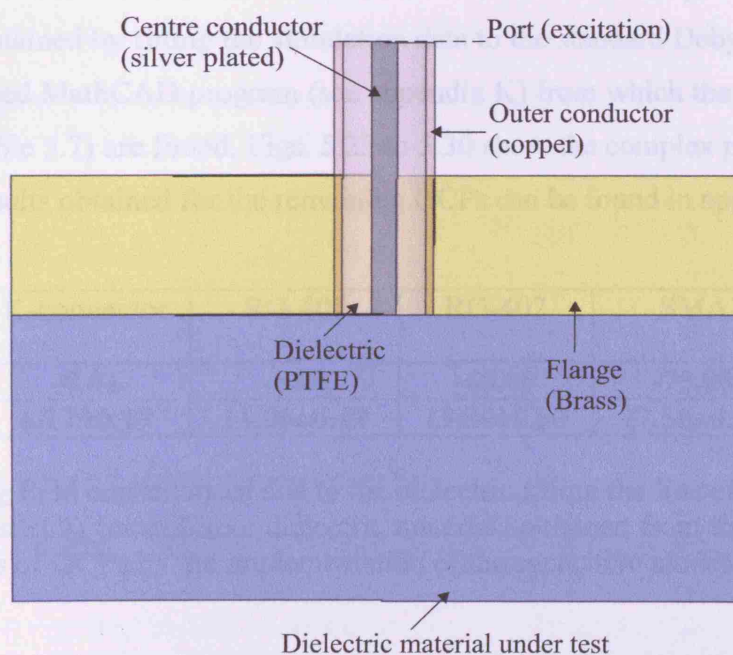


Figure 5.22 Cross section of the RG-402 coaxial probe.

Component name	Material	Conductivity (σ) S/m	Dielectric constant (ϵ_r)	Loss tangent ($\tan \delta$)
Centre conductor	Silver [4] Copper [4]	6.17×10^7 5.81×10^7	-	-
Dielectric	PTFE [4]	-	2.06	2×10^{-4}
Outer conductor	Copper [4]	5.81×10^7	-	-
Flange	Brass [4]	2.56×10^7	-	-
Dielectric Material	Air/ Debye liquids/ dielectric	-	Frequency dependent ϵ_r calculated from Debye model	Frequency dependent $\tan \delta$ calculated from Debye model

Table 5.5 List of the material properties used in modelling different types of OCP.

5.7.1 Simulation Results of Different Types of OCPs

Similarly, as mentioned in the previous section 5.6.9, the S_{11} simulation data obtained for different types of OCPs terminating those test materials were individually fed into the MathCAD code (see appendix K) that worked out the complex permittivity of those materials by fitting the simulation data to the standard Debye equations. From this the unknown quantities of the fringing field capacitances were found, as shown in table 5.6 for different OCPs. Individual values of these capacitances and the corresponding complex permittivities of these materials were determined by the implementation of the capacitive model. The results obtained for RG-402 OCP can be found below, where the complex permittivity of the materials were obtained by fitting the simulation data to the standard Debye model equations, using the developed MathCAD program (see appendix K) from which the unknown values of C_0 and C_1 (see table 5.7) are found. Figs. 5.23 to 5.30 show the complex permittivity of these materials. The results obtained for the remaining OCPs can be found in appendix L.

Fringing Capacitances	K-connector	RG-405	RG-402	SMA	RG-401
C_0 (fF)	-0.01	-5.00	-65.00	-75.00	-85.00
C_1 (fF)	6.17 ± 0.19	11.06 ± 0.42	19.30 ± 0.50	27.50 ± 0.20	34.80 ± 1.10

Table 5.6 fringing field capacitances due to the dielectric filling the line of the probe (C_0) and material under test (C_1) for different dielectric materials obtained from the HFSS simulation for different types of OCPs by the implementation of the capacitive model.

Test Materials	Fringing field capacitance due to the material under test C_0 (F)	Fringing field capacitance due to the material under test C_1 (F)	% ME error of real permittivity ϵ_1 (%)	% ME error of imaginary permittivity ϵ_2 (%)
Teflon	-6.50×10^{-14}	2.13×10^{-14}	3.32	3.38
Butanol	-6.50×10^{-14}	2.00×10^{-14}	4.57	2.30
Propan-2ol	-6.50×10^{-14}	1.95×10^{-14}	4.44	2.60
Ethanol	-6.50×10^{-14}	1.97×10^{-14}	1.94	0.58
Methanol	-6.50×10^{-14}	1.90×10^{-14}	0.36	1.41
Acetonitrile	-6.50×10^{-14}	1.88×10^{-14}	2.62	11.72
DMF	-6.50×10^{-14}	1.95×10^{-14}	1.62	1.91
Water	-6.50×10^{-14}	1.86×10^{-14}	4.97	5.77
Fringing field capacitances	-6.50×10^{-14}	$1.96 \pm 0.09 \times 10^{-14}$		

Table 5.7 fringing field Capacitances determined from HFSS Simulation for RG-402 OCP.

It is apparent from table 5.6 that the simulation results for the fringing field capacitances (i.e. C_0 and C_1) for the different sizes of probes suggest that the value of the fringing field capacitances increases with the increasing probe diameter for the wide range of materials with frequency ranging from 30 kHz to 6 GHz, due to the increased aperture size of the probe. It is also noticeable that the value of C_0 for the K-connector coaxial probe (or any smaller probes) can be negligible; however, including this value enhanced the sensitivity of the capacitive model by 1-2%. Except for the K-connector OCP, knowledge of the value of C_0 is vital for other bigger probes for the determination of permittivity of unknown materials.

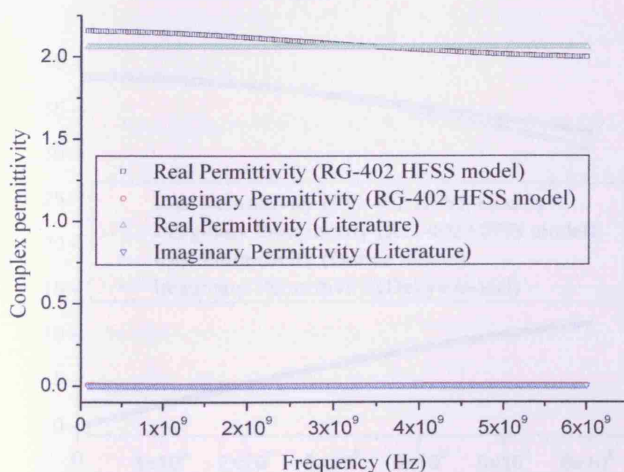


Figure 5.23 The complex permittivity of teflon as a function of frequency.

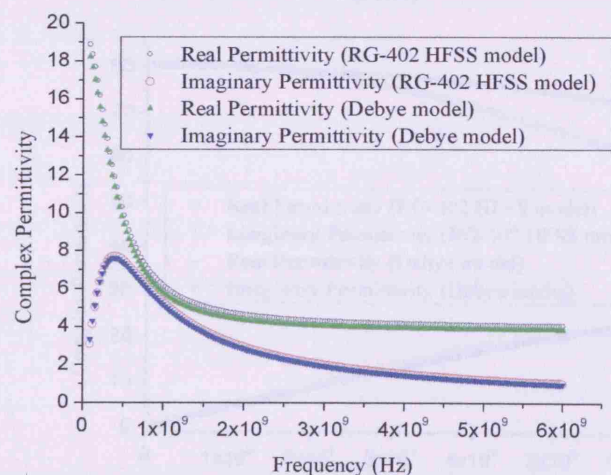


Figure 5.24 The complex permittivity of butanol as a function of frequency.

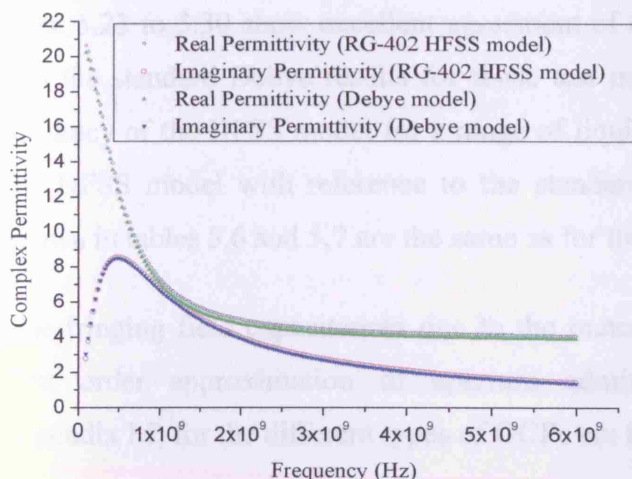


Figure 5.25 The complex permittivity of propan-2ol as a function of frequency.

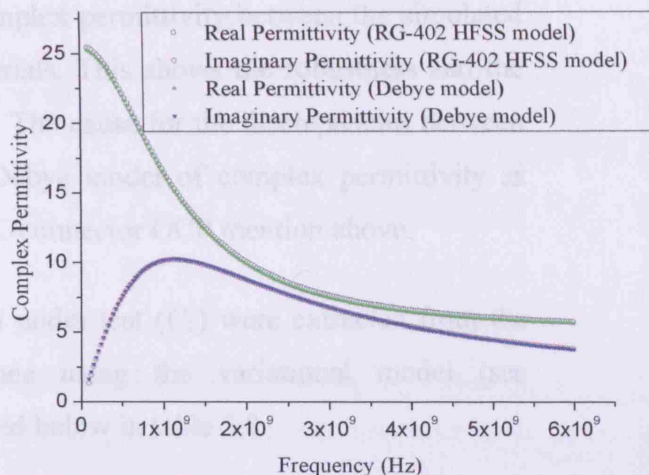


Figure 5.26 The complex permittivity of ethanol as a function of frequency.

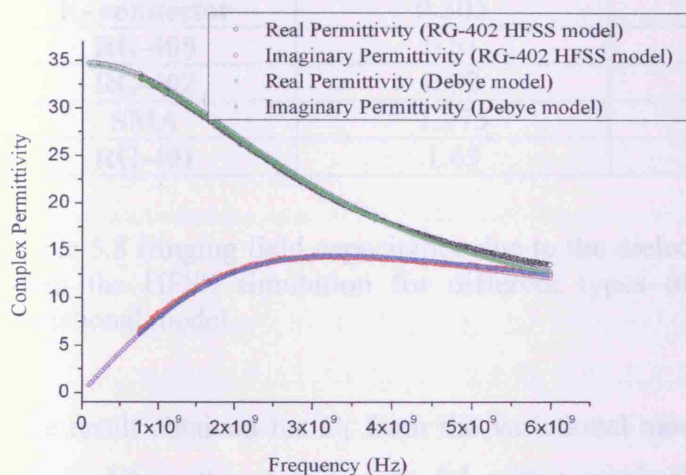


Figure 5.27 The complex permittivity of methanol as a function of frequency.

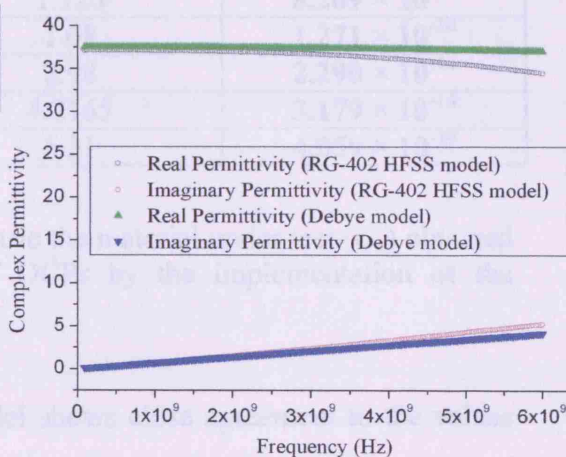


Figure 5.28 The complex permittivity of acetonitrile as a function of frequency.

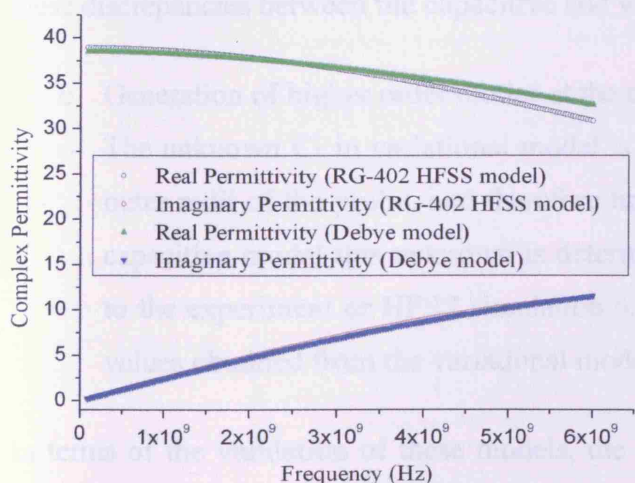


Figure 5.29 The complex permittivity of DMF as a function of frequency.

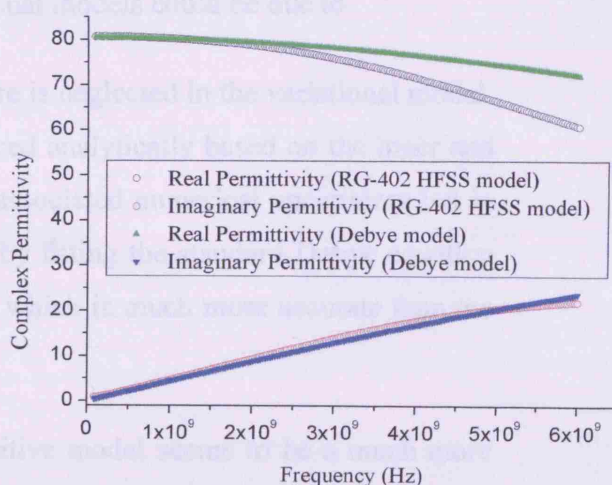


Figure 5.30 The complex permittivity of water as a function of frequency.

Figs. 5.23 to 5.30 show excellent agreement of complex permittivity between the simulated and the standard Debye results for those test materials. This shows the robustness and the accuracy of the HFSS model for a range of liquids. The cause for the discrepancies between the HFSS model with reference to the standard Debye model of complex permittivity as shown in tables 5.6 and 5.7 are the same as for the K-connector OCP mention above.

The fringing field capacitances due to the material under test (C_1) were extracted from the first order approximation of aperture admittance using the variational model (see appendix M) for the different types of OCPs are listed below in table 5.8.

OCPs	d (mm)	D (mm)	Variational model (C_1) F
K- connector	0.305	1.726	8.269×10^{-15}
RG-405	0.51	1.68	1.271×10^{-14}
RG-402	0.92	2.98	2.290×10^{-14}
SMA	1.275	4.2165	3.179×10^{-14}
RG-401	1.63	5.31	4.059×10^{-14}

Table 5.8 fringing field capacitance due to the dielectric the material under test (C_1) obtained from the HFSS simulation for different types of OCPs by the implementation of the variational model.

The result obtained for C_1 from the variational model shows close agreement to the values obtained from the capacitive model, with a maximal discrepancy of 15% for all the types of OCPs except the K-connector OCPs, where it is over estimated by about 30%. The cause for these discrepancies between the capacitive and variational models could be due to

- Generation of higher order modes at the aperture is neglected in the variational model.
- The unknown C_1 in variational model is deduced analytically based on the inner and outer radii of the probe, and therefore has an associated numerical uncertainty but in capacitive model this unknown is determined by fitting the standard Debye equation to the experiment or HFSS simulation results, which is much more accurate than the values obtained from the variational model.

In terms of the validation of these models, the capacitive model seems to be a much more robust and reliable admittance model for the characterisation of unknown materials.

5.8. Modelling and Boundary Conditions of Sapphire Dielectric Resonator

5.8.1 Construction of Sapphire Dielectric Resonator

Using a material for specific application necessitates a good knowledge of the properties of the material. Electromagnetic materials can be identified by their complex permittivities and permeabilities. The sapphire dielectric resonator (SDR) simulated in this chapter was assumed to have a sapphire dielectric puck of the relative permittivity (ϵ_r) of 9.4, loss tangent of 1.4×10^{-5} . A typical simplified cross section of sapphire dielectric resonator is shown in fig. 5.31. Dielectric resonators allow a substantial size reduction in overall dimensions for a given frequency, when compared to cavity resonators. As shown in fig. 5.31, an anisotropic sapphire single crystal, with a diameter of 9 mm and height of 5.7 mm, with its c-axis parallel to the cylinder axis, was sandwiched at the bottom of the copper housing. The inner diameter and the height of the housing were 26 mm and 16 mm, respectively. In reality, a PTFE support (or collar) needs to be introduced within the cavity to hold the sapphire dielectric in place as shown in fig. 5.31 with a diameter of 3 mm, height of 2 mm, dielectric constant (ϵ_r) of 2.06 and loss tangent of 2×10^{-4} . In this chapter, the simulations have been performed in the presence of the PTFE support with the purpose of increasing the accuracy of the model. The copper housing (or cavity wall) was assumed to have conductivity of 5.813×10^7 S/m. Here, the analysis has been performed for a 10.194 GHz SDR. The SDR, which is a resonant system, uses the resonance technique as mentioned in section 3.5, to measure the properties of the sample placed on top and on axis (in the magnetic field region) of the sapphire dielectric puck at microwave frequencies.

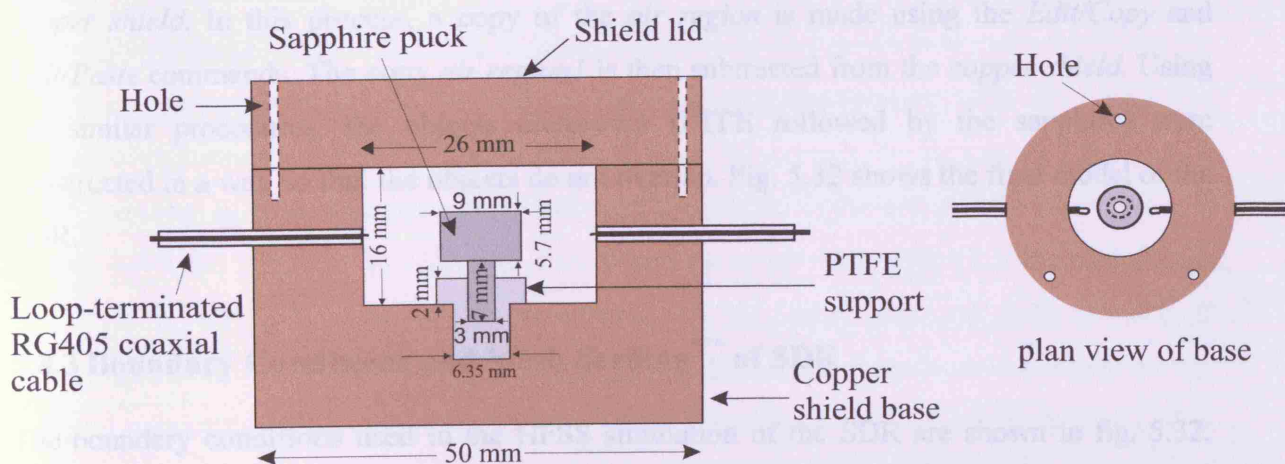


Figure 5.31 Schematic diagram of a sapphire dielectric resonator.

5.8.2 Modelling Methods in HFSS

The SDR shown in fig. 5.31 has been modelled using HFSS, utilising geometry symmetry by adding two electrical boundary walls (perfect E). This enables the modelling of a part of the structure, which reduces the size or the complexity of the design. The Eigenmode solver in HFSS used in this section calculates the natural resonances of the 3D structure using the 3D full-wave analysis and reports the resonant frequency (f_0) and quality factor (Q). The Q-factor reported by HFSS can be calculated from the real and imaginary part of f_0 . A more accurate, reliable and best method to deduce the Q-factor is to calculate from the first principles by using energies and losses obtained from the HFSS post processor, which is been followed through out this research. The elaboration of the deduction of the Q-factor is described in section 5.8.7.

The unit of measurement is chosen to be millimetres (mm) in the 3D modeller. *Global Co-ordinates* are chosen throughout the project and the entire model is centred at the origin. The first object created in the 3D modeller is the copper housing, called the *copper shield* of dimensions of height 30 mm and diameter 50 mm, which is drawn using *Draw/Cylinder* command. Then the air region of the SDR (of height 16 mm and diameter 26 mm) is drawn using *Draw/Cylinder* command and called *air region*. As mentioned in modelling of the K-connector OCP, HFSS does not allow any overlapping volume in the model. Therefore, from the above partly constructed model, it is seen that the *air region* overlaps with the *copper shield*. Hence it is necessary to create a hole in the *copper shield* to accommodate the *air region*. Thus, using the *Modeler/Boolean/ Subtract*, the *air region* is subtracted from the *copper shield*. In this process, a copy of the *air region* is made using the *Edit/Copy* and *Edit/Paste* commands. The copy *air region1* is then subtracted from the *copper shield*. Using the similar procedures, the objects *dielectrics* (PTFE followed by the sapphire) were constructed in a way so that the objects do not overlap. Fig. 5.32 shows the final model of the SDR.

5.8.3 Boundary Conditions and Mesh Seeding^{***} of SDR

The boundary conditions used in the HFSS simulation of the SDR are shown in fig. 5.32. Two symmetric perfect E and finite conductivity boundaries have been used in the

^{***} The technique of guiding HFSS's mesh construction is referred to as "seeding" the mesh.

calculations because the EM fields of the TE_{01} mode are cylindrically symmetrical. The purpose of using the finite conductivity boundary on the copper housing of the SDR is to model the copper housing as a good conductor, with the conductor's thickness is much larger than the skin depth in the given frequency range.

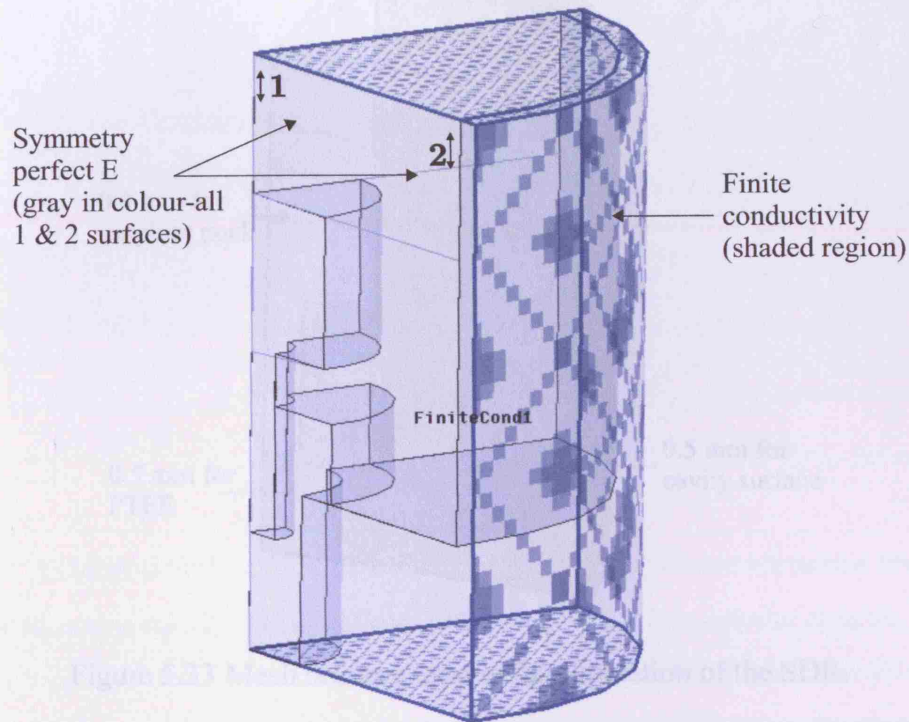


Figure 5.32 Boundary conditions used in the simulation. Finite conductivity boundaries are used for all copper surfaces.

The major challenge of deducing the resonance frequency and the Q-factor of a SDR was the high accuracy requirement. Because of this high accuracy requirement, after the initial test, mesh seeding was applied to the SDR model in order to increase the accuracy of the model. Mesh seeding is a technique of guiding HFSS's mesh construction. As mentioned in section 5.6.6, the initial simulation was started with $\lambda/4$ mesh cells, where λ is the wavelength corresponding to upper limit of frequency (here, 10.194 GHz). Since the SDR is made of several dielectric materials like PTFE and sapphire, the wavelength (λ) is dependent on the material properties and so the size of the individual mesh cell depends on the materials it is filled with. According to this, fig 5.33 shows final seeding strategy applied to the SDR model. Very fine seeding (0.3 mm) has been used for the sapphire puck. Seeding value of 0.5 mm has been used for the PTFE and a slightly bigger seeding value (0.8 mm) has been

used for the air region. As power loss on the surface of the cavity is important for the overall Q-factor calculation, a seeding of 0.5 mm has been used on the cavity surfaces.

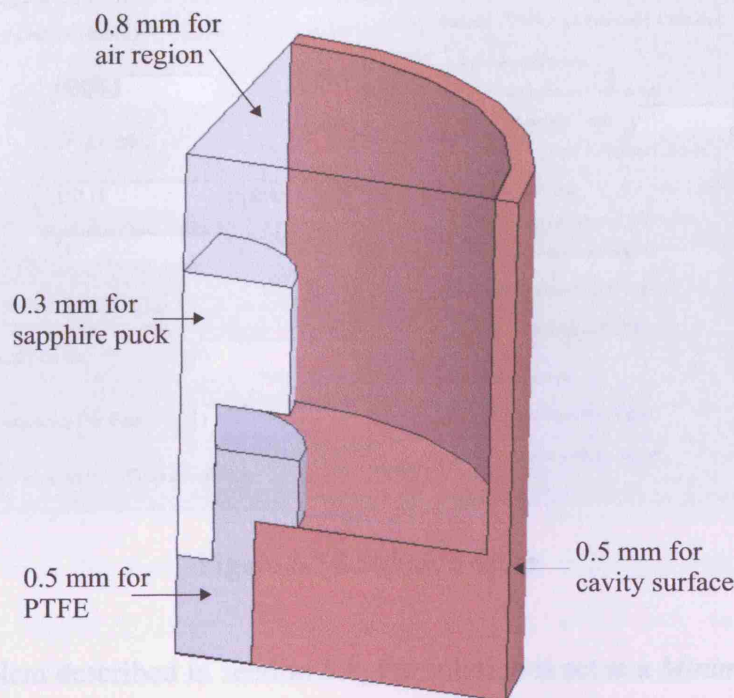


Figure 5.33 Mesh seeding used in the simulation of the SDR.

5.8.4 Assigning Materials

The assignment of the material to each object can be invoked by using the *Modeler/Assign Material* command in the *Executive* command menu. The *air region* is assigned the material *air* with values of relative permittivity and permeability set to be 1. The *copper shield* is assigned the material *copper* with a permittivity of 1 and conductivity 5.813×10^7 S/m. The remaining dielectric materials sapphire and PTFE are assigned with permittivity values of 9.4 and 2.06, and loss tangent of 1.4×10^{-5} and 2×10^{-4} , respectively.

5.8.5 Generating Solution

In order to generate the solution for the SDR structure, it is necessary to specify the solution parameters. Fig. 5.34 shows a snapshot of the features that HFSS provides to generate the solutions for the SDR problem, which is slightly different from the OCP problem because of the different solver that has been used. The solution setup is the last pre-processing step that

needs to be performed before a simulation can be started. The solution setup includes the minimum frequency, number of modes, mesh generation and adaptive option.

Figure 5.34 Solution setup.

For the SDR problem described in section 5.8, the solution is set at a *Minimum Frequency* (or resonance frequency) of 10.19 GHz, *Number of Modes* is set 1, and the number of adaptive passes is set to 6. It is necessary to specify the number of adaptive passes for which the error criterion can be met. The deviation or the error between the resonant frequencies for consecutive adaptive passes, *Max Delta Frequency Per Pass*, is set to 1%. This is necessary to achieve a higher degree of convergence. The mesh refinement percentage, *Max Refinement Per Pass*, is set to 30%. Here, lambda refinement has been chosen, which is a process of refining the initial mesh based on the material-dependent wavelength. For the Eigenmode solution, the *Lambda Target* is set to 0.1, which means that HFSS will refine the mesh until most element lengths are approximately one-tenth of a wavelength. In the executive commands window, *Solve* tab is used to start the simulation. A *Solution Monitoring* window appears which allows the monitoring of the progress of the simulation.

5.8.6 Post Processing

The simulation of this SDR took around 2 hours and 28 minutes on a 3.4 GHz CPU and 2 GB RAM machine and the memory usage was between 300 to 600 MB. Here, Eigenmode has been used as a solver to solve the SDR problem, which calculates the resonance frequency and the Q-factor of the structure and also the fields at that resonant frequency. Unlike the

driven mode solver used for the OCP problem, ports and other sources are restricted for the Eigenmode problem; the Q-factor calculated from Eigenmode does not include losses due to those sources. HFSS provides three post processors for analysing the results of the simulation such as *Fields*, *Eigenmode*, and *Eigen Q*. Fig. 5.35 shows magnetic and electric fields of the TE_{018} mode, respectively, where the H-field and E-field values in HFSS are normalised to 1 A/m and 1 V/m respectively. From fig. 5.35, it can be seen that the magnetic field intensity is solenoidal in nature, while the electric field lines are simply circles concentric with the axis of the cylinder (as expected). So it is apparent that the SDR is operating at the prime mode (TE_{018})^{†††} from the field patterns shown in fig. 5.35. The TE_{018} microwave magnetic field distribution is shown in fig. 5.36 (a), which has a maximum value in the centre of the sapphire puck, where the field is approximately uniform and parallel to the z-axis (see fig. 5.35 (a)) of the SDR, decaying rapidly with distance away from the centre of the sapphire puck. *Eigenmode* provides the resonant frequency of the structure (here, 10.3 GHz). The value f_0 obtained from the simulation was very close to the measured value of 10.194 GHz, with an error of 1.04% [$((f_{theory} - f_{HFSS})/f_{theory}) \times 100$], which has been deduced from Eq. (3.18) in chapter 3. The *Eigen Q* calculates the unloaded Q-factor of the structure; this has been obtained by implementing those equations in the HFSS field calculator described in the following section 5.8.7. The overall unloaded Q-factor (Q_u) of the SDR calculated from the HFSS calculator is 42,891 (see appendix O). The resonant frequency and the Q-factor of the SDR obtained from the HFSS model were compared to the experimental results as shown in table 5.9, where Superfish results have been included for sake of comparison.

The plot of E-field magnitude in fig. 5.36 (b) appears to be as expected because it reaches a peak and then starts decreasing with an unusual rapid drop exactly at top the end of the SDR puck. This is due the meshing limitation of the HFSS software (i.e. the end of the SDR puck is modelled as a sharp corner (due to its symmetry). It is recommended to avoid sharp edges if they are electrically not important; otherwise, if they need to be included then high mesh density must be manually assigned to those edges, which will drastically increase the simulation time and memory usage of the PC). This rapid drop in E-field was not observed in the Superfish simulation, as detailed in section 6.4.3.

^{†††} For more information regarding the TE_{018} refer to section 3.5.1 of chapter 3.

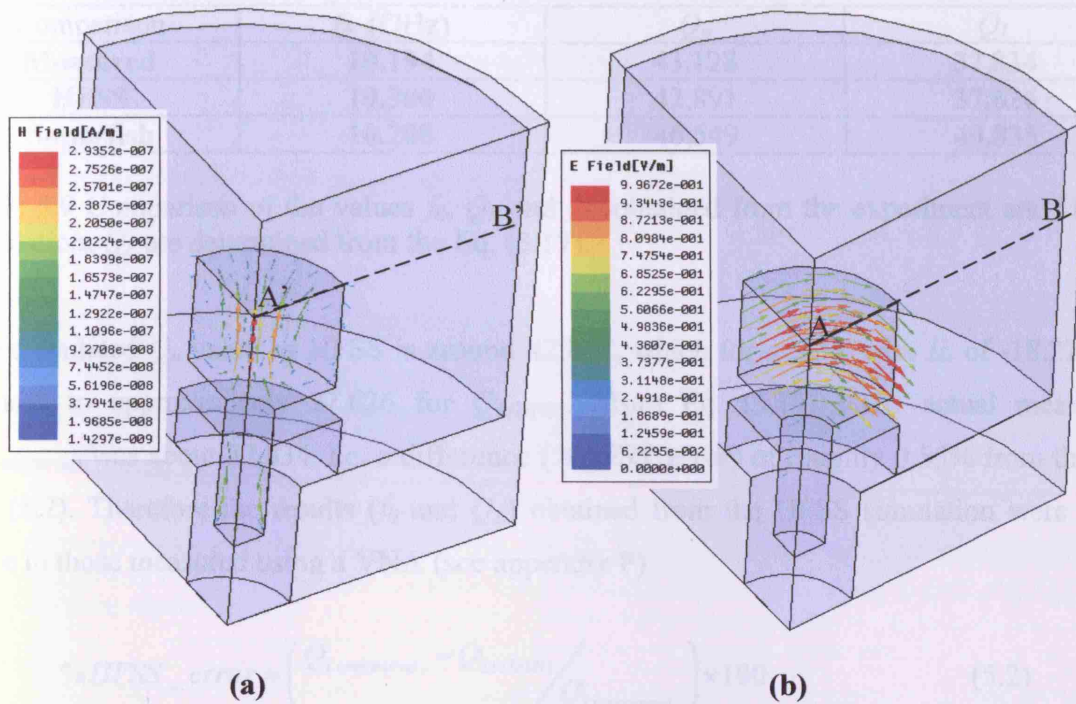


Figure 5.35 Field plots, (a) Vector plot of H-field and (b) E-field within the volume of SDR.

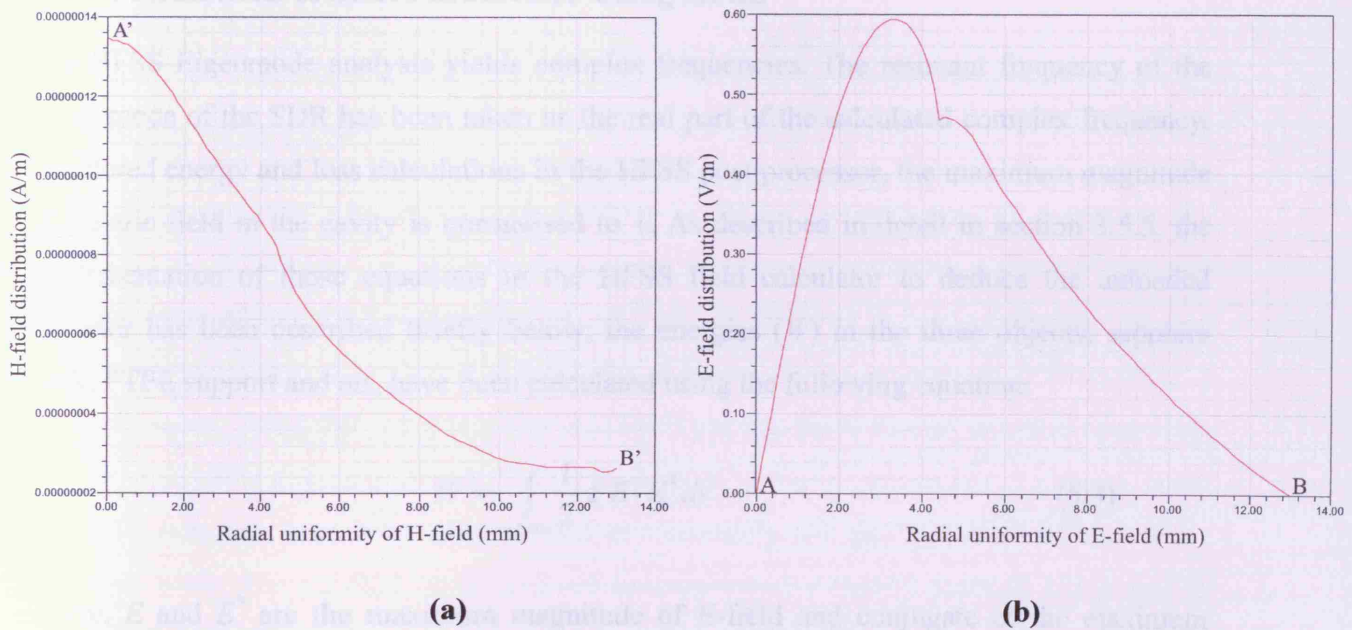


Figure 5.36 Field distribution along the radial axis of the sapphire puck as shown in fig 5.35, (a) H-field distribution, and (b) E-field distribution.

Comparison	f_0 (GHz)	Q_u	Q_L
Measured	10.194	43,128	37,834
HFSS	10.300	42,891	37,626
Superfish	10.208	46,549	40,835

Table 5.9 Comparison of the values f_0 , Q_u and Q_L obtained from the experiment and HFSS simulation. Q_L are determined from the Eq. (3.17).

The calculated Q_u value by HFSS is around 42,891, which for a SDR with IL of -18.22 dB, reduces to approximately 37,626 for $Q_{L(HFSS)}$ (from Eq. (3.17)). The actual measured $Q_{L(measured)}$ was about 37,834, i.e. a difference ($\%HFSS_error$) of roughly 0.55% from that of Eq. (5.2). Therefore the results (f_0 and Q_L) obtained from the HFSS simulation were very close to those measured using a VNA (see appendix P).

$$\%HFSS_error = \left(\frac{Q_{L(measured)} - Q_{L(HFSS)}}{Q_{L(measured)}} \right) \times 100 \quad (5.2)$$

5.8.7 Calculations of SDR Parameters Using HFSS

The HFSS Eigenmode analysis yields complex frequencies. The resonant frequency of the TE_{018} mode of the SDR has been taken as the real part of the calculated complex frequency. For stored energy and loss calculations in the HFSS post processor, the maximum magnitude of electric field in the cavity is normalised to 1. As described in detail in section 3.5.5, the implementation of those equations in the HFSS field calculator to deduce the unloaded Q-factor has been described briefly below; the energies (W) in the three objects; sapphire puck, PTFE support and air, have been calculated using the following equation:

$$W = \int_{volume} \frac{1}{2} \epsilon E \cdot E^* dv \quad (5.3)$$

where, E and E^* are the maximum magnitude of E-field and conjugate of the maximum magnitude of E-field respectively, and ϵ is the complex permittivity of those three objects mentioned above.

There are three power loss terms involved in the analysis of the SDR, namely: dielectric losses in sapphire puck and PTFE support, and cavity wall loss of the copper housing. Power loss ($P_{dielectric}$) in the dielectrics has been calculated using

$$P_{dielectric} = \int_{volume} \frac{1}{2} \omega \epsilon_0 \epsilon_r \tan \delta E \cdot E^* dv \quad (5.4)$$

where ω is the angular frequency (rad/sec) and ϵ_0 is the permittivity of free space. ϵ_r and $\tan \delta$ are the real permittivity and the loss tangent of the dielectric material, respectively.

The cavity copper loss ($P_{surface}$), has been calculated using the following equation

$$P_{surface} = \int_{surface} \frac{1}{2} E \cdot J^* ds \quad (5.5)$$

where J is the surface current density (A/m). The unloaded Q-factor has been calculated from the following equation:

$$Q_{unloaded} = \omega W / P_{loss} \quad (5.6)$$

where, W and P_{loss} are the total energy stored and the total power loss in the SDR, respectively.

5.8.8 HFSS Field Calculator

Most of the standard post processing features of HFSS are sufficient to determine the S-parameters, admittance or impedance matrix, resonant frequencies, quality factor and animated field plots, which cover most of what one needs from such a simulation tool. For those few cases where these are not sufficient, the post processor within HFSS includes a field calculator. Using this calculator (see fig. 5.37) one can perform mathematical operations on any of the field quantities within the solution space to derive specialised quantities. Here, the field calculator has been used to deduce accurately the quality factor of the above modelled SDR. The detailed steps involved in implementing those equations mentioned in section 5.8.7 into this field calculator can be found in appendix O.

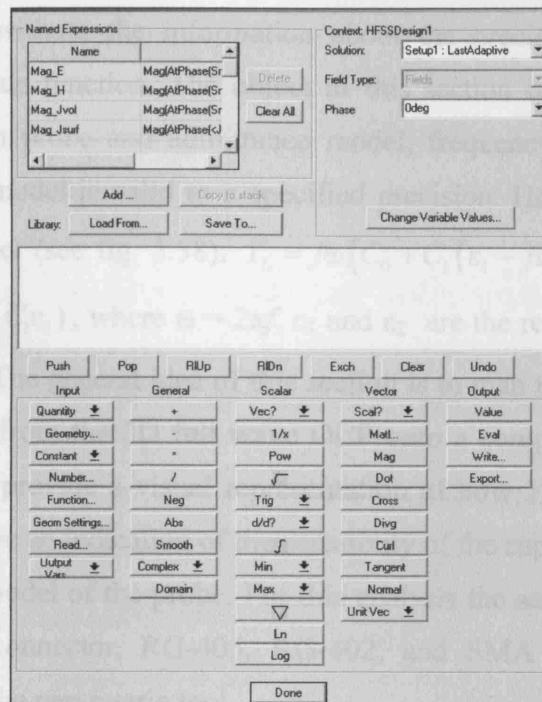


Figure 5.37 Field calculator interface

5.9 Parametric Analysis

Optimetrics is a powerful tool in HFSS that speeds up the design process and enables the user to study the effects of geometry and materials on a design by creating parameters for the dimensions and material constants of the model to be analysed. Any number of design parameters may be varied in a single nominal project design. For instance, geometric shapes, material properties, boundary conditions and source excitations are independent parameters; S-parameters, Eigen data or other HFSS computed quantities are dependent parameters. Here, further validations of the capacitive model on different types of OCPs were carried out with the aid of the Optimetrics tool. This tool is also used for the SDR for characterisation of materials with variable conductivity and film thickness to validate the results obtained in chapter 6.

5.9.1 Limitation of the Coaxial Probe System

Surprisingly, from a theoretical point of view, the range validity of the probe's use has not been systematically explored. It is recognised that a given probe will certainly not be suitable for permittivity measurements at high frequency, but it is not precisely clear what 'high' means, e.g. it could be 6 GHz, 1 GHz or 100 MHz. The precision of the values of ϵ_1 and ϵ_2

cannot be estimated without the information about the precision of the model itself to represent the admittance function. The object of this section is to propose a procedure to determine, for a given probe and admittance model, frequency and complex permittivity ranges for which the model is valid to a specified precision. Here, we consider the case of lumped capacitor model (see fig. 5.38): $Y_L = j\omega(C_0 + C_1(\epsilon_1 - j\epsilon_2))$, then $\text{Re}(Y_L) = 2\pi f C_1 \epsilon_2$ and $\text{Im}(Y_L) = 2\pi f(C_0 + C_1 \epsilon_1)$, where $\omega = 2\pi f$, ϵ_1 and ϵ_2 are the real and imaginary part of the complex permittivity. The general idea of this section is to map the complex admittance (Y_L) of the probe obtained from the 3D full wave OCP onto a complex permittivity (ϵ_1 and ϵ_2) plane. Such mappings provide a visual representation of how Y_L varies with ϵ_1 and ϵ_2 at a fixed frequency and give an indication of the sensitivity of the capacitances (i.e. C_0 and C_1) of the lumped capacitor model of the probe. For this analysis the same developed 3D full wave OCP models (i.e. K-connector, RG-405, RG-402, and SMA square flange) have been considered along with the parametric tool.

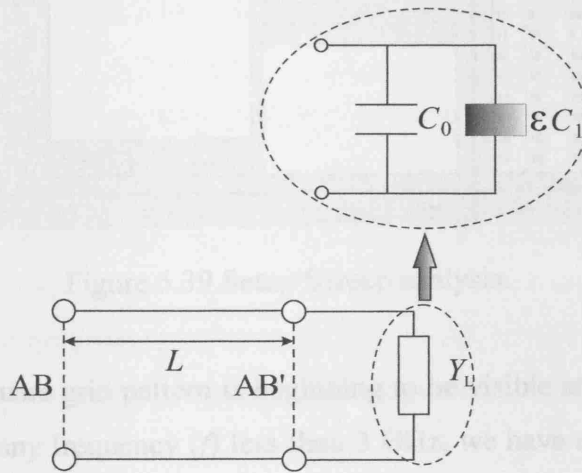


Figure 5.38 Equivalent circuit (i.e. capacitive model) of the OCP.

As an illustration of the procedure, consider the same 3D full wave K-connector OCP developed in subsections of 5.6. Before getting into the post processing step, this time the user specifies the range and the number of steps for parameters in the parametric setup as shown in fig. 5.39. Here, the complex permittivity is chosen to be the varying parameter ranging from $5 \leq \epsilon_1 \leq 100$ and $5 \leq \epsilon_2 \leq 100$. For the different values of frequency (i.e. at 0.5 GHz, 1 GHz, 2 GHz, 3 GHz and 4 GHz) the model generated sets of complex admittance (Y_L) as function of ϵ_1 and ϵ_2 . Simulation of this OCP took around 23 hours on a 3.4 GHz CPU and 2 GB RAM machine and the memory usage was around 1700 MB. Finally, the generated

complex admittance (Y_L) for the K-connector OCP was mapped onto a complex permittivity (ϵ_1 and ϵ_2) plane as shown in fig. 5.40. The vertical and horizontal lines correspond to constant values of imaginary and real parts of the complex admittance (i.e. $\text{Im}(Y_L)$ and $\text{Re}(Y_L)$), respectively. The non-uniformity of the vertical and horizontal lines seen in fig. 5.40 is due to the limitation of the mesh during the simulation process. This issue could be resolved by (i) refinement of the mesh size, which would eventually increase the simulation time enormously or, mostly, the simulation hangs up; (ii) rather considering the whole frequency range (i.e. 0.5 GHz to 4 GHz) at once, simulate the OCP model for individual frequencies.

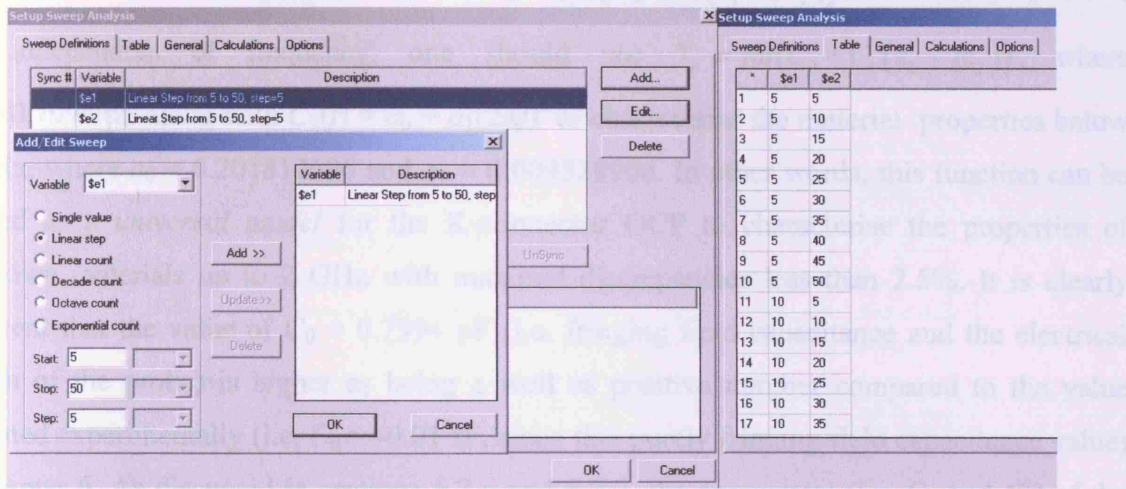


Figure 5.39 Setup Sweep analysis.

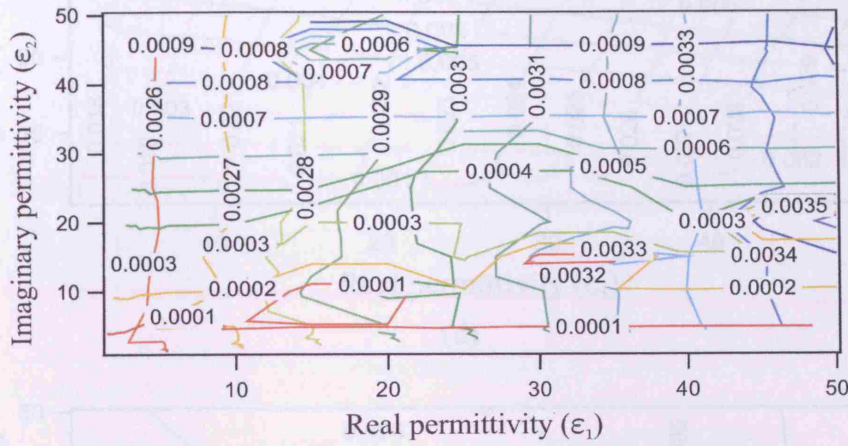
The departure from a square grid pattern is beginning to be visible at 2 GHz and it is closely manifest at 3 GHz. For any frequency (f) less than 3 GHz, we have an approximately square grid characterised by $C_0(f)$ and $C_1(f)$. To check whether C_0 and C_1 vary with frequency for whole range of complex permittivity, the calculations have been carried out on the square grids of the contour plot (i.e. fig. 5.40) for $f = 0.5, 1$, and 2 GHz. The results are shown in table 5.10. It is apparent from the results that C_0 is practically constant compared to C_1 , whereas C_1 varies by a factor of ~ 1.3 over the given frequency range of 0.5 to 2 GHz for the complex permittivity ranging from $5 \leq \epsilon_1 \leq 100$ and $5 \leq \epsilon_2 \leq 100$. The variation of C_1 can be closely represented by a quadratic function of f : $C_1(f) = a_0 + a_1(2\pi f)^2$, with $a_0 = 6.201812696$ and $a_1 = 0.009528906$, where f and C_1 are in GHz and fF, respectively, as shown in fig. 5.41. The frequency independent term of $C_1(f)$ is 6.201812696 fF which is very close to the value found in chapter 6 experimentally (i.e. 6.07 fF) within the experimental error of 2.2%. The

accuracy of this function (i.e. $C_1(f)$) can be further improved by carrying out simulation on the K-connector OCP from 0.1 GHz to 2 GHz with an interval of 0.1 GHz. This will eventually form perfect square grids characterised by $C_0(f)$ and $C_1(f)$ (i.e. from table 5.10, it is apparent that variation of C_1 is very small from 0.5 GHz to 1 GHz, but there is a drastic increment at 2 GHz due to the distortion of square grid (see fig. 5.40)).

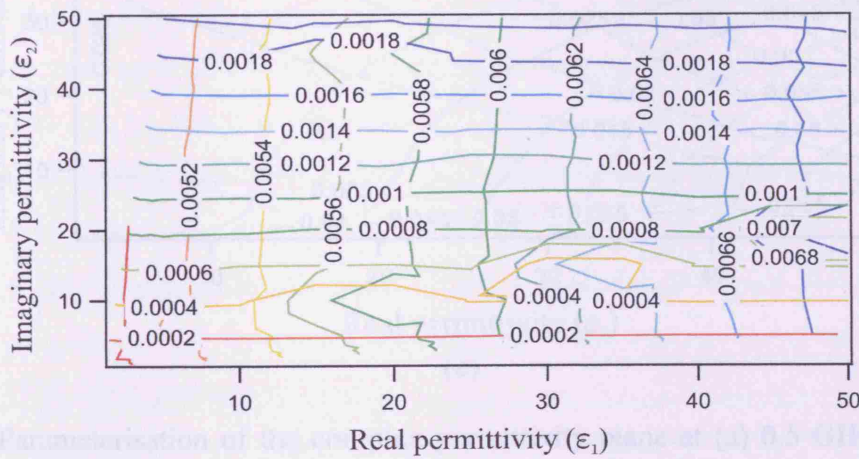
The variations of the parameters (i.e. C_0 and C_1) of the capacitive model have been revealed from the simulation of the K-connector OCP and have justified clearly that C_0 is independent of frequency whereas $C_1(f)$ is a function of frequency and needs to be taken into account. This means that instead of using the model $Y_L = j\omega(C_0 + C_1(\epsilon_1 - j\epsilon_2))$, where both C_0 and C_1 are independent of frequency, one should use $Y_L = j\omega(C_0 + C_1(\epsilon_1 - j\epsilon_2))$, where $C_0 = 0.7994$ pF along with $C_1(f) = a_0 + a_1(2\pi f)^2$ to characterise the material properties below 3 GHz, where $a_0 = 6.201812696$ and $a_1 = 0.009528906$. In other words, this function can be treated as a *universal model* for the K-connector OCP to characterise the properties of unknown materials up to 2 GHz with maximal discrepancies less than 2.5%. It is clearly apparent that the value of $C_0 = 0.7994$ pF (i.e. fringing field capacitance and the electrical length of the probe) is higher as being a well as positive number compared to the value obtained experimentally (i.e. $C_0 = -0.01$ fF, since this purely fringing field capacitance value) in chapter 6. As discussed in sections 6.2.6 and 6.2.7, the parameters (i.e. C_0 and C_1) of the capacitive models have been determined by removing the electrical length and associated losses of the probe by carrying out measurement (or simulation) with and without the sample followed by a division, therefore the value C_0 will be purely due to the fringing field of the probe and is therefore negative.

This way of calibrating the probe is very essential in experiments since the probe used in experiments is not a perfect transmission line, and so one has to remove the associated uncertainties caused by the loss and phase correction. In the case of simulation, however, the probe is considered to be perfect transmission line, so there is no associated losses due to the line, apart from the electrical length of the probe which is unavoidable. Unlike in chapter 6 or the previous sections of this chapter, the complex admittance (Y_L) found in this section folds in the electrical length of the probe, so the value of C_0 is not purely the fringing field capacitance; therefore it would be large and positive and tend to dominate the value of C_1 (i.e. capacitance due to the material under test). It would not be reasonable, therefore, to compare the result of C_0 directly from chapter 6 to the value obtained from this section (i.e. from the

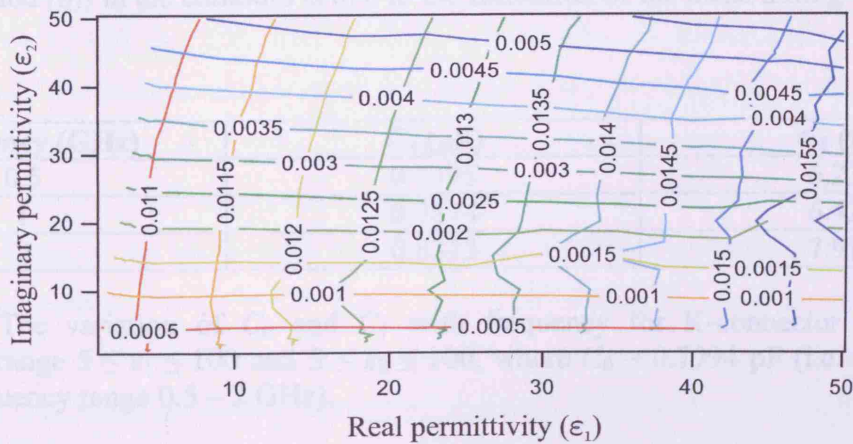
nomograms). The universal model developed in this section can be considered to be another way of extracting the properties of unknown materials without removing the electrical length of the probe.



(a)



(b)



(c)

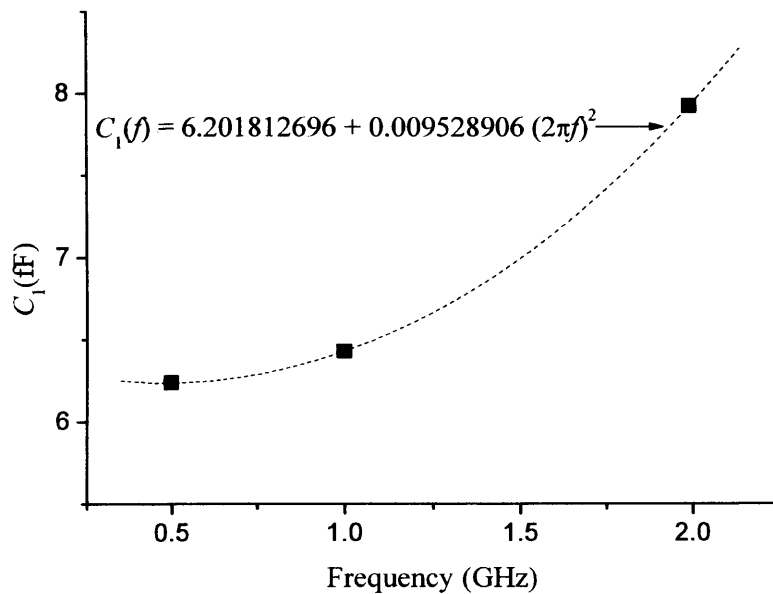


Figure 5.41 Variation of C_1 as a function of frequency.

Similarly, simulations have been carried out on the other probes modelled using RG-405 and RG-402 cables, and an SMA square flange; the nomograms and the limitation of the individual probes can be found in appendix Q. The parameterisation obtained at different frequencies for different probes revealed that the sensitivity of the parameters (i.e. C_0 and C_1) of the capacitive model of the coaxial probes depends on (i) frequency, (ii) complex permittivity of the sample under test and (iii) the size of the probe (or dimensions of the probe). Generally the coaxial probes are used at frequencies below the cut-off frequency, so that only the TEM mode propagates.

The nomograms in appendix Q as well as fig. 5.40 shows a mapping of complex admittance onto the complex permittivity (ϵ_1 and ϵ_2) plane, which provide a visual representation of how Y_L varies with ϵ_1 and ϵ_2 at a fixed frequency and give an indication of measurement sensitivity and the limitation of the capacitive model. They are a useful aid for choosing the most appropriate size of the probe for a particular measurement. A glance through the nomograms obtained from the simulations for different sizes of probes suggest that the optimum diameter of the probe falls with increasing measurement frequency and range of complex permittivity (i.e. $5 \leq \epsilon_1 \leq 100$ and $5 \leq \epsilon_2 \leq 100$), where the departure of a square grid of the nomograms is beginning to be visible at lower frequency as the size of the probe increases. An individual probe is governed by a universal function up to a certain frequency limit, beyond which the accuracy of the governing function of the model fails. This issue

could be resolved by using the pre-developed grids of individual probes, such as fig. 5.40 or Q1, Q3, or Q5 (appendix Q), to read directly the complex admittance (i.e. $\text{Re}(Y_L)$ and $\text{Im}(Y_L)$) from the measured complex permittivity (i.e. ϵ_1 and ϵ_2) at any given frequency from which the unknown parameters (i.e. C_0 and C_1) of the capacitive model could be calculated; this enables us to determine the properties of a material accurately at any desired frequency. The values of C_0 obtained from this section cannot be directly compared to the values achieved in the section 5.7.1 (see table 5.6) since C_0 folds in the electrical length of the probes, but the universal models developed in this section are considered to be another way of extracting the properties of the materials using different probes.

5.9.2 Penetration Depth of the Coaxial Probe System

Materials which do not contain magnetic components respond only to the electric field. The penetration depth, d is a measure of how deep the electromagnetic (EM) waves can penetrate into the material. It is defined as the depth into a sample where the electromagnetic wave has decayed to $1/e$ ($1/e \approx 36.8\%$) of its transmitted value. When an EM wave is incident on the surface of the material, part of it is reflected and part is transmitted into the material. This EM wave interacts with the atoms and electrons of inside the materials. Depending on their nature of the material, the EM wave might travel far into the material or may die out very quickly. For a given material, penetration depth can vary for different wavelengths (or frequencies) of EM wave, and usually is not a fixed constant. The penetration depth is a function of real and imaginary permittivity (i.e. ϵ_1 and ϵ_2 , respectively). If the $\tan \delta = \epsilon_2 / \epsilon_1$ is smaller than about 0.5, the following formula gives 97-100% of the correct value [12]:

$$d = \frac{\lambda_0 \sqrt{\epsilon_1}}{2\pi\epsilon_2} \rightarrow \frac{\lambda_0}{2\pi\sqrt{\epsilon_1} \tan \delta} \quad (5.7)$$

where λ_0 is the free space microwave wavelength (for 6 GHz, $\lambda_0 = 50$ mm ($\lambda_0 = c/f_0$)) and $\tan \delta$ is the loss tangent (or dissipation factor) of the material under test.

In order to understand the close relationship between the penetration depth (d) of the probe due to the presence of different types of materials, we consider the same full wave K-connector OCP model developed in the subsections of 5.6. The following graph shows magnitude of E-field as a function of longitudinal distance from the OCP-sample interface at a frequency of 6 GHz. It is apparent from the graph that the penetration depth (d) of E-field

decays exponentially as the loss (or $\tan\delta$) of the material increases. This is exactly similar to what is predicted in Eq. (5.7). Therefore, in our case we would expect to see less penetration depth (d) for water (since it is highly polar or lossy) compared to other material as shown in fig. 5.42.

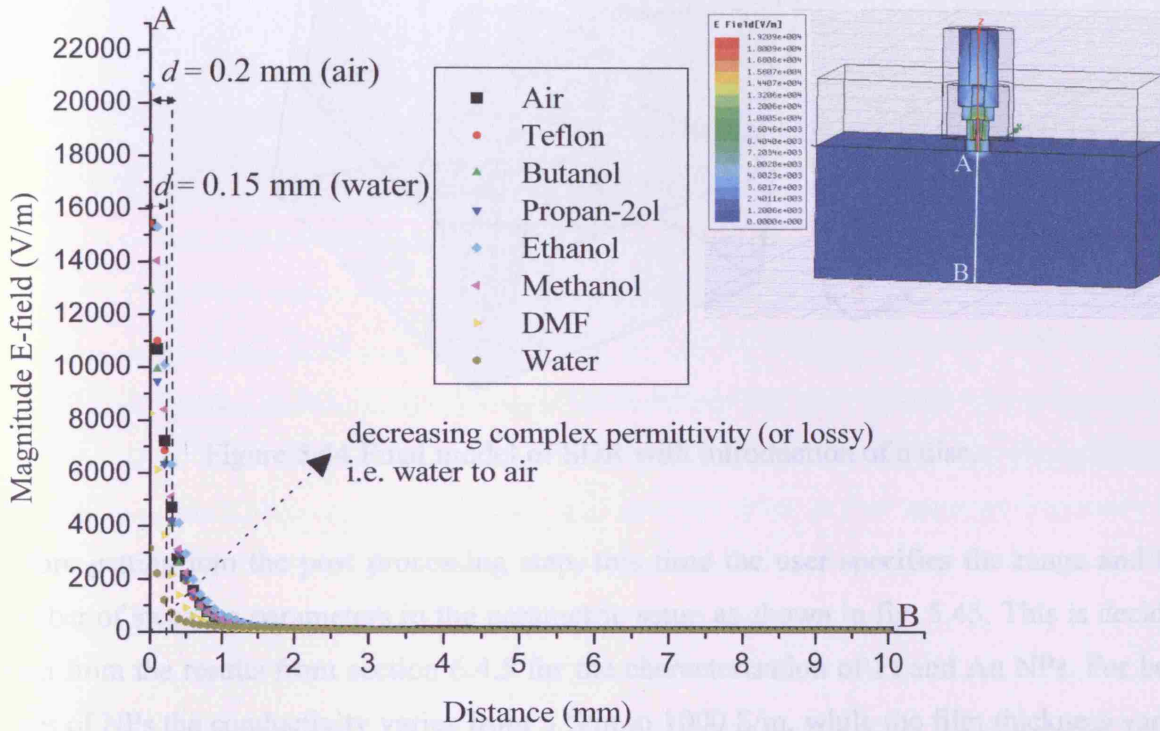


Figure 5.42 The magnitude of E-field as a function of longitudinal distance (A-B) from the OCP-sample interface at 6 GHz.

5.9.3 SDR System

In order to have a broad understanding of the results obtained for the characterisation of Pt and Au NPs of different sizes and film thickness from section 6.4.5, here we have used parametric analysis. To understand the close relationship between the conductivity (σ) and the film thickness (t), we consider the same full wave HFSS SDR model developed in the sections from 5.8.1 to 5.8.5 with an additional introduction of a disc on the top of the sapphire puck, in the region where the magnetic field is maximum as shown in fig. 5.44.

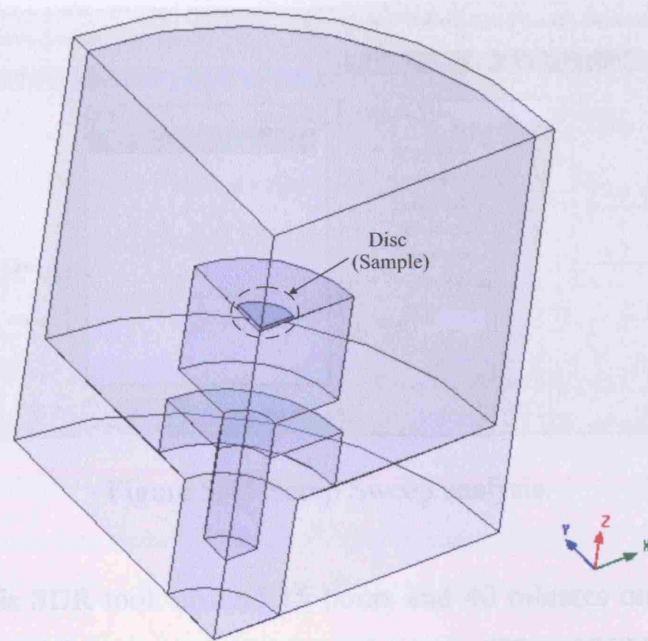


Figure 5.44 Final model of SDR with introduction of a disc.

Before getting into the post processing step, this time the user specifies the range and the number of steps for parameters in the parametric setup as shown in fig. 5.45. This is decided upon from the results from section 6.4.5 for the characterisation of Pt and Au NPs. For both types of NPs the conductivity varies from 5 S/m to 1000 S/m, while the film thickness varies from 5 μm to 25 μm , therefore the user introduces two variables; one is the conductivity, which varies as 10, 100, and 1000 S/m, and the other is thickness varying from 0.02 mm to 1 mm with a step of 0.02 mm (5 μm and 10 μm are not included because of the limitation of the HFSS software – i.e. for conductors at high frequency, since the tiny skin depth would lead to tiny mesh cells and considerably increase the simulation time enormously or, mostly, the simulation hangs up) as shown in fig. 5.45.

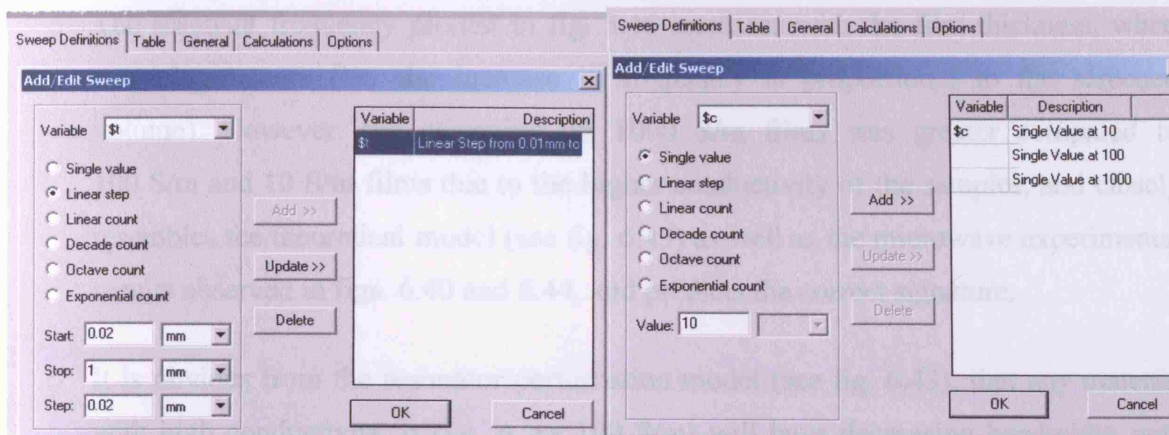


Figure 5.45 Setup Sweep analysis.

The simulation of this SDR took around 15 hours and 40 minutes on a 3.4 GHz CPU and 2 GB RAM machine and the memory usage was between 800 to 1550 MB. Here, Eigenmode has been used as a solver to solve the SDR problem, which calculates the resonance frequency and the Q-factor of the structure and also the fields at that resonant frequency for the corresponding conductivity values and film thickness. Figs. 5.46 and 5.47 show variation of f_0 and Q-factor as a function of film thickness, respectively.

5.9.4 Analysis of Results

Characterisations of different thicknesses of metal disc of range of conductivities (i.e. 10, 100 and 1000 S/m, which closely resemble the conductivity of Pt oxide and Au films) conducted in the SDR brings forth the following points:

- As shown in fig. 5.46, for a metal disc increasing conductivity results in increasing resonant frequency since the thickness of the film is much smaller than the microwave skin depth (about $\sim 500 \mu\text{m}$ at 10.3 GHz for a conductivity of 100 S/m) and so screens the H-field very effectively. It is this effective reduction in cavity volume that gives the frequency increase, only seen in metals, and a characteristic of high conductivity. Associated with this are eddy current losses that broaden the bandwidth greatly, leading to rapid decrease in Q-factor as observable in fig. 5.47 (i.e. where Q-factor is inversely proportional to the bandwidth). These simulation results closely resemble the microwave experimental results for the Pt oxide NP films observed in figs. 6.40 and 6.41, respectively, and predict the correct signature.

- The resonant frequency plotted in fig. 5.46 increases with the film thickness, when screening occurs (i.e. the increase in frequency is proportional to the screened volume). However, the screening on 1000 S/m films was greater compared to 100 S/m and 10 S/m films due to the higher conductivity of the samples, and closely resembles the theoretical model (see fig. 6.43) as well as the microwave experimental results observed in figs. 6.40 and 6.44, and predicts the correct signature.
- It is obvious from the resonator perturbation model (see fig. 6.43), that any material with high conductivity, σ (i.e. $\sigma \gg 100$ S/m) will have decreasing bandwidth with increasing conductivity (or film thickness), due to the very high screening current. A very similar trend has been observed from the simulation for 1000 S/m films as shown in fig. 5.48, where the quality factor of the resonator increases monotonically due to the presence of the high conductivity films with the increasing film thickness. This result resembles and predicts the correct signature of Au NP films observed in fig. 6.45.

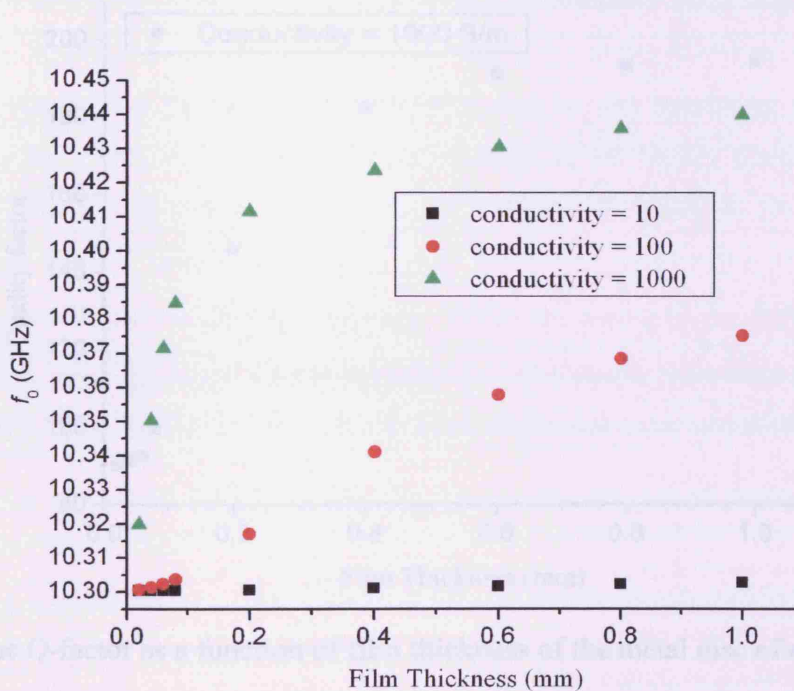


Figure 5.46 The resonant frequency (f_0) as a function of film thickness.

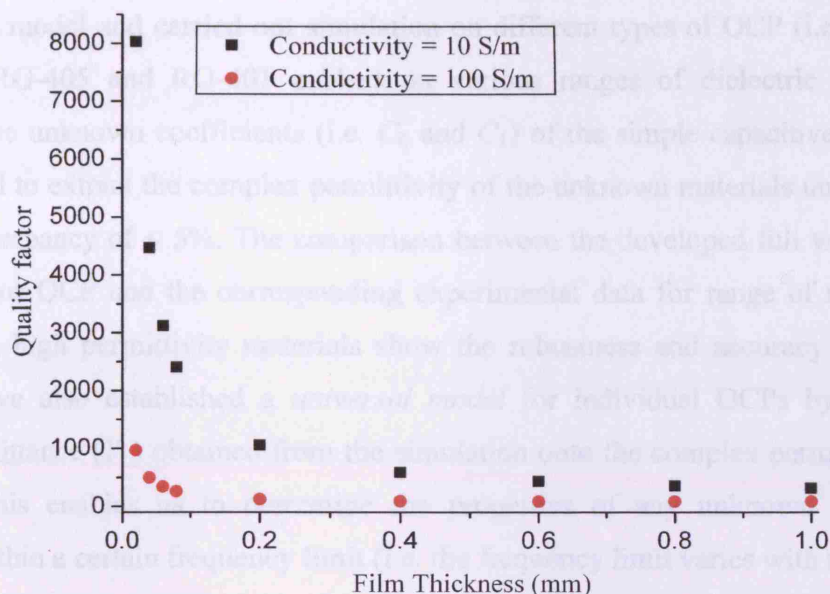


Figure 5.47 The Q-factor as a function of film thickness of the metal disc of varying conductivity (i.e. $\sigma = 10$ S/m and 100 S/m).

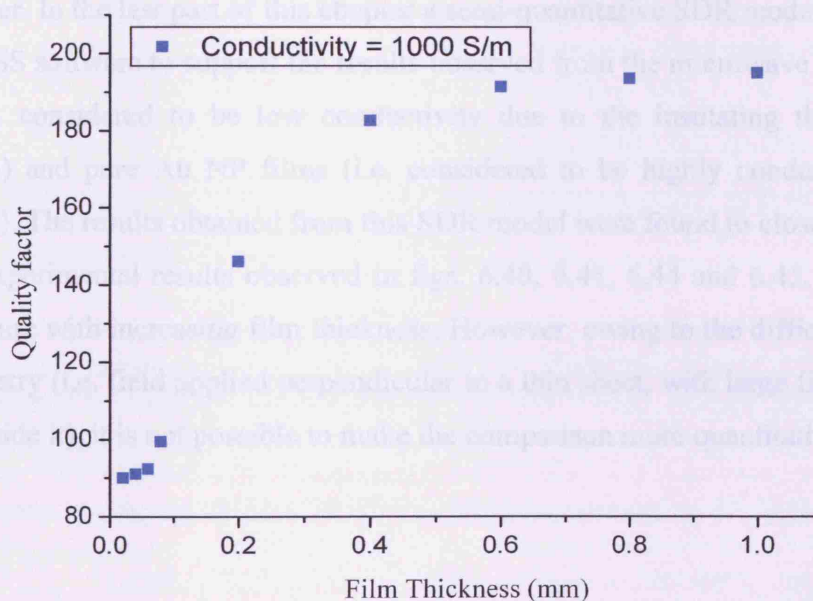


Figure 5.48 The Q-factor as a function of film thickness of the metal disc of $\sigma = 1000$ S/m.

5.10 Chapter Summary

The OCP is frequently used to characterise the dielectric properties of materials via reflection measurements. The deduction of the permittivity of the materials from the reflection data is made by assuming that the admittance of the probe/material interface is described by some simple empirical model. Such models are not universally valid. Here, we have developed a

full wave 3D model and carried out simulation on different types of OCP (i.e. K and SMA connectors, RG-405 and RG-401 cables) on various ranges of dielectric materials and established the unknown coefficients (i.e. C_0 and C_1) of the simple capacitive model which has been used to extract the complex permittivity of the unknown materials under test with a maximal discrepancy of $< 5\%$. The comparison between the developed full wave 3D model of K-connector OCP and the corresponding experimental data for range of materials from low, medium high permittivity materials show the robustness and accuracy of the model. Here, we have also established a *universal model* for individual OCPs by mapping the complex admittance (Y_L) obtained from the simulation onto the complex permittivity (ϵ_1 and ϵ_2) plane. This enables us to determine the properties of any unknown material more accurately within a certain frequency limit (i.e. the frequency limit varies with the dimensions of the probe). The development of a 3D full wave model of a sapphire dielectric resonator (SDR) using the HFSS software was explained in detail. The simulation results obtained for the SDR model from both the HFSS and Superfish software showed a very good agreement with each other. In the last part of this chapter a semi-quantitative SDR model was developed using the HFSS software to support the results observed from the microwave experiments for Pt oxide (i.e. considered to be low conductivity due to the insulating thin oxide layer, $\sigma \leq 100$ S/m) and pure Au NP films (i.e. considered to be highly conductivity samples, $\sigma \geq 1000$ S/m). The results obtained from this SDR model were found to closely resemble the microwave experimental results observed in figs. 6.40, 6.41, 6.44 and 6.45, and predict the correct signature with increasing film thickness. However, owing to the difficulties regarding sample geometry (i.e. field applied perpendicular to a thin sheet, with large field distortion in the space outside it), it is not possible to make the comparison more quantitative.

5.11 References

1. HFSS User Manual, *Ansoft, LLC*, 2008.
2. A. Porch, Private communication, 2007-8.
3. Pasternack Enterprises, “coaxial-cables”, <http://www.pasternack.com/category-COAXIAL-CABLE-36.html>, (accessed on 2nd January 2009).
4. D.M. Pozar, *Microwave Engineering*, 3rd edition, John Wiley & Sons, Inc., 2005, ISBN 0-471-44878-8.
5. J. Lou, A. Hatton, and P.E. Laibinis, “Effective Dielectric Properties of Solvent Mixtures at Microwave Frequencies”. *The Journal of Physical Chemistry A*, Vol. 101, No. 29, pp. 5262-5268, 1997.
6. M.N. Afsar, N. Suwanvisan, and Y. Wang, “Permittivity measurement of low and high loss liquids in the frequency range of 8 to 40 GHz using waveguide transmission line technique”, *Microwave and Optical Technology Letters*, Vol. 48, No. 2, pp. 275-281, 2005.
7. S. Jenkins, T.E. Hodgetts, R.N. Clarke and A.W. Preece, “Dielectric Measurements on Reference Liquids Using Automatic Network Analysers and Calculable Geometries”, *Measurement Science and Technology*, Vol. 1, pp. 691-702, August 1990.
8. W. Ronald Fawcett, *Liquids, Solutions, and Interfaces: From Classical Macroscopic Descriptions to Modern Microscopic Details*, Oxford University Press Inc., pp. 152, 2004, ISBN 0-19509-432-9.
9. M. Wu, X. Yao, and L. Zhang, “An Improved Coaxial Probe Technique for Measuring Microwave Permittivity of Thin Dielectric Materials”. *Measurement Science and Technology*, Vol. 11, No. 11, pp. 1617–1622, August 2000.
10. Anritsu, “High Return Loss Connectors and Cables – K Connectors and Accessories”, <http://www.anritsu.co.uk/files/10200-00018.pdf>, (accessed on 8th January 2008).
11. RADIALL, “DIMENSIONS OF APPLICABLE CABLES”, <http://www.online-ic.com/cat2000/coaxial/serien/95.pdf>, (accessed on 2nd January 2009).
12. P. Risman, “Terminology and Notation of Microwave Power and Electromagnetic Energy”, *Journal of Microwave Power and Electromagnetic Energy*, Vol. 26, No. 4, pp. 243-250, 1991.

CHAPTER 6

MICROWAVE CHARACTERISATION OF METALLIC NANOPARTICLES

6.1 Introduction

One of the pioneering areas of materials research involves technologies based on nanoparticles (NPs). NPs based materials are of interest because of their unique electronic and chemical properties. Measuring the electrical conductivity of such metal NPs represents a challenging and key experiment and necessitates the use of innovative experimental techniques. The direct contact measurement of the current-voltage characteristics of individual particles represents one such approach. Here we highlight an alternative, novel approach, applicable to a wide range of materials for which direct electrical contact is unfeasible: namely, contactless microwave measurements using an open ended coaxial probe (OCP) and sapphire dielectric resonator (SDR) techniques. The electronic conductivity of these NP assemblies is due to electron tunneling and it is dependent on two factors, one is the individual particle sizes and the other is the inter particle separations. There are many reasons of using microwave sensors, which are mentioned in detailed in section 3.3. The miniature open ended coaxial probe has been used in this research, since it is relatively cheap, non-destructive, convenient, broad bandwidth, needs a small measurement area and it is easy to prepare the sample.

In order to be able to use the open ended coaxial probe (OCP), an in-depth study of the aperture fields is necessary. Knowledge of the aperture fields provides information concerning the apparent aperture admittance and electromagnetic field distribution in the half space facing the aperture. The theoretical background of this research can be traced to classic papers by Levin and Papas [1]. Several formulae for determining the aperture admittance of OCPs on the basis of capacitive and variational formulation were presented in [2, 3, 4, 5]. Detailed description of these models can be found in section 3.6. The implementation and validation of aforementioned aperture admittance models has been achieved by carrying out experiments on several different dielectric materials including low, medium and high permittivity materials.

This chapter discusses the implementation and validation of full aperture admittance models (i.e. capacitive and variational models) for the OCP, by carrying out experiments on several different dielectric materials including low, medium and high permittivity materials followed by the in-depth microwave characterisation of Pt and Au NP films using both the K-connector OCP and SDR. Finally, the surface modifications of Pt NPs were carried out by means of hydrogen adsorption using the OCP technique followed by the random network circuit models to resemble the microwave experimental results.

6.2 Validation of the Coaxial Probe Models

6.2.1 Instrumentation

The coaxial probe measurement was performed using a HP8753E vector network analyser (VNA). The VNA was controlled by the PC with IEEE-488 interface bus, also known as General Purpose Interface Bus (GPIB). All data acquisition code was written in using visual basic software for HP8753E. The frequency range used for all these measurements was 30 kHz – 6 GHz with 201 data points. The VNA was switched on and allowed to stabilise for 1 hour prior to use to reduce any effects from internal thermal drift. The thickness and the uniformity of the deposited films (i.e. Pt and Au) were evaluated using a Nikon Measuring Microscope MM-800 (Nikon Corp., Tokyo, Japan) by measuring thicknesses at different places on the films. The morphological structure of the film thickness was further verified with an aid of scanning electron microscope (SEM).

6.2.2 Coaxial Probe Technique

The coaxial probe technique has been established over the last 20 years as a standard tool for evaluating electrical properties in the microwave frequency range [6]. It involves termination of a short length of flanged coaxial transmission line with the material under test, followed by measurement of the reflection coefficient (ρ) at the interface with the material. A schematic diagram of the novel miniaturised coaxial probe used in our studies is shown in fig. 6.1, based on an Anritsu K-connector (here K102F), which has an inherent bandwidth from DC up to 40 GHz. The connector's glass bead provides a convenient coaxial aperture, which can be ground flat, and polished using fine emery paper. For our probe the inner and outer radii are $a = 152.5 \mu\text{m}$ and $b = 800 \mu\text{m}$, respectively, and so $b - a \approx \lambda/35$ at 6 GHz (here λ is the probe wavelength, assuming $\epsilon_r = 4$ for the silica of the glass bead). Hence the aperture

remains electrically small over our full range of measurement frequencies, and our probe has one of the smallest aperture size of any reported in the literature. All measurements are performed using a HP8753E network analyser from 30 kHz to 6 GHz, with the system calibrated to plane AB using factory standards.

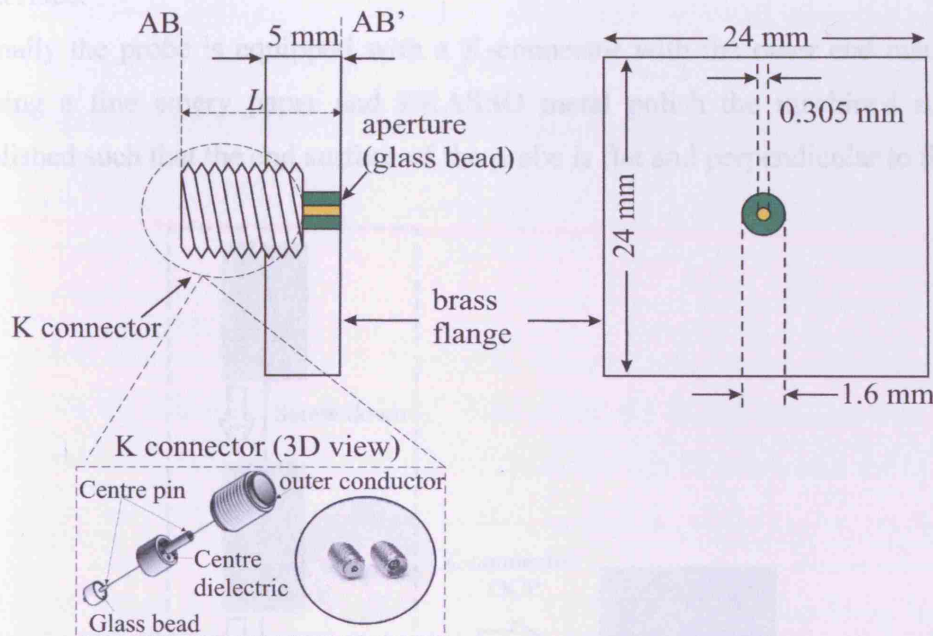


Figure 6.1 Schematic diagram of the K-connector coaxial probe.

6.2.3 Fabrication Process of K-Connector Coaxial Probe

The fabrication process of the K-connector coaxial probe assembly is given below (see fig. 6.2). The K-connector kits (i.e. glass bead, centre conductor, support bead and outer conductor) were purchased from the Anritsu Ltd., and the mounting holes for those kits were machined on brass blocks of dimensions $24 \times 24 \times 5 \text{ mm}^3$ by the mechanical workshop of Cardiff School of Engineering (see appendix R for in-depth dimensions for the hole). The following steps have been carried out in the fabrication process.

- Set the hotplate to 300 °C for SN60 solder.
- Then install the glass bead into the machined brass block.
- Insert a length of solder into the soldering access hole and cut it flush with the top of the hole.
- Place the device on the hotplate and leave it there for approximately 20-30 seconds until the solder melts.

- Leave the device on the hotplate and allow it to cool.
- Once the glass bead is soldered into the brass block, use a holding fixture to hold the brass block, then screw down the remaining parts of the K-connector into the mounting hole opening until the centre conductor protrudes through the backside interface.
- Finally the probe is equipped with a K-connector with the other end machined flat. Using a fine emery paper and BRASSO metal polish the machined surface was polished such that the end surface of the probe is flat and perpendicular to the axis.

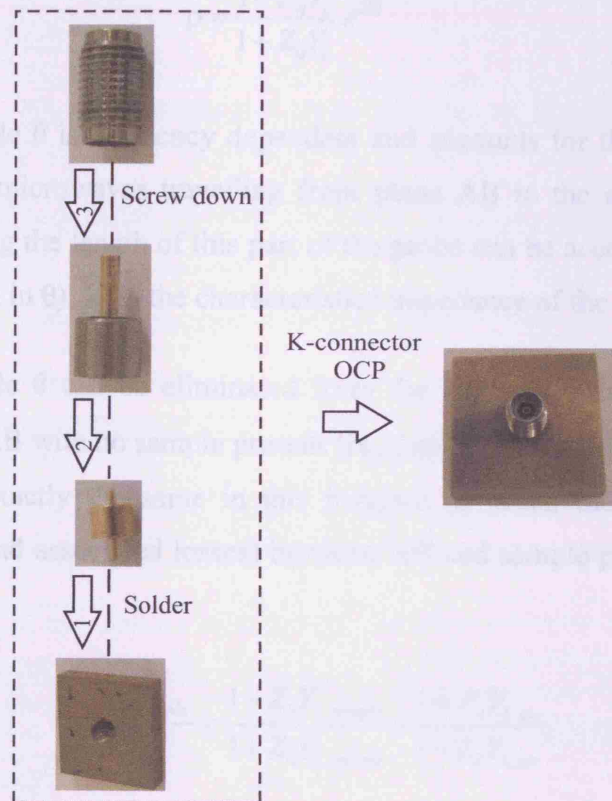


Figure 6.2 Centre conductor and support bead assembly.

As mentioned in section 3.4.3, there are two non-trivial aspects of the coaxial probe technique which need to be addressed before the permittivity of the material can be evaluated; one is that the system has to be carefully calibrated so that any stray reflections and additional path lengths are removed from the analysis routine and the other is an appropriate model for the admittance of the aperture as a function of the permittivity of the terminating material is required. Each of these issues will be discussed in detail in the following sections.

6.2.4 Microwave Calibration Procedure

As shown in fig. 6.1, it is not possible to calibrate the microwave system directly to the aperture plane (AB'). Therefore, we use the open-short-load routine to calibrate the system to the reference plane AB in fig. 6.1 using the factory standards (Agilent, 85052D, 3.5 mm Economy Calibration Kit), and consequently all microwave measurements are performed relative to this plane. In term of the aperture admittance Y_L , the measured reflection coefficient (ρ) at the reference plane (AB) with a sample terminating the probe is

$$\rho = \frac{1 - Z_0 Y_L}{1 + Z_0 Y_L} e^{j\theta} \quad (6.1)$$

where the phase angle θ is frequency dependent and accounts for the additional path length associated with the microwaves travelling from plane AB to the aperture AB' back again (note that losses along the length of this part of the probe can be accounted for by including a small imaginary term in θ); Z_0 is the characteristics impedance of the probe, i.e. 50 Ω .

The term phase angle θ can be eliminated from the analysis by measuring the reflection coefficient at plane AB with no sample present (ρ_{air}), and then with the sample (ρ_{sample}). Since the phase term is exactly the same in this instance as when the sample is present, the electrical length L (and associated losses) between AB and sample plane AB' is removed by calculating

$$\frac{\rho_{sample}}{\rho_{air}} = \frac{1 - Z_0 Y_{L,sample}}{1 + Z_0 Y_{L,sample}} \times \frac{1 + Z_0 Y_{L,air}}{1 - Z_0 Y_{L,air}} \quad (6.2)$$

where $Y_{L,sample}$, $Y_{L,air}$ are the aperture admittance with and without the sample, respectively; ρ_{sample} and ρ_{air} in Eq. (6.2) are then the reflection coefficients at the sample plane AB' with and without the sample, respectively. This calibration procedure is far superior to other procedures described in the literature since it requires no standard material other than air and it does not require subsequent disconnection of the probe. Eq. (6.2) can now be used to extract permittivity values using models that link the aperture admittance to the permittivity of the material terminating the probe.

6.2.5 Modelling the Aperture Admittance of the Probe

There are number of models for calculating the probe aperture admittance as a function of the permittivity of the terminating material. This is a difficult problem owing to the higher order waveguide modes generated at the aperture plane (AB'), a full wave analysis of which makes the inversion process of extracting permittivity almost intractable [7]. This section mainly focuses on the investigation of the two main admittance models (i.e. the capacitive and variational models discussed in sections 3.6.1 and 3.6.2, respectively).

6.2.6 Capacitive Model

The admittance, Y_L , is a relatively complicated function of the frequency (f) and complex permittivity (ϵ) of the substance under test. However, the probe behaves like two simple capacitors in parallel and it has become customary to approximate the function Y_L by the 'lumped capacitor model'. As discussed in section 3.6.1, the equivalent circuit for this model is presented in fig. 6.3. Briefly, the reflection coefficient at the aperture of the coaxial probe is obtained by considering the complex admittance of the equivalent circuit shown, which results in the approximate admittance

$$Y_{L, \text{sample}} = j\omega(C_0 + C_1(\epsilon_1 - j\epsilon_2)) \quad (6.3)$$

where ω ($\omega = 2\pi f$) is the angular frequency (rad/sec) and $\epsilon = \epsilon_1 - j\epsilon_2$ is the complex permittivity of the sample under test. A common assumption is that this model is valid for frequencies less than a few GHz, that C_0 and C_1 do not depend upon ϵ or f , and thus determine the unknowns C_0 , C_1 by measuring the admittances of substances with known permittivity and then use the calibrated probe to measure the permittivity of unknown material.

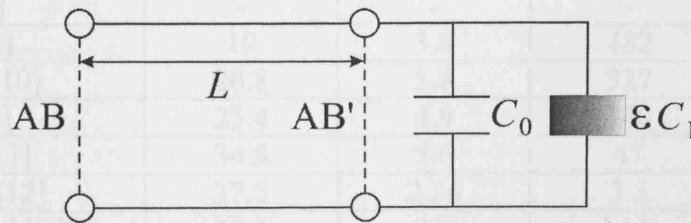


Figure 6.3 Simple lumped circuit model for the aperture together with the sample.

6.2.7 Calibration of the Probe Using Polar Liquids of Known Permittivity

It is now possible to use Eqs. (6.2) and (6.3) to determine the capacitances C_0 and C_1 from measurements of known materials terminating the probe. Experimental measurements are carried out on various reference liquids as test materials, including low, medium and high permittivity materials (see table 6.1). All these solvents were obtained commercially and used as received. These solvents are selected based on differences in their polarity and dipole strength. The results are shown in the table 6.2 below for the whole frequency range between 30 kHz to 6 GHz, extracted by fitting the experimental data to the standard Debye model equations for the complex permittivity ϵ for those test materials using the same developed MathCAD program (see appendix K), which yields $C_0 = -0.01$ fF and $C_1 = 6.07 \pm 0.08$ fF (see table 6.2). Fig. 6.4 shows the measurement configuration. The reflection coefficients of the liquids were obtained using the HP8753E VNA by immersing the probe into those test liquids. The body of the liquids in each case was approximately 100 mm in diameter by 100 mm deep. Experimentally this was found to be sufficient to avoid significant flange or volumetric resonances at these frequency limits. To maintain maximum measurement accuracy after a calibration has been performed, it is important to allow enough time for the cable (that connects the probe and to the VNA) to stabilise before making a measurement and to be sure that the cable is not flexed between the calibration and measurement and also avoid air bubbles (or air gap) between the probe and the material under test. Here, in order to minimize the movement of the probe and cable, both the probe and the cable are fixed in one position while bringing the sample to the setup using a laboratory jack, as shown in fig. 6.4. In order to remove the air bubbles while the measuring liquids, the coaxial probe is positioned so that its flange is at a slight angle from horizontal.

Solvents	ϵ_s Literature	ϵ_∞ Literature	τ (ps) Literature	ϵ_1	ϵ_2
Teflon [8]	-	-	-	2.08	0.0004
Butanol [9]	19	3.8	482	-	-
Propan-2ol [10]	20.8	3.8	327	-	-
Ethanol [9]	25.4	4.9	140	-	-
Methanol [11]	34.5	5.6	47	-	-
Acetonitrile [12]	37.5	2.26	3.2	-	-
Dimethylformamide [9]	38.5	10	14.6	-	-
Water [6]	80.4	5.2	9.4	-	-

Table 6.1 Literature values of the Debye parameters of various liquids at 20-25 °C.

The above table 6.1 shows the Debye parameters obtained from various sources in order to validate the admittance model.

Test Materials	Fringing field capacitance due to the dielectric filling the line C_0 (F)	Fringing field capacitance due to the material under test C_1 (F)	% ME error of real permittivity ϵ_1 (%)	% ME error of Imaginary permittivity ϵ_2 (%)
Teflon	-0.01×10^{-15}	6.10×10^{-15}	1.37	9.87
Butanol	-0.01×10^{-15}	6.01×10^{-15}	2.09	10.08
Propan-2ol	-0.01×10^{-15}	6.01×10^{-15}	4.48	6.68
Ethanol	-0.01×10^{-15}	6.03×10^{-15}	3.46	4.35
Methanol	-0.01×10^{-15}	6.00×10^{-15}	1.65	1.19
Acetonitrile	-0.01×10^{-15}	6.20×10^{-15}	2.11	7.67
Dimethylformamide (DMF)	-0.01×10^{-15}	6.20×10^{-15}	2.75	6.91
Water	-0.01×10^{-15}	6.00×10^{-15}	1.52	11.43
Fringing field capacitances	-0.01×10^{-15}	$6.07 \pm 0.08 \times 10^{-15}$		

Table 6.2 fringing field capacitances due to the dielectric filling the line of the probe (C_0) and material under test (C_1) for different dielectric materials obtained from the experiment.

Now having established the values of C_0 and C_1 of the admittance model, we can now apply Eq. (6.2) to find the complex permittivity ϵ of any material terminating the probe. Performing measurements of the reflection with and without the sample, Eq. (6.2) becomes

$$\frac{\rho_{sample}}{\rho_{air}} = \frac{(1 - j\omega Z_0 (C_0 + C_1 \epsilon))}{(1 + j\omega Z_0 (C_0 + C_1 \epsilon))} \times \frac{(1 + j\omega Z_0 (C_0 + C_1))}{(1 - j\omega Z_0 (C_0 + C_1))} \quad (6.4)$$

The left hand side of Eq. (6.4) is measured experimentally, so that the equation is easily inverted to find the permittivity of the material using the developed MathCAD program (see appendix K).

Table 6.2 shows the mean errors (ME) for permittivity obtained from the experiment, for each of the test liquids compared to the standard Debye determined values. The mean errors were obtained from Eq. (5.1) of chapter 5. From table 6.2, it is clearly apparent that the complex permittivity of any materials (i.e. low, medium and high permittivity materials) can be extracted with an error less than 3% for ϵ_1 and 6% for ϵ_2 over the broadband frequency ranging from 30 kHz to 6 GHz, from this capacitive model.

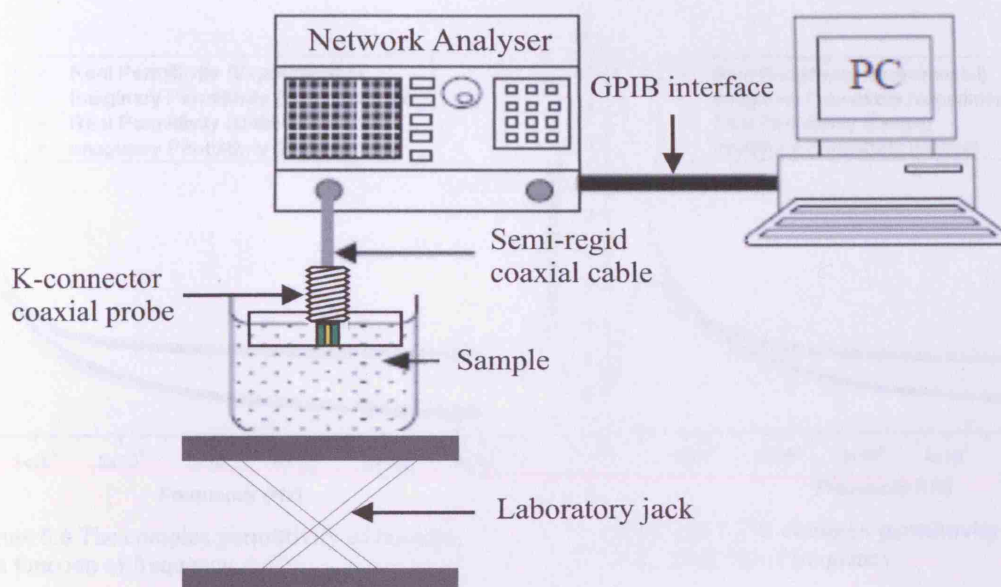


Figure 6.4 Measurement configuration.

Now we compare the Debye parameters from our measurements of those various test materials mentioned in table 6.1 obtained from the established values of C_0 and C_1 with well-known literature values listed in table 6.2 using the same developed MathCAD program (see appendix K). The complex permittivity obtained for those materials are shown in figs. 6.5 to 6.12, where the estimated uncertainties of the measurements presented above are quite low, showing very good agreement between the measured and Debye data, indicating the robustness and reliability of the simple capacitive model over the full frequency range.

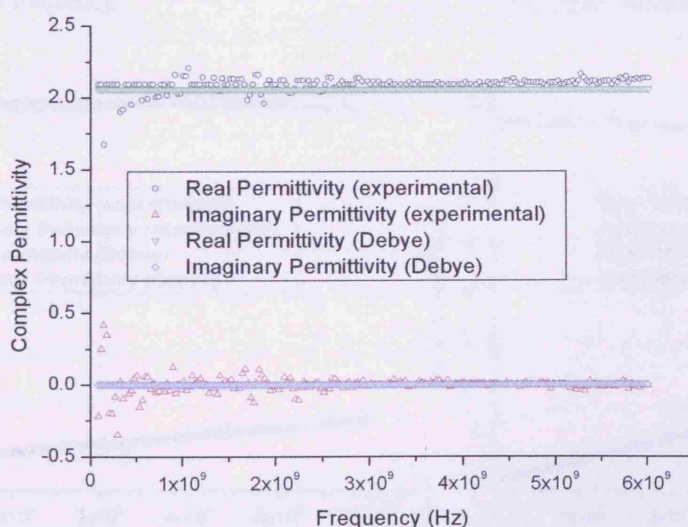


Figure 6.5 The complex permittivity of teflon as a function of frequency.

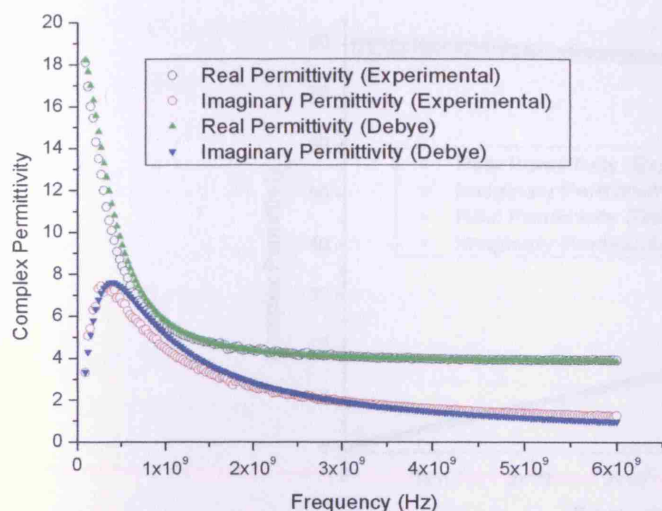


Figure 6.6 The complex permittivity of butanol as a function of frequency.

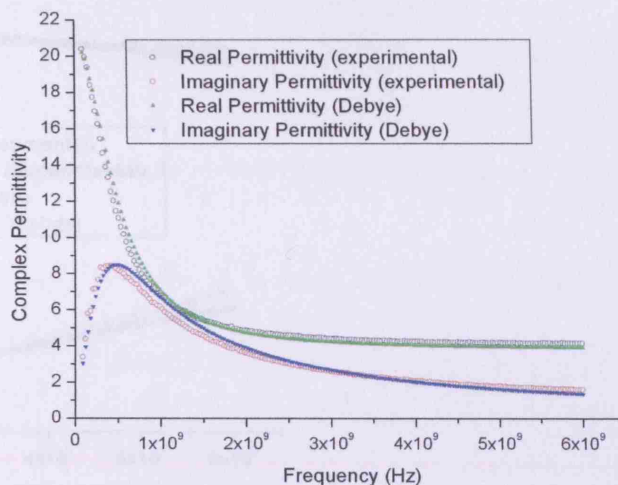


Figure 6.7 The complex permittivity of propan-2ol as a function of frequency.

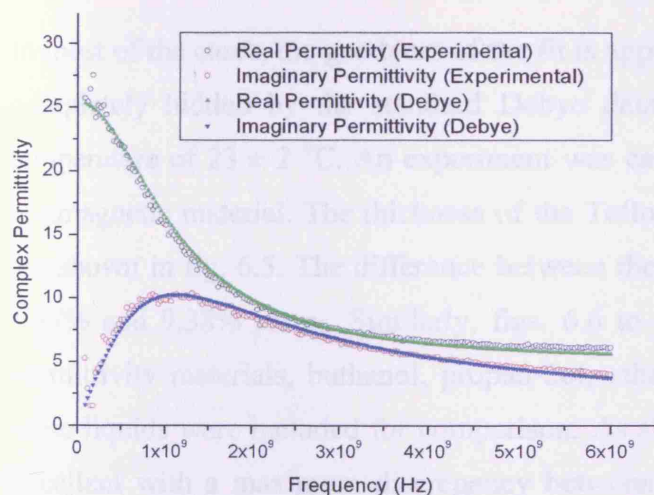


Figure 6.8 The complex permittivity of ethanol as a function of frequency.

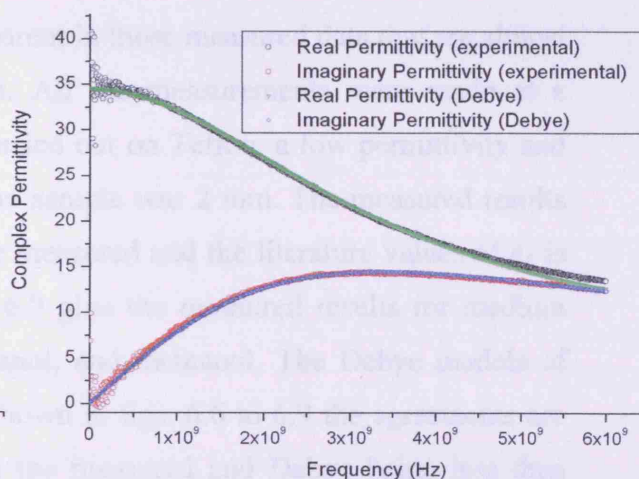


Figure 6.9 The complex permittivity of methanol as a function of frequency.

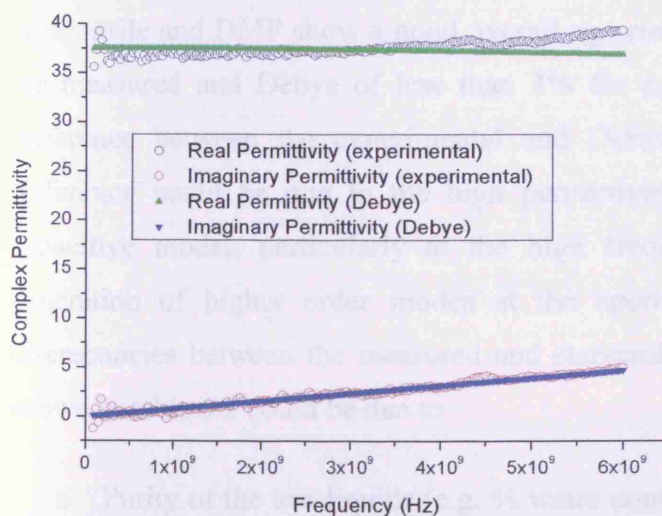


Figure 6.10 The complex permittivity of acetonitrile as a function of frequency.

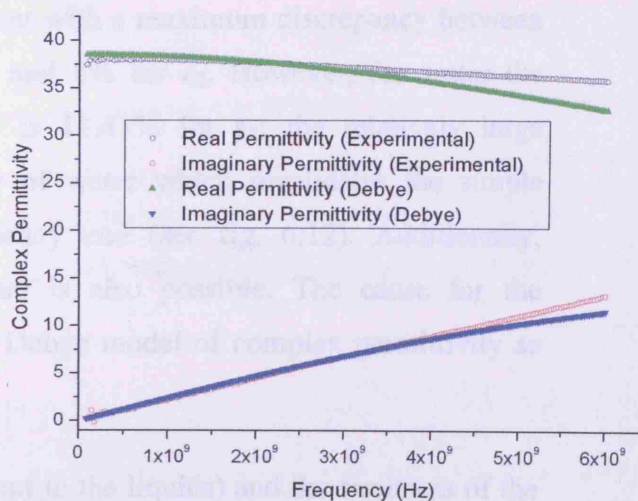


Figure 6.11 The complex permittivity of DMF as a function of frequency.

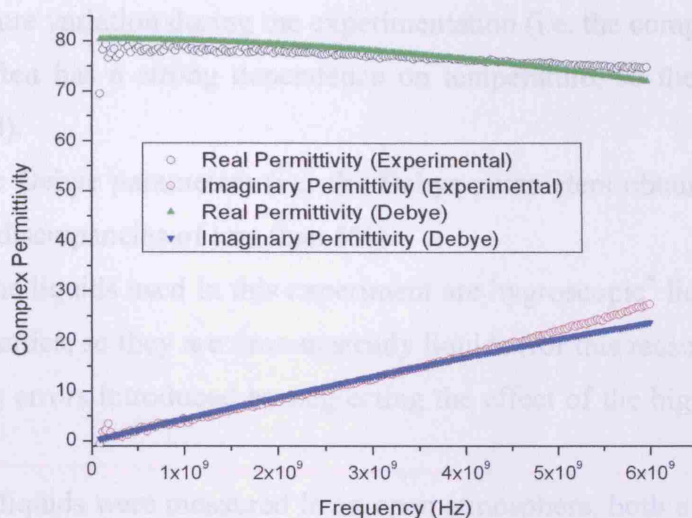


Figure 6.12 The complex permittivity of water as a function of frequency.

In most of the cases, the goodness of the fit is apparent in those measured data that are almost completely hidden by the standard Debye data. All the measurements were made at a temperature of 23 ± 2 °C. An experiment was carried out on Teflon, a low permittivity and nonmagnetic material. The thickness of the Teflon sample was 2 mm. The measured results are shown in fig. 6.5. The difference between the measured and the literature values of ϵ_1 is 1.37% and 9.38% for ϵ_2 . Similarly, figs. 6.6 to 6.9 give the measured results for medium permittivity materials, buthanol, propan-2ol, ethanol, and methanol. The Debye models of these liquids were included for comparison. As shown in figs. 6.6 to 6.9 the agreements are excellent with a maximum discrepancy between the measured and Debye being less than 4.5% for ϵ_1 and 10% for ϵ_2 . Figs. 6.10 to 6.12 show the experimental and Debye results for high permittivity materials such as acetonitrile, DMF, and water. The results obtained for acetonitrile and DMF show a good overall agreement with a maximum discrepancy between the measured and Debye of less than 3% for ϵ_1 and 8% for ϵ_2 . However, for water the difference between the experimental and Debye is 11.43% for ϵ_2 ; the relatively large difference could be due to the high permittivity of water which invalidates the simple capacitive model, particularly at the high frequency end (see fig. 6.12). Additionally, generation of higher order modes at the aperture is also possible. The cause for the discrepancies between the measured and standard Debye model of complex permittivity as shown in table 6.2 could be due to

- Purity of the test liquids (e.g. % water content in the liquids) and the freshness of the liquids (i.e. liquids from the sealed bottles are not used).

- Temperature variation during the experimentation (i.e. the complex permittivity of the liquids often has a strong dependence on temperature, so the temperature must be monitored).
- Inaccurate Debye parameters (i.e. the Debye parameters obtained from the literature itself has discrepancies of less than 5%).
- Most of the liquids used in this experiment are hygroscopic* liquids, and this changes their properties, so they are time-unsteady liquids (for this reason).
- Modelling errors introduced by neglecting the effect of the higher order modes at the aperture.
- Since the liquids were measured in an open atmosphere, both evaporative cooling and adsorption of water may cause significant property change.
- In the case of water and other polar liquids, a single Debye relaxation model has been used to characterise those liquids. At higher frequencies the single Debye model becomes less accurate on account of second relaxation, as described in the discussions in a number of papers [13, 14].
- The limitation/ restrictions of the numerical simulator.

6.2.8 Variational Model

As discussed in detailed in section 3.6.2, the variational model is another model used for calculating the probe aperture admittance, the simplest using a quasi-static approach [15] which results in the approximate admittance

$$Y_0 \approx jC_1\omega + jC_2\omega^3 + C_3\omega^4 + O(\omega^5) \quad (6.5)$$

when air terminated, the coefficients C_1 , C_2 , etc., being derived analytically in terms of the aperture geometry. Since the aperture remains electrically small over our full range of measurement frequencies, we model the probe as a lumped element capacitor C_1 when no sample is present (i.e. ignoring all other terms in Eq. (6.5)), therefore the capacitance of the unloaded probe is, from Eq. (6.5)

$$C_1 = -j \frac{Y_0}{\omega} \approx \frac{8\epsilon_0 (a+b)(E(m)-1)}{(\ln(b/a))^2}, \quad m = \frac{4ab}{(a+b)^2} \quad (6.6)$$

* Hygroscopic means the liquids readily adsorb water from the atmosphere.

where $E(m)$ is the complete elliptic integral of the first kind. For our K-connector coaxial probe $m = 0.510$ and $C_1 \approx 8.27$ fF, which have been determined from a MathCAD program (see appendix M). Having established the value of $C_1 = 8.27 \times 10^{-15}$ F, this value has been used in the developed MathCAD program (see appendix S) which works out the complex permittivity of the materials by fitting the standard Debye equation with the measured data. The comparison between the capacitive and variational models for the test liquids compared to the standard Debye model were summarised in table 6.3.

Test Materials\ Model	Capacitive Model		Variational Model	
	% mean error of real permittivity ϵ_1 (%)	% mean error of imaginary permittivity ϵ_2 (%)	% mean error of real permittivity ϵ_1 (%)	% mean error of imaginary permittivity ϵ_2 (%)
Teflon	1.37	9.87	15.65	40.45
Butanol	2.09	10.08	22.21	25.21
Propan-2ol	4.48	6.68	19.99	27.11
Ethanol	3.46	4.35	23.11	27.18
Methanol	1.65	1.19	26.00	35.94
Acetonitrile	2.11	7.67	23.94	39.21
DMF	2.75	6.91	22.87	25.67
Water	1.52	11.43	27.53	30.26

Table 6.3 Comparison of percentage mean error in calculation of permittivity for the test liquids compared to the results from the Debye equations.

Table 6.3 shows the % mean error for permittivity obtained from each model, for each test material compared to the standard Debye equation. Having compared the results obtained from the capacitive and variational models for different test liquids, clearly, it is apparent from the table 6.3 that the capacitive model is much better suited than the variational model to study the complex permittivity trends. In terms of the validation of these models, the capacitive model seems to be simple, robust and reliable admittance model for the characterisation of dielectric materials, over a wide range of permittivities. The section 6.3 discusses the microwave properties of Pt and Au NPs extracted using this established capacitive model.

In chapter 5, to validate this capacitive model further, full wave HFSS models has been developed for different types of OCPs and simulations were carried out on these test materials. The unknown values of C_0 and C_1 are determined and compared to these measured values. Chapter 5 also described the case of lumped capacitor model by mapping the complex

admittance (Y_L) onto the complex permittivity (ϵ_1 and ϵ_2) plane. Such mappings provided a visual representation of how Y_L varies with ϵ_1 and ϵ_2 at a fixed frequency and give an indication of the sensitivity of the capacitances (i.e. C_0 and C_1) of the lumped capacitor model of the probe.

6.3 Coaxial Probe System for the Characterisation of Pt and Au NPs

6.3.1 Microwave Measurement

Characterisations of Pt NPs using the coaxial probe technique were originally reported as a novel technique in the IMS 2008 conference [16]. In order to implement this technique and have more complete analysis for this thesis, three different sizes of Pt NPs (3 nm, 6.9 nm, and 8.6 nm) and Au NPs (8.2 nm, 16.5 nm, and 24.8 nm) were synthesised following the procedures mentioned in sections 4.2 and 4.5 of chapter 4. Here, we have also performed measurements of Pt oxide and ligand stabilised Au NP films as a function of film thickness for films composed of three different sizes of Pt and Au NPs.

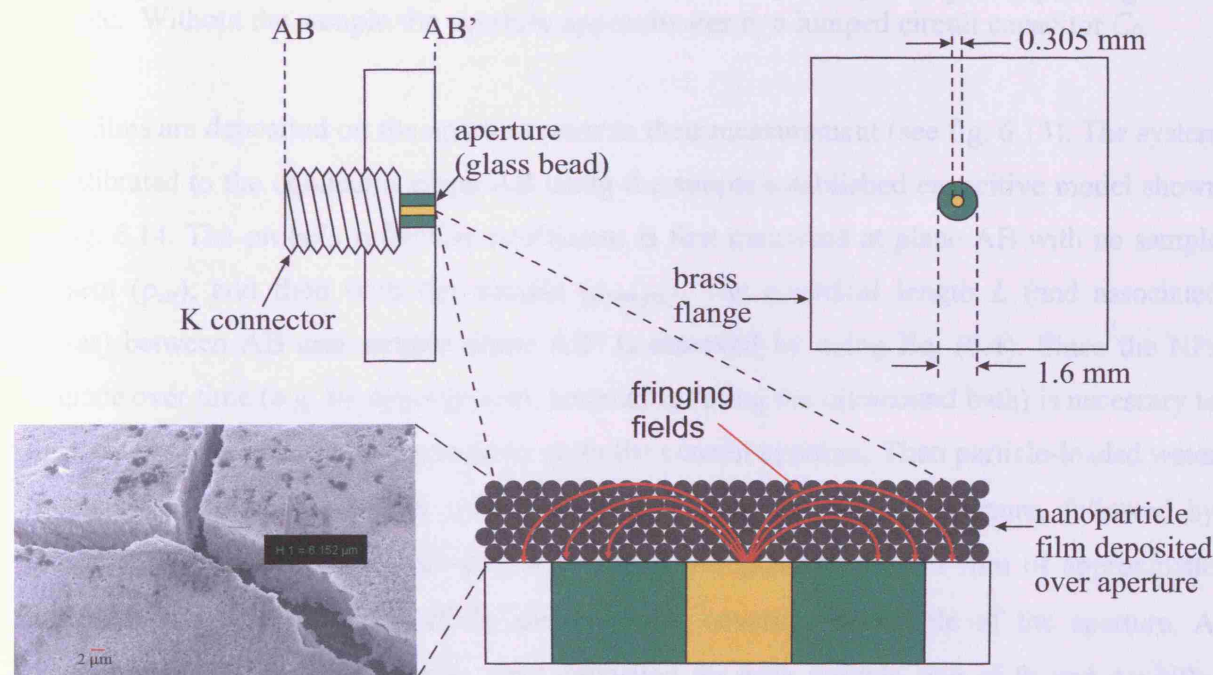


Figure 6.13 Schematic diagram of the coaxial reflectance probe. NP films are deposited directly onto the aperture, with negligibly small air gap. The scanning electron microscope (SEM) image shows the morphology of the NPs film, confirming the thickness of each droplet.

As mentioned earlier in this chapter, even though the thickness and the uniformity of the deposited films (i.e. Pt and Au) were evaluated using a Nikon Measuring Microscope MM-800 (Nikon Corp., Tokyo, Japan) by measuring thicknesses at different places on the films. This was further confirmed by the scanning electron microscope (SEM) image as shown in fig. 6.13 (note that each water droplet was found to deposit a uniform film of approximate thickness $5\ \mu\text{m}$ for all sizes of Pt and Au NPs). All measurements are performed using a HP8753E network analyzer from 1 MHz to 6 GHz, with the system calibrated to the connector plane AB using factory standards. For critical measurements the noise level was improved either by averaging or reducing the IF bandwidth.

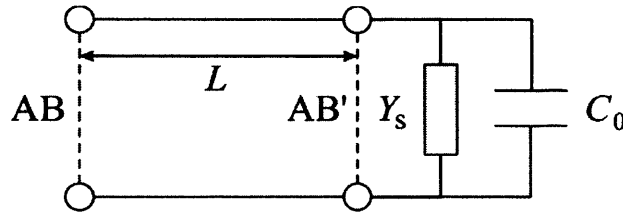


Figure 6.14 Simple lumped circuit model for the aperture together with the sample, the latter providing a shunt admittance $Y_s = G + jB$ or impedance $Z_s = 1/Y_s = R + j\omega L$ depending on the sample. Without the sample the aperture approximates to a lumped circuit capacitor C_0 .

NPs films are deposited on the aperture prior to their measurement (see fig. 6.13). The system is calibrated to the connector plane AB using the simple established capacitive model shown in fig. 6.14. The probe's reflection coefficient is first measured at plane AB with no sample present (ρ_{air}), and then with the sample (ρ_{sample}). The electrical length L (and associated losses) between AB and sample plane AB' is removed by using Eq. (6.4). Since the NPs degrade over time (e.g. by aggregation), resonating (using the ultrasound bath) is necessary to disperse the NPs prior to the deposition on to the coaxial aperture. Then particle-loaded water droplets of volume $6\ \mu\text{l}$ were deposited directly onto the coaxial aperture, followed by thorough drying. Each water droplet was found to deposit a uniform film of approximate thickness $5\ \mu\text{m}$ for all sizes of Pt and Au NPs, covering the whole of the aperture. A maximum of 5 drops and 4 drops were deposited for each particle size of Pt and Au NPs, respectively, thus forming films of overall thickness up to around $25\ \mu\text{m}$ and $20\ \mu\text{m}$, respectively. At the end of each experiment the NPs were removed from the probe using ultra pure water and then the probe surface was polished with "Brasso" and washed with soapy water and then with pure water followed by thorough drying. Two to three sets of

experiments were performed depending on the amount of NPs left for both the Pt and Au NPs, to bear out the repeatability of results.

Note that Pt NPs of different sizes (i.e. 3.0 nm, 6.9 nm and 8.6 nm) were prepared to have same amount of Pt metal, but not the same amount of NPs. Therefore the bigger particle will have larger amount of atoms (per NPs). As the total amount of Pt is constant (i.e. via the synthesis condition) it means that we have less amount of NPs of 8.6 nm compared to 6.9 nm and 3 nm, respectively (which means that 3 nm has the most amount of NPs). Therefore the only varying factors are the diameter of Pt particles as well as the number of NPs per drop. But the most important thing is that all 3 sizes of Pt NPs are covered with a very thin layer of oxide thickness ($\ll 1$ nm), since the experiment was conducted in an open environment (i.e. NPs are in contact with oxygen from air). Also before deposition the NPs were stored in water (i.e. NPs are in contact with oxygen dissolved in the water), which is confirmed by the CV shown in fig. 6.15. Therefore, all the measurements carried out in this section are for Pt metal oxide NP films (i.e. with associated oxide-oxide contacts).

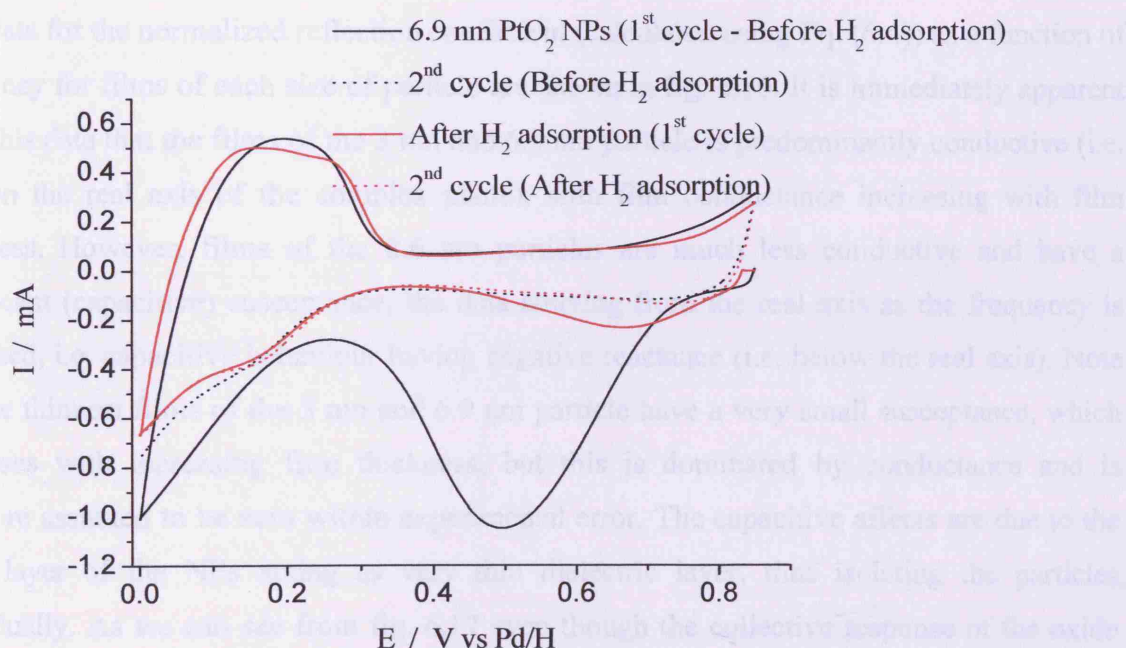


Figure 6.15 Voltammetric profile of platinum NPs before and after H_2 adsorption in 0.5 M H_2SO_4 . Sweep rate: $50 \text{ mV}\cdot\text{s}^{-1}$. It is apparent (experimental evident) from the above CV that the synthesised Pt NPs has thin layer of oxide surrounding the core of the Pt NPs.

The above graph (fig. 6.15) was obtained following a similar procedure to that mentioned in section 4.4. Very briefly, initially cleanliness of the gold electrode (i.e. working electrode on

which the NPs will be deposited) was checked. After that a cyclic voltammogram in sulphuric acid was recorded at 0.85 V (i.e. a potential where the Pt is being oxidised or, if it is already oxidised, it will not be reduced). Then the CV was recorded towards more negative potentials to check if there was some Pt in an oxide state (solid black line). The voltammetric profile shows a broad large peak centred at 0.5V (solid black line), corresponding to the reduction of Pt. This shows that there was some Pt in an oxide form at the beginning of the experiment, which is similar to the state where the microwave characterisation of Pt NPs on OCP has been carried out. On the other hand, the NPs already deposited on the gold electrode were taken to a solution where H_2 was being bubbled. The resulting CV (solid red line) shows that there is a very small peak instead of the previously described broad large peak. This result demonstrates that the contact with H_2 reduces the Pt oxide and makes metal-metal contacts (i.e. by removing the oxide layer surrounding the Pt NPs) rather than oxide-oxide layer contacts, as it is this that changes the electrical property (i.e. conductivity) of the NPs. This change in the electrical property was determined experimentally and is examined in sections 6.3.2 and 6.5 of this chapter.

Raw data for the normalized reflection coefficient (calculated using Eq. (6.4)) as a function of frequency for films of each size of particle are shown in fig. 6.16. It is immediately apparent from this data that the films of the 3 nm and 6.9 nm particle is predominantly conductive (i.e. data on the real axis of the complex plane), with film conductance increasing with film thickness. However, films of the 8.6 nm particles are much less conductive and have a significant (capacitive) susceptance, the data straying from the real axis as the frequency is increased, i.e. capacitive behaviour having negative reactance (i.e. below the real axis). Note that the thinnest films of the 3 nm and 6.9 nm particle have a very small susceptance, which decreases with increasing film thickness, but this is dominated by conductance and is therefore assumed to be zero within experimental error. The capacitive affects are due to the oxide layer of the NPs acting as very thin dielectric layer, thus isolating the particles individually. As we can see from fig. 6.17 even though the collective response of the oxide layers is more for 3 nm NPs compared to 6.9 nm and 8.6 nm NPs, respectively (i.e. this is due to the number of NPs per drop), the individual contact area between the metal oxide layers are smaller for 3 nm compare to 6.9 nm and 8.6 nm NPs, respectively. And also the number of contacts (i.e. oxide-oxide contacts) between the NPs are more for 3 nm compared to 6.9 nm and 8.6 nm NPs. Fig. 6.18 shows the contact area of individual NPs of different sizes.

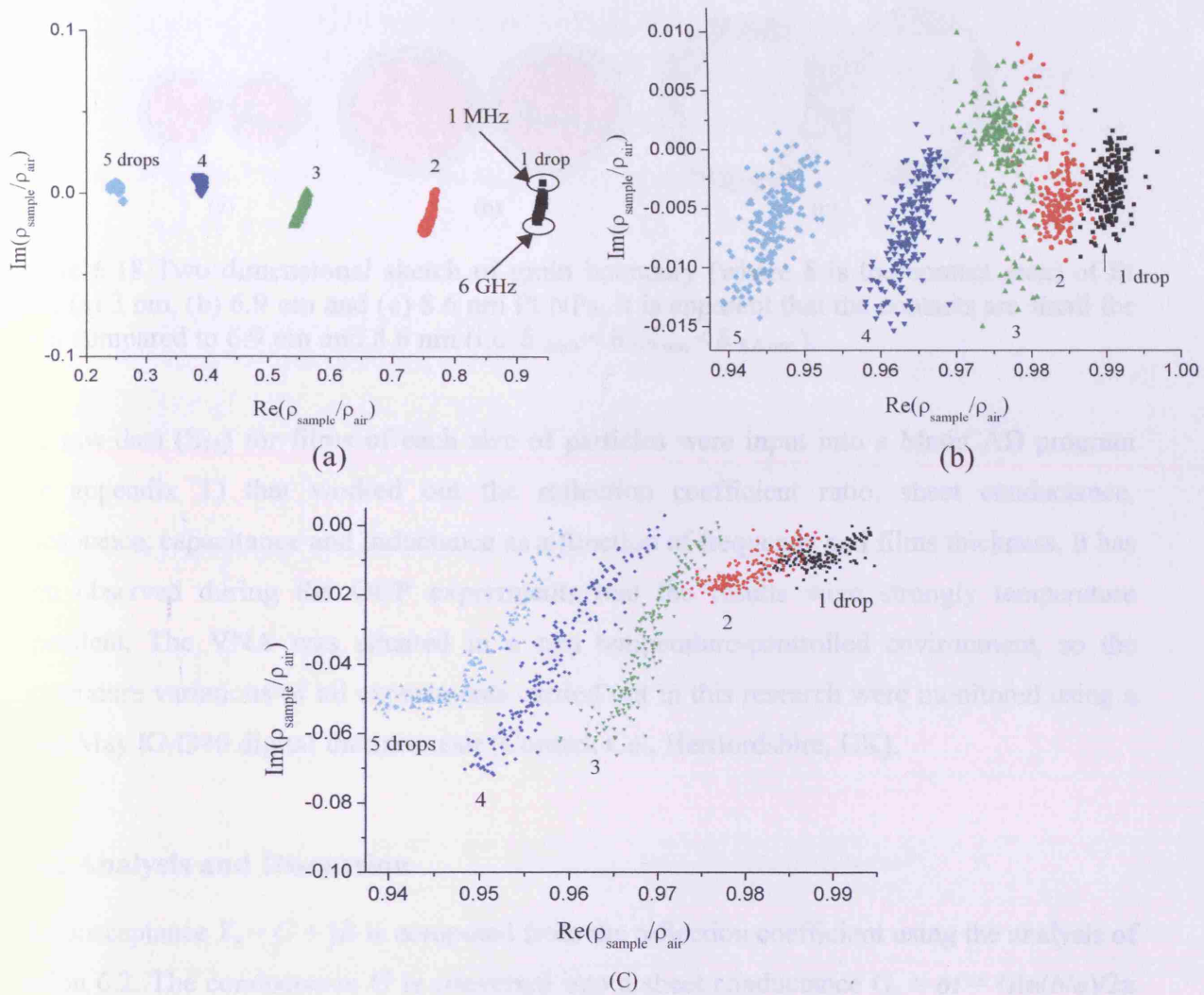


Figure 6.16 Reflection coefficient ratio (Eq. (6.4)) as a function of frequency for Pt NP films of particle size (a) 3 nm, (b) 6.9 nm and (c) 8.6 nm. Each drop deposits a uniform film of thickness approximately 5 μm . Measurements were taken from 1 MHz to 6 GHz. The trend is shown in fig. 6.16 (a), which represents all plots.

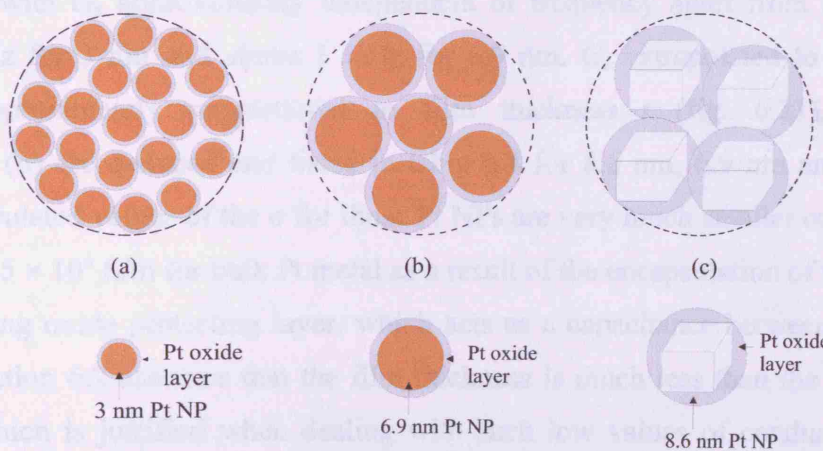


Figure 6.17 Spherical and cubic mode of two-dimensional Pt NPs structure. (a) spherical (3 nm) (b) spherical (6.9 nm) and (c) cubic (8.6 nm).

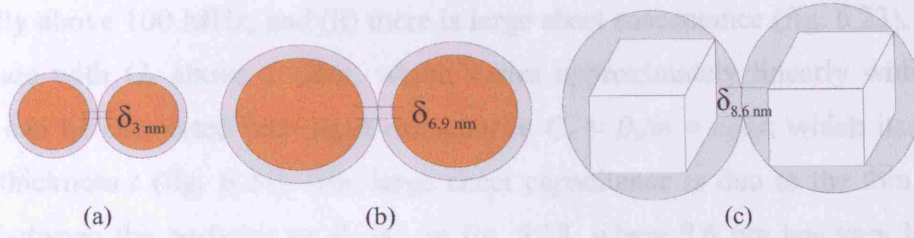


Figure 6.18 Two dimensional sketch of grain boundary (where δ is the contact area) of Pt NPs. (a) 3 nm, (b) 6.9 nm and (c) 8.6 nm Pt NPs. It is apparent that the contacts are small for 3 nm compared to 6.9 nm and 8.6 nm (i.e. $\delta_{3\text{nm}} < \delta_{6.9\text{nm}} < \delta_{8.6\text{nm}}$).

The raw data (S_{11}) for films of each size of particles were input into a MathCAD program (see appendix T) that worked out the reflection coefficient ratio, sheet conductance, susceptance, capacitance and inductance as a function of frequency and films thickness. It has been observed during the OCP experiments that the results were strongly temperature dependent. The VNA was situated in a non temperature-controlled environment, so the temperature variations of all experiments carried out in this research were monitored using a Kane-May KM340 digital thermometer (Comark Co., Hertfordshire, UK).

6.3.2 Analysis and Discussion

Film susceptance $Y_s = G + jB$ is computed from the reflection coefficient using the analysis of section 6.2. The conductance G is converted into a sheet conductance $G_s = \sigma t = G \ln(b/a)/2\pi$ and the susceptance B into a sheet susceptance $B_s = B \ln(b/a)/2\pi$. As already noted, for the 3 nm and 6.9 nm Pt NP films $G_s \gg B_s$, with B_s approximately zero within experimental error up to 6 GHz; thus the behaviour is predominantly conductive (figs. 6.19 and 6.20, respectively), with G_s approximately independent of frequency apart from a slight upturn above 3.5 GHz for 3 nm and above 1 GHz for 6.9 nm. G_s extrapolated to low frequency ($G_s(0)$) is approximately proportional to film thickness t (fig. 6.21), from which conductivities (σ) are deduced and listed in table 6.4 for 8.6 nm, 6.9 nm and 3 nm Pt NP films. The calculated values of the σ for those Pt NPs are very much smaller compared with a value of $\sigma = 9.5 \times 10^6$ S/m for bulk Pt metal as a result of the encapsulation of the metal cores by the insulating oxide protecting layer, which acts as a capacitance between the NPs. The analysis of section 6.2 assumes that the film thickness is much less than the skin depth, an assumption which is justified when dealing with such low values of conductivity. Similar data for the 8.6 nm Pt NP films is shown in fig. 6.22. In contrast to the data for the 3 nm and 6.9 nm particles, (i) G_s is further suppressed and increases monotonically with frequency,

more rapidly above 100 MHz, and (ii) there is large sheet susceptance (fig. 6.23), comparable in magnitude with G_s above 1 GHz, which varies approximately linearly with frequency. Hence, B_s can be converted into sheet capacitance $C_s \approx B_s/\omega = \epsilon_1 \epsilon_0 t$, which itself increases with film thickness t (fig. 6.24). The large sheet capacitance is due to the thin oxide layer boundary between the particles as shown in fig. 6.18, where 8.6 nm has very large contact area compare to the other two particles sizes (i.e. 6.9 nm and 3 nm) due to its cubic structure. The associated real permittivity is very large ($\epsilon_1 \approx 500$).

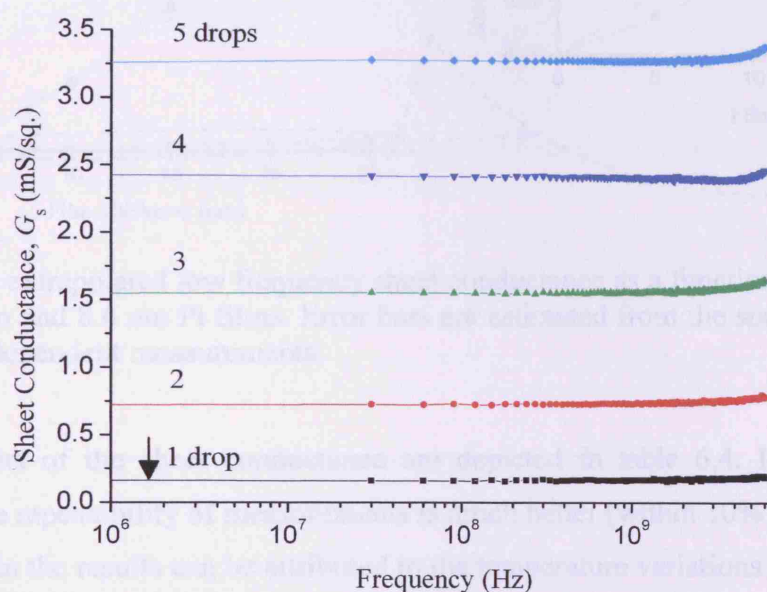


Figure 6.19 Sheet conductance as a function of frequency for 3 nm Pt films.

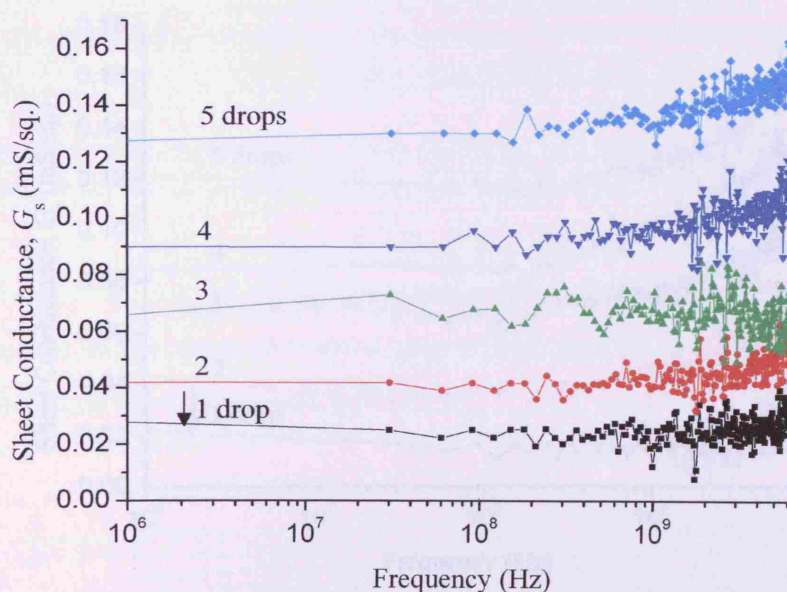


Figure 6.20 Sheet conductance as a function of frequency for 6.9 nm Pt films.

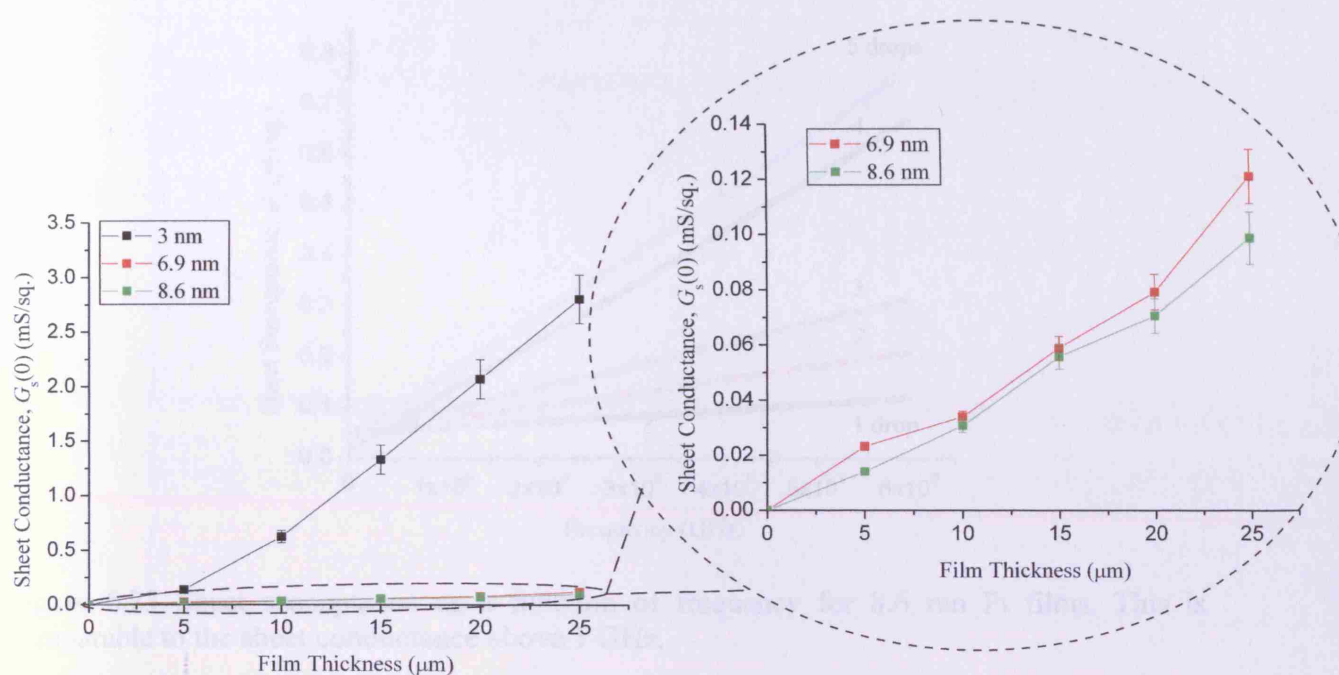


Figure 6.21 The extrapolated low frequency sheet conductance as a function of film thickness for 3 nm, 6.9 nm and 8.6 nm Pt films. Error bars are estimated from the statistical average of at least three independent measurements.

The mean results of the sheet conductance are depicted in table 6.4. It is notable from table 6.4 that the repeatability of measurements is much better (within 10% discrepancy). The slight variation in the results can be attributed to the temperature variations over the course of experiments, agglomeration of NPs and non uniformity of the films formed by the NPs.

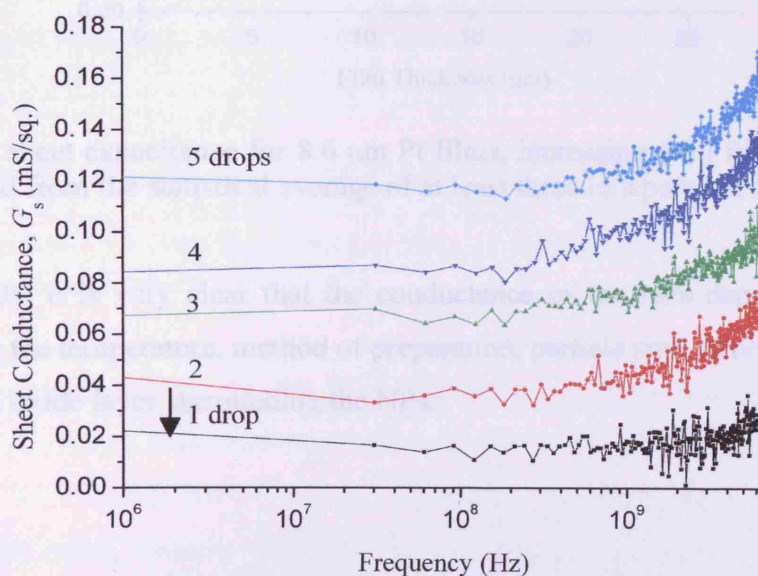


Figure 6.22 Sheet conductance as a function of frequency for 8.6 nm cubic Pt films.

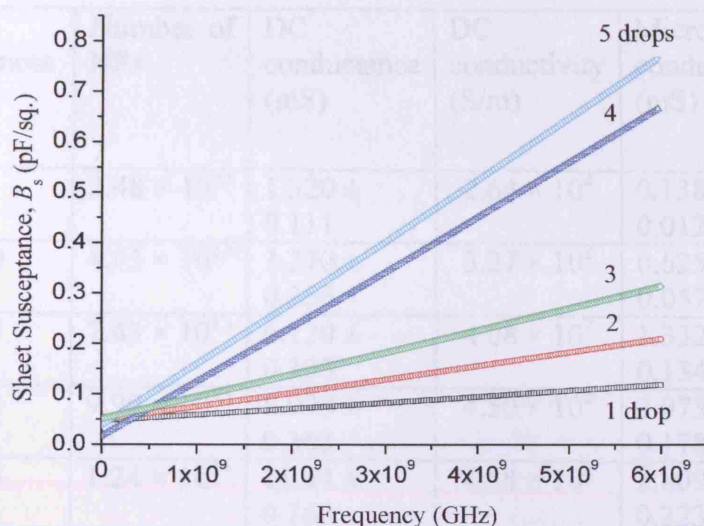


Figure 6.23 Sheet susceptance as a function of frequency for 8.6 nm Pt films. This is comparable to the sheet conductance above 1 GHz.

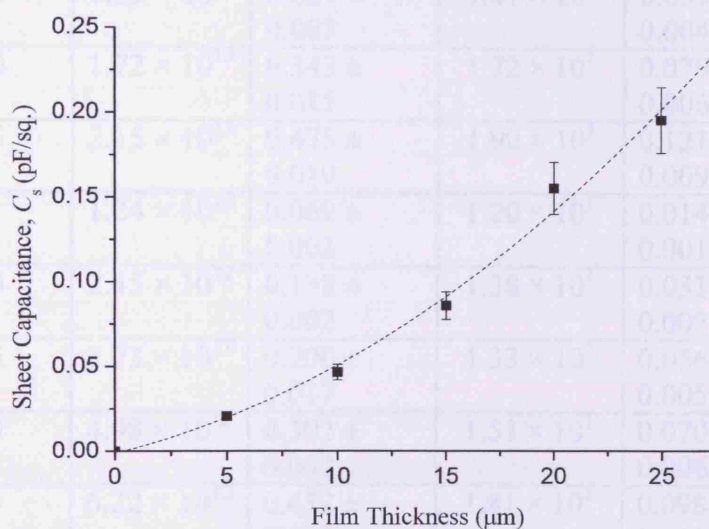


Figure 6.24 The sheet capacitance for 8.6 nm Pt films, increasing with film thickness. Error bars are estimated from the statistical average of at least three independent measurements.

From these results it is very clear that the conductance of the NPs depends upon several factors including the temperature, method of preparation, particle size, structure (i.e. spherical or cubic) and the oxide layer surrounding the NPs.

Pt NPs	Films Thickness (μm)	Number of NPs	DC conductance (mS)	DC conductivity (S/m)	Microwave conductance (mS)	Microwave conductivity (S/m)
3 nm	5	2.48×10^{13}	1.320 ± 0.111	2.64×10^2	0.138 ± 0.012	2.76×10^1
	10	4.95×10^{13}	3.270 ± 0.256	3.27×10^2	0.625 ± 0.057	6.25×10^1
	15	7.43×10^{13}	6.120 ± 0.305	4.08×10^2	1.332 ± 0.134	8.88×10^1
	20	9.90×10^{13}	8.990 ± 0.363	4.50×10^2	2.073 ± 0.178	1.04×10^2
	25	1.24×10^{14}	11.44 ± 0.160	4.58×10^2	2.809 ± 0.223	1.12×10^2
6.9 nm	5	4.29×10^{12}	0.088 ± 0.008	1.76×10^1	0.023 ± 0.002	4.65
	10	8.59×10^{12}	0.148 ± 0.014	1.48×10^1	0.034 ± 0.002	3.40
	15	1.29×10^{13}	0.221 ± 0.007	1.47×10^1	0.059 ± 0.004	3.92
	20	1.72×10^{13}	0.343 ± 0.015	1.72×10^1	0.079 ± 0.006	3.95
	25	2.15×10^{13}	0.475 ± 0.019	1.90×10^1	0.121 ± 0.009	4.83
8.6 nm	5	1.24×10^{12}	0.060 ± 0.003	1.20×10^1	0.014 ± 0.001	2.82
	10	2.45×10^{12}	0.138 ± 0.002	1.38×10^1	0.031 ± 0.002	3.07
	15	3.73×10^{12}	0.200 ± 0.017	1.33×10^1	0.056 ± 0.005	3.71
	20	4.98×10^{12}	0.302 ± 0.002	1.51×10^1	0.070 ± 0.006	3.52
	25	6.22×10^{12}	0.452 ± 0.035	1.81×10^1	0.098 ± 0.009	3.94

Table 6.4 shows the DC and microwave conductance and corresponding conductivity for different sizes of Pt NPs as a function of films thickness. All the measurements were made at a temperature of 24 ± 3 °C. The standard deviations are estimated from the statistical average of at least three independent measurements.

Moreover, the results obtained for the Pt NPs have been further justified by characterising different sizes of ligand stabilised Au NPs using the same OCP technique in a similar manner. Unlike the Pt oxide NPs, these Au NPs form a film where the individual NPs are in contact (i.e. metal-metal contact) with each other, as shown in fig. 6.25.

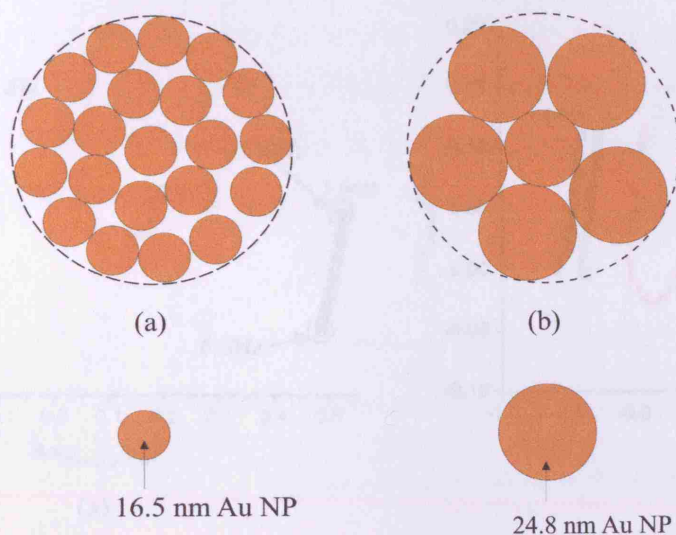


Figure 6.25 Spherical mode of two-dimensional Au NPs structure. (a) 16.5 nm and (b) 24.8 nm.

Raw data for the normalized reflection coefficient (calculated using Eq. (6.4)) as a function of frequency for films of each size of particle are shown in fig. 6.26. It is immediately apparent from this data that the films of the 16.5 nm and 24.8 nm particles are highly conductive (i.e. data on the real axis of the complex plane), with film conductance increasing with film thickness. However, both sizes of particles (i.e. 16.5 nm and 24.8 nm) have significant (capacitive) susceptance which decreases and eventually turns into considerably large inductance when the film thickness increases, the data straying from the real axis as the frequency is increased, i.e. capacitive behaviour having negative reactance (i.e. below the real axis), inductive behaviour having positive reactance (i.e. above the real axis). The increased inductance with increased film thickness is due the high density of metal-metal contacts between the NPs.

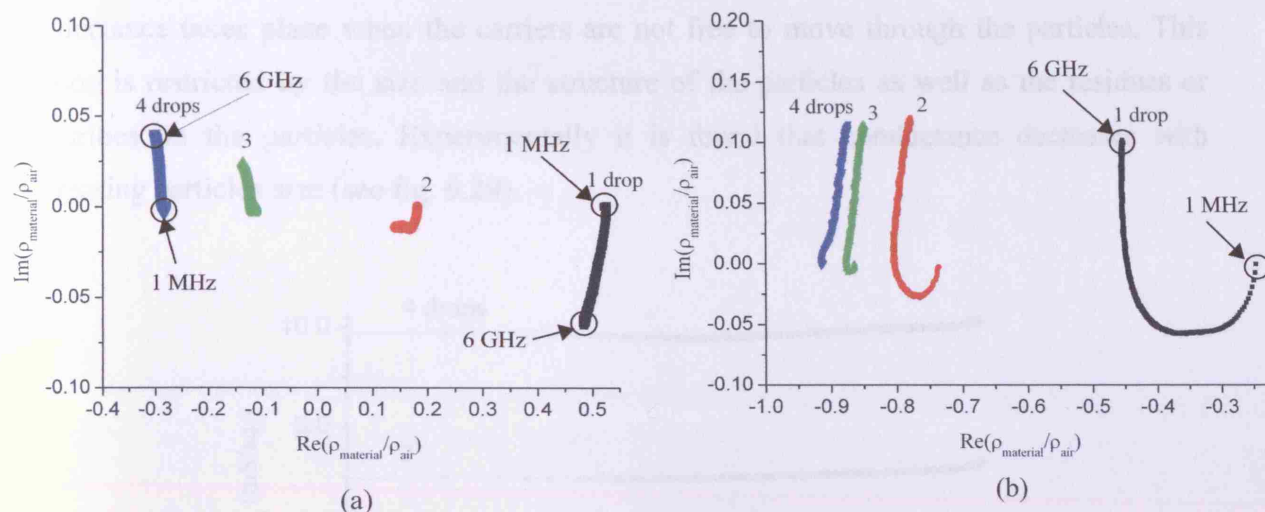


Figure 6.26 Reflection coefficient ratio (Eq. (6.4)) as a function of frequency for Au NPs films of particle size (a) 16.5 nm and (b) 24.8 nm. Each drop deposits a uniform film of thickness approximately 5 μm . Measurements were taken from 1 MHz to 6 GHz. The trend is shown in fig. 6.26 (a), which represents for all plots.

As already noted, for the 16.5 nm Au NP films $G_s \gg B_s$, with B_s approximately zero within experimental error up to 6 GHz; thus the behaviour is predominantly conductive (fig. 6.27), with G_s approximately independent of frequency. Unlike for the 16.5 nm, the 24.8 nm Au NP films have upturns which occur at a frequency of around 5 GHz for the thinnest film (5 μm) and eventually it shifts towards the lower frequency end with increasing film thickness (i.e. the upturn occurs at around 100 MHz for the 20 μm film). This can be seen only for the 24.8 nm Au films. G_s extrapolated to low frequency ($G_s(0)$) is approximately proportional to film thickness t (fig. 6.28), from which conductivities (σ) are deduced and listed in table 6.5 for 16.5 nm and 24.8 nm Au NPs. In comparison to the bulk gold metal (σ of 4.1×10^7 S/m), these NPs are 3 to 4 orders of magnitude less conductive, as a result of the encapsulation of the metal cores by the insulating organic protecting layer (i.e. impurities, residues from the synthesis), agglomeration of the NPs, and non-uniformity of the film. In contrast to the data for the 16.5 nm particles, (i) G_s is further increased and also increases monotonically with frequency, more rapidly above 100 MHz (for 20 μm), (ii) $G_s(0)$ no longer varies linearly with film thickness (fig. 6.29), instead increasing more rapidly for thicker films. This rapid increase in the conductance is due to the metal-metal contact having larger area for the 24.8 nm compared to the 16.5 nm particles, which enables the charge carriers (i.e. the Au conduction electrons) to move freely between neighbouring particle states with significantly low impedance between the particles compared to the 16.5 nm particles. The dispersion in the

conductance takes place when the carriers are not free to move through the particles. This motion is restricted by the size and the structure of the particles as well as the residues or impurities on the particles. Experimentally it is found that conductance decreases with decreasing particles size (see fig. 6.29).

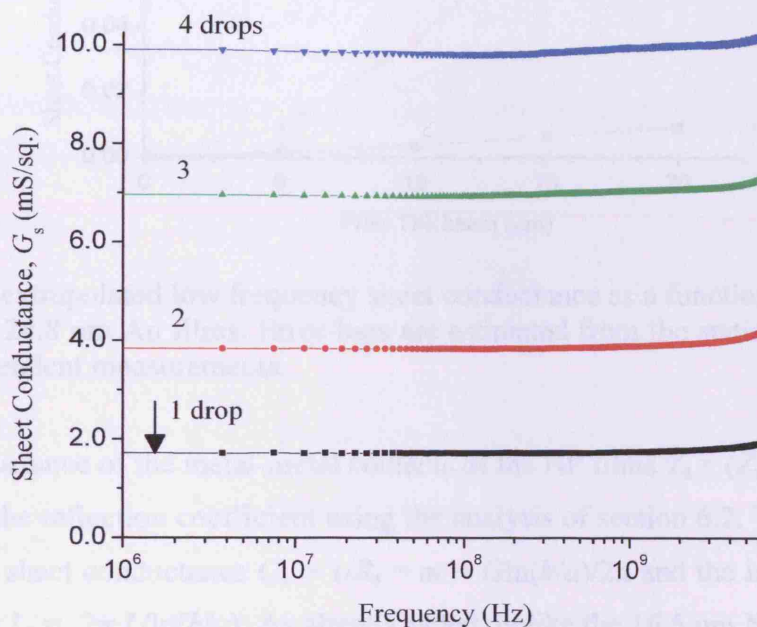


Figure 6.27 Sheet conductance as a function of frequency for 16.5 nm Au films.

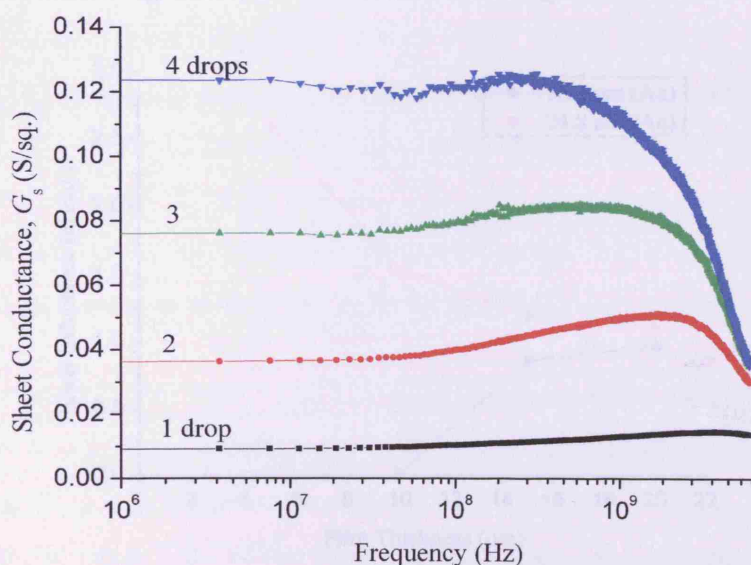


Figure 6.28 Sheet conductance as a function of frequency for 24.8 nm Au films.

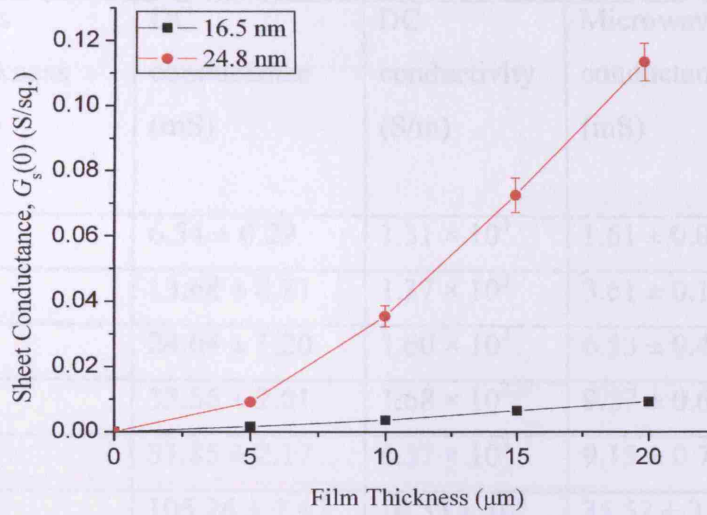


Figure 6.29 The extrapolated low frequency sheet conductance as a function of film thickness for 16.5 nm and 24.8 nm Au films. Error bars are estimated from the statistical average of at least three independent measurements.

The internal inductance of the metal-metal contacts of the NP films $Y_s = (Z_s)^{-1} = (R + j\omega L)^{-1}$ is computed from the reflection coefficient using the analysis of section 6.2. The resistance R is converted into a sheet conductance $G_s = 1/R_s = \sigma t = G \ln(b/a)/2\pi$ and the inductance L into a sheet inductance $L_s = 2\pi \cdot L / \ln(b/a)$. As already noted, unlike the 16.5 nm NPs films, 24.8 nm Au NP films large internal inductance, $L_s \gg G_s$, thus the behaviour is highly inductive (fig. 6.26 (a)), with G_s dependent of frequency (fig. 6.28). L_s extrapolated are exponentially decreases with the increasing film thickness as shown in fig. 6.30.

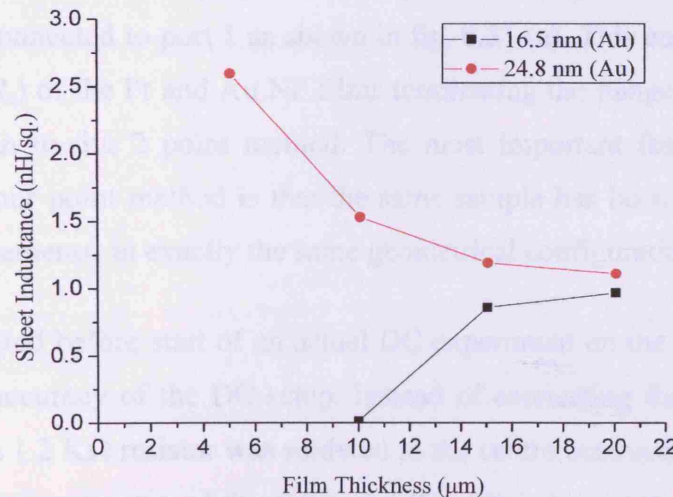


Figure 6.30 The sheet inductance for 16.5 nm and 24.8 nm Au films as a function of film thickness. The internal inductance of 16.5 nm NP film of first drop is not shown in the graph as exhibits purely (capacitive) susceptance (or negative reactance/ inductance), which increases with increasing frequency.

Au NPs	Films Thickness (μm)	DC conductance (mS)	DC conductivity (S/m)	Microwave conductance (mS)	Microwave conductivity (S/m)
16.5 nm	5	6.54 ± 0.29	1.31×10^3	1.61 ± 0.07	3.22×10^2
	10	13.68 ± 0.81	1.37×10^3	3.61 ± 0.18	3.61×10^2
	15	24.04 ± 1.20	1.60×10^3	6.53 ± 0.40	4.35×10^2
	20	33.56 ± 2.01	1.68×10^3	9.27 ± 0.62	4.64×10^2
24.8 nm	5	31.85 ± 2.17	6.37×10^3	9.15 ± 0.78	1.83×10^3
	10	105.26 ± 7.47	10.53×10^3	35.52 ± 3.23	3.55×10^3
	15	181.49 ± 17.40	12.10×10^3	72.51 ± 5.29	4.83×10^3
	20	242.72 ± 20.15	12.14×10^3	113.22 ± 5.77	5.66×10^3

Table 6.5 shows the DC and microwave conductance and corresponding conductivity for different sizes of Au NPs as a function of film thickness. All the measurements were made at a temperature of 24 ± 3 °C. The standard deviations are estimated from statistical average of at least three independent measurements.

6.3.3 DC Measurement

The DC measurements of both the Pt and Au NPs have been obtained by biasing the port (i.e. port 1) of the 8753E VNA (i.e. via the back of the VNA) with a BNC probe connected to a digital multi-meter (DMM) through a DMM probe which provides dc bias on the OCP centre conductor connected to port 1 as shown in fig. 6.31 (a). This enables the measurement of the resistance (R_s) of the Pt and Au NP films terminating the flange of the probe using the DMM, which is an in-situ 2 point method. The most important feature of this two point method over the four point method is that the same sample has been used for both DC and microwave measurements, in exactly the same geometrical configuration.

A trial was conducted before start of an actual DC experiment on the NP films to determine the measurement accuracy of the DC setup. Instead of connecting the probe directly to the VNA, one end of a 1.2 K Ω resistor was soldered to the centre conductor of the RG-402 cable and other end to the outer core of the cable and this setup was connected to the VNA port (i.e. port 1) through a SMA connector as shown fig. 6.31 (b). It turned out to be that the DC result obtained through biasing the port of the VNA (see fig. 6.31 (b) – (i)) was exactly same

as the results from DMM (see fig. 6.31 (b) – (ii)). Therefore, the DC measurements on the NP films from this setup give the actual DC resistance of the films.

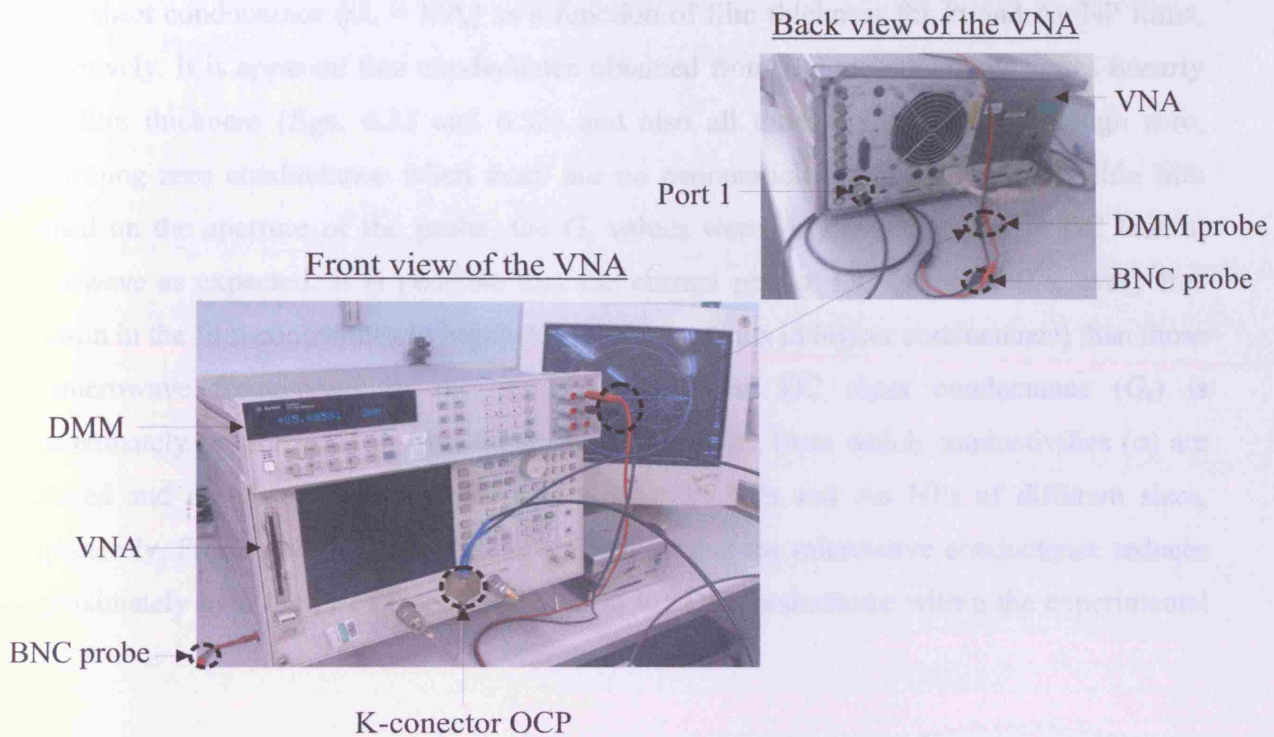


Figure 6.31 (a) Shows the experimental setup of the DC measurement.

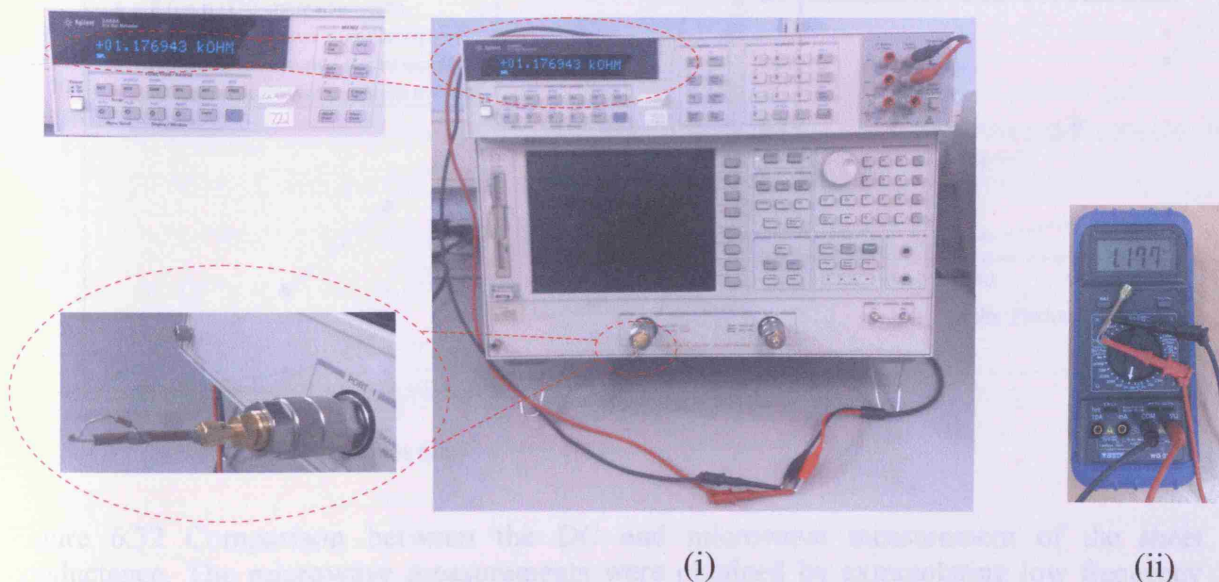


Figure 6.31 (b) Shows a trial experimental setup of the DC measurement. (i) shows the DC measurement of a 1.2 K Ω resistor via biasing the port of the VNA and (ii) direct measurement of the actual value of the resistor using the DMM.

6.3.4 Analysis of Results

Figs. 6.32 and 6.33 show the comparison between the DC and the microwave measurement of the sheet conductance ($G_s = 1/R_s$) as a function of film thickness for Pt and Au NP films, respectively. It is apparent that conductance obtained from DC measurements varies linearly with film thickness (figs. 6.32 and 6.33) and also all those six graphs go through zero, confirming zero conductance when there are no nanoparticles present. For every thin film formed on the aperture of the probe, the G_s values were very much greater at DC than at microwave as expected. It is possible that the current path at DC is longer (i.e. every free electron in the film contributes to conduction, which results in higher conductance) than those at microwave frequencies in the thinner films. The DC sheet conductance (G_s) is approximately proportional to film thickness t (fig. 6.32), from which conductivities (σ) are deduced and are listed in tables 6.4 and 6.5 for Pt NPs and Au NPs of different sizes, respectively. From tables 6.4 and 6.5, it is apparent that the microwave conductance reduces approximately by a factor of three compared to the DC conductance within the experimental error.

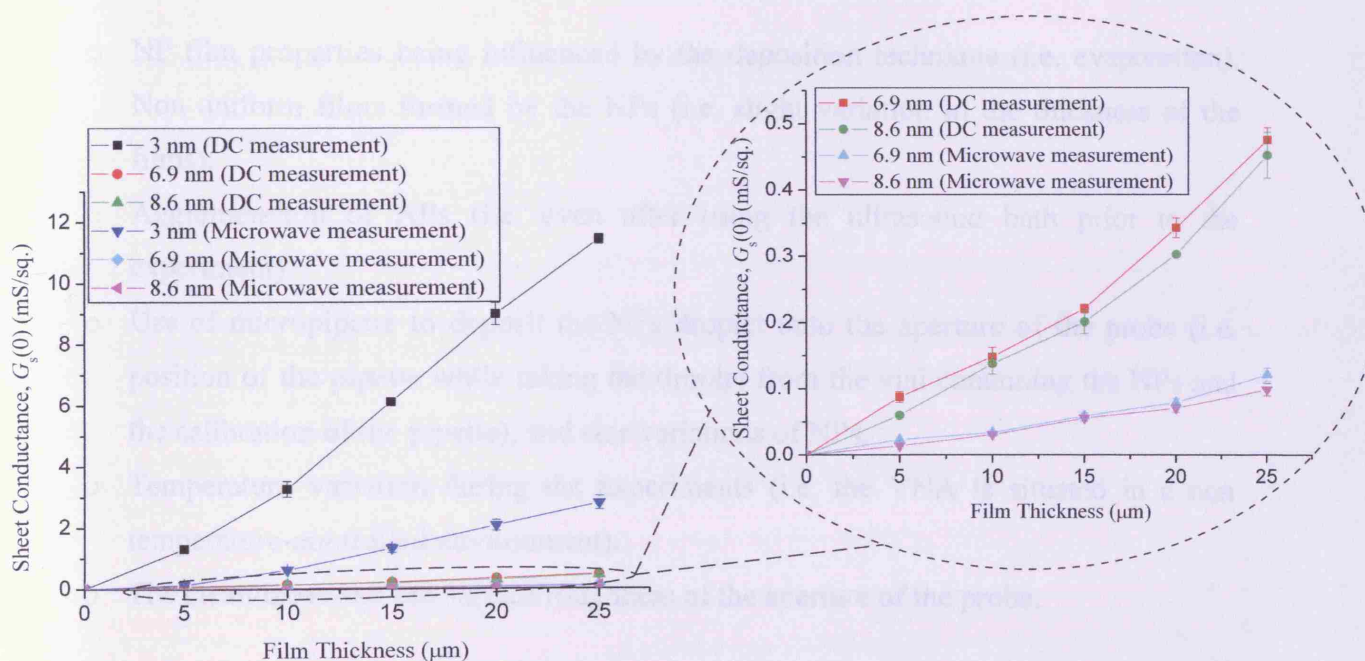


Figure 6.32 Comparison between the DC and microwave measurement of the sheet conductance. The microwave measurements were obtained by extrapolating low frequency sheet conductance as a function of film thickness for different sizes of Pt films (8.6 nm, 6.9 nm and 3 nm) and the DC measurement using the DMM. Error bars are estimated from statistical average of at least three independent measurements.

From fig. 6.32 (see table 6.4), it is clearly apparent that the DC conductance of Pt films of various particle sizes are much higher than the microwave conductance. The conductance of the NPs seems to increase due to a better compactness of the NPs, leading to enhanced coupling among the NPs through inter-particle contacts. Therefore the DC conductance of the 3 nm Pt film is high compared to 6.9 nm and 8.6 nm Pt films, and also follow the same trend as observed in the microwave measurement (i.e. 3 nm Pt films have higher conductance compared to 10.7 nm and 13.5 nm Pt films). It is important to note that the films formed by these Pt NPs are different in size and also in physical structure (i.e. spherical (6.9 nm) and cubic (8.6 nm)). This implies that the conductance not only depends on the size of the NPs but also on their physical structure.

As discussed earlier for the microwave conductance of the Au NPs films, similar trends were observed in the DC conductance of Au NP films (i.e. 24.8 nm Au films have higher conductance compared to 16.5 nm Au films). This is due to the large area of inter-particle contacts for 24.8 nm compared to 16.5 nm Au NPs. The common cause for the numerical errors in the experimental results listed in tables 6.4 and 6.5 could be due to

- NP film properties being influenced by the deposition technique (i.e. evaporation). Non uniform films formed by the NPs (i.e. slight variation in the thickness of the films).
- Agglomeration of NPs (i.e. even after using the ultrasound bath prior to the experiment).
- Use of micropipette to deposit the NPs droplet onto the aperture of the probe (i.e. position of the pipette while taking the droplet from the vial containing the NPs and the calibration of the pipette), and size variations of NPs.
- Temperature variation during the experiments (i.e. the VNA is situated in a non temperature-controlled environment).
- The cleanliness and the surface roughness of the aperture of the probe.

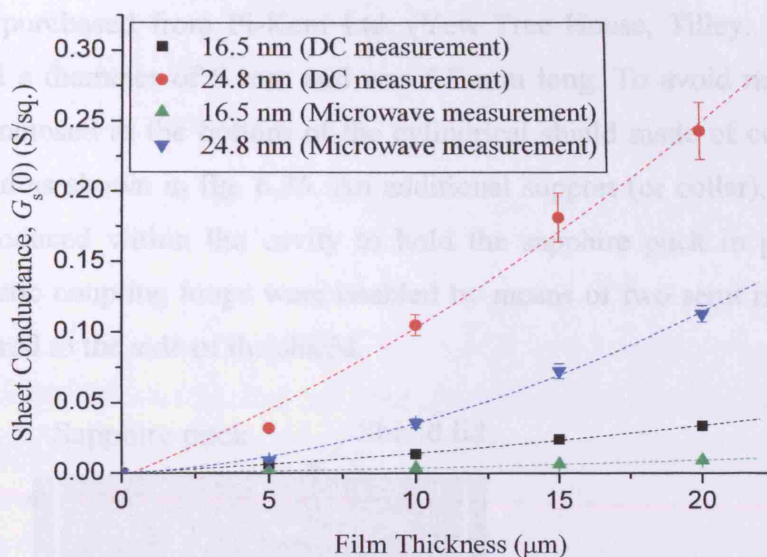


Figure 6.33 Comparison between the DC and microwave measurement of the sheet conductance. The microwave measurements were obtained by extrapolating low frequency sheet conductance as a function of film thickness for different sizes of Au films (16.5 nm and 24.8 nm) and the DC measurement using the DMM. Error bars are estimated from the statistical average of at least three independent measurements.

6.4 SDR System for the Characterisation of Pt and Au NPs

6.4.1 Construction of SDR

The cylindrical SDR employed in this research is a device made from a single crystal sapphire puck, operating in TE_{018} mode. Sapphire being an anisotropic material, its dielectric constant depends upon the direction of electric field, with $\epsilon_1 = 9.4$ for E-field along its basal ab plane and $\epsilon_1 = 11$ along its c axis [17]. To attain symmetrical well defined modes, the cylindrical sapphire crystal is machined with the c axis aligned with the cylindrical z axis as shown in fig. 6.34, which is used for the construction of SDR studied here.

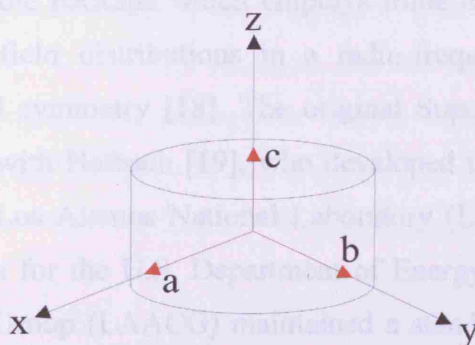


Figure 6.34 c axis oriented sapphire puck.

This puck was purchased from Pi-Kem Ltd. (Yew Tree House, Tilley, Wem, Shropshire, UK), which had a diameter of 9 mm and was 5.7 mm long. To avoid radiation losses, the resonator was enclosed at the bottom of the cylindrical shield made of copper and covered with a copper lid as shown in fig. 6.35. An additional support (or collar), which is made of PTFE, was introduced within the cavity to hold the sapphire puck in place as shown in fig. 6.35. Magnetic coupling loops were enabled by means of two semi rigid coaxial cables (RG-405), soldered to the side of the shield.

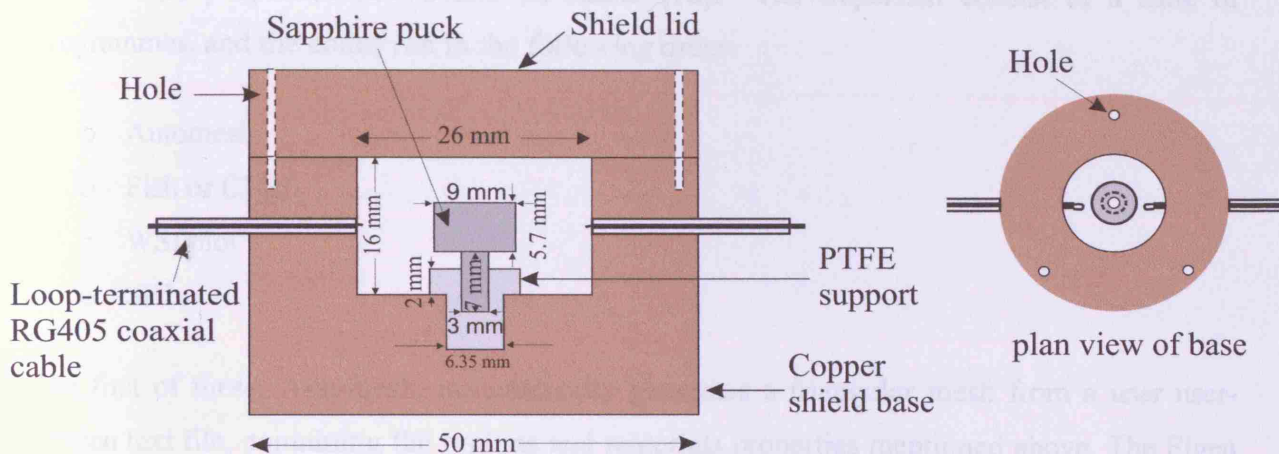


Figure 6.35 Schematic diagram of a sapphire dielectric resonator.

The approximate resonant frequency of the SDR under consideration was determined using Eq. (3.18) in chapter 3, which was around 10.448 GHz. This value of f_0 was used as a starting point for working out the exact resonant frequency with the aid of Superfish, as detailed in the following section.

6.4.2 Superfish Analysis of SDR

Superfish is a freely available package which employs finite element methods to solve the resonant frequencies and field distributions in a radio-frequency (RF) cavity with 2D Cartesian or 3D cylindrical symmetry [18]. The original Superfish codes were written by Holsinger in collaboration with Halbach [19], who developed the theory, in the 1970s. The package was produced by Los Alamos National Laboratory (LANL), which is operated by the University of California for the U.S. Department of Energy. For several years, the Los Alamos Accelerator Code Group (LAACG) maintained a standard version of Superfish for Cray, UNIX, and VAX machines. A PC version was created in 1985 when Young adapted an

older Cray version to run on IBM-PC compatible computers. A major revision (Version 5) commenced in 1992 and the codes have been under nearly continuous development since that year. The latest version is Superfish 7.18[†] that was published on 2nd February 2007 and was used in this research. Superfish is based on solving Helmholtz equation. The first stage of solving a cavity problem in Superfish is to describe the cavity layout in manner that could be used as input for the solution of the Helmholtz equation [18]. Regions containing different materials such as air, sapphire and PTFE in the SDR being analysed must be identified and the material properties (i.e. ϵ and μ) stated [18]. The Superfish consist of a suite of programmes, and the codes run in the following order:

- Automesh
- Fish or CFish
- WSFplot
- SF7

The first of these, Automesh, automatically generates a triangular mesh from a user user-written text file, containing the regions and materials properties mentioned above. The Eigen value problem is then solved by either the Fish or CFish program depending upon whether the geometry to be solved contains real or complex variables for the permittivity and permeability. Fish or CFish must be run after Automesh to determine the resonant frequency in the cavity. The Superfish code was written for problems with cylindrical symmetry, thereby implying that one half of the problem geometry needs to be specified in the user input file. In cylindrical coordinates, Fish and CFish compute solutions for the TM modes; however, Superfish can also solve for TE modes if the user interchanges E and H and applies the appropriate boundary conditions. This means swapping the material properties (i.e. $\epsilon \rightarrow \mu$ and $\mu \rightarrow \epsilon$) in the user input file for Automesh. Since the axially symmetric SDR was employed in TE₀₁₈ mode, the cylindrical coordinate system is used for its Superfish simulation and the user input text file (see appendix U) was written accordingly. Finally, Fish was run since real variables for permittivity and permeability were considered, following which, WSFplot was executed to plot the contours of the parameters rE , where E is the azimuthal electric field. These closely resemble the lines of H-field, as illustrated in fig. 6.36.

[†] This version of software can be downloaded free of cost from the website of LANL (http://laacg1.lanl.gov/laacg/services/download_sf.phtml).

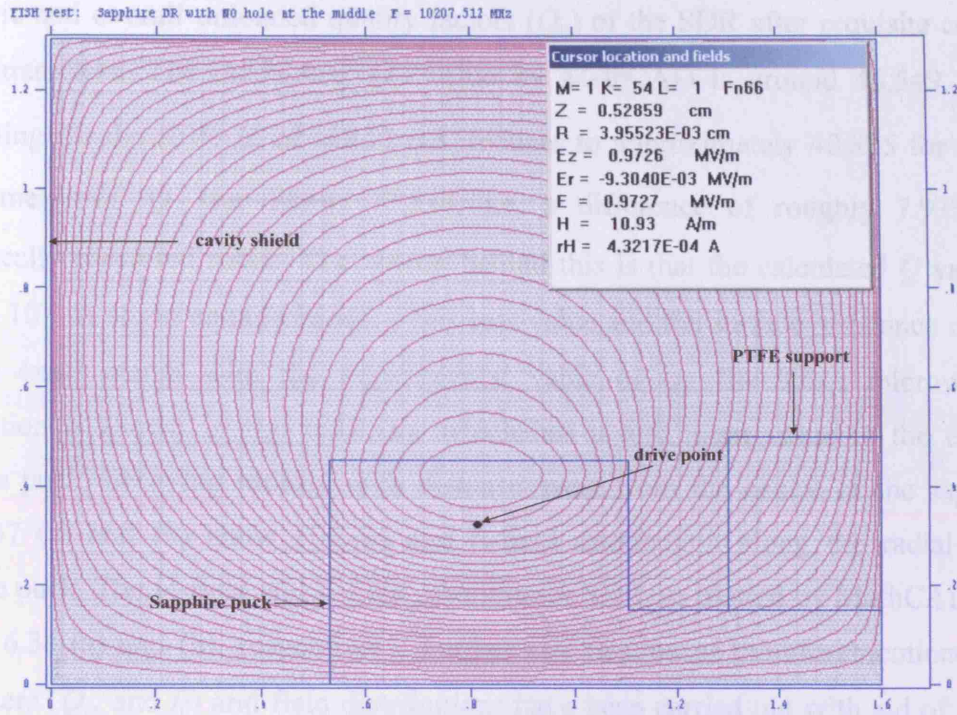


Figure 6.36 Shows the contours of the parameters rE , where E is the azimuthal electric field. These closely resemble the lines of H -field.

As expected the field is much more concentrated within the sapphire puck compared to the air region. The value of f_0 obtained from Superfish simulation was 10.208 GHz, which is very close to the measured value using a VNA.

6.4.3 Calculation of Unloaded Q Using MathCAD Program

The output result from Fish is read by the postprocessor SF7, which allows the interpolation of fields at various points. For the TE mode problem geometries, SF7 calculates the field components at a large number of user defined points, which are then numerically integrated to calculate the quantities such as conductor losses on the wall of the enclosure and the energy stored in the cavity. SF7 writes file OUTSF7.TXT that contains a table of fields at the requested coordinates r and z (or x and y) coordinates[‡]. For RF problems in cylindrical coordinates the code reports E_z , E_r , E and H_ϕ , which have to be converted to their complementary quantities (i.e. H_z , H_r , H and E_ϕ). In this research, results from OUTSF7.TXT file were input into a MathCAD code (see Appendix P) that worked out the conductor,

[‡] In Superfish, the cylindrical coordinates are designated as z , r , and ϕ as against the normal convention of z , ρ , and ϕ adapted by most standard texts.

dielectric and overall unloaded quality factors (Q_u) of the SDR after requisite conversion of field parameters. The calculated Q_u value by MathCAD is around 46,549, which after accounting for the SDR IL of -18.22 dB, reduces to approximately 40,835 for the Q_L . The actual measured Q was about 37,834, i.e. a difference of roughly 7.93% from the theoretically predicted result. The reason behind this is that the calculated Q value assumes $\tan \delta \approx 10^{-5}$. A slight enhancement of this loss value and the surface resistance of the copper provide exact match with the experimental value of Q . The $TE_{01\delta}$ microwave H-field distribution is shown in fig. 6.37 (a), which has a maximum value in the centre of the sapphire puck, decaying rapidly with distance away from the centre of the sapphire puck. Fig. 6.37 (a) and (b) show H-field and E-field distribution along the radial axis of the sapphire puck. The H-field and E-field contours for SDR, as plotted by MathCAD, are shown in figs. 6.38 (a) and (b), respectively. Further clarification of the aforementioned resonator parameters (Q_u and f_0) and field distributions have been carried out with aid of Ansoft High Frequency Structure Simulator (HFSS), commercially available for the electromagnetic modelling and analysis of three dimensional structures, which was described in detail in chapter 5.

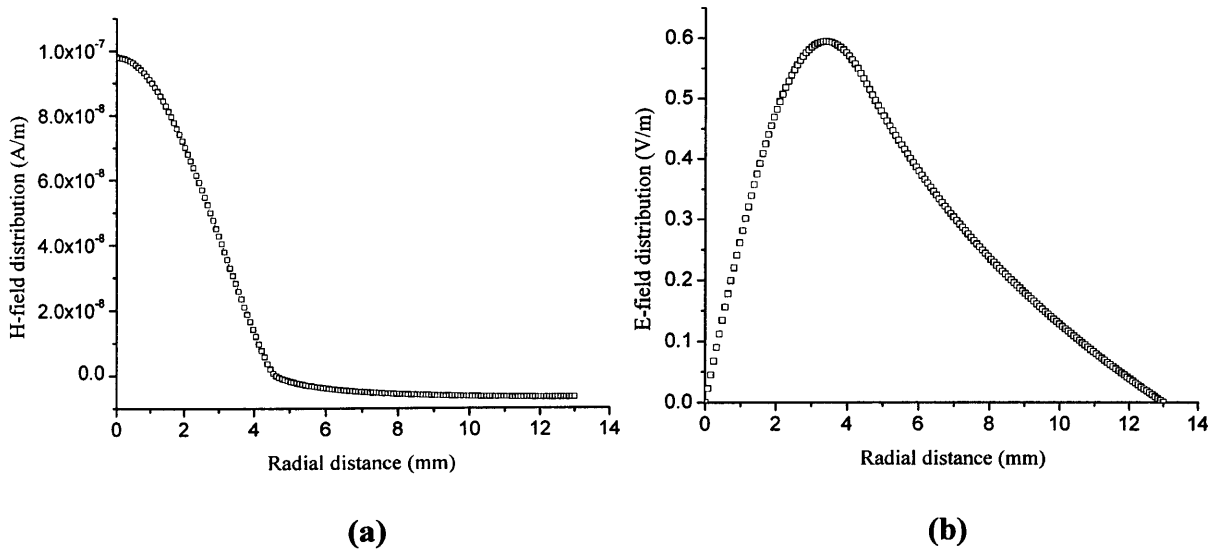


Figure 6.37 Field distributions along the radial axis of the sapphire puck.

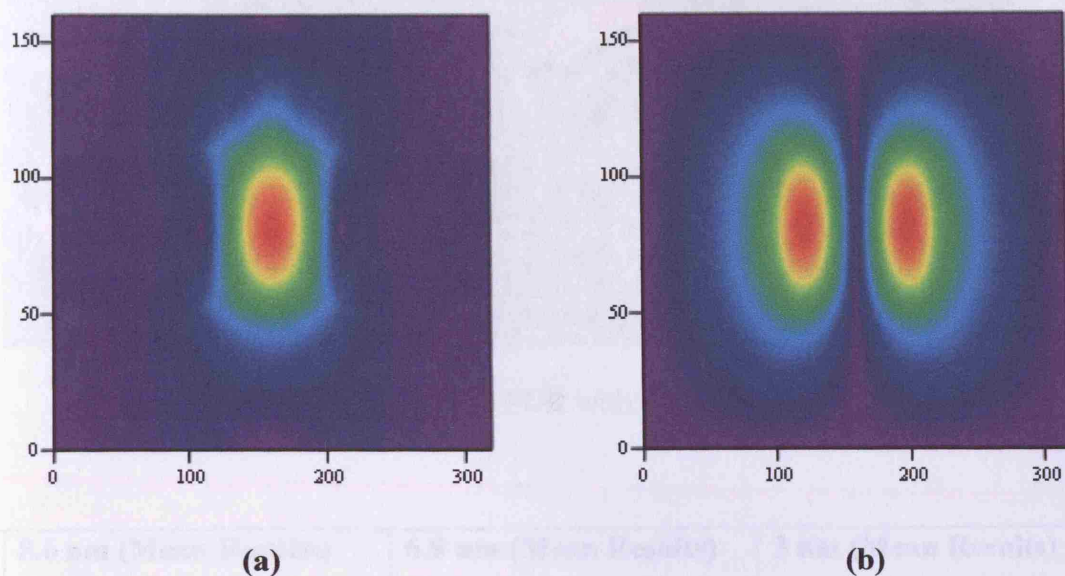


Figure 6.38 (a) H-field and (b) E-field contours in SDR computed by a MathCAD program.

6.4.4 SDR Experiment

In-situ characterisation of Pt and Au NPs were carried out with the aid of SDR. Prior to the deposition of the NPs, an ultrasound bath was used to disperse them. Then particle-loaded water droplets of volume $6\ \mu\text{l}$ were deposited directly onto the region of high magnetic field (i.e. centre of the sapphire puck as shown in fig. 6.39) in the resonator, followed by thorough drying. The measurement system is composed of two steps, each requiring experimental measurements of the f_0 and the Q_L . The Agilent Hewlett-Packard 8510C network analyser operating at transmission mode (S_{21}) was employed to measure power transmission coefficient $|S_{21}|^2$ in the frequency domain. The peak of $|S_{21}|^2$ corresponds to the resonant frequency and the quality factor is related to the 3 dB width of the $|S_{21}|^2$ response, (i.e. the half the power bandwidth). The VNA was interfaced through an IEEE-488 GPIB bus to a PC running IGOR Pro software (i.e. a scientific data analysis and programming software tool made by Wavemetrics Inc., USA), which was chosen because of its powerful built in curve fitting routines. The in-built Lorentzian curve fitting was used to extract the microwave parameters of interest such as Q_L , f_0 and bandwidth (f_B) from the VNA data.

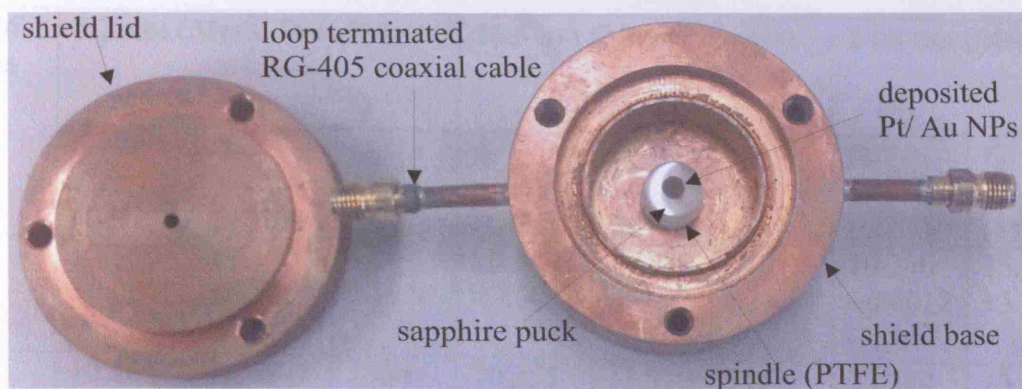


Figure 6.39 Photograph of the SDR with deposited Pt/ Au NPs.

No. of drops	8.6 nm (Mean Results)			6.9 nm (Mean Results)			3 nm (Mean Results)		
	f_0 (GHz)	f_B (MHz)	Q_L	f_0 (GHz)	f_B (MHz)	Q_L	f_0 (GHz)	f_B (MHz)	Q_L
1	10.1930 ± 0.0008	0.834 ± 0.036	12238 ± 536	10.1934 ± 0.0006	1.029 ± 0.022	9903 ± 214	10.1951 ± 0.0011	7.189 ± 0.712	1419 ± 140
2	10.1931 ± 0.0009	1.117 ± 0.064	9130 ± 521	10.1936 ± 0.0009	1.370 ± 0.090	7454 ± 490	10.1952 ± 0.0014	13.899 ± 1.155	736 ± 61
3	10.1932 ± 0.0011	1.198 ± 0.081	8510 ± 574	10.1938 ± 0.0001	1.524 ± 0.108	6705 ± 477	10.1953 ± 0.0003	23.557 ± 1.909	434 ± 35
4	10.1933 ± 0.0014	1.262 ± 0.091	8078 ± 586	10.1941 ± 0.0014	1.766 ± 0.097	5775 ± 318	10.1954 ± 0.0010	37.477 ± 2.331	275 ± 17
5	10.1935 ± 0.0012	1.424 ± 0.066	7160 ± 333	10.1942 ± 0.0011	1.948 ± 0.123	5235 ± 331	-	-	-
Empty SDR	10.1930 $\pm 2 \times 10^{-6}$	0.2762 ± 0.0001	36912 ± 8	10.1930 $\pm 8 \times 10^{-4}$	0.2726 ± 0.004	37394 ± 581	10.1949 $\pm 7 \times 10^{-5}$	0.2695 ± 0.0008	37834 ± 118

Table 6.6 Q_L , f_0 and f_B results for the Pt NPs of different sizes in the SDR. All the measurements were made at a temperature of 25 ± 3 °C. The standard deviations are estimated from the statistical average of at least three independent measurements.

No. of drops	8.2 nm (Mean Results)			16.5 nm (Mean Results)			24.8 nm (Mean Results)		
	f_0	f_B	Q_L	f_0	f_B	Q_L	f_0	f_B	Q_L
	(GHz)	(MHz)		(GHz)	(MHz)		(GHz)	(MHz)	
1	10.360 ± 0.0010	11.376 ± 0.581	911 ± 46	10.354 ± 0.0007	19.070 ± 0.053	540 ± 2	10.340 ± 0.0012	35.352 ± 3.50	293 ± 26
2	10.361 ± 0.0013	7.769 ± 0.474	1334 ± 81	10.355 ± 0.0007	11.370 ± 1.530	915 ± 125	10.344 ± 0.0014	13.735 ± 0.948	753 ± 30
3	10.362 ± 0.0014	5.737 ± 0.140	1807 ± 44	10.356 ± 0.0014	7.087 ± 0.022	1456 ± 7	10.347 ± 0.0007	9.998 ± 0.525	1035 ± 62
4	10.364 ± 0.0006	4.697 ± 0.104	2207 ± 49	10.359 ± 0.0001	5.450 ± 0.435	1899 ± 154	10.348 ± 0.0014	8.996 ± 0.568	1150 ± 92
5	10.366 ± 0.0012	3.864 ± 0.070	2683 ± 48	10.361 ± 0.0012	4.845 ± 0.688	2151 ± 308	10.350 ± 0.0010	8.243 ± 0.384	1255 ± 38
Empty SDR	10.203 $\pm 5 \times 10^{-5}$	0.2586 ± 0.0002	39461 ± 21	10.203 $\pm 2 \times 10^{-4}$	0.2555 ± 0.004	39932 ± 688	10.203 $\pm 9 \times 10^{-5}$	0.2551 ± 0.002	39993 ± 379

Table 6.7 Q_L , f_0 and f_B results for the Au NPs of different sizes in the SDR. All the measurements were made at a temperature of 24 ± 3 °C. The standard deviations are estimated from statistical average of at least three independent measurements. The Q_L of the empty resonator in this experiment is slightly different from the previous experiment (see table 6.6), since the collar/ support (i.e. made of PTFE) of the resonator was replaced with a new collar (since the previous collar was worn out).

A trial was conducted before the start of the actual experiments on the SDR to determine the measurement accuracy of the IGOR Pro code. It turned out to be that the most accurate results were obtained when firstly, the frequency span (i.e. the difference between the start and stop frequency) on the VNA was set to twice the resonator bandwidth and secondly, the $|S_{21}|^2$ plot was symmetrical with respect to f_0 . The number of points was also set to 801 points and 256 averages for HP8510C to ensure high resolution as well as stable and repeatable measurements. Initially, the experiments were carried out on different sizes of synthesised Pt NPs, from 1 drop to a maximum of 5 drops. Each droplet was found to deposit a uniform film of approximate thickness of 5 μm . The results obtained from this technique provided the motivation to characterise Au NPs of different sizes. Similarly, the experiments were carried out on different sizes of synthesised Au NPs, from 1 drop to a maximum of 5 drops. Each

droplet was found to deposit a uniform film of approximate thickness of 5 μm . Two to three set of experiments were performed depending on the amount of NPs left for both the Pt and Au NPs, and ten measurements per each particle size were taken in each set, to bear out the repeatability of results.

The mean results for the three sets of experiments for the Pt and Au NPs are depicted in tables 6.6 and 6.7, whilst variation of f_0 , Q_L and f_B are shown in figs. 6.40 through 6.45.

6.4.5 Analysis of Results

Introducing a metal disk in a region of high H-field but zero E-field should give rise to frequency increase [17], which can be evidently observed from figs. 6.40 and 6.43. In reality, the finite sample size means that there will be some E-field present at the sample which will pull down the frequency downwards a little, but nothing as large as when placing in a maximum E-field.

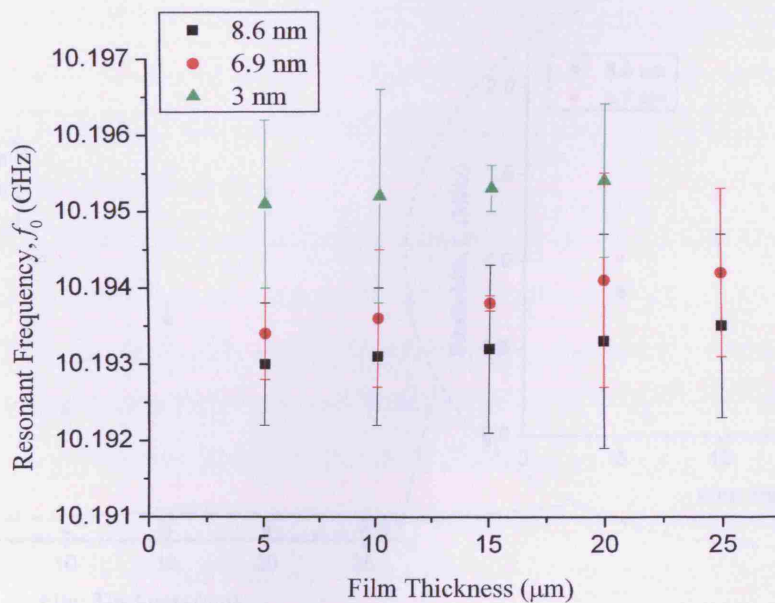


Figure 6.40 The resonant frequency as a function of different size of Pt NP films of different thickness. Error bars are estimated from the statistical average of at least three independent measurements.

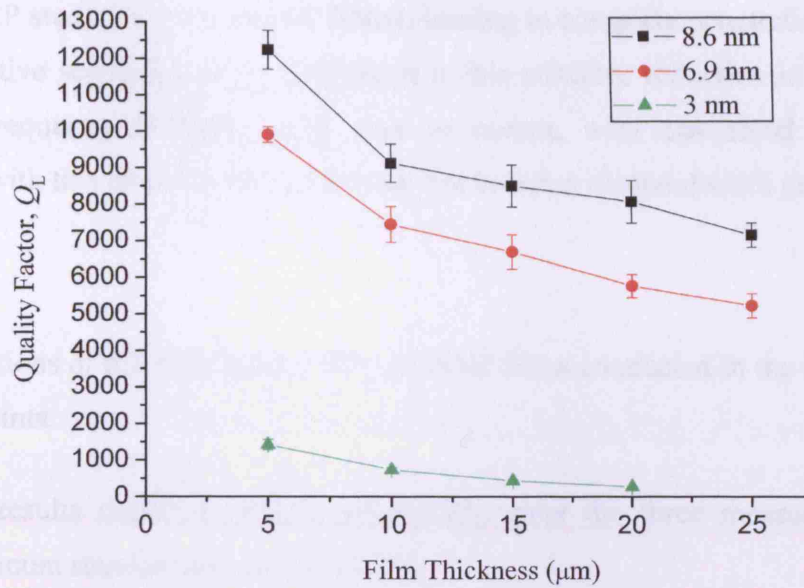


Figure 6.41 The loaded quality factor as a function of different size of Pt NP films of different thickness. Error bars are estimated from the statistical average of at least three independent measurements.

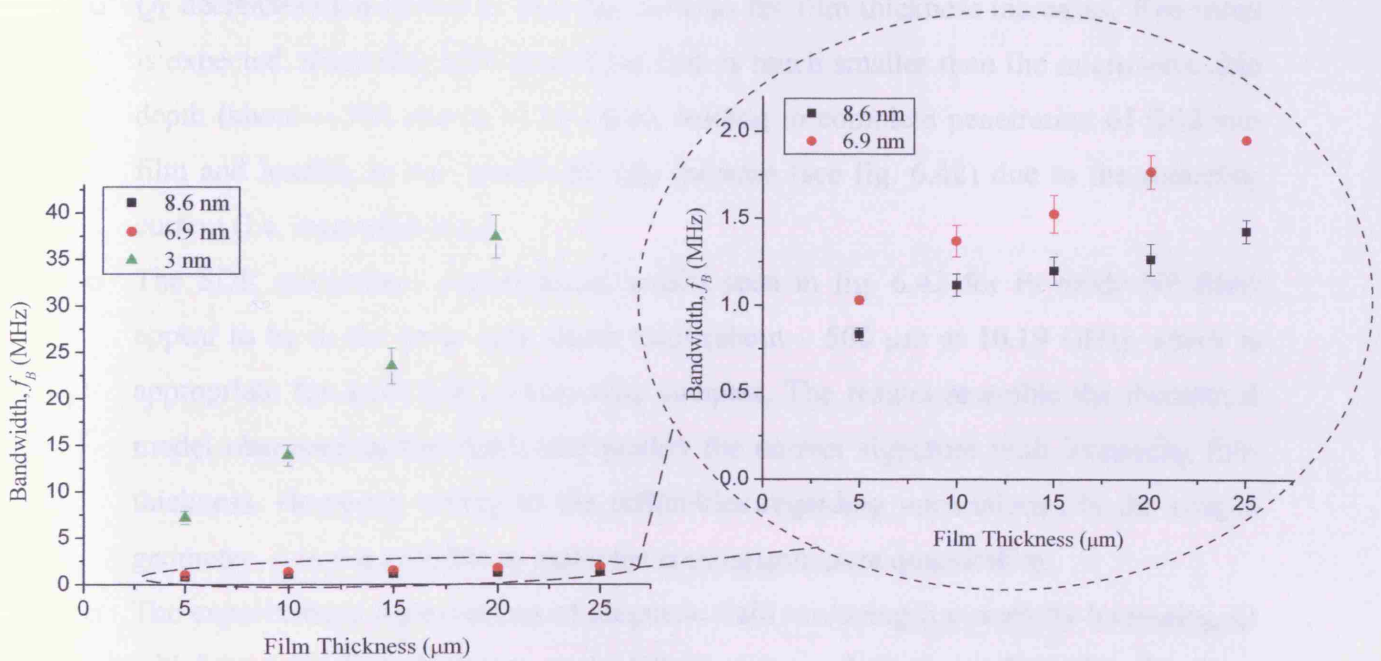


Figure 6.42 The bandwidth as a function of different size of Pt NP films of different thickness. Error bars are estimated from the statistical average of at least three independent measurements.

As shown in fig. 6.40, in the case of Pt film of increasing conductivity, the frequency increases since the thickness of the film is much smaller than the microwave skin depth (about $\sim 500 \mu\text{m}$ at 10.19 GHz for the highest value of conductivity (i.e. $\sim 100 \text{ S/m}$) obtained

from the OCP study for Pt oxide NP films), leading to complete penetration of field into film and so effective screening of the H-field. It is this effective reduction in cavity volume that gives the frequency increase, only seen in metals, with associated high conductivity. Associated with this are eddy current losses that broaden the bandwidth greatly, as observable in fig. 6.42.

Characterisations of different sizes of Pt oxide NP films conducted in the SDR bring forth the following points:

- The results depict excellent repeatability over the three measurement sets with a maximum standard deviation of 10%.
- The resonant frequency plotted in fig. 6.40 increases with the film thickness, when screening occurs (i.e. the increase in frequency is proportional to the screened volume).
- Q_L decreases monotonically (see fig. 6.41) as the film thickness increases. This result is expected, since the thickness of the film is much smaller than the microwave skin depth (about $\sim 500 \mu\text{m}$ at 10.19 GHz), leading to complete penetration of field into film and leading to the bandwidth (f_B) increase (see fig. 6.42) due to the screening current (i.e. increased loss).
- The SDR microwave experimental results seen in fig. 6.42 for Pt oxide NP films appear to be in the large skin depth limit (about $\sim 500 \mu\text{m}$ at 10.19 GHz), which is appropriate for such low conductivity samples. The results resemble the theoretical model observed in fig. 6.43, and predict the correct signature with increasing film thickness. However, owing to the difficulties regarding uncertainties in the sample geometry, it is not possible to make the comparison more quantitative.
- The experimental observations of magnetic field screening (i.e. seen by increasing f_0) with increasing film thickness on the NP films were relatively small for Pt oxide films (since the samples have low conductivity - see fig. 6.40) compared to the Au films (due to its high conductivity - see fig. 6.44). This behaviour resembles the theoretical results observed in fig. 6.43, but again detailed quantitative comparison is not possible.

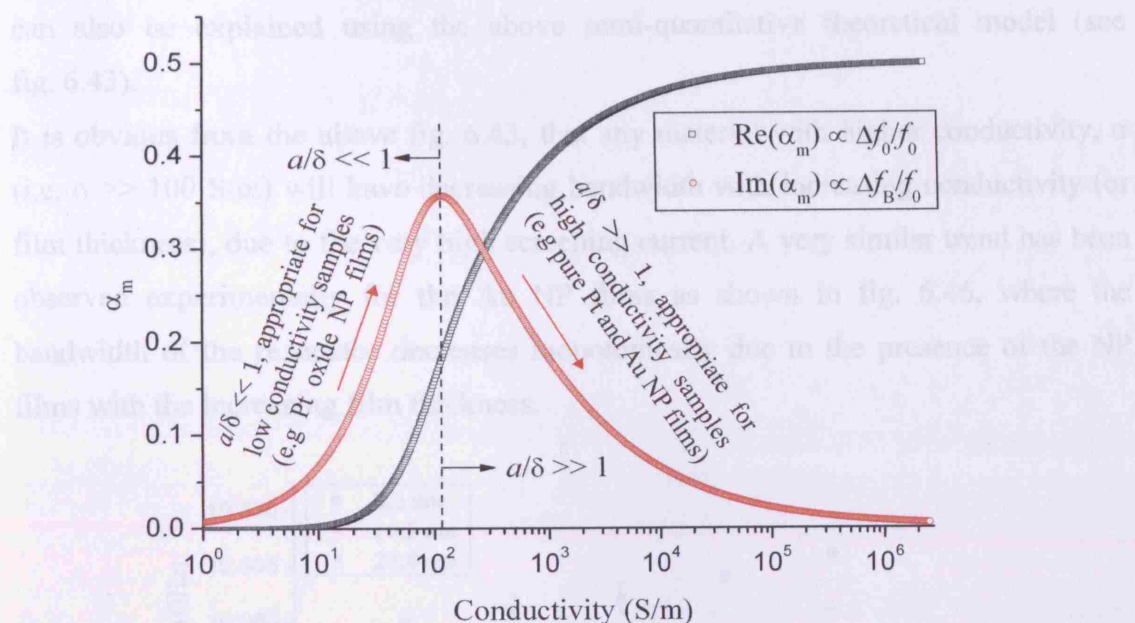


Figure 6.43 The variations of $\Delta f_0/f_0$ (screening) and $\Delta f_B/f_0$ (eddy current loss) with increasing conductivity of a sample in a resonator where the magnetic field is maximum. Where $\Delta f_0/f_0$, stands for fractional frequency shift, Δf , with respect to the resonant frequency, f_0 , and $\Delta f_B/f_0$, corresponds to the change of bandwidth, Δf_B , of the resonator with respect to the resonant frequency, f_0 , due to the presence of the sample. This graph has been directly copied from section 2.9.1, where the in-depth resonator perturbation theory behind this graph can be found.

Characterisations of different size of Au NP films conducted in the SDR bring forth the following points:

- The results depict good repeatability over the three measurement sets with a maximum standard deviation of 10%.
- The resonant frequency plotted in fig. 6.44 increases with the film thickness, when screening occurs (i.e. the increase in frequency is proportional to the screened volume). However, the screening on these NP films was relatively higher than the Pt oxide NP films due to the highly conductivity of the samples, and closely resemble the theoretical prediction as observed in fig. 6.43.
- Q_L increases monotonically (see fig. 6.45) as the film thickness increases. This result is unexpected, since the thickness of the film is much smaller than the microwave skin depth (about $\sim 150 \mu\text{m}$ at 10.3 GHz), leading to complete penetration of field into film and leading to the bandwidth (f_B) increase due to the screening current, which is also not observed experimentally (see fig. 6.46). However, these experimental results

can also be explained using the above semi-quantitative theoretical model (see fig. 6.43).

- It is obvious from the above fig. 6.43, that any material with higher conductivity, σ (i.e. $\sigma \gg 100$ S/m) will have decreasing bandwidth with increasing conductivity (or film thickness), due to the very high screening current. A very similar trend has been observed experimentally for the Au NP films as shown in fig. 6.46, where the bandwidth of the resonator decreases monotonically due to the presence of the NP films with the increasing film thickness.

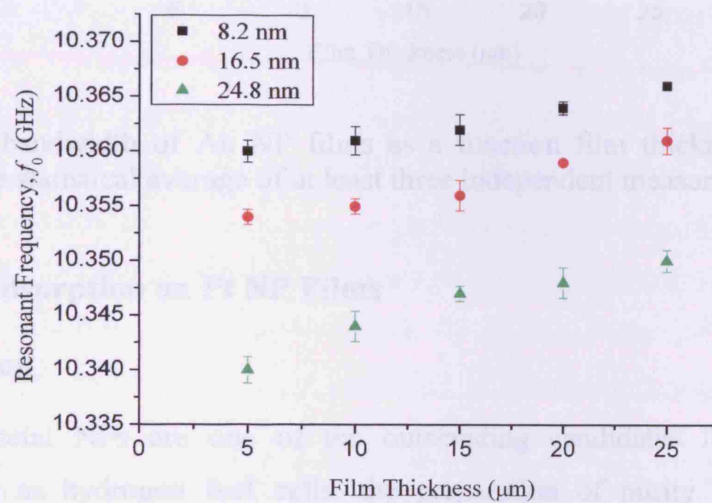


Figure 6.44 The resonant frequency of Au NP films as a function film thickness. Error bars are estimated from the statistical average of at least three independent measurements.

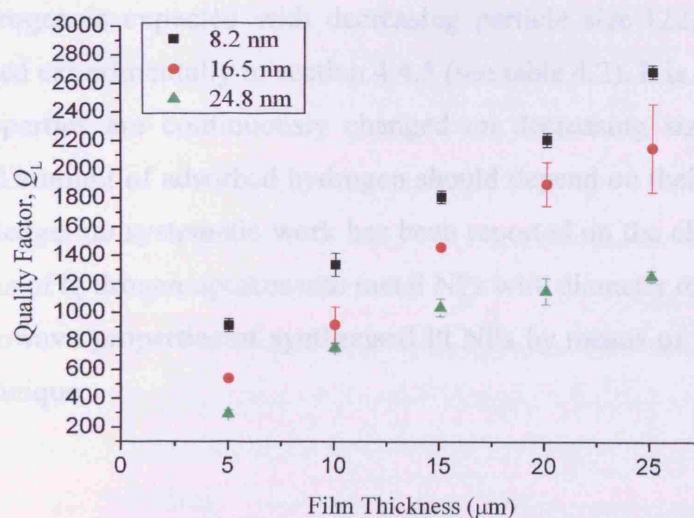


Figure 6.45 The loaded quality factor of Au NP films as a function film thickness. Error bars are estimated from the statistical average of at least three independent measurements.

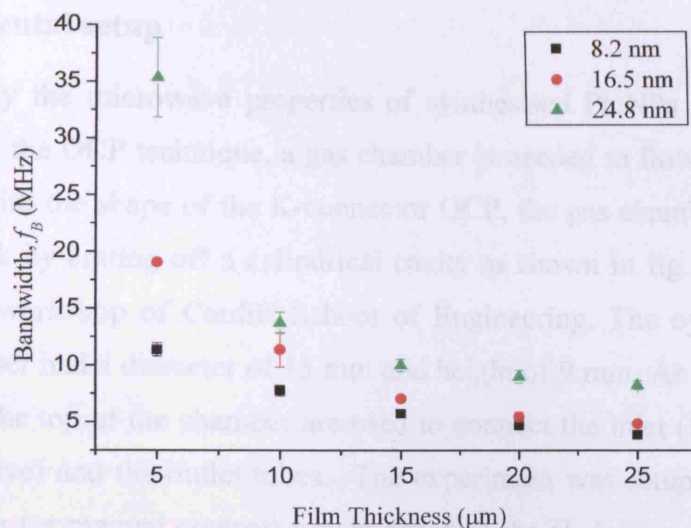


Figure 6.46 The bandwidth of Au NP films as a function film thickness. Error bars are estimated from the statistical average of at least three independent measurements.

6.5 Hydrogen Adsorption on Pt NP Films

6.5.1 Introduction

Size-controlled metal NPs are one of the outstanding candidates for wide ranges of applications such as hydrogen fuel cells, the preparation of purity hydrogen, practical hydrogen adsorbents, etc. Pt NPs can absorb a large amount of hydrogen [20]. Unlike Pt, Au does not adsorb hydrogen when it is in contact with H_2 gas [21]. Since the proportion of activated atoms on the surface increases with decreasing the size of the particles, greater adsorption of hydrogen is expected with decreasing particle size [22]; this statement has already being proved experimentally in section 4.4.5 (see table 4.2). It is also possible that the NPs, physical properties are continuously changed on decreasing size [23], because the electronic state and amount of adsorbed hydrogen should depend on their size. To the best of the author's knowledge, no systematic work has been reported on the changes of microwave properties by means of hydrogen uptakes into metal NPs with diameter of several nm. Herein, we study the microwave properties of synthesised Pt NPs by means of hydrogen adsorption using the OCP technique.

6.5.2 Experimental setup

In order to study the microwave properties of synthesised Pt NPs by means of hydrogen adsorption using the OCP technique, a gas chamber is needed to flow the gas onto the OCP. In accordance with the shape of the K-connector OCP, the gas chamber was fabricated on a cubic brass block by cutting off a cylindrical cavity as shown in fig. 6.47, manufactured by the mechanical workshop of Cardiff School of Engineering. The cylindrical cavity of the fabricated chamber had a diameter of 15 mm and height of 9 mm. As shown in fig. 6.47, two holes drilled in the top of the chamber are used to connect the inlet (i.e. connected to the H₂ lecture bottle valve) and the outlet tubes. The experiment was setup as shown in fig. 6.48, where a regulator (or manual control) was attached to the H₂ lecture bottle valve prior to its usage to (make sure the outlet of the control is closed prior to opening the lecture bottle valve). Both the gas chamber and the OCP were held tightly by the four screws along with the O-ring (i.e. air tight, thus minimising the gas leakage). In connection with the health and safety, the H₂ gas flowing through the chamber on the NPs was collected through the outlet tube attached to a beaker containing water (i.e. H₂ dissolved into the water is therefore not exposed to the environment). Here, we have performed measurements on Pt NP films as a function of film thickness for films composed of three different particle sizes. All measurements are performed using a HP8753E network analyzer from 30 MHz to 6 GHz, with the system calibrated to the connector plane AB using factory standards. The reflection coefficient (ρ_{material}) of the Pt NP films upon exposure to H₂ gas was monitored using the dynamic flow arrangement shown in fig. 6.48. The integrated PC of the VNA was used to run Agilent IntuiLink connectivity software, which is a free connectivity software developed by Agilent Technologies to gather the measurement (i.e. S_{11}) data to PC. Initially few readings were taken without the exposure of H₂ on the Pt NPs and followed by H₂ exposure until no changes were seen in the Smith chart (i.e. S_{11} data) of the VNA. The H₂ gas was exposed to the Pt NP film for a minute, where most of the reductions of the Pt metal took place in the first 40-60 seconds, resulting in permanently reduced Pt films. The raw data obtained from this experiment were input into the same MathCAD program (see appendix V) that worked out the sheet conductance as a function of films thickness. The DC conductance ($G_s = 1/R_s$) was measured by means of the DMM using the same setup mentioned in section 6.3.3 after the H₂ exposure on the NP films. Three set of experiments were performed for the Pt NP films and ten to fifteen measurements per each particle size were taken in each set, to bear out the repeatability of results.

The mean results for the three sets of experiments for the Pt NPs are depicted in table 6.8, where the DC resistance and microwave conductance for different sizes of Pt NPs as a function of films thickness are listed.

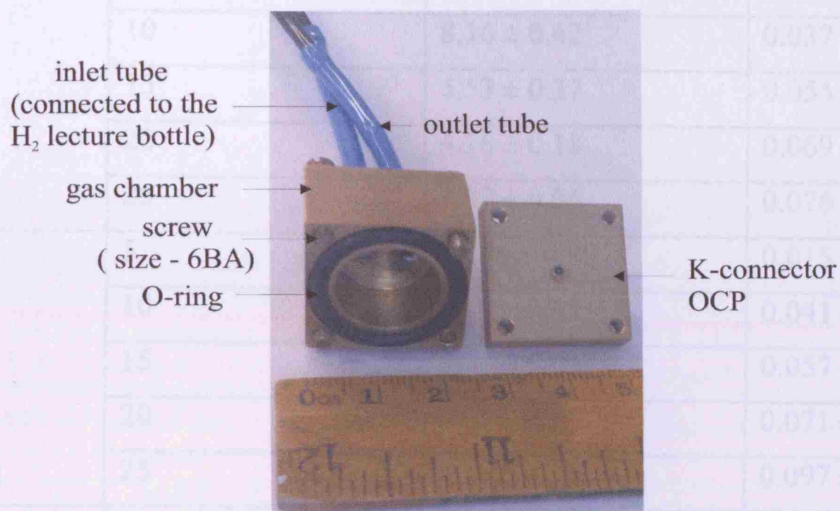


Figure 6.47 Photograph of the gas chamber along with the K-connector OCP.

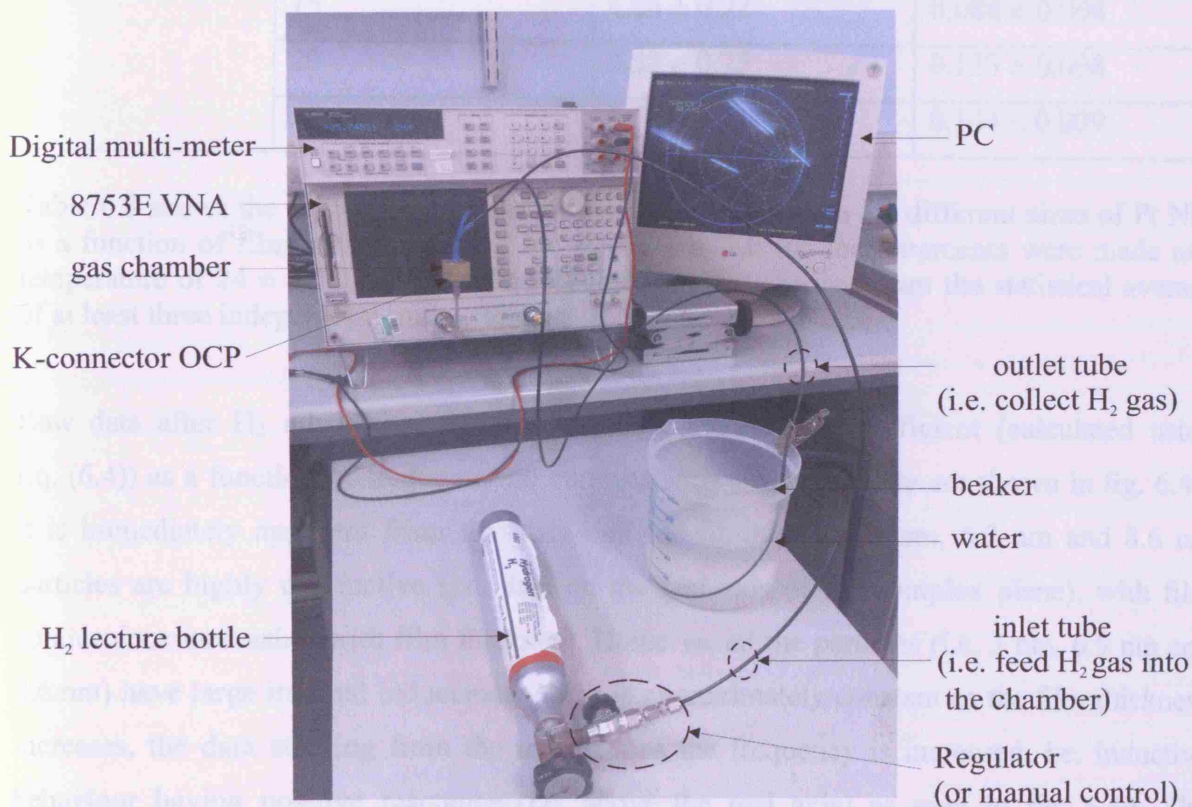
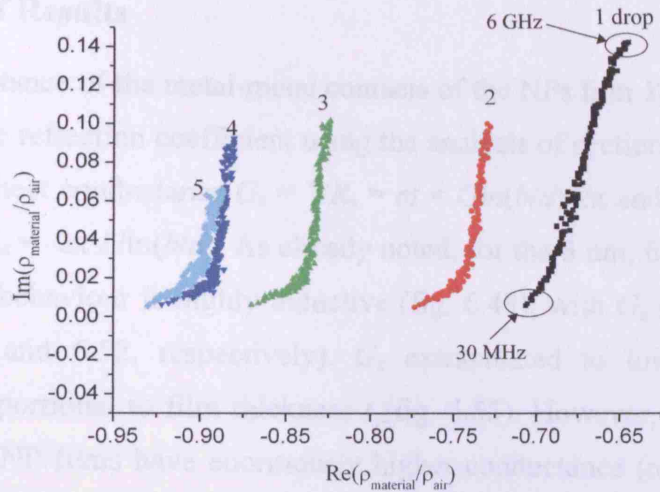


Figure 6.48 Experimental set up for measuring the microwave properties of the Pt NPs as a function of film thickness upon exposure to H₂ gas.

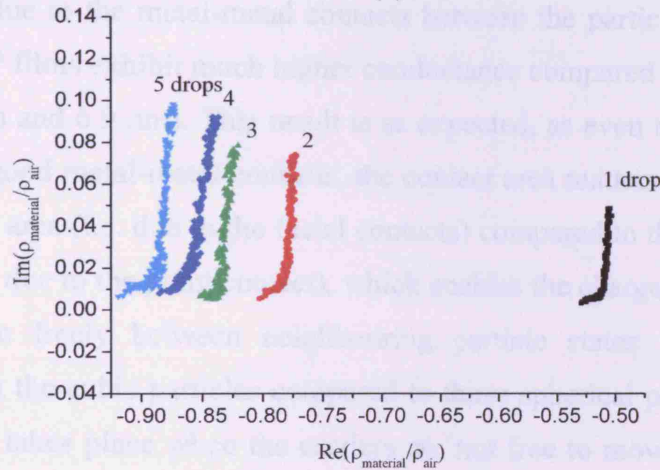
Pt NPs	Films Thickness (μm)	DC Resistance (Ohm)	Microwave conductance (S)
3 nm	5	17.63 ± 2.44	0.015 ± 0.001
	10	8.16 ± 0.42	0.037 ± 0.004
	15	5.53 ± 0.37	0.055 ± 0.002
	20	4.16 ± 0.18	0.069 ± 0.006
	25	3.87 ± 0.06	0.076 ± 0.006
6.9 nm	5	15.66 ± 0.90	0.015 ± 0.001
	10	7.39 ± 0.05	0.041 ± 0.001
	15	4.91 ± 0.03	0.057 ± 0.001
	20	4.15 ± 0.12	0.071 ± 0.003
	25	3.23 ± 0.13	0.097 ± 0.006
8.6 nm	5	5.96 ± 0.04	0.047 ± 0.002
	10	4.51 ± 0.13	0.071 ± 0.004
	15	4.04 ± 0.22	0.088 ± 0.004
	20	3.58 ± 0.25	0.133 ± 0.008
	25	3.52 ± 0.21	0.144 ± 0.009

Table 6.8 shows the DC resistance and microwave conductance for different sizes of Pt NPs as a function of films thickness after H_2 adsorption. All the measurements were made at a temperature of 24 ± 3 °C. The standard deviations are estimated from the statistical average of at least three independent measurements.

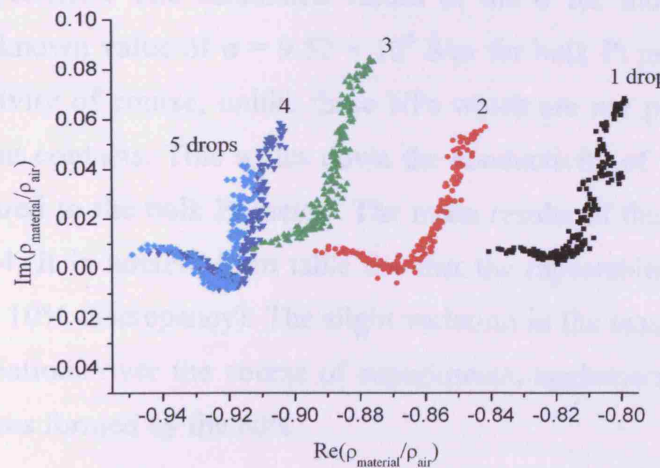
Raw data after H_2 adsorption for the normalized reflection coefficient (calculated using Eq. (6.4)) as a function of frequency for films of each size of particle are shown in fig. 6.49. It is immediately apparent from this data that the films of the 3 nm, 6.9 nm and 8.6 nm particles are highly conductive (i.e. data on the real axis of the complex plane), with film conductance increasing with film thickness. However, all the particles (i.e. 3 nm, 6.9 nm and 8.6 nm) have large internal inductance which is approximately constant as the film thickness increases, the data straying from the real axis as the frequency is increased, i.e. inductive behaviour having positive reactance (i.e. above the real axis) as seen in fig. 6.49. The existence of the inductance with increased film thickness is due the high density of metal-metal contacts between the NPs.



(a)



(b)



(c)

Figure 6.49 Reflection coefficient ratio (Eq. (6.4)) as a function of frequency for Pt NPs films of particle size (a) 3 nm (b) 6.9 nm and (c) 8.6 nm. Each drop deposits a uniform film of thickness approximately 5 μm . Measurements were taken from 30 MHz to 6 GHz. The trend is shown in fig. 6.49 (a), which repeats for all plots.

6.5.3 Analysis of Results

The internal inductance of the metal-metal contacts of the NPs film $Y_s = (Z_s)^{-1} = (R + j\omega L)^{-1}$ is computed from the reflection coefficient using the analysis of section 6.2. The resistance R is converted into a sheet conductance $G_s = 1/R_s = \sigma t = G \ln(b/a)/2\pi$ and the inductance L into a sheet inductance $L_s = 2\pi \cdot L / \ln(b/a)$. As already noted, for the 3 nm, 6.9 nm and 8.6 nm Pt NP films $L_s \gg G_s$, the behaviour is highly inductive (fig. 6.49), with G_s dependent on frequency (figs. 6.50, 6.51 and 6.52, respectively). G_s extrapolated to low frequency ($G_s(0)$) is approximately proportional to film thickness t (fig. 6.55). However, unlike the Pt oxide NP films, the pure Pt NP films have enormously higher conductance (or conductivity). For the latter it is found experimentally that the conductance increases with increasing particle size as seen in fig. 6.55, due to the metal-metal contacts between the particles. It is noticeable that 8.6 nm cubic Pt NP films exhibit much higher conductance compared to the other spherical Pt NP films (i.e. 3 nm and 6.9 nm). This result is as expected, as even though all three sizes of Pt NPs have very good metal-metal contacts, the contact area matters. The cubic Pt NP films have larger contact area (i.e. due to the facial contacts) compared to the spherical 6.9 nm and 3 nm NP films (i.e. due to the point contact), which enables the charge carriers (Pt conduction electrons) to move freely between neighbouring particle states with significantly low impedance between the cubic particles compared to those spherical particles. The dispersion in the conductance takes place when the carriers are not free to move through the particles. This motion is restricted by the size and the shape of the particles as well as the residues or impurities on the particles. The calculated values of the σ for those Pt NPs are smaller compared with the known value of $\sigma = 9.52 \times 10^6$ S/m for bulk Pt metal. The bulk material has perfect connectivity of course, unlike these NPs which are not perfectly connected, but have very good point contacts. This scales down the conductivity of these Pt NP films by a factor of 10^3 compared to the bulk Pt metal. The mean results of the sheet conductance are depicted in table 6.4. It is notable from table 6.4 that the repeatability of measurements is much better (within 10% discrepancy). The slight variation in the results can be attributed to the temperature variations over the course of experiments, agglomeration of NPs and non-uniformity of the films formed by the NPs.

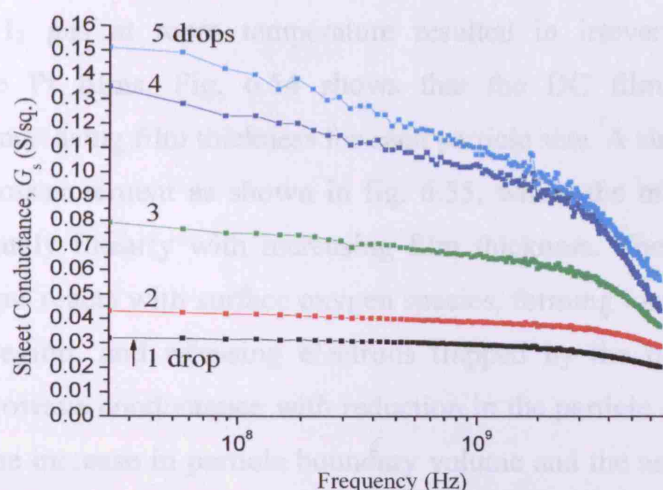


Figure 6.50 Sheet conductance as a function of frequency for 3 nm Pt films after the H_2 adsorption.

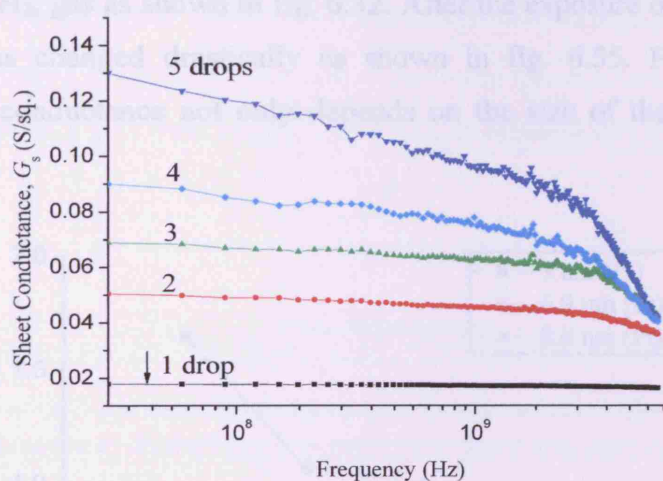


Figure 6.51 Sheet conductance as a function of frequency for 6.9 nm Pt films after the H_2 adsorption.

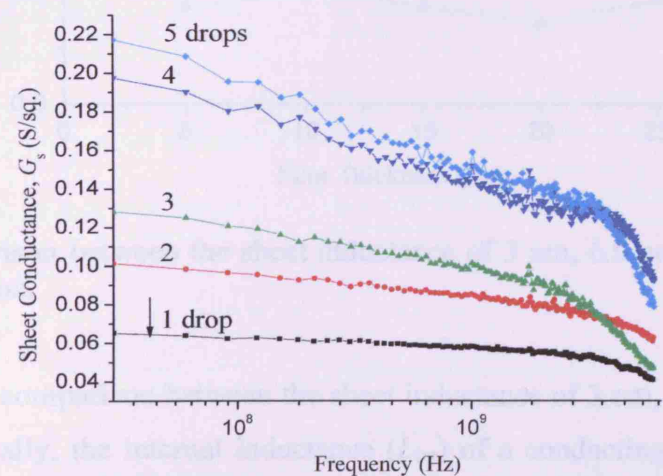


Figure 6.52 Sheet conductance as a function of frequency for 8.6 nm Pt films after the H_2 adsorption.

The exposure to H_2 gas at room temperature resulted in irreversible changes in the conductance of the Pt films. Fig. 6.54 shows that the DC film resistance decreases exponentially with increasing film thickness for each particle size. A similar trend is observed for the microwave measurement as shown in fig. 6.55, where the microwave conductance increases approximately linearly with increasing film thickness. The conductivity of PtO_2 increases when H_2 gas reacts with surface oxygen species, forming ionized oxygen vacancies in the subsurface region, and releasing electrons trapped by the oxygen adsorbate. The decrease in the microwave conductance with reduction in the particle size may be due to the size effects. Also, the increase in particle boundary volume and the associated impedance to the flow of charge carriers in small particle films will decrease the conductance. Both the DC and microwave conductances of 6.9 nm and 8.6 nm Pt NPs were close to each other before the exposure of the H_2 gas as shown in fig. 6.32. After the exposure of the H_2 on these NPs, the conductance has changed drastically as shown in fig. 6.55. From this it could be concluded that the conductance not only depends on the size of the NPs but also on the structure of the NPs.

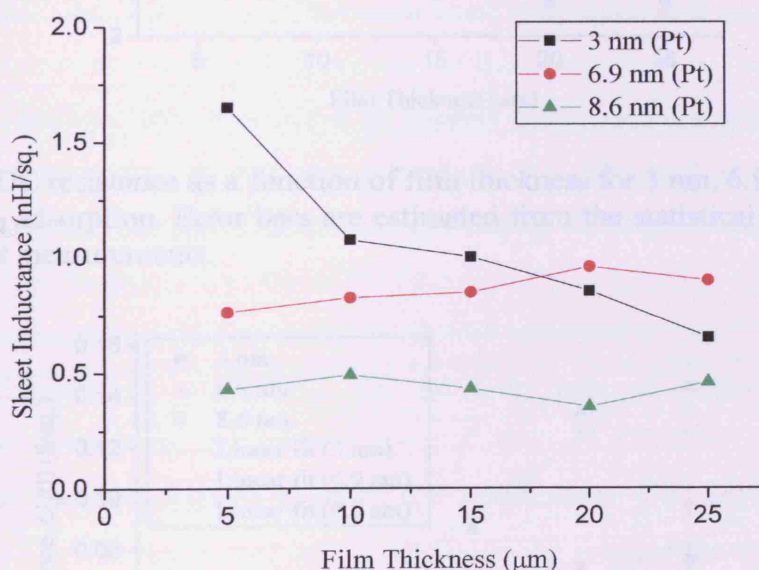


Figure 6.53 Comparison between the sheet inductance of 3 nm, 6.9 nm and 8.6 nm Pt films after the H_2 adsorption.

Fig. 6.53 shows the comparison between the sheet inductance of 3 nm, 6.9 nm and 8.6 nm Pt NP films. Theoretically, the internal inductance (L_{int}) of a conducting film (where the skin depth (δ) \ll thickness of the film (t)) with thickness t , width, w , and length l could derived as

$L_{\text{int}} = \mu_0 \delta \frac{l}{w}$ (detailed analysis is presented in appendix W), it is apparent from this expression that the internal conductance is independent of the film thickness (t). As it is apparent from the above experimental results (see fig. 6.53), the internal inductance of all three Pt NP films are approximately independent of the film thickness and increases with decreasing film thickness due to the high density of metal-metal contacts between the particles. Note that the 5 μm thick film of 3 nm Pt NPs exhibits an unusual internal inductance behaviour assumed to be due to the poor connectivity between the particles.

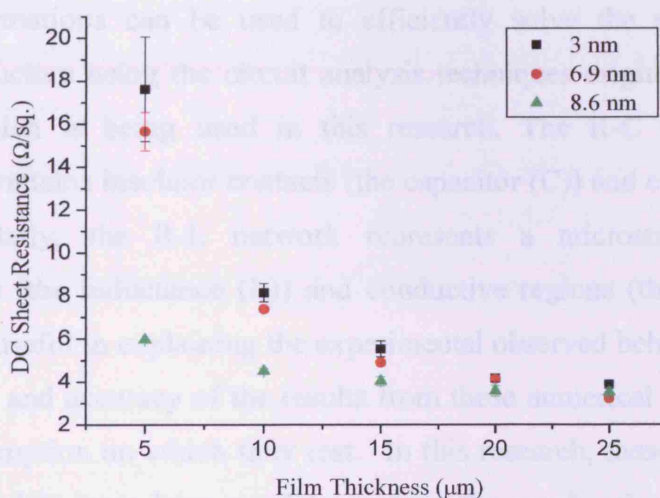


Figure 6.54 The DC resistance as a function of film thickness for 3 nm, 6.9 nm and 8.6 nm Pt films after the H_2 adsorption. Error bars are estimated from the statistical average of at least three independent measurements.

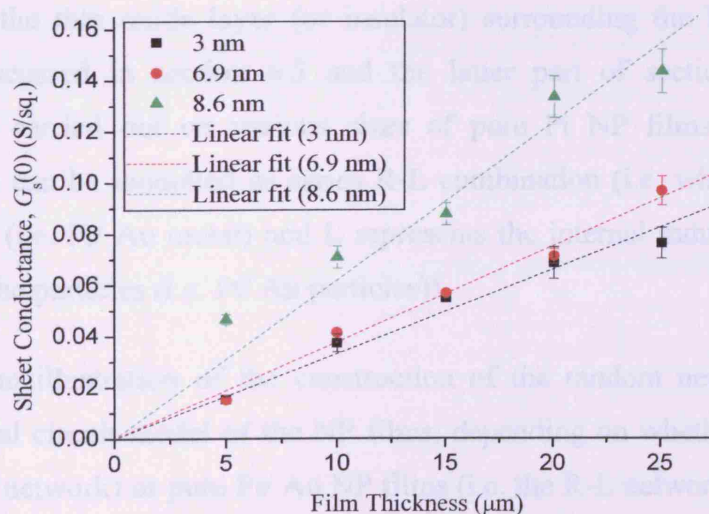


Figure 6.55 The extrapolated low frequency sheet conductance as a function of film thickness for 3 nm, 6.9 nm and 8.6 nm Pt films after the H_2 adsorption. Error bars are estimated from the statistical average of at least three independent measurements.

6.6 Random Network Circuit Construction

The experimental microwave studies have shown that simple modelling based on random network arrangement of NPs would provide a comprehensive description of electrical properties of a microstructure of a real two-phase (i.e. conductor-insulator) composite material system across a wide range of frequencies. The electrical response of large networks of randomly positioned resistors and capacitors were initially, obtained using commercial circuit simulation software [24, 25, 26]. There are many advantages of using these network systems to represent material properties. Particularly, for bounded 2D square lattice networks, equivalence transformations can be used to efficiently solve the system by taking the advantage of the structure using the circuit analysis techniques originally devised by Frank and Lobb [27], which is being used in this research. The R-C network represents a microstructure that contains insulator contacts (the capacitor (C)) and conductive regions (the resistor (R)). Similarly, the R-L network represents a microstructure that contains metal-metal contacts (the inductance (L)) and conductive regions (the resistor (R)). These networks have been useful in explaining the experimental observed behaviour of the material; however the validity and accuracy of the results from these numerical models depend on the accuracy of the assumption on which they rest. In this research, these simulation results of the two network models have been used to support the results signatures observed from microwave experiments for Pt and Au NP films. As discussed in section 6.3.1, the experiments were carried out on different sizes of Pt oxide NPs films, which can be modelled as a parallel R-C combination (i.e. where R represents the conductive region (i.e. Pt metal) and C represents the thin oxide layer (or insulator) surrounding the Pt NPs as shown in fig. 6.17). As discussed in section 6.5 and the latter part of section 6.3.2, where the experiments were carried out on various sizes of pure Pt NP films and Au NP films, respectively, these can be modelled as series R-L combination (i.e. where R represents the conductive region (i.e. Pt/ Au metal) and L represents the internal inductance of the metal-metal contacts of the particles (i.e. Pt/ Au particles)).

Fig. 6.56 shows an illustration of the construction of the random network circuits as an equivalent electrical circuit model of the NP films, depending on whether it is Pt oxide NP films (i.e. the R-C network) or pure Pt/ Au NP films (i.e. the R-L network). Analyses of their electrical behaviour with frequency of both circuits were constructed using a MATLAB program. The MATLAB script was originally written by Daniel Slocombe (PhD student,

Cardiff School of Engineering) and suitably modified by the author. The MATLAB script allowed a large number (225) of circuits to be produced quickly and efficiently. The script had input variables for the circuit size (i.e. values of R and C, or R and L). In the R-C and R-L networks presented in this research the values of the resistances, capacitances, and inductances were the same values as obtained from the microwave experiments (see appendix X). The MATLAB script constructed a network of components from its top left corner (see appendix Y). All the vertical and horizontal components were placed with both R and C in parallel (i.e. for Pt oxide films) or R and L in series (i.e. for Pure Pt and Au films). The components were placed between 'nodes'. The nodes can be visualised as a square grid/lattice of dots. The script inserted R and C in parallel or R and L in series randomly between these nodes with the values of the R, C and L being defined at the beginning of the construction, which are those values obtained from the microwave experiments with a random standard deviation. In all cases the frequency is varied from 1 Hz to 6 GHz, similar frequency range analysed in the microwave experiment.

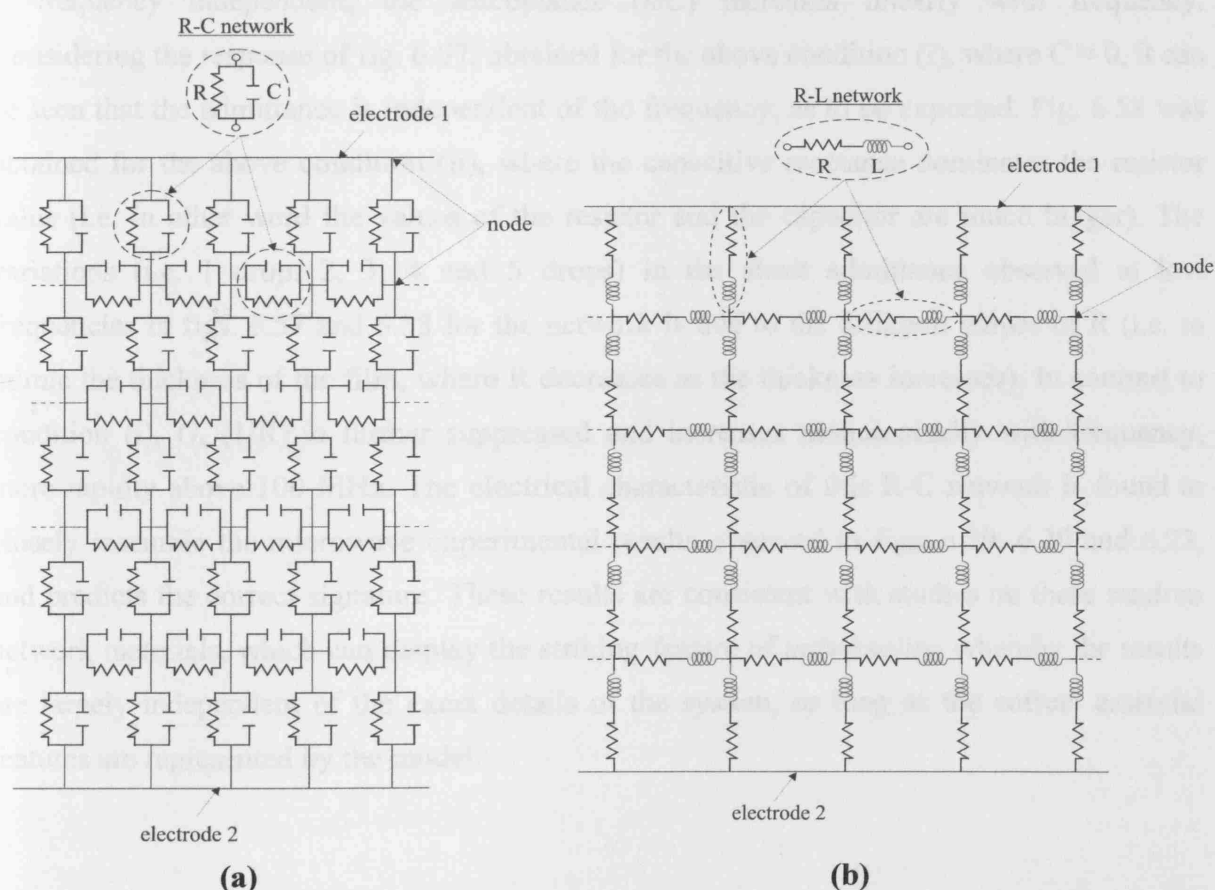


Figure 6.56 Illustration of 5×5 random (a) R-C network and (b) R-L network. An example of 5×5 random R-C network and R-L network is shown above, although the actual network used in this research is much larger (15×15).

6.6.1 Typical Response of the R-C Network

The following results are obtained for the case of Pt oxide NPs films for two different compositions of resistors and capacitors, namely

- i. In the case of 3 nm and 6.9 nm Pt oxide films where the sheet conductance ($G_s = 1/R$) is much larger than the sheet susceptance ($B_s = \omega C$), i.e. $1/R \gg \omega C$, with capacitance is approximately zero.
- ii. In the case of 8.6 nm Pt oxide films, where sheet susceptance is much larger than the sheet conductance (i.e. $\omega C \gg 1/R$).

The frequency dependent admittance ($Y = G + jB$) plotted is presented in figs. 6.57 and 6.58. This data has been generated from the data of 255 individual network MATLAB simulations for the combination of parallel R and C with a side length of 15 components. To understand the plots emerging from these graphs, it is important to note that while the conductance ($1/R$) is frequency independent, the susceptance (ωC) increases linearly with frequency. Considering the response of fig. 6.57, obtained for the above condition (i), where $C \approx 0$, it can be seen that the admittance is independent of the frequency, as to be expected. Fig. 6.58 was obtained for the above condition (ii), where the capacitive reactance dominates the resistor value (i.e. in other word the values of the resistor and the capacitor are much bigger). The variations (i.e. 1 drop, 2, 3, 4 and 5 drops) in the sheet admittance observed at low frequencies in figs. 6.57 and 6.58 for the network is due to the different values of R (i.e. to mimic the thickness of the film, where R decreases as the thickness increases). In contrast to condition (i), G_s ($1/R$) is further suppressed and increases monotonically with frequency, more rapidly above 100 MHz. The electrical characteristic of this R-C network is found to closely resemble the microwave experimental results observed in figs. 6.19, 6.20 and 6.22, and predicts the correct signature. These results are consistent with studies on these random network materials, which can display the striking feature of *universality*, whereby the results are largely independent of the exact details of the system, so long as the correct essential features are represented by the model.

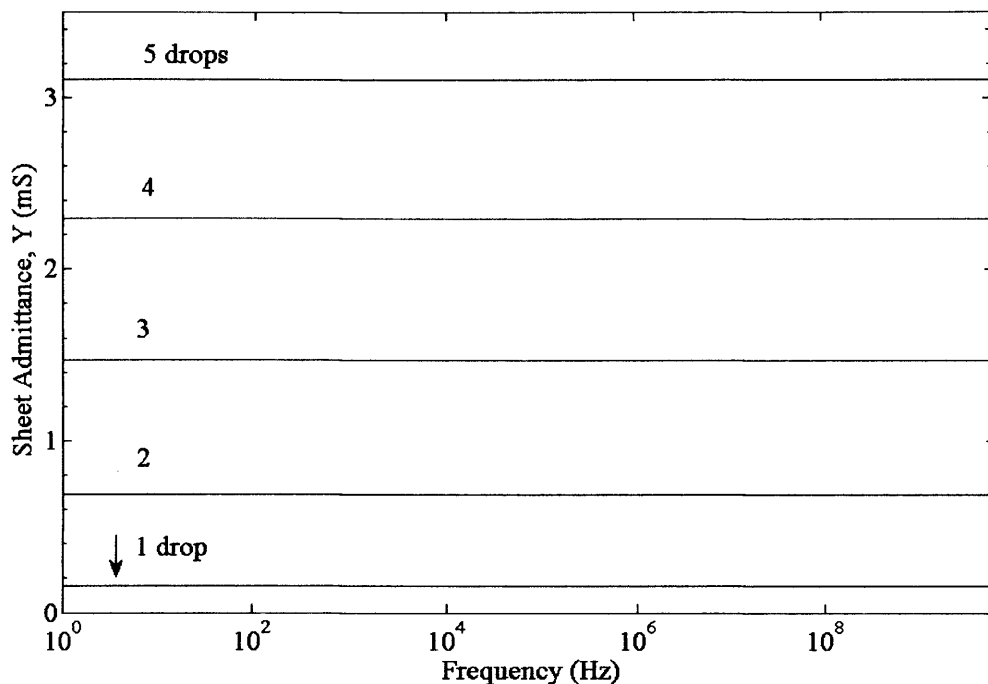


Figure 6.57 Sheet admittance (Y) as a function of frequency representing condition (i), where $1/R \gg \omega C$, with capacitance (C) of approximately zero. This graph closely resembles the sheet conductance obtained for 3 nm and 6.9 nm Pt oxide NP films from microwave experiments.

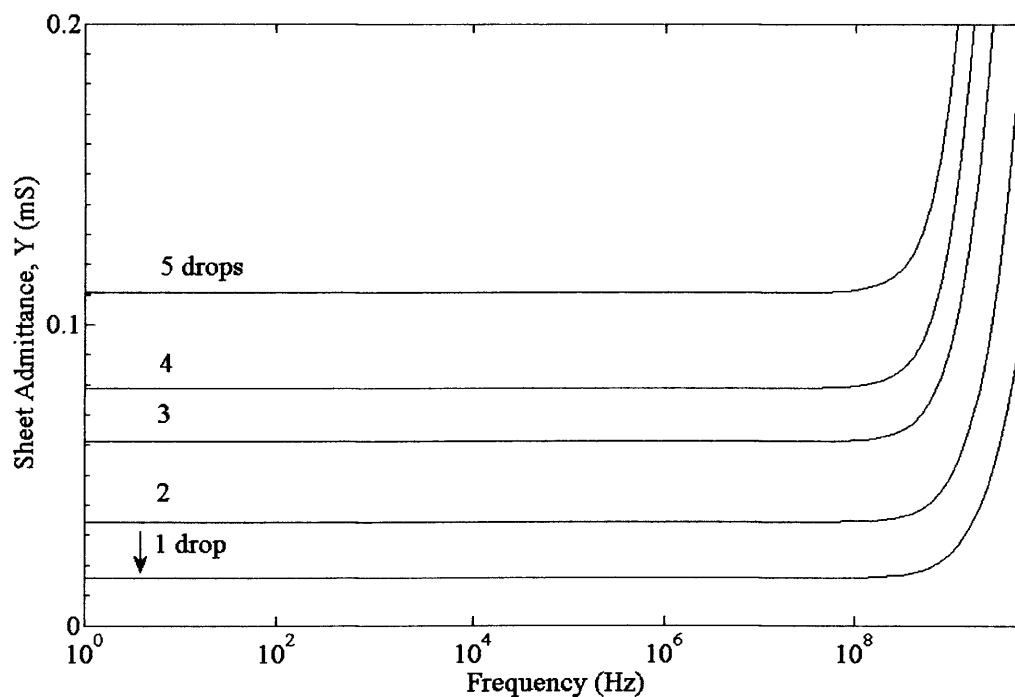


Figure 6.58 Sheet admittance (Y) as a function of frequency representing condition (ii), where $\omega C \gg 1/R$, with the values of C and R are taken from experiments. This graph closely resembles the sheet conductance obtained for 8.6 nm Pt oxide NP films from microwave experiments.

6.6.2 Typical Response of R-L Network

The frequency dependent admittance ($Y = Z^{-1} = (R + j\omega L)^{-1}$) plotted as a function of R and L is presented in fig. 6.59. The following result is obtained for the case of pure Pt and Au NP films for the following composition of resistors and inductors.

- i. In the case of Pt (i.e. 3 nm, 6.9 nm and 8.6 nm) NP films after the H₂ adsorption and Au (i.e. 16.5 nm and 24.8 nm) NPs film, where in both instances the sheet inductance (L) is much larger than the sheet conductance due to the metal-metal contacts, i.e. $\omega L \gg 1/R$.

Similar to R-C network model, fig. 6.59 has been generated from the data of MATLAB simulations of 255 individual networks with unit cells composed of series R and L with a side length of 15 components (i.e. series R and L). Consider the response of fig. 6.59, obtained from the above condition (i), where L varies from 0.5 nH to 3 nH (see appendix X). The variations (i.e. 1 drop, 2, 3, 4 and 5 drops) in the sheet admittance observed at the low frequencies in fig. 6.59 for the network is due to the different values of R (i.e. to mimic the thickness of the film, where R decreases as the thickness increases). The electrical characteristic of this R-L network is found to closely resemble the experimental results observed (figs. 6.50, 6.51 and 6.52), and predicts the correct signature.

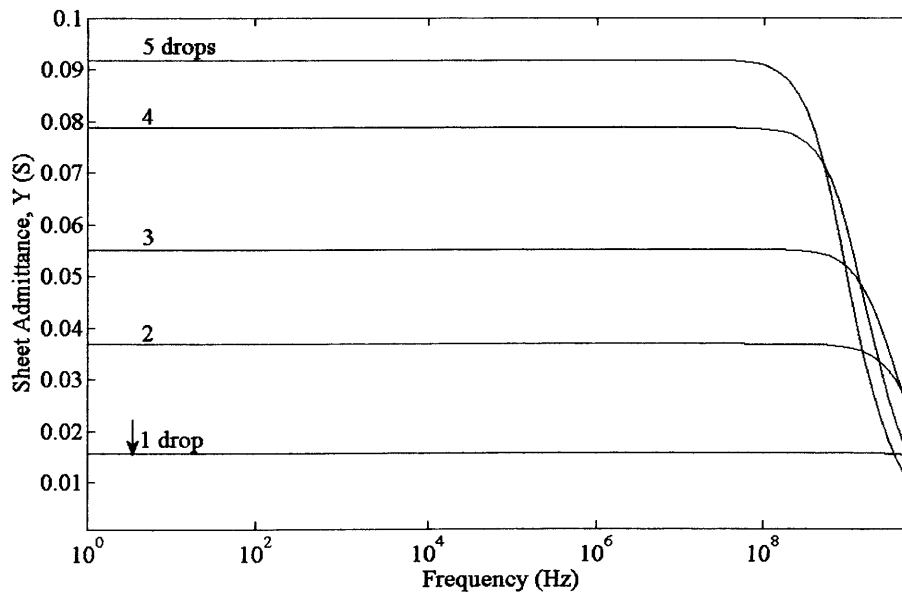


Figure 6.59 Sheet Admittance (Y) as a function of frequency representing condition (i), where $\omega L \gg 1/R$, with the values of R and L are taken from the experiments. This graph closely resembles the sheet conductance obtained for Pt and Au NP films from microwave experiments.

6.7 Chapter Summary

This chapter presents a novel technique that has been developed to perform broadband characterisation of Pt and Au NPs films composed of different sizes of particles. The implementation and validation of a full aperture admittance model (i.e. capacitive) for the miniature open ended coaxial probe (OCP), by carrying out experiments on several different dielectric materials including low, medium and high permittivity materials. Initially, electrical properties (i.e. conductivity) of Pt oxide particles were investigated using an OCP. Smaller Pt particle films (i.e. 3 nm and 6.9 nm) exhibit a frequency-independent, metal-like response, which is predominately conductive in nature, increasing approximately linearly with increasing film thickness, albeit with a massively suppressed conductivity compared to the bulk Pt metal (factor $> 10^5$) due to the inter-grain contacts between a thin oxide layer surrounding the individual particle, which acts as a capacitor. Films of larger Pt NPs (i.e. 8.6 nm cubic) have even lower conductivity; this can be understood qualitatively since although there is now a larger area of inter-grain contacts compared to the smaller particles (i.e. 3 nm and 6.9 nm spherical), due to the shape of the particle (i.e. cubic), the contact resistance will increase as the particle size is increased due to the presence of an oxide layer surrounding the particles and also there will be fewer contacts, the latter being the over-riding factor. Similarly, investigations were carried out on Au NPs films of different sizes followed by the surface modification of Pt NPs by means of hydrogen (H_2) gas adsorption. Unlike the Pt oxide NPs films, this time the Pt NP films after the H_2 adsorption and the Au NPs films were formed with metal-metal contacts, where the area of the inter-grain contacts between the particles are big for bigger particles and small for smaller particles. This allows conduction to take place more easily in the bigger NPs films compared to the smaller particle films. This eventually results in larger conductance in larger NPs compared to the smaller NP films, with conductance increasing approximately linearly with increasing thickness of the films for both types of particles (i.e. Pt and Au), albeit with a massively suppressed conductivity compared to the bulk Pt metal (factor $> 10^3$) and Au metal (factor $> 10^3$) as expected. Pt NP films after the H_2 adsorption exhibit much higher sheet conductance (G_s) compared to the Pt oxide NP films, with highly suppressed by the internal inductance due to the high density of the metal-metal contacts. The extrapolated sheet conductance at low frequency (i.e. $G_s(0)$) of those films is approximately proportional to the film thickness, and in the latter it is observed that the conductance increases with increasing particle size due to the metal-metal contacts

between the particles. Pure Pt NP films exhibit thickness independent internal inductance behaviour, which is supported by the theoretical prediction.

Single frequency measurements were carried out on Pt NP films (i.e. particles surrounded with oxide layer) and Au NPs films using SDR. The results of Pt oxide and Au films resemble the theoretical resonator perturbation model observed in fig. 6.43, and predict the correct signature with increasing film thickness. However, owing to the difficulties regarding sample geometry, it is not possible to make the comparison more quantitative. Finally, the results obtained from the microwave studies for the Pt oxide, pure Pt and Au NP films were theoretically supported with a simple modelling based on random R-C and R-L network arrangements, which closely resemble and predict the correct signature.

6.8 References

1. H.R. Levine, and C.H. Papas, "Theory of Circular Diffraction Antenna", *Journal of Applied Physics*, Vol. 22, pp. 29-43, 1951.
2. T.W. Athey, M.A. Stuchly, and S.S. Stuchly, "Measurement of Radio Frequency Permittivity of Biological Tissues with an Open-Ended Coaxial Line: Part 1 - Experimental Results". *IEEE Transaction on Microwave Theory and Techniques*, Vol. 30, No.1, pp. 82-86, January 1982.
3. X. Dong, and Y.H. Wang, "Broadband Characterisations of Material Permittivity with a Small Sized Open Ended Coaxial Probe", *ASCE Proceedings*, pp.1-5, 2006.
4. M. Moukanda, F. Ndagijimana, J. Chilo, and P. Saguet, "A Coaxial Fixture Used for Extracting Complex Permittivity of Thin Layers", *IEEE Annual on Wireless and Microwave Technology Conference*, pp. 1-5, December 2006.
5. D.K Misra, "A Quasistatic Analysis of Open-Ended Coaxial Lines", *IEEE Transaction on Microwave Theory and Techniques Society*, Vol. 35, No. 10, pp. 925-928, October 1987.
6. M. Wu, X. Yao, and L. Zhang, "An Improved Coaxial Probe Technique for Measuring Microwave Permittivity of Thin Dielectric Materials". *Measurement Science and Technology*, Vol. 11, No. 11, pp. 1617-1622, August 2000.
7. C.L. Pournaropoulos, and D.K. Misra, "A Study on the Coaxial Aperture Electromagnetic Sensor and its Application in Material Characterisation" *IEEE Transactions on Instrumentation and Measurement*, Vol. 43, No. 2, pp. 111-115, April 1994.
8. D.M. Pozar, *Microwave Engineering*, 3rd edition, John Wiley & Sons, Inc., 2005, ISBN 0-471-44878-8.
9. J. Lou, A. Hatton, and P.E. Laibinis, "Effective Dielectric Properties of Solvent Mixtures at Microwave Frequencies". *The Journal of Physical Chemistry A*, Vol. 101, No. 29, pp. 5262-5268, 1997.
10. M.N. Afsar, N. Suwanvisan, and Y. Wang, "Permittivity measurement of low and high loss liquids in the frequency range of 8 to 40 GHz using waveguide transmission line technique", *Microwave and Optical Technology Letters*, Vol. 48, No. 2, pp. 275-281, 2005.
11. S. Jenkins, T.E. Hodgetts, R.N. Clarke and A.W. Preece, "Dielectric Measurements on Reference Liquids Using Automatic Network Analysers and Calculable Geometries", *Measurement Science and Technology*, Vol. 1, pp. 691-702, August 1990.
12. W. Ronald Fawcett, *Liquids, Solutions, and Interfaces: From Classical Macroscopic Descriptions to Modern Microscopic Details*, Oxford University Press Inc., pp. 152, 2004, ISBN 0-19509-432-9.

13. K. Lamkaouchi, A. Balana, G. Delbos and W.J. Ellison, "Permittivity measurements of Lossy Liquids in the Range 26-110 GHz" *Measurement Science and Technology*, Vol. 14, pp. 444-450, 2003.
14. C. Ronne, L. Thrane, P. Astrand, A. Wallqvist, K.V. Mikkelsen and S.R. Keiding, "Investigation of the Temperature Dependence of Dielectric Relaxation in Liquids Water by THz Spectroscopy and Molecular Dynamics Simulation", *Journal of Physical Chemistry*, Vol. 107, No. 14, pp. 5319-5331, 1997.
15. D.K. Misra, "A Quasistatic Analysis of Open-Ended Coaxial Lines", *IEEE Transaction on Microwave Theory and Techniques Society*, Vol. 35, No. 10, pp. 925-928, October 1987.
16. A. Sulaimalebbe, A. Porch, F.J. Vidal-Iglesias and G. Attard, "Microwave Properties of Platinum Nanoparticles Films", *IEEE MTT-S International Microwave Symposium Digest*, pp. 1585 – 1588, June, 2008.
17. A. Porch, *Private communication*, 2008-9.
18. Reference Manual for the Poisson/ Superfish Group of Codes, *Los Alamos Accelerator Code Group, MS H829, Los Alamos National Laboratory*, January 1987.
19. K. Halbach and R.F. Holsinger, "SUPERFISH - A Computer Program for Evaluation of RF Cavities with Cylindrical Symmetry", *Particle Accelerators*, Vol. 7, pp. 213- 222, 1976.
20. H. Kobayashi, M. Yamauchi, H. Kitagawa, Y. Kubota, K. Kata and M. Takata, "Hydrogen Adsorption in the Core/Shell Interface of Pd/Pt Nanoparticles", *Journal of the American Chemical Society*, Vol. 130, No. 6, pp. 1818-1819, 2008.
21. D.P Smith, *Hydrogen in Metals*, University of Chicago Press, 1948.
22. F.J. Vidal-Iglesias, *Private communication*, 2007-8.
23. T. Teranishi, H. Hori and M. Miyake, "ESR Study on Palladium Nanoparticles", *The Journal of Physical Chemistry A*, Vol. 101, No. 30, pp. 5774-5776, 1997.
24. D.P. Almond and B. Vainas, "The Dielectric Properties of Random R–C Networks as an Explanation of the 'Universal' Power Law Dielectric Response of Solids", *Journal of Physics: Condensed Matter*, Vol. 11, No. 46, pp. 9081-9093, 1999.
25. B. Vainas, D.P. Almond, J. Luo, R. Stevens, "An Evaluation of Random R-C Networks for Modelling the Bulk ac Electrical Response", *Solid State Ionics*, Vol. 126, No. 1-2, pp. 65-80, 1999.
26. SIMetrix, Newbury Technology Ltd, Thatcham, Berks, RG18 4LZ, UK.
27. D.J Frank and C.J Lobb, "Highly Efficient Algorithm for Percolative Transport Studies in Two Dimensions", *Physical Review B*, Vol. 37, No. 1, pp. 302-307, 1998.

CHAPTER 7

CONCLUSIONS AND RECOMMENDATIONS

7.1 Conclusions

A chemical method has been used for the synthesis of different sizes of Pt and Au NPs because it has high control over particle size and the shape, has low cost, reproducibility and involves a simple reaction process. Moreover, in most of the synthesis process, the precipitated NPs could be cleaned very easily by removing the chemicals involved in the synthesis process. The cleanliness of the synthesised NPs was checked by the cyclic voltammogram (CV). The NPs were then characterised by a transmission electron microscope (TEM) from which the structure and the size of the NPs were determined.

In this thesis, we have presented a practical and novel miniature coaxial probe technique for convenient, fast, accurate measurement of synthesised NP films. Both the probe aperture admittance models (i.e. capacitive and variational models) and the measurement system have been described in great detail. The accuracy and the robustness of these aperture admittance models for the open ended coaxial probe (OCP) were investigated in detail by carrying out experiments on several different dielectric materials including low, medium and high permittivity materials. The measured data are found to be in very good agreement with the published data. In terms of the validation of these models, the capacitive model seems to be simple, robust and reliable admittance model for the characterisation of a wide range of dielectric materials, with discrepancies less than 3% for ϵ_1 and 7% for ϵ_2 over the broadband frequency ranging from 30 kHz to 6 GHz. There are numerous benefits of this OCP technique over the other methods, namely, in-situ (or contactless), broadband measurement, convenient, fast, non-destructive and ease of sample preparation.

It was found that the slight differences between the Debye model and the capacitive model are due to the uncertainty of the Debye parameters of the test liquids obtained from the literature, water adsorption and other contamination from the atmosphere, temperature variations during the course of the experiment, freshness (i.e. liquids from the sealed bottles are not used) and the purity (e.g. % water content in the liquids) of the liquids. Taking all

these into account in future projects would not only decrease the discrepancies between the Debye and the capacitive models but also increase the accuracy of the capacitive model.

One of the biggest contributions of this work has been the development of an actual 3D full wave K-connector OCP using the commercially available Ansoft High Frequency Structure Simulator (HFSS) software. It turned out to be enormously challenging – especially due to the limited availability of the catalogue data for the K-connector. The 3D full wave K-connector OCP model further validated the aforementioned capacitive model very accurately. Nonetheless, it turns out to be a very accurate and robust 3D full wave model for the characterisation of any dielectric materials.

The OCP is used to characterise the dielectric properties of materials via reflection measurements. The deduction of complex permittivity of material from the reflection coefficient (i.e. S_{11}) data is made by assuming that the aperture of the probe/ material interface is described by a simple empirical model. Such models are not universally valid. In the last phase of this research, a novel *universal model* has been proposed for individual OCPs (i.e. K-connector, RG-405, RG-402 and SMA OCPs) based on the 3D full wave models by mapping the complex admittance (Y_L) obtained from the simulation onto the complex permittivity (ϵ_1 and ϵ_2) plane. This enables us to determine the properties of any unknown material more accurately below a certain frequency limit (i.e. the frequency limit varies with the dimensions of the probe).

It has been demonstrated that the OCP can be used for measurements of microwave properties of NP films composed of different sizes. The microwave conductivity (or ac conductivity) of the Pt oxide NP films was studied as a function of frequency and films thickness. The films show a wide range of conductivities, when the conductivity starts to increase as the particle size decreases, the films exhibit a frequency-independent, metal-like response which is predominately conductive in nature, increasing approximately linearly with increasing film thickness, albeit with a massively suppressed conductivity compared to the bulk Pt metal (factor $> 10^5$). This is due to the inter-grain contacts of thin oxide layer surrounding the individual particles, which acts as a capacitance between the particles, where the contact area between the NPs depends on the metal particle shape and size. The DC conductance of this Pt oxide NP films exhibits a similar trend as for the microwave conductance, however, the conductance values were very much greater at DC than at microwave.

The Au films of the 16.5 nm and 24.8 nm particles are highly conductive, with film conductance increasing with film thickness. However, both sizes of particles have significant capacitances which decrease and eventually turn into considerably large inductances when the film thickness increases. The increased inductance with increased film thickness is due to the high density of metal-metal contacts between the NPs.

Pt NP films after the H₂ adsorption exhibit much higher sheet conductance (G_s) compared to the Pt oxide NP films, with highly suppressed by the internal inductance due to the high density of the metal-metal contacts. The extrapolated sheet conductance at low frequency (i.e. $G_s(0)$) of those films is approximately proportional to the film thickness, and in the latter it is observed that the conductance increases with increasing particle size due to the metal-metal contacts between the particles. Pure Pt NP films exhibit thickness independent internal inductance behaviour, which is supported by the theoretical prediction.

Single frequency measurements were carried out on Pt NP films (i.e. particles surrounded with oxide layer) and Au NPs films using SDR. The results of Pt oxide and Au films compare well with the theoretical resonator perturbation model described in section 2.8.1, and predicted the correct signature. However, owing to the difficulties regarding sample geometry, it is not possible to make the comparison more quantitative.

Finally, the results obtained from the microwave experimental studies for the Pt oxide, pure Pt and Au NP films were theoretically supported with a simple modelling based on random R-C and R-L network arrangements, which closely resembled and predicted the correct qualitative signature.

7.2 Recommendations

The measurements in this research were conducted in a non-constant temperature environment, which was found to affect the accuracy of results obtained. Although variations in ambient temperature over the course of the experiment were monitored, its influence on the obtained results was not determined because the recorded temperature did not represent that of NPs films. It is thus recommended for future projects that such experiments are carried out in a temperature controlled environment to enhance the better reproducibility of the results. It is also recommended to carry out experiments on the NP films by varying the temperature of the sample (e.g. using a oil bath (uniform temperature distribution)) by having

a set-up shown in fig. 7.1 and monitoring the variation as close as possible (e.g. using thermocouple) so as to establish temperature dependent electrical properties.

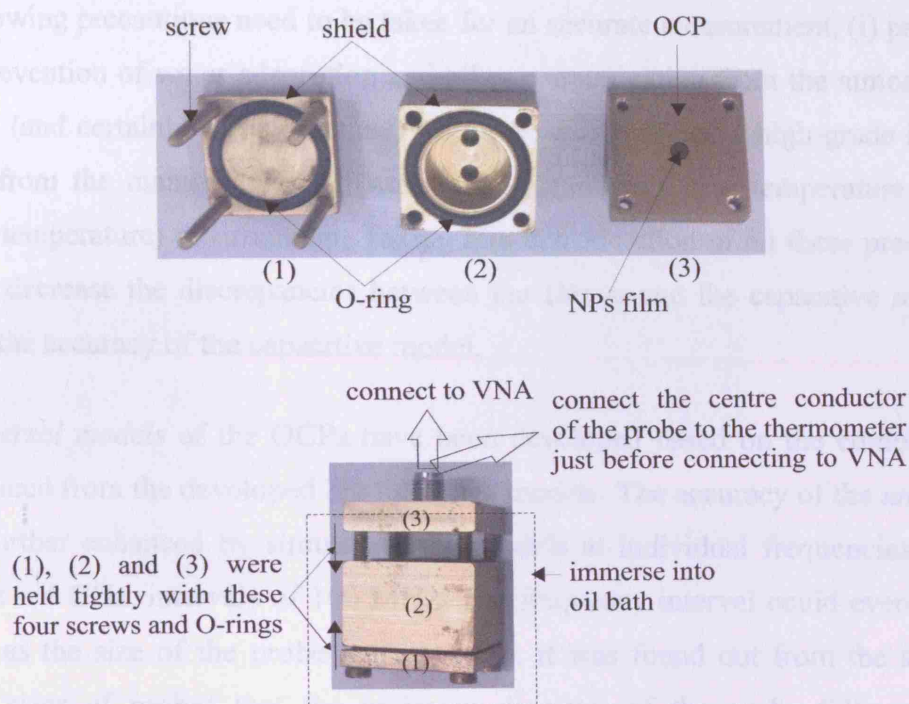


Figure 7.1 Experimental setups for the temperature dependent electrical properties of NPs films.

Depositing the NPs directly onto the aperture of the OCP or onto the sapphire puck of the SDR using a micropipette forms a slightly non-uniform thickness of film. Since the thicknesses of the films are very important in the electrical characterisation of NP films, it is thus recommended for future projects that depositions are carried out using a spin coater which would form a uniform thin film. Alternatively, rather than using the chemical methods for the synthesis of NPs, physical methods such as the sputter deposition technique can be also used to form a uniform film thickness of NPs. Even though the film thickness can be controlled using the sputter deposition, however, it has drawbacks such as being expensive, time consuming, producing impure samples, and unable to achieve smaller particles sizes (e.g. 3 nm).

It was found out that the slight differences between the Debye model and the capacitive model are due to the uncertainties of the Debye parameters of the test liquids obtained from the literature, temperature variations during the experiment and also due to the preparation

and handling of these liquids. Apart from the uncertainty of the Debye parameters of the test liquids, the discrepancies between the Debye and the capacitive models can be further minimised by giving consideration to the preparation of test liquids prior to measurement. The following precautions need to be taken for an accurate measurement, (i) precautions such as the prevention of water adsorption and other contamination from the atmosphere, (ii) it is adequate (and certainly more practical) to use a fresh bottle of a high-grade liquid obtained directly from the manufacturer, (iii) taking measurements in a temperature controlled (or constant temperature) environment. Taking into consideration of all these precautions would not only decrease the discrepancies between the Debye and the capacitive models but also increase the accuracy of the capacitive model.

The *universal models* of the OCPs have been developed based on the complex admittance data obtained from the developed 3D full wave models. The accuracy of the *universal models* can be further enhanced by simulating the models at individual frequencies ranging from 100 MHz – 4 GHz, intervals of 100 MHz. The frequency interval could even be reduced to 50 MHz as the size of the probe increases (i.e. it was found out from the simulations for different sizes of probes that the optimum diameter of the probe falls with increasing measurement frequency). This would eventually increase the simulation time enormously (e.g. due to the number of mesh elements), but it is worth performing this simulation in future to improve the accuracy of the universal models of the probes.

The sensitivity of the OCP fails as the number of nanoparticles per drop reduces (i.e. diluting the sample to a fewer NPs), since this does not cover the whole aperture of the probe completely. This issue could be overcome by using a microstrip transmission line as a resonator by having a slot (or gap) on the transmission line where it resonates at quarter wavelength as shown in fig. 7.2, mounted on H-block. This enables to study the microwave properties of intra-particles by depositing fewer NPs into the gap of the resonator, whilst controlling the gap size of the resonator to enhance the sensitivity of the measurement for fewer NPs. A trial was conducted on a very small droplet of ultra pure water (since the NPs are suspended in water) into the gap of this resonator. It turned out to be enormously challenging task to get the droplet into the gap due to the high surface tension of water. This issue could be resolved by drilling a small hole through the gap on to the substrate and carrier plate (gold plated) and connecting a high pressure tube and using a vacuum pump to evacuate the gap, enabling the fluid to flow into the gap. Once this issue has been resolved this would

be a very sensitive technique for the measurement of the microwave properties of small particles. This could be carried out in future work on the subject.

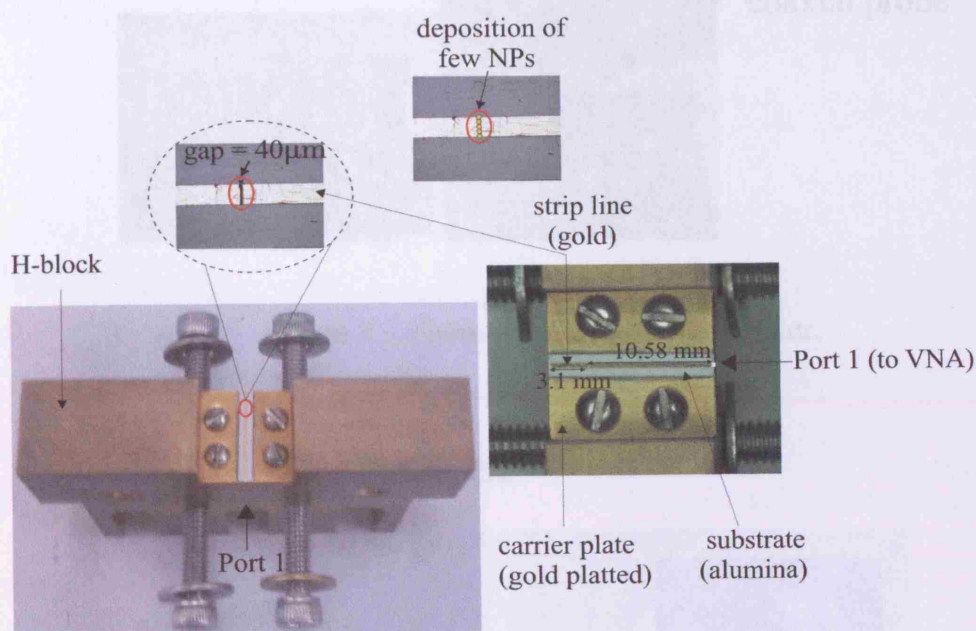


Figure 7.2 Photograph of the microstrip resonator set-up mounted on H-block, where NPs are deposited directly into the gap, with negligibly small air gap.

A further miniaturised K-connector coaxial probe as shown in fig. 6.3 has been fabricated to use as a sensitive sensor for the microwave-electrochemical study. The same K-connector reported in chapter 6 has been used to fabricate and assemble miniature OCP with brass flange of diameter 9 mm. The reason why the flange size had to be reduced to 9 mm diameter was to enable it to fit into the electrochemical cell. The initial phase of this project was to coat the end of the probe with thin gold film to avoid corrosion of the brass when it was in-contact with H_2SO_4 . Coating the probe with a thin gold film was carried out as shown in fig. 7.3 using the BAL-TEC SCD 005 Sputter Coater. Then a trial was carried out using this miniature probe to obtain a cyclic voltammetry profile of NaCl solution as shown in fig. 7.4, and the result was not as expected (i.e. the result shows corrosion of brass). This issue could be resolved by having a thicker film of gold. Once this issue has been resolved this technique could be a sensitive sensor for the microwave-electrochemical study. This could be carried out in future work on the subject.



Figure 7.3 Photograph of a Sputter Coater.

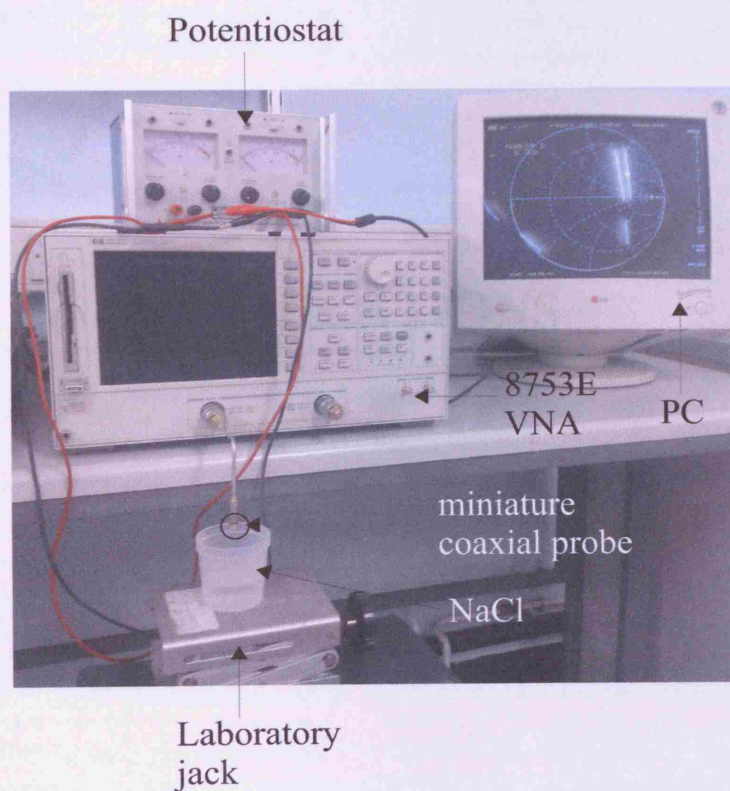


Figure 7.4 Experimental set-up for characterisation of NaCl.

PUBLICATIONS

Microwave Properties of Platinum Nanoparticle Films

¹Aslam Sulaimalebbe, ¹Adrian Porch, ²F.J. Vidal-Iglesias, ²Gary Attard

¹School of Engineering, Cardiff University, 1-5 The Parade, Cardiff, CF24 3AA, U.K.

²School of Chemistry, Cardiff University, Park Place, Cardiff, CF10 3AT, U.K.

Abstract — The electrical properties of platinum (Pt) nanoparticle films have been investigated experimentally using a microwave coaxial reflectance probe up to 6 GHz, for films composed of 26 nm and 11 nm particles. Larger particle films exhibit a conductive response, but with conductivity hugely suppressed (by a factor of $> 10^5$) compared to bulk Pt. Smaller particle films exhibit an even greater suppression of conductivity and a predominantly capacitive response above 1 GHz. The overriding factor in reduced conductance for smaller particles is the inter-grain contact resistance, which increases rapidly as particle size reduces.

Index Terms — Metal nanoparticles, microwave coaxial reflectance probe, electrical conductivity, reflection coefficient, capacitance, admittance.

I. INTRODUCTION

METAL nanoparticles offer enormous promise as functional units for the development of sensors, photo-electrochemical and general nanoelectronic devices due to their ease of synthesis and stability [1]. However, they exhibit unconventional properties and functionalities which differ significantly from those of the bulk parent metals, with the intriguing possibility of a size-induced metal insulator transition [2] when the number of atoms N in a metal cluster becomes small enough for the Kubo gap $\delta_K = E_F / N$ to be comparable with the thermal energy kT . The Fermi energy for platinum (Pt) is $E_F = 8.8$ eV and its unit cell volume is 0.022 nm³, so the associated critical volume of Pt clusters is about 1.4 nm³ at room temperature, increasing to 5.8 nm³ at 4.2 K.

The direct measurement of the electrical conductivity of metal nanoparticles presents a key challenge and necessitates the use of innovative experimental techniques. There have been numerous reports of four point resistance measurements of nanoparticle films at low frequencies [3], and in situ resistance measurements of nanoparticle gold suspensions within a solvent [4]. More recently, broadband spectroscopy of nanoparticle metal colloids has been reported up to microwave frequencies using a commercial coaxial reflectance probe [5]. Here, we present broadband microwave measurements of platinum nanoparticles at room temperature using a novel, miniature coaxial probe, which offers a simple and convenient means of probing their electrical properties. We have performed measurements of Pt nanoparticle films as a function of film thickness for films composed of two nanoparticle sizes (26 nm and 11 nm, detailed in Section III).

II. COAXIAL PROBE TECHNIQUE

The coaxial probe technique has been established over the last 20 years as a standard tool for evaluating electrical properties in the microwave frequency range [6]. It involves termination of a short length of flanged coaxial transmission line with the material under test, followed by measurement of the reflection coefficient ρ at the interface with the material. A schematic diagram of the coaxial probe used in our studies is shown in Fig. 1, based on an Anritsu K-connector (here K102F), which has an inherent bandwidth from DC up to 40 GHz. The connector's glass bead provides a convenient coaxial aperture, which can be ground flat, polished using fine emery paper, and cleaned easily for film removal. All measurements are performed using a HP8753 network analyzer from 1 MHz to 6 GHz, with the system calibrated to plane AB using factory standards.

Nanoparticle films are deposited on the aperture prior to their measurement (see Section III). The system is calibrated to the connector plane AB using the simple model shown in Fig. 2. The probe's reflection coefficient is first measured at plane AB with no sample present ($\rho_{m,0}$), and then with the sample (ρ_m). The electrical length L (and associated losses) between AB and sample plane AB' is removed by calculating

$$\frac{\rho_m}{\rho_{m,0}} = \left(\frac{1 - Z_0 Y}{1 + Z_0 Y} \right) \cdot \left(\frac{1 + Z_0 Y_0}{1 - Z_0 Y_0} \right) \equiv \frac{\rho}{\rho_0} \quad (1)$$

where Y and Y_0 are the aperture admittances with and without the sample, respectively, and $Z_0 = 50\Omega$; ρ and ρ_0 in (1) are then the reflection coefficients at the sample plane AB' with and without the sample, respectively.

There are a number of models for calculating the probe aperture admittance, the simplest using a quasi-static approach [7] which results in the approximate admittance

$$Y_0 \approx jC_0 \omega + jC_1 \omega^3 + C_2 \omega^4 + O(\omega^5) \quad (2)$$

when air terminated, the coefficients C_0 , C_1 , etc., being derived analytically in terms of the aperture geometry.

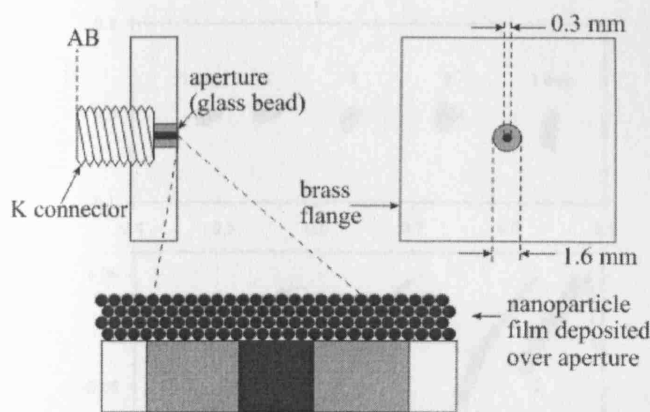


Fig. 1. Schematic diagram of the coaxial reflectance probe. Platinum films are deposited directly onto the aperture, with negligibly small air gap.

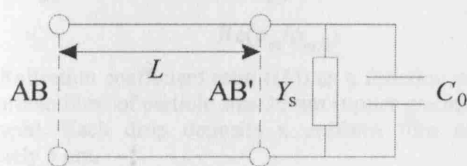


Fig. 2. Simple lumped circuit model for the aperture together with the sample, the latter providing a shunt admittance $Y_s = G + jB$. Without the sample the aperture approximates to a lumped circuit capacitor C_0 .

For our probe the inner and outer radii are $a = 150 \mu\text{m}$ and $b = 800 \mu\text{m}$, respectively, and so $b - a \approx \lambda / 40$ at 6 GHz (here λ is the probe wavelength, assuming $\epsilon_r \approx 4$ for the silica of the glass bead). Hence the aperture remains electrically small over our full range of measurement frequencies and we model the probe as a lumped element capacitor C_0 when no sample is present (i.e. ignoring all other terms in (2)), and a parallel combination of C_0 and sample admittance Y_s when the sample is present (see Fig. 2). The capacitance of the unloaded probe is, from (2)

$$C_0 = -j \frac{Y_0}{\omega} \approx \frac{8\epsilon_0(a+b)(E(m)-1)}{(\ln(b/a))^2}, \quad m = \frac{4ab}{(a+b)^2} \quad (3)$$

where $E(m)$ is the complete elliptic integral of the second kind. For our probe $m = 0.532$ and $C_0 \approx 8.03 \text{ fF}$.

To validate this experimentally we performed separate measurements with the probe dipped into pure methanol and ethanol. Assuming that in this case $Y \approx j\omega\epsilon C_0$, fitting the experimental data to the standard Debye equations for the complex relative permittivity ϵ for both polar liquids yields $C_0 = 8.2 \pm 0.5 \text{ fF}$, in close agreement with the value calculated from (3). Hence, in what follows we assume that $C_0 = 8 \text{ fF}$.

Having found $Y_0 \approx j\omega C_0$, it is straightforward to invert (1) to find the admittance Y at the plane AB' when the sample is present, from which the sample admittance contribution Y_s is found using $Y_s = Y - j\omega C_0$ (see Fig. 2).

III. EXPERIMENTAL RESULTS

Pure platinum nanoparticles were produced by two methods. Large spherical particles were produced by hydrazine reduction of Pt metal precursors, of resulting diameter $26 \pm 4 \text{ nm}$ (as measured by SEM, see Fig. 3). Smaller, cubic particles (of dimension $11 \pm 1 \text{ nm}$) were produced using the method of Rampino and Nord [8] and Henglein et al. [9]. The surface cleanliness of both sets of nanoparticles was confirmed by cyclic voltammetric profiling and they were stored in ultra pure water at the same volume concentration (i.e. 3.15×10^{10} and 1.04×10^{12} nanoparticles per μl for the large and small particles, respectively). Particle-loaded water droplets of volume $6 \mu\text{l}$ were deposited directly onto the coaxial aperture, followed by thorough drying. Each water droplet was found to deposit a uniform film of approximate thickness $5 \mu\text{m}$ for both sizes of particles, covering the whole of the aperture. A maximum of 5 drops were deposited for each particle size, thus forming films of overall thickness up to around $25 \mu\text{m}$.

Raw data for the normalized reflection coefficient (calculated using (1)) as a function of frequency for films of each size of particle are shown in Fig. 4. It is immediately apparent from this data that the films of the 26 nm particles are predominantly conductive (i.e. data on the real axis of the complex plane), with film conductance increasing with film thickness. However, films of the 11 nm particles are much less conductive and have a significant (capacitive) susceptance, the data straying from the real axis as the frequency is increased. Note that the thinnest film of the 26 nm particles has a very small susceptance, which decreases with increasing film thickness, but this is dominated by conductance and is therefore assumed to be zero to within experimental error.

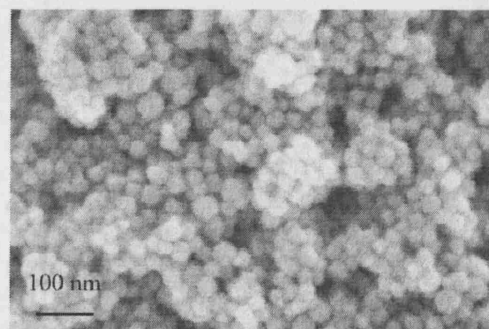


Fig. 3. Scanning electron microscope (SEM) photograph of a film of the 26 nm platinum particles.

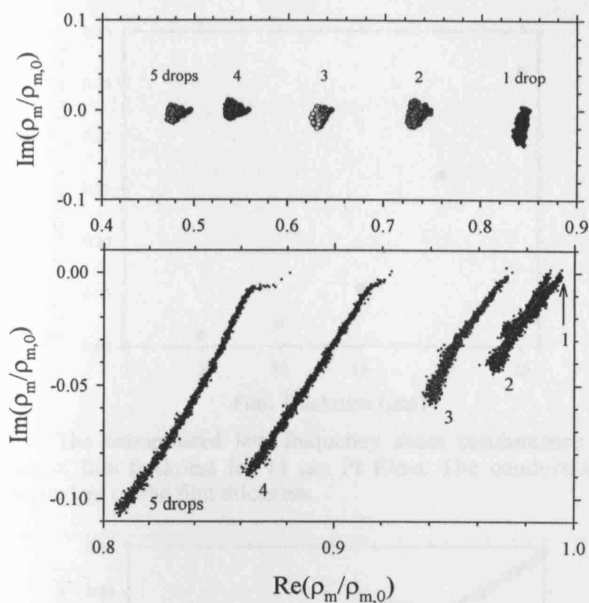


Fig. 4. Reflection coefficient ratio ((1)) as a function of frequency for nanoparticle films of particle size 26 nm (upper graph) and 11 nm (lower graph). Each drop deposits a uniform film of thickness approximately 5 μm .

IV. ANALYSIS AND DISCUSSION

Film susceptance $Y_s = G + jB$ is computed from the reflection coefficient using the analysis of section II. The conductance G is converted into a sheet conductance $G_s = \sigma t = G \ln(b/a)/2\pi$ and the susceptance B into a sheet susceptance $B_s = B \ln(b/a)/2\pi$. As already noted, for the 26 nm Pt nanoparticle films $G_s \gg B_s$, with B_s approximately zero within experimental error up to 6 GHz; thus the behavior is predominantly conductive (Fig. 5), with G_s approximately independent of frequency apart from a slight upturn above 3 GHz. G_s extrapolated to low frequency ($G_s(0)$) is approximately proportional to film thickness t (Fig. 6), from which a conductivity $\sigma \approx 65 \text{ S/m}$ is found, compared with a value of $\sigma \approx 10^7 \text{ S/m}$ for bulk Pt metal. The analysis of Section II assumes that the film thickness is much less than the skin depth, an assumption which is justified when dealing with such low values of conductivity. Similar data for the 11 nm Pt nanoparticle films are shown in Figs. 7 and 8. In contrast to the data for the 26 nm particles, (i) G_s is further suppressed and increases monotonically with frequency, more rapidly above 100 MHz, (ii) $G_s(0)$ no longer varies linearly with film thickness, instead increasing more rapidly for thicker films, and (iii) there is large sheet susceptance (Fig. 9), comparable in magnitude with G_s above 1 GHz, which varies approximately linearly with frequency. Hence, B_s can be converted into sheet capacitance $C_s \approx B_s / \omega = \epsilon_1 \epsilon_0 t$, which itself varies approximately linearly with film thickness t (Fig. 10). The associated real permittivity is very large ($\epsilon_1 \approx 800$).

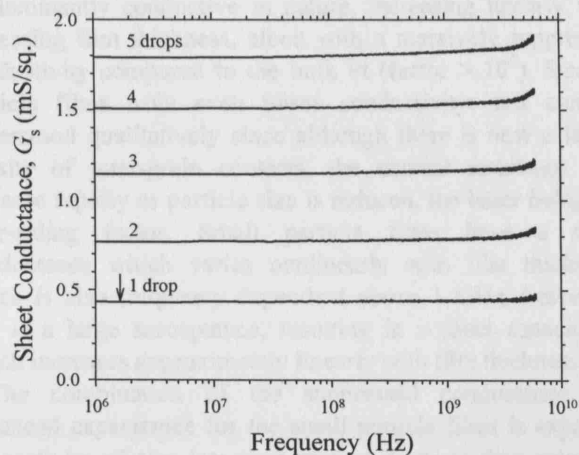


Fig. 5. Sheet conductance as a function of frequency for 26 nm Pt films.

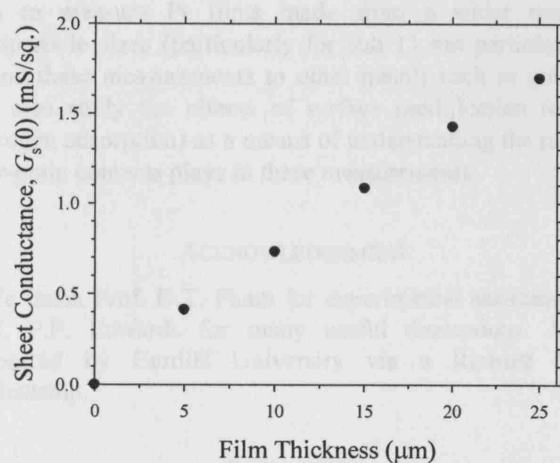


Fig. 6. The extrapolated low frequency sheet conductance as a function of film thickness for 26 nm Pt films, giving a conductivity of 65 S/m.

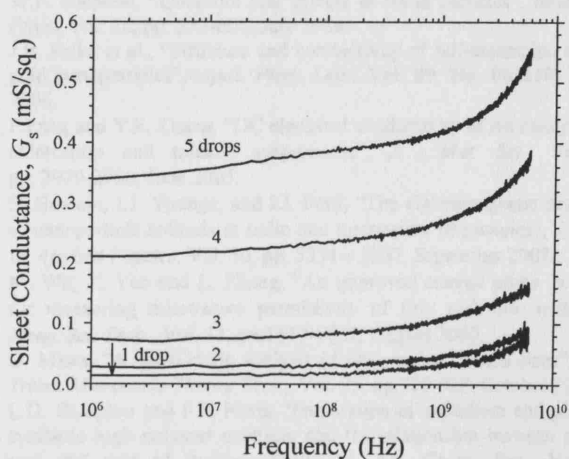


Fig. 7. Sheet conductance as a function of frequency for 11 nm Pt films.

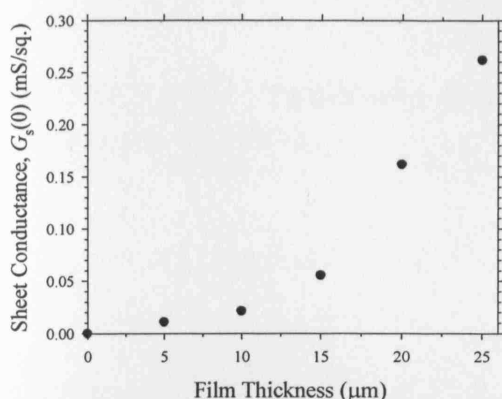


Fig. 8. The extrapolated low frequency sheet conductance as a function of film thickness for 11 nm Pt films. The conductivity is now dependent on the film thickness.

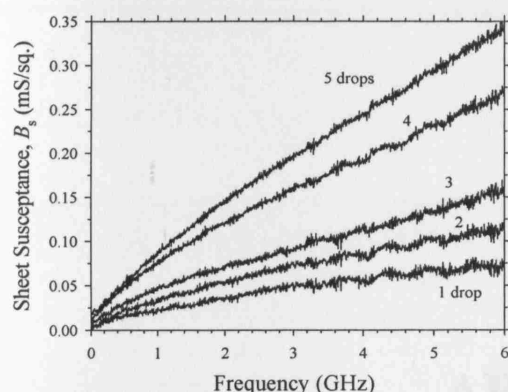


Fig. 9. Sheet susceptance as a function of frequency for 11 nm Pt films. This is comparable to the sheet conductance above 1 GHz.

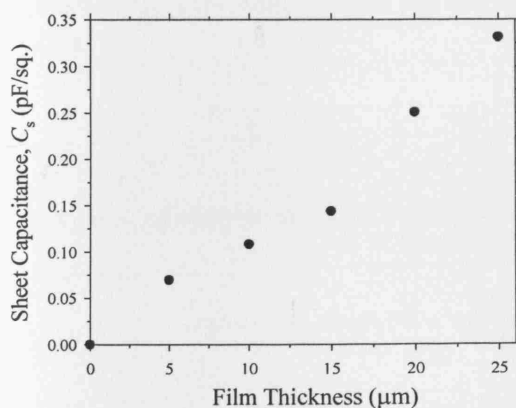


Fig. 10. The sheet capacitance for 11 nm Pt films, increasing approximately linearly with film thickness.

V. CONCLUSIONS AND FUTURE WORK

We have performed broadband characterization (1 MHz to 6 GHz) of platinum nanoparticle films composed of two sizes of pure particles (26 nm and 11 nm). Larger particle films exhibit a frequency-independent, metal-like response which is

predominantly conductive in nature, increasing linearly with increasing film thickness, albeit with a massively suppressed conductivity compared to the bulk Pt (factor $> 10^5$). Smaller particle films have even lower conductivity; this can be understood qualitatively since although there is now a larger density of inter-grain contacts, the contact resistance will increase rapidly as particle size is reduced, the latter being the over-riding factor. Small particle films have a sheet conductance which varies nonlinearly with film thickness, which is also frequency dependent above 1 GHz. Linked to this is a large susceptance, resulting in a sheet capacitance which increases approximately linearly with film thickness.

The combination of the suppressed conductance and enhanced capacitance for the small particle films is expected for particles of size less than around 2 nm as they enter the regime for the size-induced metal insulator transition, but is unexpected for particles as large as 11 nm. In the future we plan to measure Pt films made from a wider range of nanoparticle sizes (particularly for sub 11 nm particles), and extend these measurements to other metals such as gold. We will also study the effects of surface modification (e.g. by hydrogen adsorption) as a means of understanding the role that inter-grain contacts plays in these measurements.

ACKNOWLEDGEMENT

We thank Prof. D.T. Pham for experimental assistance, and Prof. P.P. Edwards for many useful discussions. A.S. is supported by Cardiff University via a Richard Whipp Studentship.

REFERENCES

- [1] H.-S.P. Wong "Nanoelectronics – Opportunities and challenges", *International Journal of High Speed Electronics and Systems*, Vol. 16, pp. 83-94, March 2006.
- [2] W.P. Halperin, "Quantum size effects in metal particles", *Revs. Mod. Phys.*, Vol. 58, pp. 533-606, July 1986.
- [3] J.B. Pelka et al., "Structure and conductivity of self-assembled films of gold nanoparticles", *Appl. Phys. Lett.*, Vol. 89, No. 063110, August 2006.
- [4] F.Fang and Y.F. Zhang, "DC electrical conductivity of Au nanoparticle/chloroform and toluene suspensions", *J. Mat. Sci.*, Vol. 40, pp. 2979-2980, June 2005.
- [5] S. Hussain, I.J. Youngs, and I.J. Ford, "The electromagnetic properties of nanoparticle colloids at radio and microwave frequencies", *J. Phys. D: Applied Physics*, Vol. 40, pp. 5331 – 5337, September 2007.
- [6] M. Wu, X. Yao and L. Zhang, "An improved coaxial probe technique for measuring microwave permittivity of thin dielectric materials", *Meas. Sci. Tech.*, Vol. 11, pp.1617-1622, August 2000.
- [7] D. Misra, "A quasi-static analysis of open-ended coaxial lines", *IEEE Trans. Microwave Theory Tech.*, Vol. 35, pp.925-928, October 1987.
- [8] L.D. Rampino and F.F. Nord, "Preparation of palladium and platinum synthetic high polymer catalysts and the relationship between particle size and rate of hydrogenation", *J. Am. Chem. Soc.*, Vol. 63, pp.2745-2749, October 1941.
- [9] A. Henglein., B.G. Ershov, and M. Marlow, "Adsorption Spectrum and some chemical reactions of colloidal platinum in aqueous solution", *J. Phys. Chem.*, Vol. 99, pp.14129-14136, September 1995.

APPENDIXES

APPENDIX A: Two-Port Resonator Analysis with Asymmetrical and Symmetrical Coupling

1. Asymmetrical Coupling

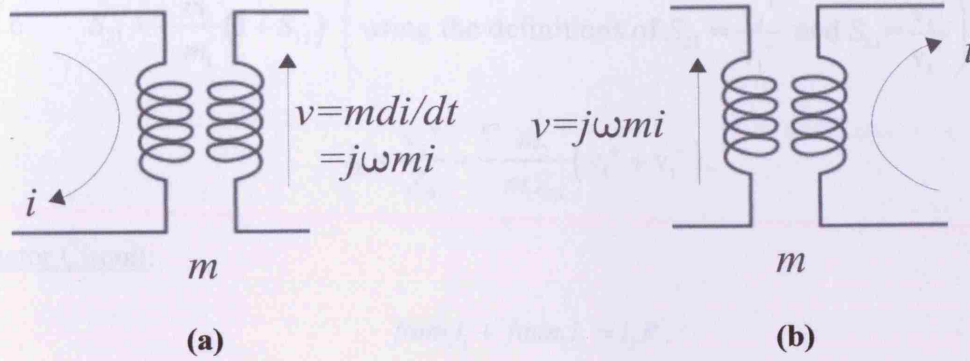


Figure A1 The polarity of the voltage induced in the secondary coil is positive when current is flowing in a clockwise direction in the primary, as shown in (a) whereas the same current flowing in the same direction in the secondary coil induces a voltage of equal magnitude but opposite polarity in the primary, as illustrated in (b).

It follows from above that the equivalent circuit of a resonator at resonance, with induced voltage polarities, would be as depicted in fig. A2.

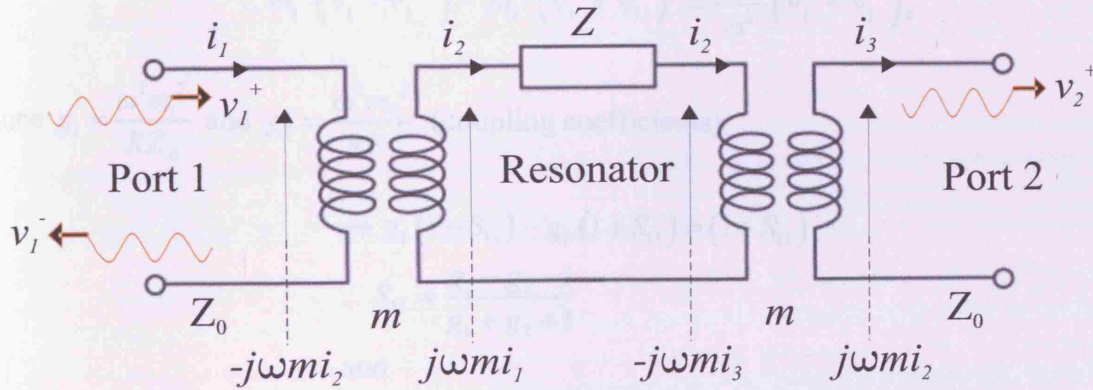


Figure A2 Equivalent circuit of a two-port resonator at resonance. Note the polarities of voltages induced in the input, resonator, and output circuits.

Now, the voltage/current equations for the three circuits of fig. A2 can be written as below [1, 2]:

Input Circuit:

$$v_1^+ + v_1^- = -j\omega m i_2, \quad (A.1)$$

$$v_1^+ - v_1^- = i_1 Z_0 \quad (\text{A.2})$$

Output Circuit:

$$v_2^+ = j\omega m_2 i_2 = -\frac{m_2}{m_1} (v_1^+ + v_1^-) \quad (\text{A.3})$$

$$\text{i.e. } S_{21} = -\frac{m_2}{m_1} (1 + S_{11}) \left(\text{using the definitions of } S_{21} = \frac{v_2^+}{v_1^+} \text{ and } S_{11} = \frac{v_1^-}{v_1^+} \right)$$

$$i_3 = \frac{v_2^+}{Z_0} = -\frac{m_2}{m_1 Z_0} (v_1^+ + v_1^-). \quad (\text{A.4})$$

Resonator Circuit:

$$j\omega m_1 i_1 + j\omega m_2 i_3 = i_2 R. \quad (\text{A.5})$$

Since $i_1 = \frac{1}{Z_0} (v_1^+ - v_1^-)$ (from Eq. (A.2)) and $i_3 = -\frac{m_2}{m_1 Z_0} (v_1^+ + v_1^-)$ (from Eq. (A.4)),

Eq. (A.5) can be rewritten as

$$\frac{j\omega m_1}{Z_0} (v_1^+ - v_1^-) - \frac{j\omega m_2^2}{Z_0 m_1} (v_1^+ + v_1^-) = \frac{jR}{\omega m_1} (v_1^+ + v_1^-) \quad (\text{A.6})$$

$$\therefore m_1^2 (v_1^+ - v_1^-) - m_2^2 (v_1^+ + v_1^-) = \frac{Z_0 R}{\omega^2} (v_1^+ + v_1^-), \quad (\text{A.7})$$

Since $g_1 = \frac{\omega^2 m_1^2}{R Z_0}$ and $g_2 = \frac{\omega^2 m_2^2}{R Z_0}$ (coupling coefficients)

$$\rightarrow g_1 (1 - S_{11}) - g_2 (1 + S_{11}) = (1 + S_{11})$$

$$\therefore S_{11} = \frac{g_1 - g_2 - 1}{g_1 + g_2 + 1} \quad (\text{A.8})$$

and

$$S_{22} = \frac{g_2 - g_1 - 1}{g_1 + g_2 + 1}$$

From Eqs. (A.3) and (A.8) S_{21} can be written as

$$\begin{aligned} -\frac{m_1}{m_2} S_{21} &= 1 + S_{11} = 1 + \frac{g_1 - g_2 - 1}{g_1 + g_2 + 1} = \frac{2g_1}{g_1 + g_2 + 1} \\ \therefore S_{21} &= -\frac{m_2}{m_1} \left(\frac{2g_1}{g_1 + g_2 + 1} \right) = -\frac{2\sqrt{g_1 g_2}}{g_1 + g_2 + 1} \end{aligned} \quad (\text{A.9})$$

Therefore,

$$S_{21} = \frac{-2\sqrt{g_1 g_2}}{1 + g_1 + g_2}. \quad (\text{A.10})$$

Off Resonance Scenario:

However, at a point off resonance the resonator impedance would not be purely resistive. To examine this, let $\omega = \omega_0 + \Delta\omega$, where $\Delta\omega$ is very small. The resonator impedance (Z) can now be derived for this off resonance situation, starting from Eq. (3.1) of chapter 3 as below:

$$\begin{aligned} Z &= R + j\omega L \left(1 - \frac{1}{\omega^2 LC} \right) \\ &= R + j\omega L \left(\frac{\omega^2 - \omega_0^2}{\omega^2} \right) \end{aligned} \quad (\text{A.11})$$

since $\omega_0^2 = 1/LC$. Now $\omega^2 - \omega_0^2 = \omega_0^2 (1 + \Delta\omega/\omega_0)^2 - \omega_0^2 \approx 2\omega_0 \Delta\omega$ for small ω [1]. Therefore,

$$\begin{aligned} Z &\approx R + 2jL\Delta\omega \\ &\approx R + 2jL\omega_0 x \end{aligned} \quad (\text{A.12})$$

where $x = \frac{\Delta\omega}{\omega_0} = \frac{\omega - \omega_0}{\omega_0}$. Given that the unloaded quality factor of the series RLC circuit is

$Q_u = \frac{\omega_0 L}{R}$ [1], Eq. (A.12) can be rewritten as

$$Z = R(1 + 2jQ_u x) \quad (\text{A.13})$$

It follows that S_{21} at a point slightly off the resonance can be found by

$$\begin{aligned} \text{Let } R &\rightarrow R(1 + 2jQ_u x) \\ \therefore g_1(1 - S_{11}) - g_2(1 + S_{11}) &= (1 + 2jQ_u x)(1 + S_{11}) \\ \therefore S_{11} &= \frac{g_1 - g_2 - (1 + 2jQ_u x)}{1 + g_1 + g_2 + 2jQ_u x} \end{aligned} \quad (\text{A.14})$$

Furthermore, from Eq. (A.10) S_{21} can be written as

$$S_{21} = \frac{-2\sqrt{g_1 g_2}}{1 + g_1 + g_2 + 2jQ_u x} \quad (\text{A.15})$$

2. Symmetrical Coupling

At resonance:

In this research the coupling loops were made nearly identical to ensure symmetrical input/output couplings (i.e. $m = m_1 = m_2$). Because of the symmetrical coupling they have the same coupling coefficients (i.e. $g = g_1 = g_2$); therefore, from Eq. (A.10) S_{21} at resonance can be written as

$$S_{21} = -\frac{2g}{1+2g} \quad (\text{A.16})$$

Additionally, from Eq. (A.8) S_{11} at resonance can be written as

$$S_{11} = -\frac{1}{1+2g} \quad (\text{A.17})$$

where the coupling coefficient $g = \omega^2 m^2 / RZ_0$

Off Resonance Scenario:

From Eqs. (A.14) and (A.15) S_{11} and S_{22} can be written, respectively, as follows:

$$\begin{aligned} S_{11} &= \frac{-(1+2jQ_u x)}{1+2g+2jQ_u x} \\ S_{21} &= \frac{-2g}{1+2g+2jQ_u x} \end{aligned} \quad (\text{A.18})$$

References

- [1] A. Porch, *Private Communication*, 2008-9.
- [2] D. M. Pozar, *Microwave Engineering*, Third Edition, John Wiley & Sons, N.Y., 2005, ISBN 0-471-44878-8.

APPENDIX B: Detailed Derivation to Obtain the Locus of $\varepsilon(\omega)$ in the Debye Model

Set

$$x = \varepsilon_1$$

$$y = \varepsilon_2$$

$$u = \omega\tau$$

therefore,

$$x = \varepsilon_\infty + \frac{\varepsilon_s - \varepsilon_\infty}{1 + u^2} \quad (\text{B.1})$$

$$y = (\varepsilon_s - \varepsilon_\infty) \cdot \frac{u}{1 + u^2} \quad (\text{B.2})$$

from Eq. (B.1),

$$\frac{1}{1 + u^2} = \frac{x - \varepsilon_\infty}{\varepsilon_s - \varepsilon_\infty} \quad (\text{B.3})$$

substituting Eq. (B.3) in Eq. (B.2) gives,

$$u = \frac{y}{x - \varepsilon_\infty} \quad (\text{B.4})$$

Substitute for u in either Eq. (B.1) or Eq. (B.2), e.g. substitute in Eq. (B.2)

$$y = (\varepsilon_s - \varepsilon_\infty) \cdot \frac{y}{x - \varepsilon_\infty} \cdot \frac{1}{1 + \frac{y^2}{(x - \varepsilon_\infty)^2}} \quad (\text{B.5})$$

therefore,

$$(x - \varepsilon_\infty) + \frac{y^2}{x - \varepsilon_\infty} = \varepsilon_s - \varepsilon_\infty$$

$$x^2 - 2x\varepsilon_\infty + \varepsilon_\infty^2 + y^2 = (\varepsilon_s - \varepsilon_\infty)x - \varepsilon_s\varepsilon_\infty + \varepsilon_\infty^2$$

$$x^2 - (\varepsilon_s + \varepsilon_\infty)x + y^2 = -\varepsilon_s\varepsilon_\infty$$

i.e.

$$\begin{aligned} \left[x - \frac{1}{2}(\epsilon_s + \epsilon_\infty) \right]^2 + y^2 &= -\epsilon_s \epsilon_\infty + \frac{1}{4}(\epsilon_s + \epsilon_\infty)^2 \\ &= \frac{1}{4}\epsilon_\infty^2 + \frac{1}{2}\epsilon_s \epsilon_\infty + \frac{1}{4}\epsilon_s^2 - \epsilon_s \epsilon_\infty \end{aligned} \quad (\text{B.6})$$

Therefore,

$$\left[x - \frac{1}{2}(\epsilon_s - \epsilon_\infty) \right]^2 + y^2 = \frac{1}{4}(\epsilon_s - \epsilon_\infty)^2 \quad (\text{B.7})$$

The above Eq. (B.7) is in the form of $(x - x_0)^2 + (y - y_0)^2 = R^2$, i.e. it maps out a circle

centre at: $\epsilon_1 = \frac{1}{2}(\epsilon_s + \epsilon_\infty)$, $\epsilon_2 = 0$

radius: $\frac{1}{2}(\epsilon_s - \epsilon_\infty)$

The circle passes through points:

$$\begin{aligned} \epsilon_1 &= \epsilon_s, \quad \epsilon_2 = 0 \\ \epsilon_1 &= \epsilon_\infty, \quad \epsilon_2 = 0 \end{aligned}$$

Hence, the Cole-Cole plot (i.e. plot of ϵ on the complex plane as frequency varies) looks like

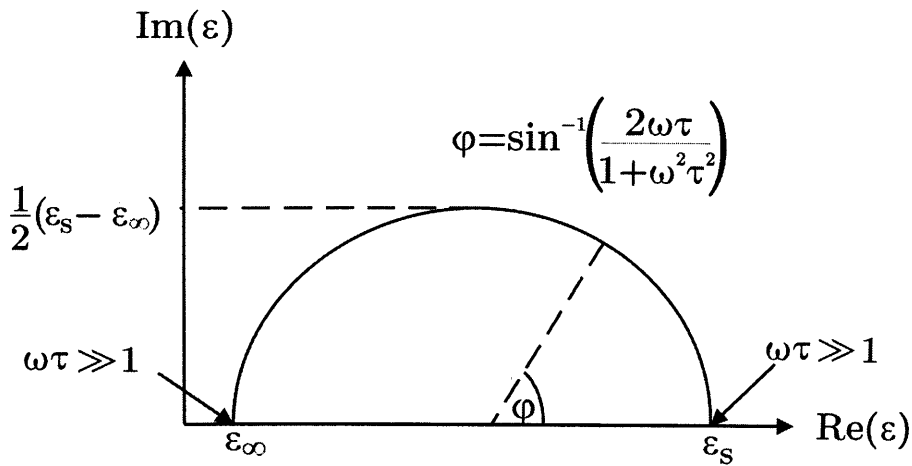


Figure B1 Cole-Cole plot of ϵ on the complex plane as ω varies.

APPENDIX C: Detailed Procedure of Synthesis of Pt NPs (3.0 nm)

C1: Preparation of 10 ml 0.1 molar (M) of Pt solution from a concentrated H₂PtCl₆ solution

NOTE: In the synthesis process of different sizes (8.6 nm, 6.9 nm and 3.0 nm) of Pt NPs, 7.5×10^{-5} moles of this noble metal were prepared.

- I. The molecular weight (Mw) of Pt is 195.078 g/mol (see periodic table, appendix D). Therefore, for

10 ml 0.1 M H₂PtCl₆

$$0.1 \frac{\text{mol}}{\text{L}} \times (10 \times 10^{-3}) \text{L} \rightarrow 10^{-3} \text{mol}$$

- II. Since the Mw of Pt is 195.078 g/mol, therefore,

$$1 \text{ mol} \rightarrow 195.078 \text{ g}$$

$$\therefore 10^{-3} \text{ mol} \rightarrow 10^{-3} \text{ mol} \times 195.078 \frac{\text{g}}{\text{mol}} \\ = 0.195078 \text{ g of Pt needed}$$

- III. Since the mass percentage of Pt on the concentrated H₂PtCl₆ solution is 24.95%

$$\therefore \text{The effective Pt needed} = \frac{0.195078}{\frac{24.95}{100}} \text{ g of H}_2\text{PtCl}_6 \text{ needed} \\ = 0.7819 \text{ g of H}_2\text{PtCl}_6$$

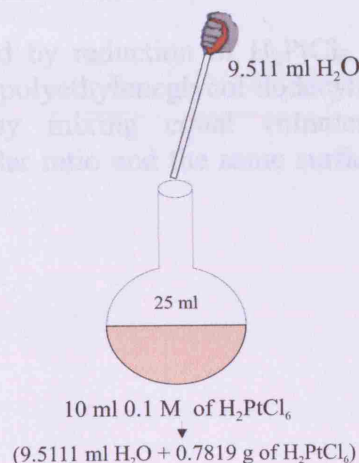
- IV. Therefore, to prepare 10 ml 0.1 M Pt solution, the effective Pt needed is 0.7819 g of the concentrated H₂PtCl₆ solution, the remainder being H₂O. How do we determine the amount of H₂O needed to add to make the total volume of 10 ml?

Step 1

- First place the H₂PtCl₆ container on the scale and make the scale to zero g.
- Then take 1 ml of H₂PtCl₆ from that container and note down the weight (say X g).
- X = 1.5993 g (for 1ml of H₂PtCl₆)

$$\therefore \frac{1 \text{ ml}}{1.5993 \text{ g}} \times 0.7819 \text{ g} = Y \text{ ml} \\ \therefore Y = 0.4889 \text{ ml}$$

- Therefore the amount of H₂O needed to prepare 10 ml = 10 ml – 0.4889 ml
= 9.5111 ml of H₂O needed



- For this calculation we have assumed that the volumes are additive.

Step 2

- Finally add 9.5111 ml of H₂O to the 0.7819 g of the concentrated H₂PtCl₆ solution to prepare 10 ml of a 0.1 M Pt solution.

C2: Calculations of the Reagents Needed for the Synthesis of Pt NPs (3.0 nm)

Platinum nanoparticles (diameter of 3.0 nm) were obtained by reduction of H₂PtCl₆ with hydrazine using water-in-oil micro-emulsions of water / polyethyleneglycol-dodecylether (Brij®30) / n-heptane. The synthesis was attained by mixing equal volumes of micro-emulsions that have the same water to surfactant molar ratio and the same surfactant concentration.

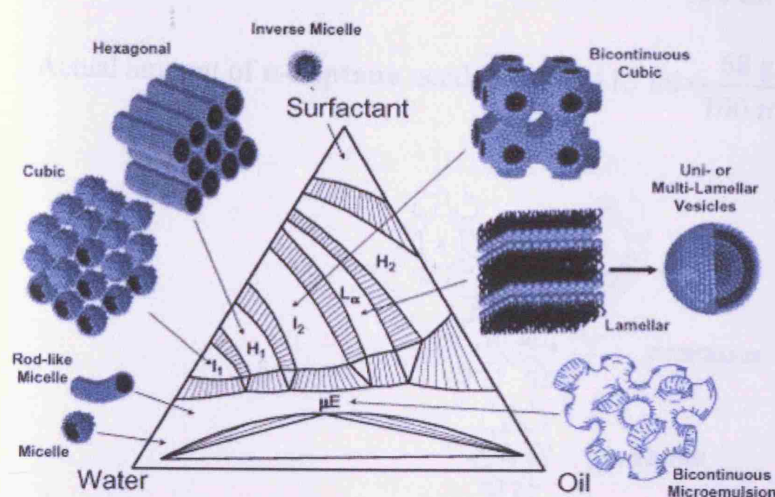


Figure C1 Scheme of the different structures in a ternary water/ surfactant/ oil system.

When mixing with the water (H₂O), the oil (n-heptane) and the surfactant (Brij®30) the system reaches equilibrium. That equilibrium will depend upon the amount of water, oil and surfactant. For different oils and different surfactants, the equilibrium is different. Fig. C1 represents a scheme of a micro-emulsion system of 3 components in equilibrium for a system, which is not ours (water/n-heptane/ Brij®30). For our system we know that we can have water-in-oil micelles (water is inside the micelle) when the water content is from 0-6% volume and the content for Brij®30 and n-heptane that we have employed are 80.46% for n-heptane and 16.54% for Brij®30*† (note that Brij®30 + n-heptane makes 97% and the remaining 3% is platinum salt or hydrazine (N₂H₄)). These values have been chosen since they give stable micelles*. These percentages quoted are in volume. Fig. C2 shows a scheme of the synthesis of the nanoparticles in micro-emulsion.

* 12. F.J Vidal-Iglesias, Private communication, 2007-9.

† J. Solla-Gullon, A. Rodes, V. Montiel, A. Aldaz, and J. Clavilier, "Electrochemical characterisation of platinum-palladium nanoparticles prepared in a water-in-oil microemulsion", *Journal of Electroanalytical Chemistry*, Vol. 554-555, pp. 273-284, September 2003.

i. Calculation of 97% (Brij®30 + n-heptane) of the micro-emulsion

Therefore the required amount of Brij®30 and n-heptane to a prepare total volume of 25 ml of micro-emulsion is

$$\text{Amount of Brij®30 needed} = 25 \text{ ml} \times \frac{16.54}{100} = 4.135 \text{ ml}$$

$$\text{Amount of n-heptane needed} = 25 \text{ ml} \times \frac{80.46}{100} = 20.115 \text{ ml}$$

For a higher accuracy in the preparation process, the amounts of those two previous compounds were weight measured. Therefore the actual amount needed in our case is

$$\text{Actual amount of Brij®30 needed} = 4.135 \text{ ml} \times \frac{95 \text{ g}}{100 \text{ ml}} = 3.928 \text{ g}$$

$$\text{Actual amount of n-heptane needed} = 20.115 \text{ ml} \times \frac{68 \text{ g}}{100 \text{ ml}} = 13.678 \text{ g}$$

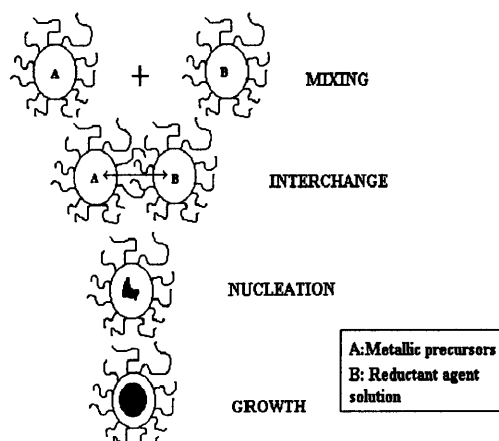


Figure C2 General synthesis scheme of metallic nanoparticles in micro-emulsion.

ii. Similarly, calculation for the remaining 3% (platinum salt or hydrazine (N_2H_4)) of the micro-emulsion

The amount required of $H_2O + N_2H_4$ to prepare total volume of 25 ml micro-emulsion is:

$$\text{Amount of } H_2O + N_2H_4 \text{ needed} = 25 \text{ ml} \times \frac{3}{100} = 0.75 \text{ ml}.$$

It is important to highlight that the water percentage has to be the same in both cases, when the platinum salt or hydrazine is inside the micelles (water-in-oil micro-emulsion).

In order to reduce the platinum, we need to use a reducing agent, which in our case was hydrazine (N₂H₄). To be sure that all the platinum (7.5 x 10⁻⁵ mol) is reduced a stoichiometric excess is added, and in our case this factor was 25.

$$\rightarrow \text{mass} = 25 \times (7.5 \times 10^{-5} \text{ mol}) \times 50.06 \frac{\text{g}}{\text{mol}} = 0.09386 \text{ g of N}_2\text{H}_4$$

For this calculation, it has to be taken into account that the hydrazine used was hydrazine monohydrate. That is the reason why the molecular weight is 50.06 instead of 32.02 g/mol.

As the density of N₂H₄ monohydrate is 1.03 g/ml, the volume of N₂H₄ needed is

$$\text{Volume} = \frac{\text{mass}}{\text{density}}$$

Therefore,

$$\text{Volume of N}_2\text{H}_4 \text{ needed} = \frac{0.09386 \text{ g}}{1.03 \text{ g/ml}} = \mathbf{0.091 \text{ ml}}$$

Finally the required H₂O = 0.75 ml – 0.091 ml = **0.659 ml**

The quantity required of **0.1 M H₂PtCl₆ solution** to prepare a total volume of 25 ml micro-emulsion is **0.75 ml** $\left(25 \text{ ml} \times \frac{3}{100} \right)$.

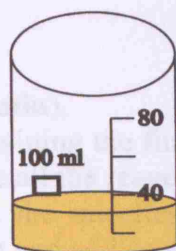
C3: Synthesis of Pt NPs (3.0 nm)

Finally, once the required quantities of the reagents are determined, 3.0 nm Pt NPs were synthesised as follows:

Step 1 (see fig. C3)

- First place a beaker (maximum volume of 100 ml) on a scale and zero it.
- Then weigh 3.928 g of **Brij®30**.
- Then zero the scale.
- Now weigh 13.678 g of **n-heptane**.
- Remove the beaker from the scale and put it in an ultrasound bath for a couple of seconds to make sure both the reagents are completely mixed.
- Take 0.75 ml of the prepared 0.1 M Pt solution (see C1) using a micropipette[‡]
- Now inject that volume (0.75 ml) of Pt solution into the same beaker (consisting of **Brij®30 + n-heptane**).
- Put the beaker (consisting of **Brij®30 + n-heptane + Pt** solution) in an ultrasound bath for few seconds to make sure all the reagents are completely mixed.
- Since n-heptane vaporises more quickly than other reagents, temporarily seal the beaker to avoid the changes in the total volume of the emulsion.

[‡] Pipette that dispense between 1 and 1000 µl are termed micropipette.



Total Volume: 25 ml

n-heptane - 13.678 g

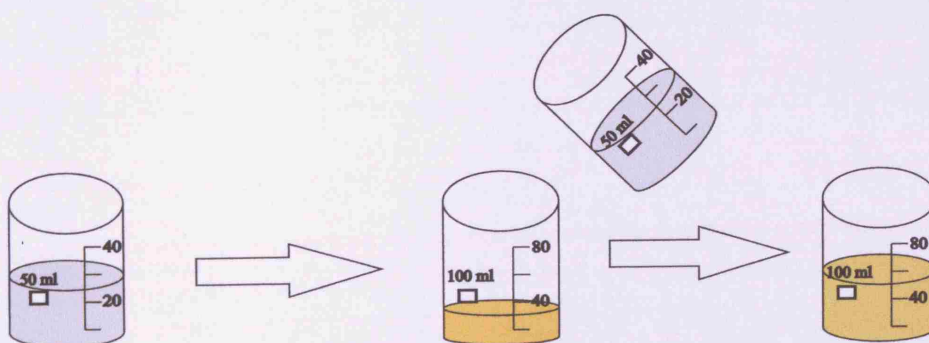
Brij®30 - 3.928 g

Metal (Pt) solution - 0.75 ml

Figure C3 1st beaker containing micro-emulsions.

Step 2 (see fig. C4)

- Place another beaker (maximum volume of 50 ml) on a scale and zero it.
- Then weigh 3.928 g of **Brij®30**.
- Then zero the scale.
- Now weigh 13.678 g of **n-heptane**.
- Now remove the beaker from the scale and put it in an ultrasound bath for a couple of seconds to make sure both the reagents are completely mixed.
- Take **0.659 ml** of ultra pure water (H_2O) using a micropipette.
- Inject that volume of H_2O into the beaker containing **Brij®30 + n-heptane**.
- Use the same micropipette with a different tip and take **0.091 ml** of N_2H_4 .
- Inject that volume of N_2H_4 into the beaker containing **Brij®30 + n-heptane + H_2O** .
- Put the beaker (consisting of **Brij®30 + n-heptane + H_2O + N_2H_4**) in an ultrasound bath for few seconds to make sure all the reagents are completely mixed.
- Now pour the reagents (consisting of **Brij®30 + n-heptane + H_2O + N_2H_4**) from this beaker into the previously prepared reagent beaker (containing **Brij®30 + n-heptane + Pt solution**).



Total Volume: 25 ml

n-heptane - 13.678 g

Brij®30 - 3.928 g

Ultra pure water (H_2O) - 0.659 ml

Reductant (N_2H_4) - 0.091 ml

Figure C4 2nd beaker containing micro-emulsions with hydrazine and squeme representing the synthesis of the platinum NPs after mixing both beakers.

Step 3 (see fig. C5)

- **Wait** for few minutes (~ 20 min).
- Put the **beaker** (mixed) containing the final micro-emulsions into an **ultrasound** bath for few seconds to make sure all the reagents are completely mixed.
- Then add **acetone** to break the micelles. Let the formed nanoparticles precipitate. Then remove the supernatant and add acetone again and repeat this process 3 times.
- Collect the synthesised Pt NPs and wash them 3-4 times with ultra pure water to completely eliminate the surfactant molecules and the acetone from the previous cleaning.
- Finally store the nanoparticles in ultra pure water.

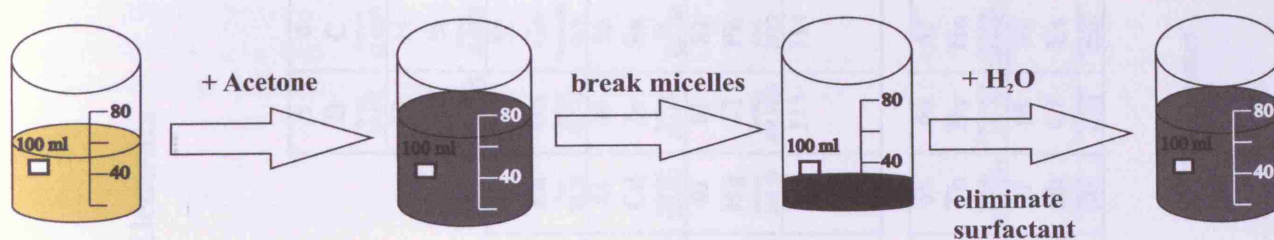


Figure C5 Schematic of the process of breaking the micelles, eliminating the surfactant and finally storing the synthesised Pt NPs in ultra pure water.

The Periodic Table of the Elements

¹ B. May, "The Periodic Table - Atomic Number, Symbol, Element Name, 1991 IUPAC approved names", *Widener University Science Division*, <http://science.widener.edu/~svanbram/ptable.html> (accessed on 5th August 2009).

APPENDIX E: Detailed Procedure of Synthesis of Spherical Pt NPs (6.9 nm)

NOTE: In the synthesis process of Pt NPs (6.9 nm), 7.5×10^{-5} moles of this noble metal were prepared.

E1: Calculations of the Reagents (K_2PtCl_4 , $NaBH_4$, and H_2O) needed for this Synthesis process

E1 (a): Calculation of required K_2PtCl_4

I. Preparation of the Pt solution from K_2PtCl_4 salt.

i. For this synthesis procedure, the Pt concentration has to be 6.5×10^{-4} M. Therefore, if the same amount of moles of platinum is desired for the different synthesis, 7.5×10^{-5} moles of platinum will be prepared (see Appendix C and F for the other Pt NPs).

$$6.5 \times 10^{-4} \frac{\text{mol}}{\text{L}} = \frac{7.5 \times 10^{-5} \text{ mol}}{X \text{ L}}$$

Therefore, X = 115.38 mL of a K_2PtCl_4 solution, where X is the volume to prepare.

ii. Therefore, and since the molecular weight (Mw) of Pt is 195.078 g/mol (see periodic table, appendix D),

$$1 \text{ mol} \rightarrow 195.078 \text{ g}$$

$$\begin{aligned} \therefore 7.5 \times 10^{-5} \text{ mol} &\rightarrow 7.5 \times 10^{-5} \text{ mol} \times 195.078 \frac{\text{g}}{\text{mol}} \\ &= 0.01463 \text{ g of Pt needed} \end{aligned}$$

iii. Since the Pt mass percentage on the concentrated K_2PtCl_4 solution is 46.67%

$$\begin{aligned} \therefore \text{The effective Pt needed} &= \frac{0.01463}{\frac{46.67}{100}} \text{ g} \\ &= 0.03135 \text{ g of } K_2PtCl_4 \text{ needed} \end{aligned}$$

iv. Since the effective mass of Pt (0.03135 g) needed is very small for the preparation of this diluted Pt solution, it is better to prepare a highly concentrated Pt solution (say prepare 10 ml 0.01 M of K_2PtCl_4 and dilute that Pt solution to obtain 6.5×10^{-4} M K_2PtCl_4).

II. Synthesis of 10 ml 0.01 M of Pt solution from K_2PtCl_4 salt.

10 ml 0.01 M K_2PtCl_4

$$0.01 \frac{\text{mol}}{\text{L}} \times (10 \times 10^{-3}) \text{ L} \rightarrow 10^{-4} \text{ mol of } K_2PtCl_4 \text{ needed}$$

Since the molecular weight of Pt is 195.078 g/ mol, therefore,

$$1 \text{ mol} \rightarrow 195.078 \text{ g}$$

$$\begin{aligned}\therefore 10^{-4} \text{ mol} &\rightarrow 10^{-4} \text{ mol} \times 195.078 \frac{\text{g}}{\text{mol}} \\ &= 0.0195078 \text{ g of Pt needed}\end{aligned}$$

Since the mass percentage of Pt on the concentrated K_2PtCl_4 salt is 46.67%

$$\begin{aligned}\therefore \text{The effective mass Pt needed} &= \frac{0.0195078}{\frac{46.67}{100}} \text{ g} \\ &= 0.0417994 \text{ g of } \text{K}_2\text{PtCl}_4 \text{ needed}\end{aligned}$$

III. Now, how do we prepare 115.38 ml 6.5×10^{-4} M of Pt solution from the highly concentrated 0.01 M of Pt solution?

$$1\text{L} \rightarrow 0.01 \text{ mol}$$

$$\therefore \text{XL} \rightarrow 7.5 \times 10^{-5} \text{ mol (where X is the unknown quantity)}$$

Therefore the required quantity (X) needed from the highly concentrated 0.01 M Pt solution to make 6.5×10^{-4} M of Pt solution is

$$X = \frac{1\text{L}}{0.01 \text{ mol}} \times (7.5 \times 10^{-5}) \text{ mol} = 7.5 \text{ mL of } 0.01 \text{ M Pt solution needed}$$

IV. Therefore to prepare 115.38 ml 6.5×10^{-4} M K_2PtCl_4 , follow the steps below.

Step1

- Take **7.5 ml** of Pt solution from the highly concentrated 0.01 M Pt solution using a micropipette.
- Then inject that volume of Pt solution into an empty beaker.
- Now add **107.88 ml** ($115.38 \text{ ml} - 7.5 \text{ ml}$) of **water** to the beaker containing 7.5 ml of Pt solution to make a total volume of 115.38ml.
- Finally 115.38 ml 6.5×10^{-4} M of K_2PtCl_4 is prepared.

E1 (b): Calculation of required NaBH_4

I. Synthesis of 115.38 ml 0.01 M of NaBH_4 .

i. 115.38 ml 0.01 M NaBH_4

$$0.01 \frac{\text{mol}}{\text{L}} \times (115.38 \times 10^{-3})\text{L} \rightarrow 1.1538 \times 10^{-3} \text{ mol}$$

Calculation of molecular weight of NaBH₄ (Mw of individual elements were found from the periodic table, see appendix D),

$$\begin{aligned}\text{Na} &\rightarrow 22.98977 \text{ g/mol} \\ \text{B} &\rightarrow 10.811 \text{ g/mol} \\ \text{H}_4 &\rightarrow \frac{(1.00794 \times 4) \text{ g/mol}}{1} \\ \therefore \text{NaBH}_4 &\rightarrow 37.83253 \text{ g/mol}\end{aligned}$$

$$1 \text{ mol} \rightarrow 37.83253 \text{ g/mol}$$

$$\begin{aligned}1.1538 \times 10^{-3} \text{ mol} &\rightarrow (1.1538 \times 10^{-3}) \text{ mol} \times 37.83253 \text{ g/mol} \\ &= 0.04365 \text{ g} \\ &\approx 0.04365 \text{ g of NaBH}_4 \text{ added}\end{aligned}$$

Therefore, to prepare 115.38 ml 0.01 M of NaBH₄, add **115.38 ml** of water with **0.04365 g of NaBH₄**.

E2: Synthesis of Pt NPs

Step 1: Prepared condition

H₂O Volume (ml)	K₂PtCl₄ weight (g)	NaBH₄ Weight (g)
115.384615	0.0313496	0.04365

Step 2: Put NaBH₄ in the desiccator^{*}

- Make sure to add more than the required amount of NaBH₄ in the desiccator, one or two days in advance of the synthesis of Pt NPs.

Step 3: Measuring 0.04365 g of NaBH₄ on the scale

- First place the beaker on the scale and make it to zero.
- Then weigh 0.04365 g of NaBH₄.
- Since we need 115.384615 ml of water, we cannot directly measure it on the scale (since Max 50g).

Step 4: Preparation of 115.38 ml of 0.01 M NaBH₄

- Collect 100 ml of H₂O using a volumetric flask.

^{*} Desiccators are sealed enclosures containing desiccants used to protect chemicals which react with water from humidity. Here the desiccator has been used to remove traces of water from an almost dry chemical.

- Then pour a small amount of H₂O (measured) onto the vial of the measured NaBH₄ and rinse it back to another beaker (Volume of the beaker ~ 200 ml).
- Repeat the above procedure 2-3 times (in order to dissolve NaBH₄ completely) and pour the remaining H₂O into the beaker (containing dissolved NaBH₄).
- Now the remaining 15.3846 ml (115.384615 ml – 100 ml) of H₂O are needed.
- Use the scale to measure the remaining amount (15.3846 ml) of water and pour it into the beaker containing dissolved NaBH₄ and store it into the fridge for 3 hrs.

Step 5: Preparation of 115.384615 ml of K₂PtCl₄

- Follow the step 3, but this time, weigh 0.0313496 g of K₂PtCl₄.
- Now follow exactly the same procedures in step 4 above, instead of NaBH₄, dissolve K₂PtCl₄ into the 115.384615 ml H₂O.
- Store the prepared K₂PtCl₄ solution in a fridge for 3 hrs.

Step 5: Synthesis of Spherical Pt NPs (6.9 nm)

- Once the 115.385 ml of 0.01 M NaBH₄ solution aged for 3 hours, then it was added dropwise to the 6.5×10^{-4} M of K₂PtCl₄ solution, with vigorous stirring at ice cold temperature.
- Wait for 20 min for the complete reaction to take place.
- The solution was brown-yellowish at the beginning, and finally it became dark grey.

In this synthesis, we have the Pt salt and the reducing agent; there is neither any colloid nor any surfactant.

APPENDIX F: Detailed Procedure of Synthesis of Pt cubic NPs (8.6 nm)

F1: Calculations of the Reagents (K_2PtCl_4 , and sodium polyacrylate) needed for this Synthesis process

In order to prepare a 10^{-4} M K_2PtCl_4 and 10^{-4} M sodium polyacrylate (NaPAA) as previously reported^{}, and also to have 7.5×10^{-5} moles of Pt, the total volume of the solution containing all the reagents (K_2PtCl_4 , NaPAA) should be 750 ml*
i.e. $\left(\left(7.5 \times 10^{-5} \right) \text{ mol} \div 10^{-4} \frac{\text{mol}}{\text{L}} = 0.75 \text{ L} = 750 \text{ ml} \right)$.

F1 (a): Calculation of the required amount of Pt solution needed for the synthesis of Pt cubic NPs

I. The source of platinum that is going to be used is a concentrated K_2PtCl_4 solution. For the synthesis procedure, to minimise experimental errors, a more diluted solution will be used (a 0.01 M solution). The molecular weight (Mw) of Pt is 195.078 g/mol (see periodic table, appendix D). Therefore, to prepare 10 ml of this solution.

10 ml 0.01 M K_2PtCl_4

$$0.01 \frac{\text{mol}}{\text{L}} \times (10 \times 10^{-3}) \text{ L} \rightarrow 10^{-4} \text{ mol}$$

II. Since the Mw of Pt is 195.078 g/mol, therefore,

$$1 \text{ mol} \rightarrow 195.078 \text{ g}$$

$$\therefore 10^{-4} \text{ mol} \rightarrow 10^{-4} \text{ mol} \times 195.078 \frac{\text{g}}{\text{mol}} \\ = 0.0195078 \text{ g of Pt needed}$$

III. Since the mass percentage of Pt on the concentrated K_2PtCl_4 solution is 46.67%

$$\therefore \text{The effective Pt needed} = \frac{0.0195078}{\frac{46.67}{100}} \text{ g of } K_2PtCl_4 \\ = 0.0418 \text{ g of } K_2PtCl_4 \text{ needed}$$

IV. Once the required amount of Pt is known, how do we prepare 10 ml 0.01 M of K_2PtCl_4 ?

^{*} 1. L. D. Rampino, and F. F. Nord "Preparation of Palladium and Platinum Synthetic High Polymer Catalysts and the Relationship between Particle Size and Rate of Hydrogenation" *Journal of the American Chemical Society*, Vol. 63, No. 10, pp. 2745-2749, October 1941.

2. A. Henglein, B. G. Ershov, and M. Malow "Absorption Spectrum and Some Chemical Reactions of Colloidal Platinum in Aqueous Solution", *The Journal of Physical Chemistry*, Vol. 99, No. 38, pp. 14129-14136, September 1995.

Step 1

- Place a volumetric flask (max volume 10 ml) on a scale and zero it.
- Weigh **0.0418 g** of **K₂PtCl₄** salt.
- Remove the flask containing K₂PtCl₄ salt from the scale and keep adding H₂O until the total volume of Pt solution reaches 10ml.
- Finally 10ml 0.01 M of K₂PtCl₄ solution is prepared.

V. How do we determine the required amount of 0.01 M of Pt solution for the synthesis of Pt cubic NPs?

Step 1

- It is known that the total volume of the solution should be 750 ml and, as previously reported by Rampino and Nord*, the final concentration of K₂PtCl₄ should be 10⁻⁴ M. Therefore, the required amount from the 0.01 M Pt solution for the Pt cubic synthesis is

$$750 \text{ ml} \times \frac{10^{-4} \frac{\text{mol}}{\text{L}}}{0.01 \frac{\text{mol}}{\text{L}}} = \mathbf{7.5 \text{ ml } 0.01 \text{ M } K_2PtCl_4 \text{ needed}}$$

- Therefore the amount required of **0.01 M** of **Pt** solution is **7.5 ml**.

F1 (b): Calculation of reagent needed for 25 ml 0.1 M of NaPAA

I. Synthesis of 25 ml of 0.1 M NaPAA.

25 ml of 0.1 M NaPAA

$$0.1 \frac{\text{mol}}{\text{L}} \times (25 \times 10^{-3}) \text{L} \rightarrow 25 \times 10^{-4} \text{mol}$$

For this polymer, the average molecular weight is 2100 g / mol, (indicated in the reagent container).

$$1 \text{ mol} \rightarrow 2100 \frac{\text{g}}{\text{mol}}$$

$$\begin{aligned} 25 \times 10^{-4} \text{ mol} &\rightarrow (25 \times 10^{-4}) \times 2100 \text{ g} \\ &= \mathbf{5.25 \text{ g of NaPAA needed}} \end{aligned}$$

II. Therefore, to prepare **25 ml 0.1 M NaPAA** solution, the effective **NaPAA** needed is **5.25g**; the remainder will be H₂O. How do we determine the amount of H₂O needed to add to make the total volume 25 ml?

Step 1

- First place a small beaker (maximum volume 50 ml) on a scale and zero it.
- Then weigh 5.25 g of **NaPAA**.
- Keeping the beaker on the scale, zero it again.
- Now keep on adding H₂O into the beaker containing the NaPAA until all the NaPAA is completely dissolved. An ultrasound bath was used to help us dissolve the NaPAA.
- The solution is then transferred into a 25 ml volumetric flask and H₂O is added until the total volume reaches 25 ml; practically it is observed that 22 ml of H₂O are needed to prepare 25 ml 0.1 M of NaPAA (e.g. to prepare **NaPAA** 0.1 M add 2.625 g in 11ml or **1.313 g in 5.5 ml of H₂O**).

III. How do we determine the required amount of 0.1 M NaPAA for the synthesis of cubic Pt NPs?

Step 1

- As discussed previously in F1 (a), the final concentration of NaPAA should be 10⁻⁴ M; therefore, the amount required from the 0.1 M NaPAA solution for the Pt cubic synthesis is

$$750 \text{ ml} \times \frac{10^{-4} \frac{\text{mol}}{\text{L}}}{0.1 \frac{\text{mol}}{\text{L}}} = \mathbf{0.75 \text{ ml } 0.1 \text{ M of NaPAA needed}}$$

- Therefore the amount required of **0.1 M of NaPAA** solution is **0.75 ml**.

F2: Synthesis of Pt cubic NPs (8.6 nm)

Finally, once the required quantities of the reagents are determined, 8.6 nm Pt cubic NPs were synthesised as follows:

Step 1 (see fig. F1)

- Take an empty and clean beaker (max volume 1L).
- Use a volumetric flask (max volume 250ml) to collect 750 ml of H₂O and fill the empty beaker.
- Use a micropipette to take out 7.5 ml of H₂O from the filled beaker (750 ml).
- Now replace those 7.5 ml of H₂O with 7.5 ml of 0.01 M K₂PtCl₄ solution (see F1 (a)) using the micropipette.
- Shield the beaker completely and store it for 3 days.

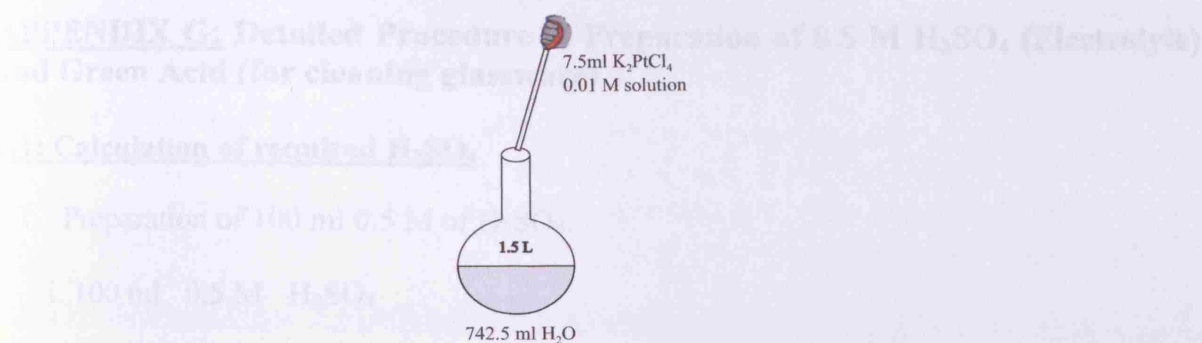


Figure F1 Beaker containing Pt solution + H₂O.

Step 2 (see fig. F2)

- On the 4th day take the beaker and add 0.75 ml 0.1 M of NaPAA solution.
- Then bubble argon gas for 20 min in the solution containing the reagents (Pt metal, NaPAA) to deoxygenate the solution.
- Now bubble H₂ at a steady flow rate through that solution for 5 min to reduce the Pt ions.
- Seal the beaker and cover it completely with aluminium foil and leave it for 14 hrs.

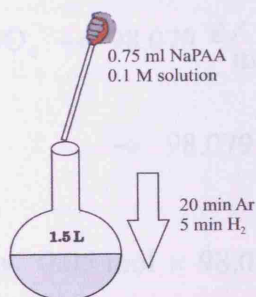


Figure F2 Beaker containing Pt solution, H₂O and NaPAA. The Pt ions were reduced by bubbling H₂.

Step 3 (see fig. F3)

- After 14 hrs, open the beaker and add ~3.75 g of NaOH to break the colloid and let the nanoparticles precipitate (takes around 12 h).
- The precipitate formed by the metallic nanoparticles was washed several times (3-4 times) with ultra pure water to eliminate the polyacrylate.
- Finally the nanoparticles were kept in ultra pure water.

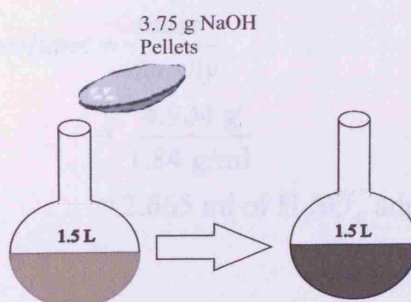


Figure F3 Introduction of NaOH into the beaker containing Pt solution, H₂O and NaPAA.

APPENDIX G: Detailed Procedure of Preparation of 0.5 M H₂SO₄ (Electrolyte) and Green Acid (for cleaning glassware)

G1: Calculation of required H₂SO₄

I. Preparation of 100 ml 0.5 M of H₂SO₄.

i. 100 ml 0.5 M H₂SO₄

$$0.5 \frac{\text{mol}}{\text{L}} \times (100 \times 10^{-3})\text{L} \rightarrow 0.05 \text{ mol}$$

Calculation of Mw of H₂SO₄ (Mw of individual elements were found from the periodic table, see appendix D),

$$\text{H}_2 \rightarrow 2 \times 1.00794 \frac{\text{g}}{\text{mol}}$$

$$\text{S} \rightarrow 32.066 \frac{\text{g}}{\text{mol}}$$

$$\text{O}_4 \rightarrow \underline{(4 \times 15.9994) \frac{\text{g}}{\text{mol}}}$$

$$\therefore \text{H}_2\text{SO}_4 \rightarrow 98.079 \frac{\text{g}}{\text{mol}}$$

$$1 \text{ mol} \rightarrow 98.079 \frac{\text{g}}{\text{mol}}$$

$$\begin{aligned} 0.05 \text{ mol} &\rightarrow 0.05 \text{ mol} \times 98.079 \frac{\text{g}}{\text{mol}} \\ &= 4.904 \text{ g of H}_2\text{SO}_4 \text{ added} \end{aligned}$$

Therefore, to prepare 100 ml 0.5 M of H₂SO₄, weigh **4.904 g** of H₂SO₄ and add water for the total volume of 100 ml using a volumetric flask.

OR

Otherwise, since the density of the H₂SO₄ is known (i.e. 1.84 g/ml - written on the bottle), therefore the volume needed to prepare 100 ml 0.5 M of H₂SO₄ is:

$$\begin{aligned} \text{volume} &= \frac{\text{mass}}{\text{density}} \\ &= \frac{4.904 \text{ g}}{1.84 \text{ g/ml}} \\ &= 2.665 \text{ ml of H}_2\text{SO}_4 \text{ added} \end{aligned}$$

II. Therefore to prepare 100 ml 0.5 M of H_2SO_4 , follow the steps below.

Step 1

- Take **2.665 ml** of H_2SO_4 highly concentrated using a micropipette.
- Then inject the H_2SO_4 solution into a volumetric flask (max volume 100 ml).
- Now add water to the flask containing 2.665 ml of H_2SO_4 to make a total volume of 100 ml.
- Finally 100 ml 0.5 M of H_2SO_4 is prepared.

G2: Preparation of Green Acid

Here, the green acid is used for cleaning (removes organics) the vessels (or glassware) prior to the experiments carried out in this research. The following steps have been carried out to prepare the green acid for cleaning glassware.

Step 1

- Add approximately 100 ml of H_2SO_4 (98% purity) to a suitable container.
- Then add 6-7 grains of KMnO_4 (Potassium permanganate).
- Wait for the KMnO_4 to dissolve in the 100 ml of H_2SO_4 until the solution becomes medium green (i.e. not too dark or too light – depending on the grains of KMnO_4).

APPENDIX H: Cyclic Voltammetry Profiles of Spherical Pt NPs (6.9 nm)

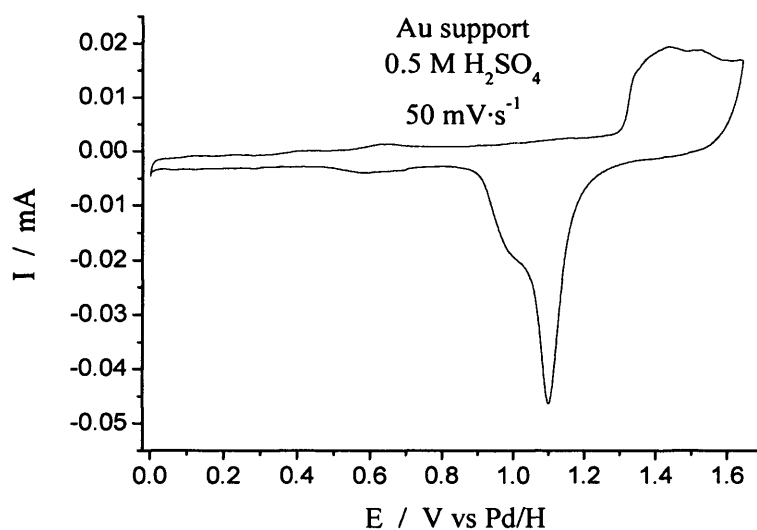


Figure H1 Voltammetric profile of the gold support. Test solution 0.5 M H₂SO₄. Sweep rate: 50 mV·s⁻¹.

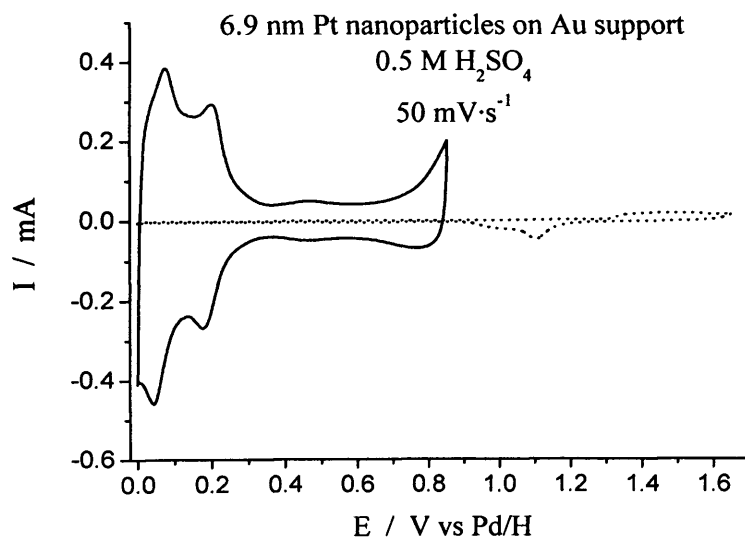


Figure H2 Voltammetric profile of platinum NPs (solid line) and the gold support electrode (dotted line) in 0.5 M H₂SO₄. Sweep rate: 50 mV·s⁻¹.

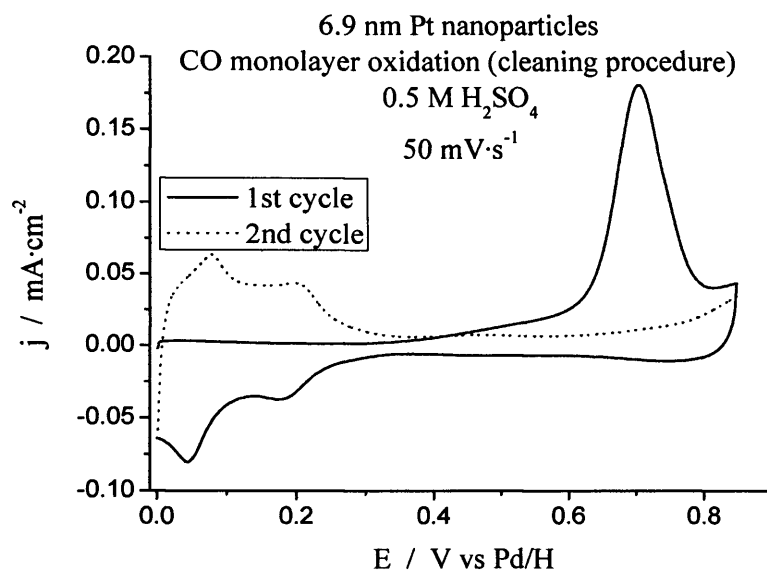


Figure H3 CO monolayer oxidation on Pt NPs. Test solution: 0.5 M H₂SO₄. Sweep rate: 50 mV·s⁻¹.

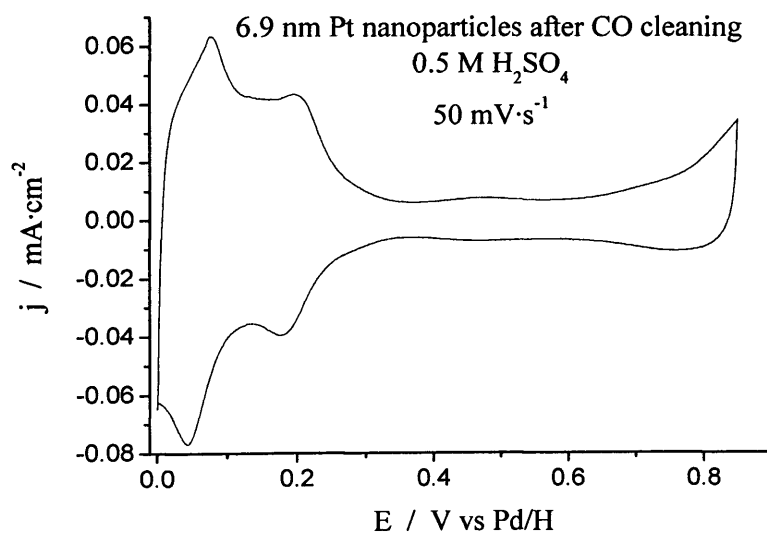


Figure H4 Voltammetric profile of Pt NPs after CO cleaning in 0.5 M H₂SO₄. Sweep rate: 50 mV·s⁻¹.

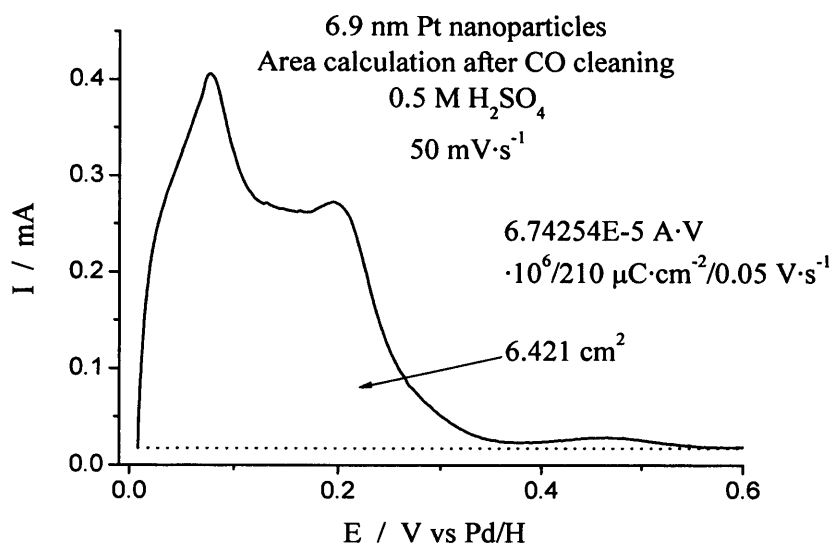


Figure H5 Area calculation of the deposited Pt NPs.

For the Pt cubic 6.9 nm Pt NPs

$$\text{Charge} = \frac{\text{Area}}{\text{Sweep rate}}$$

From the area and the sweep rate the real catalyst surface area can be obtained as follows.

$$6.74254 \times 10^{-2} \text{ mA} \times V \times \frac{\text{mC/s}}{\text{mA}} \times \frac{\text{cm}^2}{0.21 \text{ mC}} \times \frac{\text{s}}{0.05 \text{ V}} = 6.421 \text{ cm}^2$$

If we assume that the nanoparticles are spherical, the number of nanoparticles can be calculated as followed:

$$\text{Number of nanoparticles} = \frac{6.421 \text{ cm}^2}{4\pi r^2 \text{ m}^2} \cdot \frac{10^{-4} \text{ m}^2}{\text{cm}^2} \text{ nanoparticles}$$

where r is the main radius of the nanoparticles ($6.9 \text{ nm}/2 = 3.45 \text{ nm}$). Therefore for the 6 μl deposited (area 6.421 cm^2) the number of nanoparticles is:

$$\text{Number of nanoparticles} = \frac{6.421 \text{ cm}^2}{4\pi (3.45 \times 10^{-9})^2 \text{ m}^2 / 6\mu\text{l}} \cdot \frac{10^{-4} \text{ m}^2}{\text{cm}^2} = 4.293 \times 10^{12} \frac{\text{nanoparticles}}{6\mu\text{l}}$$

APPENDIX I: Cyclic Voltammetry Profile of Spherical Pt NPs (3.0 nm)

Pt nanoparticles, after cleaning, were analysed by cyclic voltammetry. With this electrochemical technique, the surface area of the nanoparticles could be evaluated. For this purpose, the nanoparticles were deposited on top of a gold electrode that was used as a support. Gold was used because no electrochemical process takes place between 0 and 0.85 V (vs Pd/H), which is the potential window that will be used to study the platinum nanoparticles. Fig. I1 shows the voltammetric profile of the gold electrode in a 0.5 M H₂SO₄ solution.

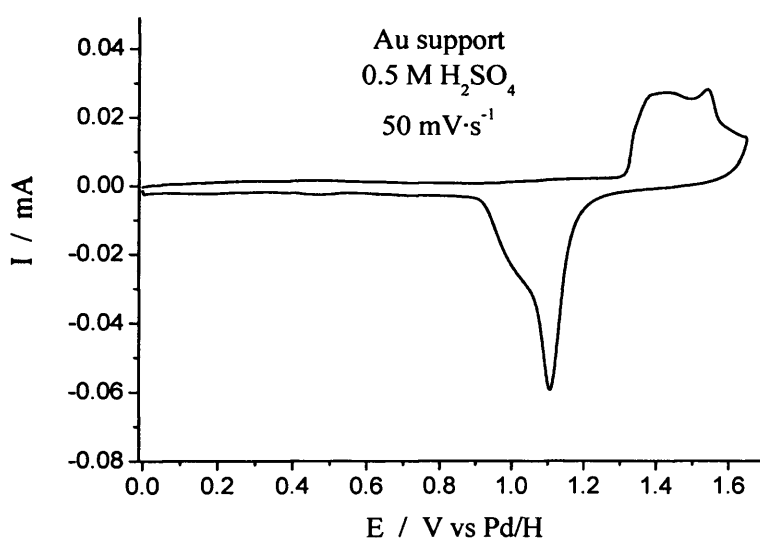


Figure I1 Voltammetric profile of the gold support. Test solution 0.5 M H₂SO₄. Sweep rate: 50 mV·s⁻¹.

Once the gold purity and the solution cleanliness were checked, a known amount of the solution containing the platinum nanoparticles was deposited on top of the gold electrode. In order to evaporate the water and avoid contamination in the sample, the electrode was exposed to a flow of nitrogen or argon. After the water evaporation the particles were strongly attached to the gold electrode. Afterwards, the electrode was transferred to the same cell and a new voltammogram was performed from 0 to 0.85 V to avoid surface reconstruction of the Pt nanoparticles. This voltammogram is shown in fig. I2 where, the voltammogram presented in fig. I1 is added for the sake of comparison.

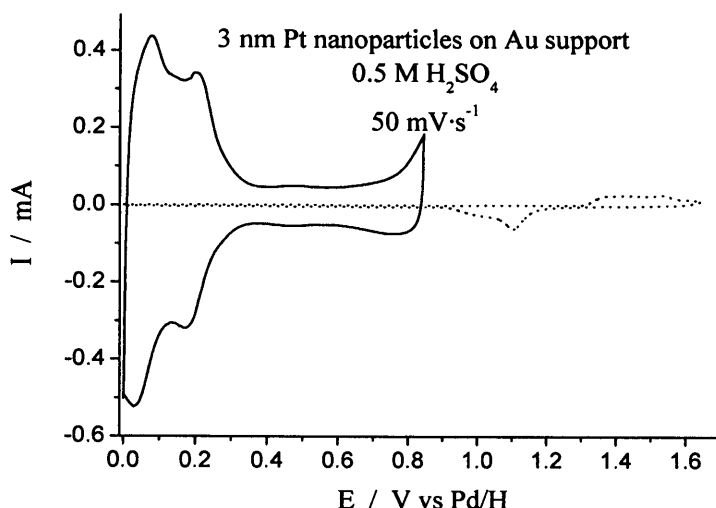


Figure I2 Voltammetric profile of platinum NPs (solid line) and the gold support electrode (dotted line) in 0.5 M H₂SO₄. Sweep rate: 50 mV·s⁻¹.

Nevertheless, these platinum nanoparticles are not completely clean. Some residues from the synthesis process can be adsorbed on their surface and they have to be removed before calculating the area of the platinum nanoparticles. In order to clean the nanoparticles a CO monolayer was adsorbed on the nanoparticles (by inserting the electrode in a CO saturated solution for several seconds) and later oxidised, as shown in fig. I3. This method has been reported by J. Solla-Gullon et al^{*} to clean this type of nanoparticles.

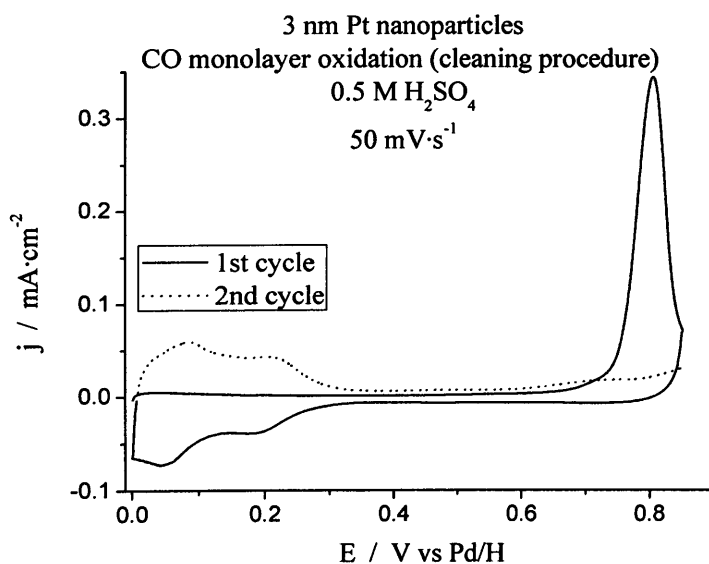


Figure I3 CO monolayer oxidation on Pt NPs. Test solution: 0.5 M H₂SO₄. Sweep rate: 50 mV·s⁻¹.

^{*} J. Solla-Gullon, V. Montiel, A. Aldaz, J. Clavilier, "Electrochemical characterisation of platinum nanoparticles prepared by microemulsion: how to clean them without loss of crystalline surface structure", *Journal of Electroanalytical Chemistry*, Vol. 491, pp. 69-71, July 2000.

Once the CO was oxidised, and it was checked that no more CO was left in the solution, a new voltammogram was recorded in the same conditions used previously for the results shown in fig. I2. The voltammetric profile shown in fig. I4 corresponds to the clean platinum nanoparticles on the gold support electrode.

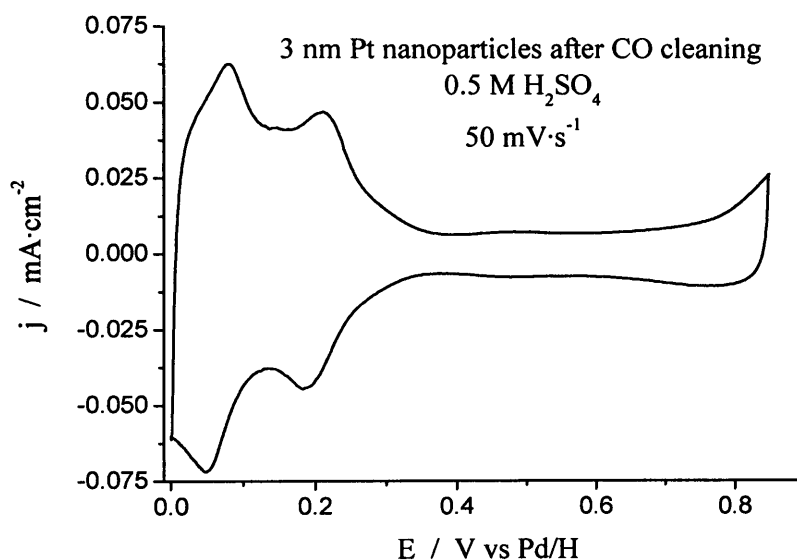


Figure I4 Voltammetric profile of Pt NPs after CO cleaning in 0.5 M H₂SO₄. Sweep rate: 50 mV·s⁻¹.

Once a clean voltammetric profile is recorded it is possible to measure the area of the platinum nanoparticles. For polyoriented platinum, it is known that the charge associated to the hydrogen adsorption desorption process and anion adsorption (processes taking place from 0 to 0.6 V) give 210 $\mu\text{C cm}^{-2}$ [†]. Therefore from the area of the voltammetric profile shown in fig. I5 it is possible to calculate the area of the nanoparticles used in this experiment.

[†]R. Woods, *Chemisorption at electrodes*, in: A.J Bard (Ed.), *Electroanalytical Chemistry: a Series of Advances*, Marcel Dekker, Inc., New York, Vol.9, pp.1, 1976.

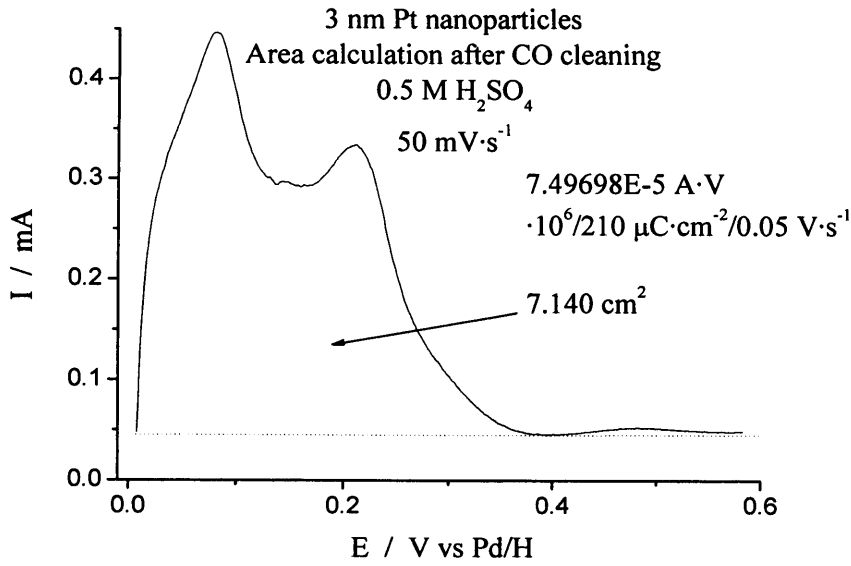


Figure I5 Area calculation of the deposited Pt NPs.

For the Pt cubic 3.0 nm Pt NPs

$$\text{Charge} = \frac{\text{Area}}{\text{Sweep rate}}$$

From the area and the sweep rate the real catalyst surface area can be obtained as follows.

$$7.49698 \times 10^{-2} \text{ mA} \times V \times \frac{\text{mC/s}}{\text{mA}} \times \frac{\text{cm}^2}{0.21 \text{ mC}} \times \frac{\text{s}}{0.05 \text{ V}} = 7.140 \text{ cm}^2$$

If we assume that the nanoparticles are spherical, the number of nanoparticles can be calculated as followed:

$$\text{Number of nanoparticles} = \frac{7.140 \text{ cm}^2}{4\pi r^2 \text{ m}^2} \cdot \frac{10^{-4} \text{ m}^2}{\text{cm}^2} \text{ nanoparticles}$$

where r is the main radius of the nanoparticles ($3.0/2=1.5$ nm). Therefore for the 6 μl deposited (area 7.140 cm^2) the number of nanoparticles is:

$$\text{Number of nanoparticles} = \frac{7.140 \text{ cm}^2}{4\pi (1.5 \times 10^{-9})^2 \text{ m}^2 / 6\mu\text{l}} \cdot \frac{10^{-4} \text{ m}^2}{\text{cm}^2} = 2.525 \times 10^{13} \frac{\text{nanoparticles}}{6\mu\text{l}}$$

Appendix J: Detailed Procedure for the Synthesis of Au NPs (8.2, 16.5, and 24.8 nm)

Au NPs of different sizes (8.2 nm, 16.5 nm, and 24.8 nm) were synthesised as previously reported by Panigrahi et al^{*}.

Total volume solution (ml)	Total Volume of 10 ⁻² M HAuCl ₄ (μl)	Volume of citrate (1 wt %) (μl)	Particle size (nm)
50	1250	2000	8
50	1250	1000	16
50	1250	750	25

Table J1: Details for the Size-Selective Synthesis of Gold Nanoparticles by the Frens Method^{*}

From the above table J1, the amount of Au used for the total volume of 50 ml solution is:

$$0.01 \frac{\text{mol}}{\text{L}} \times 1250 \times 10^{-6} \text{ L} = 1.25 \times 10^{-5} \text{ mol}$$

In the synthesis process of different sizes (8.2 nm, 16.5 nm and 24.8 nm) of Au NPs, 7.5×10^{-5} moles (i.e. similar to the Pt NPs synthesis) of this noble metal were prepared, therefore

$$\text{Required amount of Au moles} = \frac{7.5 \text{ mol}}{1.25 \times 10^{-5} \text{ mol}} = 6 \text{ times the amount of Au moles used in table J1.}$$

The values listed in table J1 can be recalculated as follows,

Total volume solution (ml)	Total Volume of HAuCl ₄ (10 ⁻²) (ml)	Volume of citrate (1% by weight) (ml)	Particle size (nm)
50 × 6 = 300	1.25 × 6 = 7.5	2 × 6 = 12	8
50 × 6 = 300	1.25 × 6 = 7.5	1 × 6 = 12	16
50 × 6 = 300	1.25 × 6 = 7.5	0.75 × 6 = 4.5	25

Table J2: Recalculated Values for the Size-Selective Synthesis of Gold NPs by the Frens Method^{*}.

J1: Preparation of 25 ml of 0.01 molar (M) Pt solution from concentrated HAuCl₄.

- I. The molecular weight (Mw) of Au is 196.97 g/mol (see periodic table, appendix D). Therefore, for

^{*} S. Panigrahi, S. Basu, A. Praharaj, A. Pande, S. Jana, A. Pal, S. K. Ghosh and T. Pal, "Synthesis and size-selective Catalysis by Supported Gold Nanoparticles: study on Heterogeneous and Homogeneous Catalytic Process", *Journal of Physical Chemistry*, Vol. 111, pp. 4596-4605, December 2007.

25 ml 0.01 M HAuCl_4

$$0.01 \frac{\text{mol}}{\text{L}} \times (25 \times 10^{-3}) \text{ L} \rightarrow 2.5 \times 10^{-4} \text{ mol}$$

II. Since the Mw of Au is 196.97 g/mol, therefore,

$$1 \text{ mol} \rightarrow 196.97 \text{ g}$$

$$\therefore 2.5 \times 10^{-4} \text{ mol} \rightarrow 2.5 \times 10^{-4} \times 196.97 \frac{\text{g}}{\text{mol}}$$
$$= 0.04924 \text{ g of Au needed}$$

III. Since the mass percentage of Au on the concentrated HAuCl_4 solution is 41.29 %

$$\text{The effective Au needed} = \frac{0.04924}{\frac{41.29}{100}} \text{ g of } \text{HAuCl}_4 \text{ needed}$$
$$= 0.11925 \text{ g of } \text{HAuCl}_4 \text{ used}$$

IV. Therefore, to prepare 25 ml 0.01 M Au solution, the effective Au needed is 0.11925 g of the concentrated HAuCl_4 solution; once the required quantity of the HAuCl_4 is determined, 25 ml of 0.01 M Au solution were prepared as follows

Step 1

- First place a beaker (max volume of 50 ml) on a scale and make it to zero.
- Then weigh **0.11925 g of HAuCl_4** .
- Remove the beaker from the scale and keep on adding water to the beaker containing HAuCl_4 using a volumetric flask until the total volume of the Au solution becomes 25 ml.

Step 2

- **Finally 25 ml 0.01 M of HAuCl_4 were prepared.**

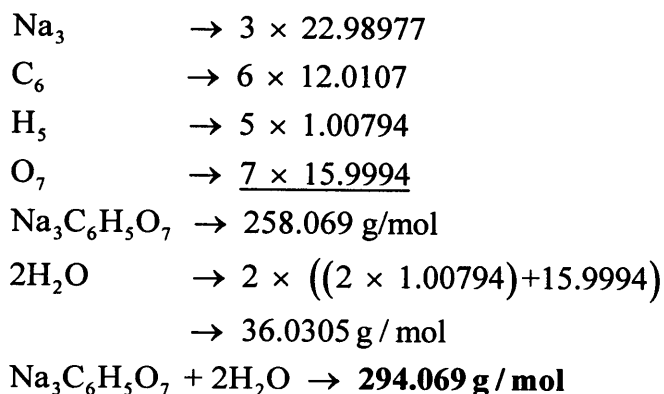
J2: Calculation of reagent needed for 25 ml of 1% by trisodium citrate dehydrate

Total Volume of the citrate solution = 25 ml

- I. To prepare 25 ml of 1% trisodium citrate then we need to dissolve 0.25 g $\left(1\% \text{ weight} = 25 \times \frac{1}{100} = 0.25 \text{ g}\right)$ in 25 ml of ultra pure water (if the citrate purity was 100%). Since the purity of the citrate is only 99% therefore for 100% we need $0.2525 \text{ g} \left(\frac{0.25 \text{ g}}{99} \times 100 = 0.2525 \text{ g}\right)$.

II. Since the citrate used in the synthesis of Au NPs is trisodium citrate dehydrate, but actually trisodium citrate is required.

III. The calculations of Mw of trisodium citrate dehydrate ($\text{Na}_3\text{C}_6\text{H}_5\text{O}_7 + 2\text{H}_2\text{O}$)



The Mw of trisodium citrate dehydrate is 294.069 g, which includes 2 water molecules (where the Mw of H_2O = 18.0153 g),

IV. Therefore the required **trisodium citrate** dehydrate:

$$0.2525 \times \frac{294.069}{(294.069 - 36.0305)} = \mathbf{0.2878 \text{ g}}$$

J3: Preparation of 25 ml of 1% by trisodium citrate dehydrate

Step 1

- First place a small beaker (maximum volume 50 ml) on a scale and zero it.
- Then weigh **0.2877 g** of **trisodium citrate** dehydrate.
- Keeping the beaker on the scale, again it again.
- Now keep on adding H_2O into the beaker containing the trisodium citrate dehydrate until it is completely dissolved. An ultrasound bath was used to help dissolve it.
- The solution is then transferred into a 25 ml volumetric flask and H_2O is added until the total volume reaches 25 ml.

J4: Synthesis of Au NPs (8.2, 16.5, and 24.8 nm)

Finally, once the reagents (Au and sodium citrate solutions) are prepared, follow the steps mentioned in section 4.5.2 of chapter 4 to synthesise Au NPs of different sizes (8.2 nm, 16.5 nm, and 24.8 nm).

APPENDIX K: Determination of Complex Permittivity of Unknown Materials Using Capacitive Model

$$f_{start} := 30 \cdot 10^3 \quad \text{Start Frequency} \quad NP := 201 \quad \text{Number of points}$$

$$f_{stop} := 6 \cdot 10^9 \quad \text{Stop Frequency} \quad n := 0 \dots 200 \quad j := \sqrt{-1}$$

$$f_n := f_{start} + \frac{n}{NP - 1} \cdot (f_{stop} - f_{start})$$

data0 - S₁₁ data of empty probe (air) - either from experiment or HFSS simulation

data1 - S₁₁ data of sample under test - either from experiment or HFSS simulation

data0 := READPRN("D:\My PhD work\My PhD work\IEEE Journal\data18.d1")

data1 := READPRN("D:\My PhD work\My PhD work\IEEE Journal\data19.d1")

$$Z_0 := 50 \quad \omega := 2 \cdot \pi \cdot f$$

$$x0_n := data0_{n,0} \quad y0_n := data0_{n,1} \quad x1_n := data1_{n,0} \quad y1_n := data1_{n,1}$$

$$S11_air_n := x0_n + j \cdot y0_n \quad S11_sample_n := x1_n + j \cdot y1_n$$

$$\rho_n := \frac{S11_sample_n}{S11_air_n} \quad \text{Eliminating the electrical length } L \text{ between AB and AB' - see section 6.2.2}$$

C0 and C1 are the fringing field capacitances due to the dielectric filling the line of the probe and due to material under test, respectively.

$$C0 := -0.01 \cdot 10^{-15} \quad C1 := 6.03 \cdot 10^{-15}$$

$$\tau := 14 \cdot 10^{-11} \quad \text{Relaxation time of each dipole} \quad freq := \frac{1}{2 \cdot \pi \cdot \tau} \quad freq = 1.137 \times 10^9$$

ε_{1_d} and ε_{2_d} are the real and imaginary part of the Debye model of the material under testy, respectively.

$$\epsilon1_d_n := 4.9 + \frac{(25.4 - 4.9)}{1 + (2\pi f_n)^2 \cdot (\tau)^2} \quad \epsilon2_d_n := \frac{(25.4 - 4.9) \cdot [2\pi f_n \cdot (\tau)]}{1 + (2\pi f_n)^2 \cdot (\tau)^2}$$

$$Y_{a_n} := j \cdot \omega_n \cdot (C0 + C1) \quad \text{Aperture admittance without the sample (air)}$$

$$\Gamma_{a_n} := \frac{(1 - Z_0 \cdot Y_{a_n})}{(1 + Z_0 \cdot Y_{a_n})} \quad \text{Measured reflection coefficient at the reference plane AB without the sample}$$

$$\Gamma_{nn} := \text{inverse_}\Gamma_{a_n} \quad \text{inverse_}\Gamma_{a_n} := \frac{(1 + Z_0 \cdot Y_{a_n})}{(1 - Z_0 \cdot Y_{a_n})}$$

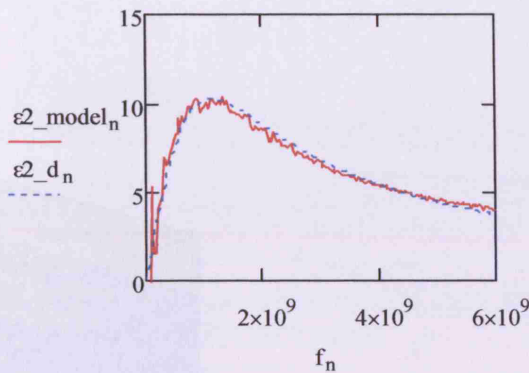
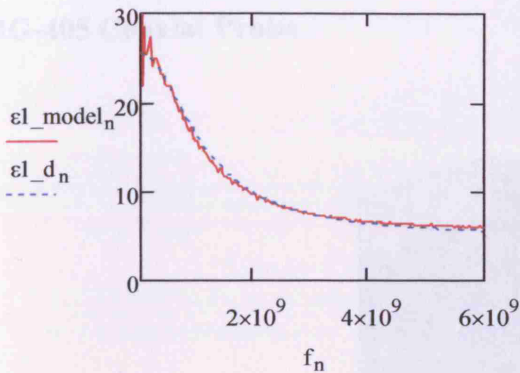
$$Y_{s_n} := \left(\frac{1}{Z_0} \right) \cdot \frac{(\Gamma_{nn} - \rho_n)}{(\Gamma_{nn} + \rho_n)} \quad \text{Aperture admittance with the sample}$$

$$\epsilon_{model_n} := \frac{1}{C1} \cdot \left(\frac{Y_{s_n}}{j \cdot \omega_n} - C0 \right) \quad \text{Inverted to find complex permittivity of the sample}$$

$\epsilon 1_model$ and $\epsilon 2_model$ are the measured real and imaginary part of the complex permittivity of the material under test, respectively.

$$\epsilon 1_model_n := \text{Re}(\epsilon model_n)$$

$$\epsilon 2_model_n := -\text{Im}(\epsilon model_n)$$



Error Calculations

$$n := 4 \dots 200 \quad \text{Number_of_points} := (200 - 4)$$

$$\text{Percent_}\epsilon 1_model_n := \frac{\left| \left| \epsilon 1_model_n \right| - \left| \epsilon 1_d_n \right| \right|}{\left| \epsilon 1_d_n \right|} \cdot 100$$

$$\text{Mean_}\epsilon 1model_ \%_error_A := \frac{\sum_{n=3}^{200} \text{Percent_}\epsilon 1_model_n}{\text{Number_of_points}}$$

$$\text{Mean_}\epsilon 1model_ \%_error_A = 3.463$$

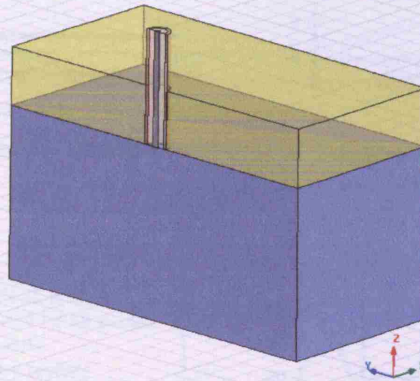
$$\text{Percent_}\epsilon 2_model_n := \frac{\left| \left| \epsilon 2_model_n \right| - \left| \epsilon 2_d_n \right| \right|}{\left| \epsilon 2_d_n \right|} \cdot 100$$

$$\text{Mean_}\epsilon 2model_ \%_error_A := \frac{\sum_{n=3}^{200} \text{Percent_}\epsilon 2_model_n}{\text{Number_of_points}}$$

$$\text{Mean_}\epsilon 2model_ \%_error_A = 4.35$$

APPENDIX L: Fringing Field Capacitances and Corresponding Complex Permittivity of the Test Materials Obtained From the HFSS Simulation for Different Types of OCPs

A. RG-405 Coaxial Probe



I. Fringing Field Capacitances determined from HFSS Simulation

Test Materials	Fringing field capacitance due to the material under test C_0 (F)	Fringing field capacitance due to the material under test C_1 (F)	% ME error of real permittivity ϵ_1 (%)	% ME error of Imaginary ϵ_2 permittivity (%)
Teflon	-0.50×10^{-14}	1.17×10^{-14}	3.33	3.48
Butanol	-0.50×10^{-14}	1.14×10^{-14}	2.88	2.79
Propan-2ol	-0.50×10^{-14}	1.16×10^{-14}	4.72	3.38
Ethanol	-0.50×10^{-14}	1.15×10^{-14}	2.03	2.33
Methanol	-0.50×10^{-14}	1.07×10^{-14}	0.41	2.94
Acetonitrile	-0.50×10^{-14}	1.08×10^{-14}	1.51	10.09
DMF	-0.50×10^{-14}	1.07×10^{-14}	0.77	6.13
Water	-0.50×10^{-14}	1.07×10^{-14}	1.12	6.58
Fringing field capacitances	-0.50×10^{-14}	$1.11 \pm 0.05 \times 10^{-14}$		

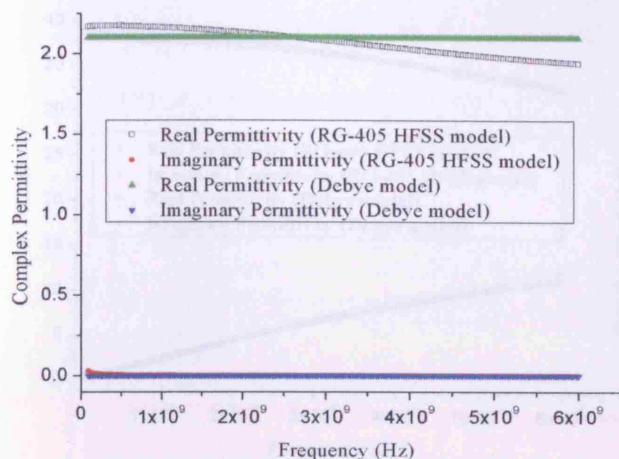


Figure 1 The complex permittivity of teflon as a function of frequency.

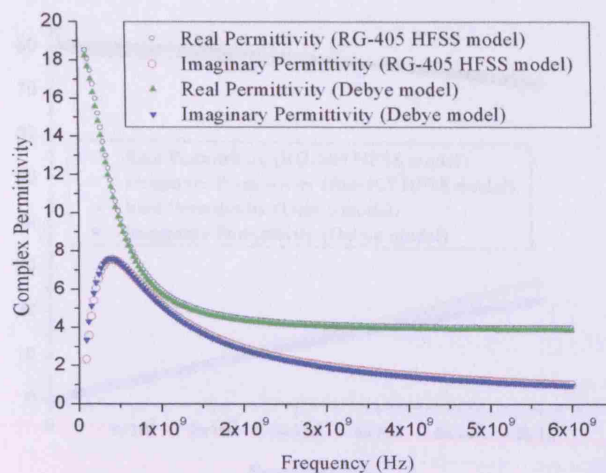


Figure 2 The complex permittivity of butanol as a function of frequency.

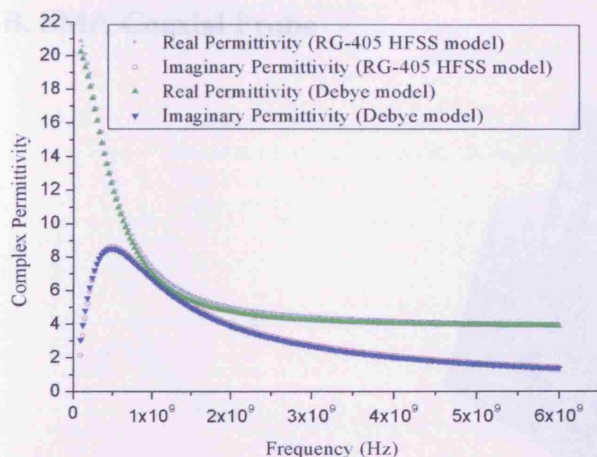


Figure 3 The complex permittivity of propan-2ol as a function of frequency.

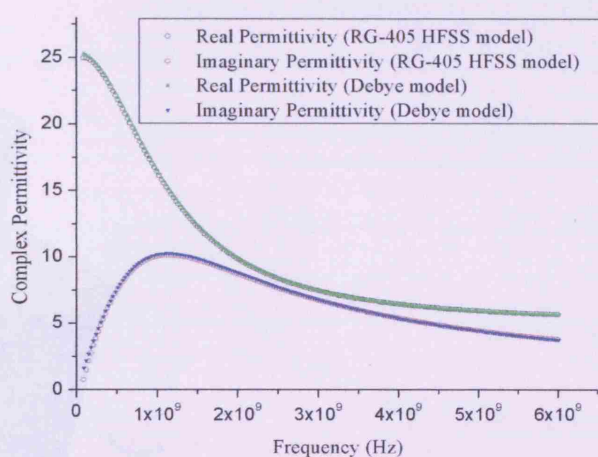


Figure 4 The complex permittivity of ethanol as a function of frequency.

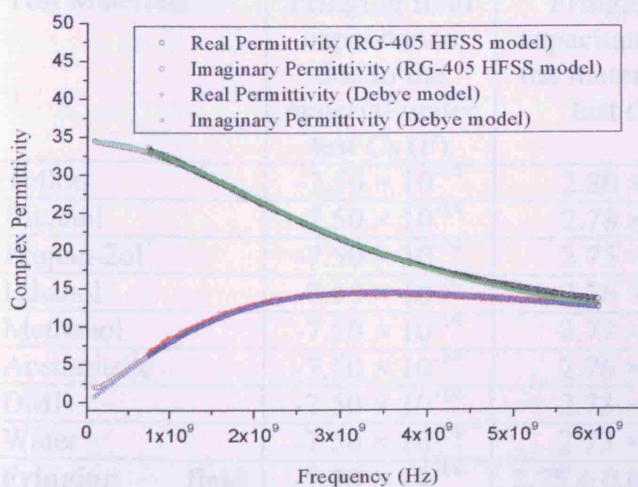


Figure 5 The complex permittivity of methanol as a function of frequency.

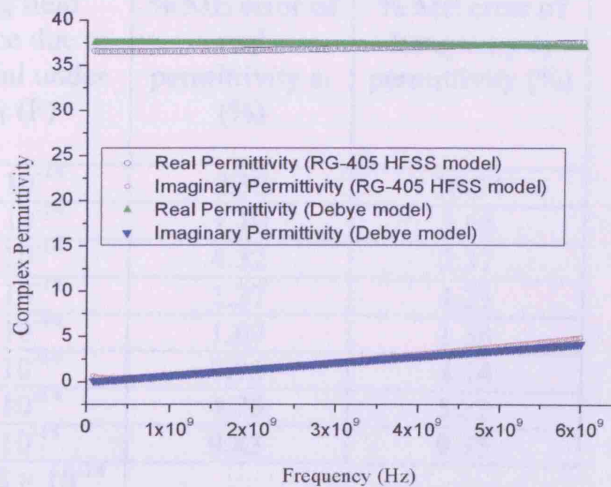


Figure 6 The complex permittivity of acetonitrile as a function of frequency.

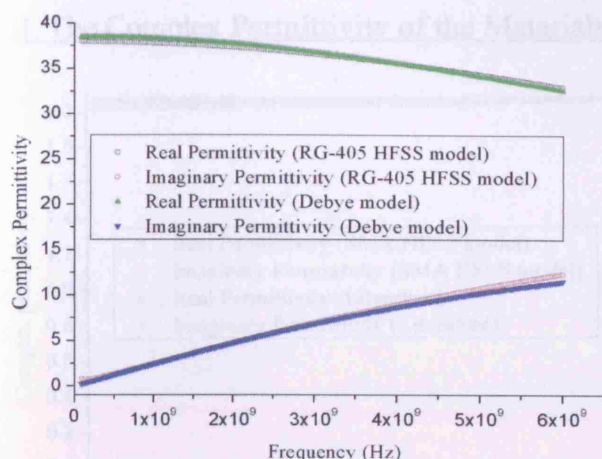


Figure 7 The complex permittivity of DMF as a function of frequency.

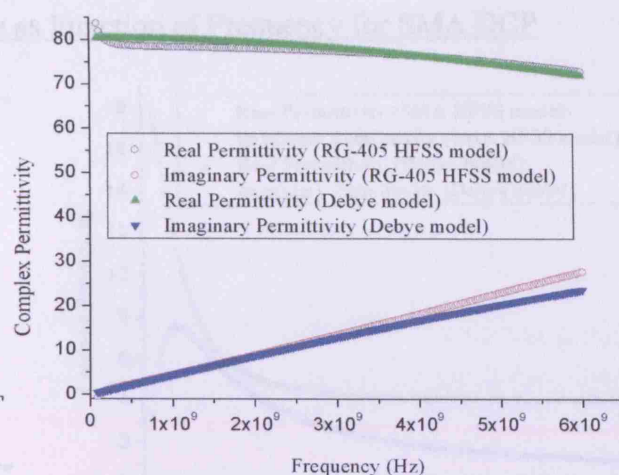
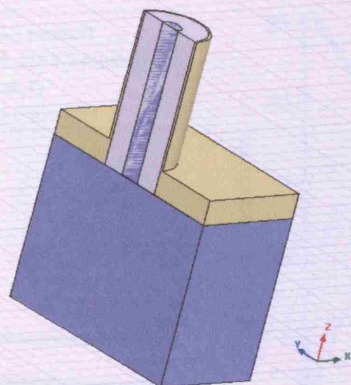


Figure 8 The complex permittivity of water as a function of frequency.

B. SMA Coaxial Probe



I. Fringing Field Capacitances determined from HFSS Simulation

Test Materials	Fringing field capacitance due to the material under test C_0 (F)	Fringing field capacitance due to the material under test C_1 (F)	% ME error of real permittivity ϵ_1 (%)	% ME error of Imaginary ϵ_2 permittivity (%)
Teflon	-7.50×10^{-14}	2.80×10^{-14}	2.30	10.34
Butanol	-7.50×10^{-14}	2.78×10^{-14}	1.10	1.65
Propan-2ol	-7.50×10^{-14}	2.75×10^{-14}	4.32	2.37
Ethanol	-7.50×10^{-14}	2.76×10^{-14}	1.37	1.21
Methanol	-7.50×10^{-14}	2.72×10^{-14}	1.69	1.38
Acetonitrile	-7.50×10^{-14}	2.76×10^{-14}	7.96	4.14
DMF	-7.50×10^{-14}	2.73×10^{-14}	4.76	5.22
Water	-7.50×10^{-14}	2.73×10^{-14}	9.83	9.75
Fringing field capacitances	-7.50×10^{-14}	$2.75 \pm 0.03 \times 10^{-14}$		

II. The Complex Permittivity of the Materials as Function of Frequency for SMA OCP

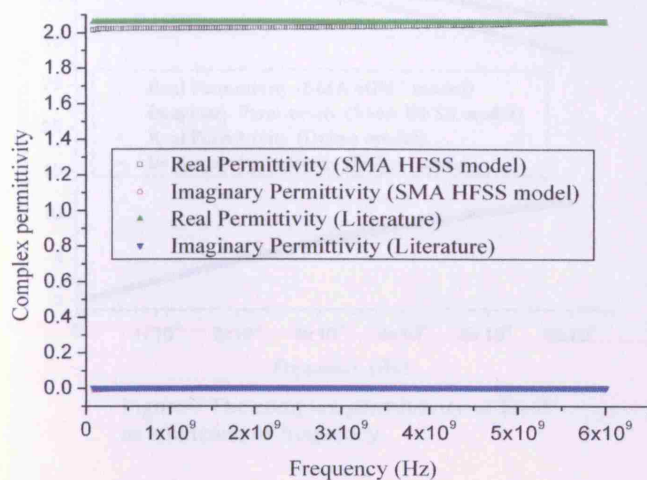


Figure 1 The complex permittivity of teflon as a function of frequency.

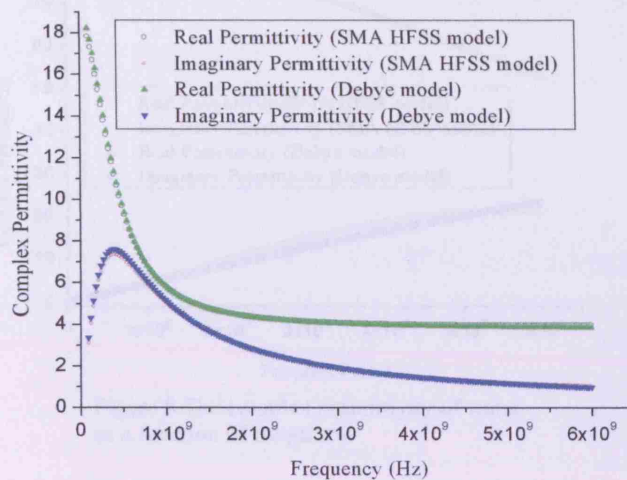


Figure 2 The complex permittivity of butanol as a function of frequency.

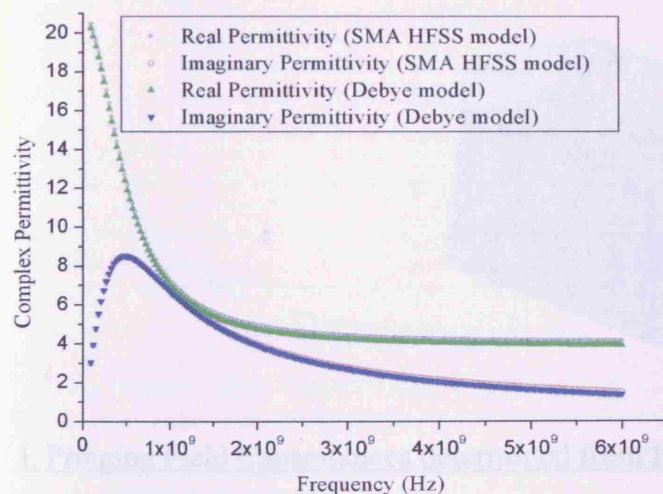


Figure 3 The complex permittivity of propan-2ol as a function of frequency.

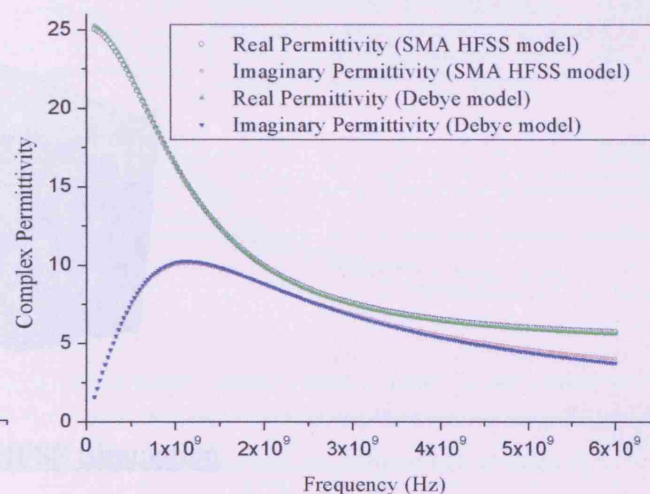


Figure 4 The complex permittivity of ethanol as a function of frequency.

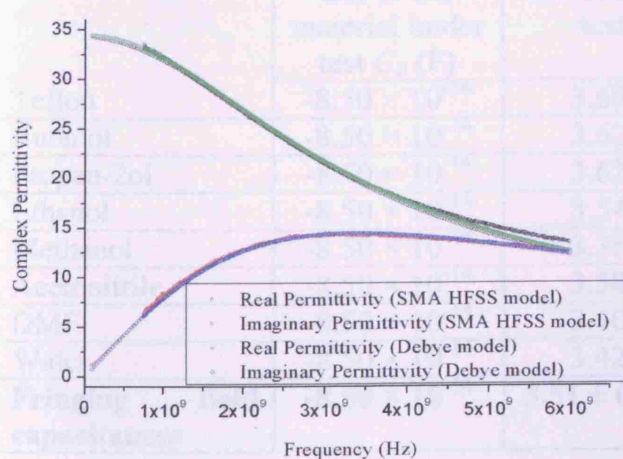


Figure 5 The complex permittivity of methanol as a function of frequency.

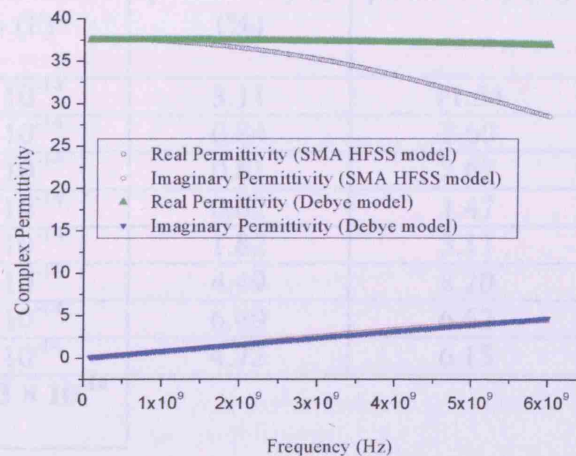


Figure 6 The complex permittivity of acetonitrile as a function of frequency.

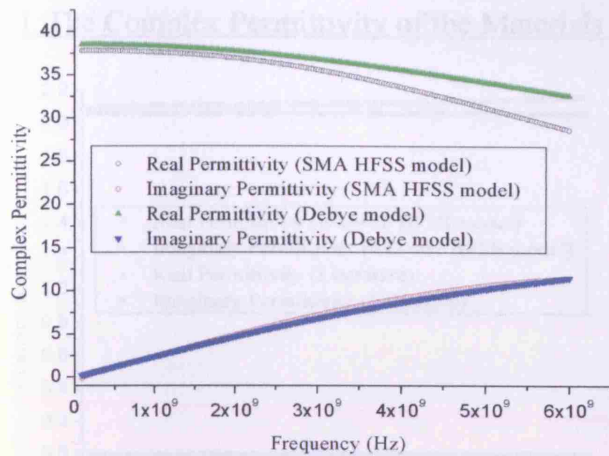


Figure 7 The complex permittivity of DMF as a function of frequency.

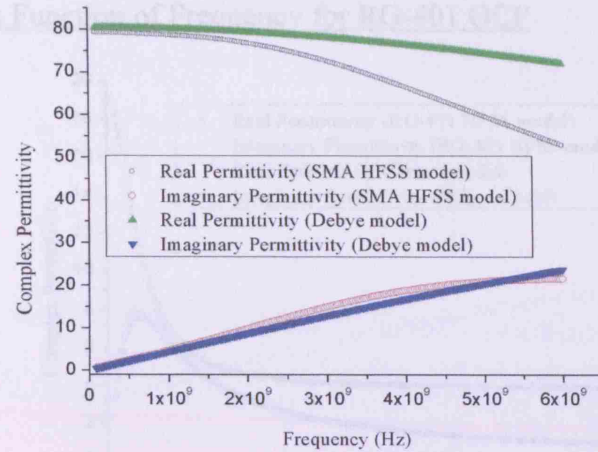
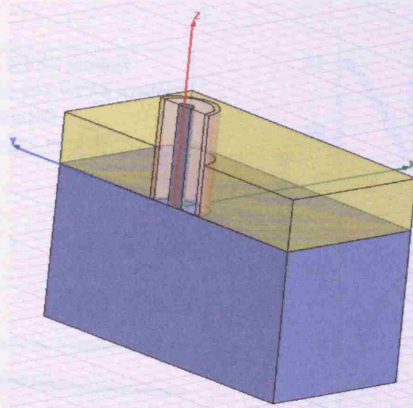


Figure 8 The complex permittivity of water as a function of frequency.

C. RG-401 Coaxial Probe



I. Fringing Field Capacitances determined from HFSS Simulation

Test Materials	Fringing field capacitance due to the material under test C_0 (F)	Fringing field capacitance due to the material under test C_1 (F)	% ME error of real permittivity ϵ_1 (%)	% ME error of Imaginary ϵ_2 permittivity (%)
Teflon	-8.50×10^{-14}	3.69×10^{-14}	3.11	11.54
Butanol	-8.50×10^{-14}	3.62×10^{-14}	0.84	2.60
Propan-2ol	-8.50×10^{-14}	3.62×10^{-14}	0.81	2.63
Ethanol	-8.50×10^{-14}	3.54×10^{-14}	0.62	1.47
Methanol	-8.50×10^{-14}	3.38×10^{-14}	1.82	3.11
Acetonitrile	-8.50×10^{-14}	3.38×10^{-14}	4.49	8.20
DMF	-8.50×10^{-14}	3.40×10^{-14}	6.49	6.62
Water	-8.50×10^{-14}	3.42×10^{-14}	4.72	6.15
Fringing field capacitances	-8.50×10^{-14}	$3.51 \pm 0.13 \times 10^{-14}$		

II. The Complex Permittivity of the Materials as Function of Frequency for RG-401 OCP

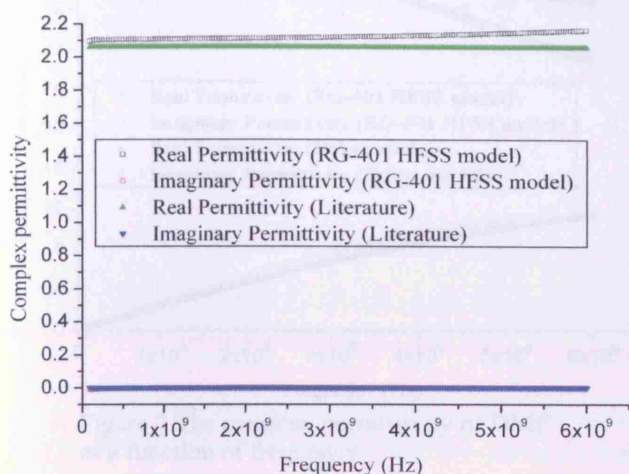


Figure 1 The complex permittivity of teflon as a function of frequency.

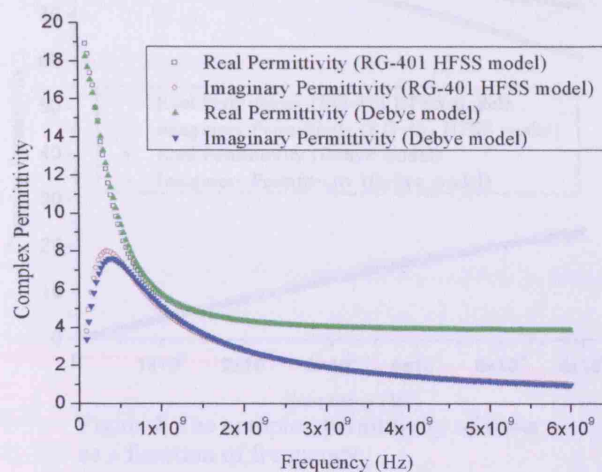


Figure 2 The complex permittivity of butanol as a function of frequency.

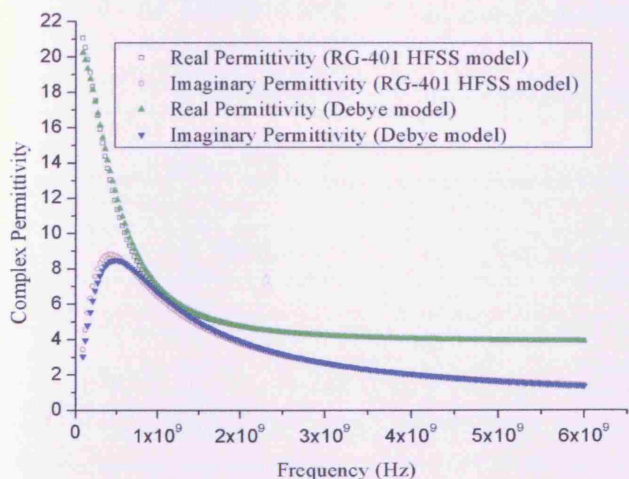


Figure 3 The complex permittivity of propan-2ol as a function of frequency.

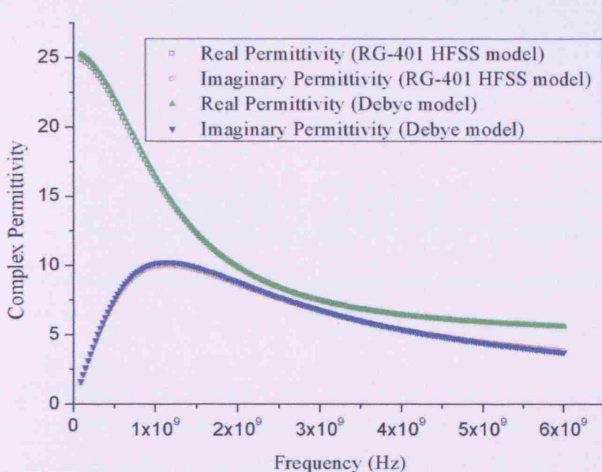


Figure 4 The complex permittivity of ethanol as a function of frequency.

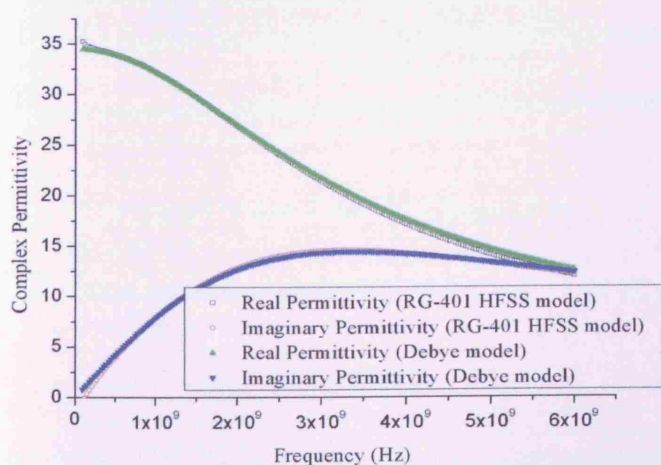


Figure 5 The complex permittivity of methanol as a function of frequency.

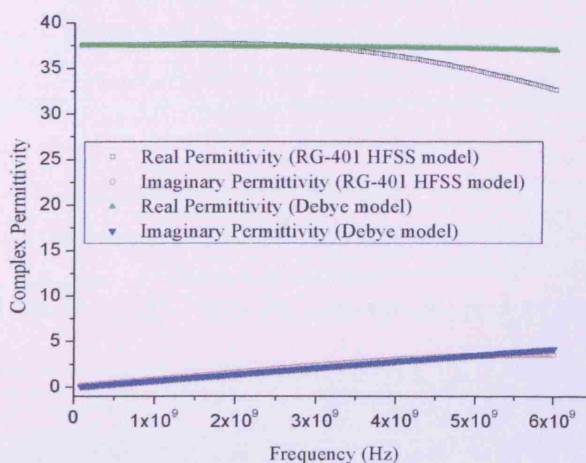


Figure 6 The complex permittivity of acetonitrile as a function of frequency.

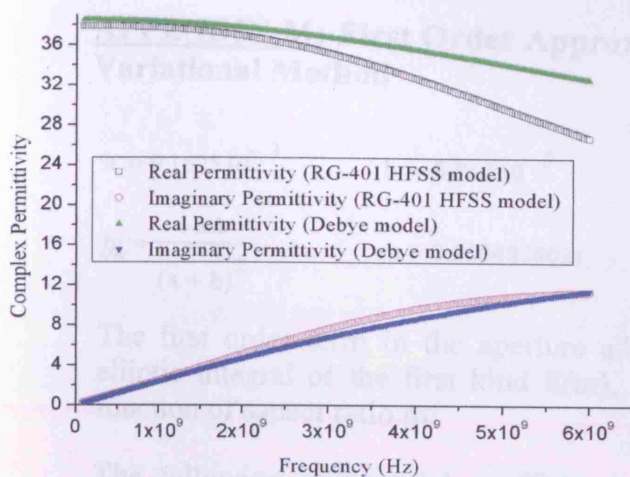


Figure 7 The complex permittivity of DMF as a function of frequency.

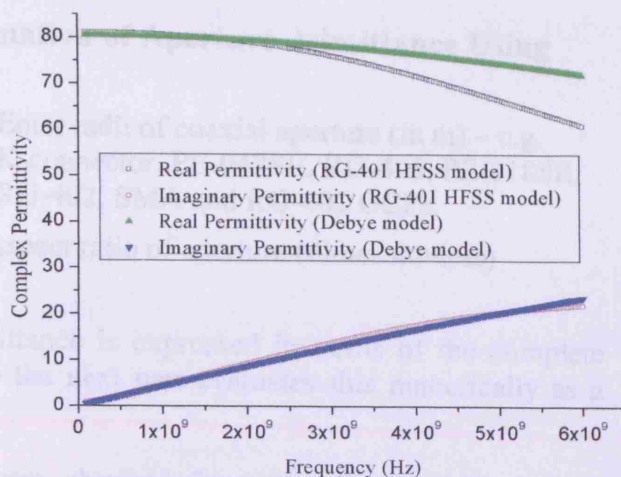


Figure 8 The complex permittivity of water as a function of frequency.

$$\epsilon_{\infty} = 1$$

$$c_1 = 1.54321141431 \quad d_1 = 0.2499134814$$

$$c_2 = 1.0416601228 \quad d_2 = 0.0000000000$$

$$c_3 = 0.04757781246 \quad d_3 = 0.0000000000$$

$$c_4 = 0.0173438411 \quad d_4 = 0.0000000000$$

$$\epsilon(\omega) = \sum_{n=1}^N \left[\frac{c_n}{1 + j\omega\tau_n} \right] + \sum_{n=1}^M \left[\frac{d_n}{1 + j\omega\tau_n} \right] + \epsilon_{\infty}$$

$$\epsilon_{\infty} = 8.85418 \times 10^{-12}$$

$$C_1 = \frac{8.85418 \times 10^{-12} (10^{-9} - 1)}{\ln\left(\frac{1}{10^{-9}}\right)}$$

This is the constant C_1 required for the probe admittance model (see Fig. 6.6 of chapter 6). It is the effective capacitance of the open circuit probe end.

$$C_1 = 3.28319 \times 10^{-18} \text{ (units of F)}$$

For a Σ -connector probe with $a = 0.1525$ mm and $b = 0.863$ mm the theoretical value of C_1 is 8.176-13 F.

APPENDIX M: First Order Approximation of Aperture Admittance Using Variational Method

$$a := 0.1525 \cdot 10^{-3} \quad b := 0.863 \cdot 10^{-3} \quad \text{Enter radii of coaxial aperture (in m) – e.g. K-connector, PE-047SR, RG-405, PE-118SR, RG-402, SMA and RG-401 OCPs.}$$

$$m := \frac{4 \cdot a \cdot b}{(a + b)^2} \quad m = 0.5104824021 \quad \text{Aspect ratio of aperture (dimensionless)}$$

The first order term in the aperture admittance is expressed in terms of the complete elliptic integral of the first kind $E(m)$, so the next part evaluates this numerically as a function of aspect ratio m :

The following polynomial coefficients were obtained from *Handbook of Mathematical Function* by M. Abramowitz, and I.A Stegun, pp. 592* (see appendix N).

$$c_0 := 1$$

$$c_1 := 0.44325141463 \quad d_1 := 0.2499836831$$

$$c_2 := 0.06260601220 \quad d_2 := 0.0920018003$$

$$c_3 := 0.04757383546 \quad d_3 := 0.0406969752$$

$$c_4 := 0.01736506451 \quad d_4 := 0.0052644963$$

$$E(p) := \sum_{n=0}^4 \left[c_n \cdot (1-p)^n \right] + \sum_{n=1}^4 \left[\left[d_n \cdot (1-p)^n \right] \cdot \ln \left(\frac{1}{1-p} \right) \right]$$

$$\epsilon_0 := 8.854 \cdot 10^{-12}$$

$$C1 := \frac{8 \cdot \epsilon_0 \cdot (a + b) \cdot (E(m) - 1)}{\left(\ln \left(\frac{b}{a} \right) \right)^2} \quad \text{This is the constant C1 required for the probe admittance model (see Eq. 6.6 of chapter 6). It is the effective capacitance of the open circuit probe end.}$$

$$C1 = 8.2688193098 \times 10^{-15} \text{ (units of F)}$$

For a K-connector probe with $a = 0.1525$ mm and $b = 0.863$ mm the theoretical value of $C1$ is $8.27e-15$ F.

* M. Abramowitz, and I.A Stegun, *Handbook of Mathematical Function*, New York: Dove Publications, Inc., pp. 589-592, 1965, ISBN 0-486-61272-4.

APPENDIX N: Necessary Polynomial Coefficients for the Calculation of $E(m)^*$

592

ELLIPTIC INTEGRALS

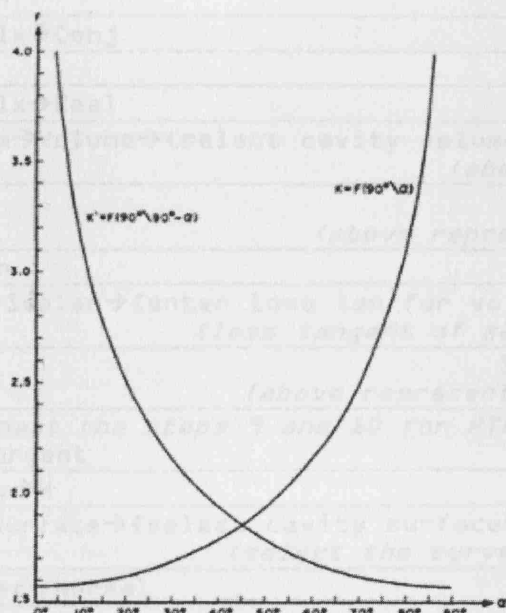


FIGURE 17.1. Complete elliptic integral of the first kind

17.3.35

$$E(m) = [1 + a_1 m_1 + a_2 m_1^2] + [b_1 m_1 + b_2 m_1^2] \ln(1/m_1) + \epsilon(m)$$

$$|\epsilon(m)| < 4 \times 10^{-8}$$

$$a_1 = .46301 \ 51 \quad b_1 = .24527 \ 27$$

$$a_2 = .10778 \ 12 \quad b_2 = .04124 \ 96$$

17.3.36

$$E(m) = [1 + a_1 m_1 + \dots + a_4 m_1^4] + [b_1 m_1 + \dots + b_4 m_1^4] \ln(1/m_1) + \epsilon(m)$$

$$|\epsilon(m)| < 2 \times 10^{-8}$$

$$a_1 = .44325 \ 141463 \quad b_1 = .24998 \ 368310$$

$$a_2 = .06260 \ 601220 \quad b_2 = .09200 \ 180037$$

$$a_3 = .04757 \ 383546 \quad b_3 = .04069 \ 697526$$

$$a_4 = .01736 \ 506451 \quad b_4 = .00526 \ 449639$$

17.4. Incomplete Elliptic Integrals of the First and Second Kinds

Extension of the Tables

Negative Amplitude

17.4.1 $F(-\varphi|m) = -F(\varphi|m)$

17.4.2 $E(-\varphi|m) = -E(\varphi|m)$

* M. Abramowitz, and I.A. Stegun, *Handbook of Mathematical Functions*, New York: Dover Publications, Inc., pp. 589-592, 1965, ISBN 0-486-61272-4.

APPENDIX O: HFSS Field Calculator Code for Calculation of SDR Unloaded Q

Field Calculator Operation

Resulting Stack Display (top entry only unless mentioned)

1. Qty→H	CVc : <Hx, Hy, Hz>
2. Push	<i>(above entry duplicated)</i>
3. Cmplx→Conj	CVc : Conj(<Hx, Hy, Hz>)
4. Dot	CSc : Dot(<Hx, Hy, Hz>, Conj(...
5. Cmplx→Real	Sc1 : Real(Dot(<Hx, Hy, ...
6. Geom→Volume→{select cavity volume}	Vol : ObjectList(cavity) <i>(above is the selection for modelled SDR)</i>
7. ∫	Sc1 : Integrate(ObjectList(cavity) <i>(above represents energy stored in cavity volume)</i>
8. Push	<i>(above entry duplicated)</i>
9. Num→Scalar→{enter loss tan for volume}	Sc1 : {1.4 × 10 ⁻⁵ } <i>(loss tangent of sapphire dielectric fill within cavity)</i>
10. *	Sc1 : *(Integrate(ObjectList(sapphire) <i>(above represents energy lost in sapphire dielectric)</i>
11. repeat the steps 9 and 10 for PTFE dielectric using 2 × 10 ⁻⁵ as loss tangent	
11. Qty→H	CVc : <Hx, Hy, Hz>
Geom→Surface→{select cavity surfaces}	Srf : ObjectFaces(cavity_faces) <i>(select the curve wall, top and bottom of the cavity)</i>
Unit Vec→Normal	Vec : Normal(ObjectFaces(cav_faces)
Cross	CVc : Cross(<Hx, Hy, Hz>, Norm...
Push	<i>(above entry duplicated)</i>
Cmplx→Conj	CVc : Conj(Cross(<Hx, Hy, Hz>, ...
Dot	CSc : Dot(Cross(<Hx, Hy, Hz>, ...
Cmplx→Real	Sc1 : Real(Dot(Cross(<Hx, ...
Geom→Surface→{select cavity surfaces}	Srf : ObjectFaces(cav_faces)
∫	Sc1 : Integrate(ObjectFaces(...
Num→Scalar→2	Sc1 : 2
Const→Pi	Sc1 : 3.14159265358979
Const→Frequency	Sc1 : {current freq, in Hz}
*	Sc1 : {numerical result, pi*f}
Num→Scalar→{enter μ _r for walls}	Sc1 : {entered value, unitless}
*	Sc1 : {numerical result, pi*f*μ _r }
Const→Mu0	Sc1 : 1.25663706144E-006
*	Sc1 : {numerical, pi*f*μ _r *μ ₀ }
Num→Scalar→{enter wall conductivity}	Sc1 : {entered value, s/meter}
*	Sc1 : {numerical, pi*f*μ _r *μ ₀ *σ}
√	Sc1 : {numerical, sqrt of above}
*	Sc1 : {numerical result, 2*above}
1/x	Sc1 : {numerical result} <i>(above is skin depth/2)</i>
*	Sc1 : *(Integrate(ObjectFaces... <i>(above is energy lost in walls)</i>
+	Sc1 : (*(Integrate(ObjectFaces...
/	Sc1 : /(+(*(Integrate(...
Eval <i>(above is final Q of SDR)</i>	Sc1 : {numerical result}

APPENDIX P: MathCAD for Calculation of Unloaded and Loaded Quality Factor of SDR (e.g. Superfish model, HFSS model)

$R_c := 1.3 \cdot 10^{-2}$ radius of cavity in m
 $L_c := 1.6 \cdot 10^{-2}$ length of cavity in m
 $R_d := 4.52 \cdot 10^{-2}$ radius of dielectric resonator in m
 $L_d := 5.72 \cdot 10^{-2}$ length of dielectric resonator in m
 $N := 160$ number of points along the radial and longitudinal directions

$$\Delta r := \frac{R_c}{N} \quad \Delta z := \frac{L_c}{N}$$

$$\mu_0 := 4 \cdot \pi \cdot 10^{-7} \quad \epsilon_0 := 8.854 \cdot 10^{-12}$$

$A := \text{READPRN}("C:\text{LANL}\backslash\text{SF7_SDRNOHOLE.txt}")$

$$f := A_{(N+1)^2, 0} \cdot 10^9 \quad \text{Resonant frequency (Hz), computed by Super Fish } f = 1.02075 \times 10^{10}$$

$$\omega := 2 \cdot \pi \cdot f$$

$$\rho := 2 \cdot 10^{-8} \quad R_s := \sqrt{\pi \cdot \mu_0 \cdot f \cdot \rho} \quad \text{Resistivity (m) and surface resistance of cavity walls (i.e. copper)}$$

$$R_s = 0.02839 \quad \text{In reality the } R_s \text{ is 25 \% more than ideal case}$$

$$\delta := \sqrt{\frac{2}{\omega \cdot \mu_0 \cdot \frac{1}{\rho}}} \quad \delta = 7.04491 \times 10^{-7} \quad \frac{1}{\rho} = 5 \times 10^7$$

Output file from SF in the order of z, r, Hz, Hr, H and E

	1	2	3	4
0	0	0	0	0
1	0	$8.41688 \cdot 10^{-3}$	0	$8.41688 \cdot 10^{-3}$
2	0	0.01686	0	0.01686
3	0	0.02528	0	0.02528
4	0	0.03378	0	0.03378
5	0	0.04234	0	...

A =

$$m := 0..N \quad n := 0..N$$

$$H_{z,m,n} := A_{n+m \cdot (N+1), 2}$$

$$H_{r,m,n} := A_{n+m \cdot (N+1), 3}$$

$$r_m := m \cdot \Delta r$$

$$H_{tot,m,n} := A_{n+m \cdot (N+1), 4}$$

$$E\phi_{m,n} := A_{n+m \cdot (N+1), 5}$$

$$z_n := n \cdot \Delta z$$

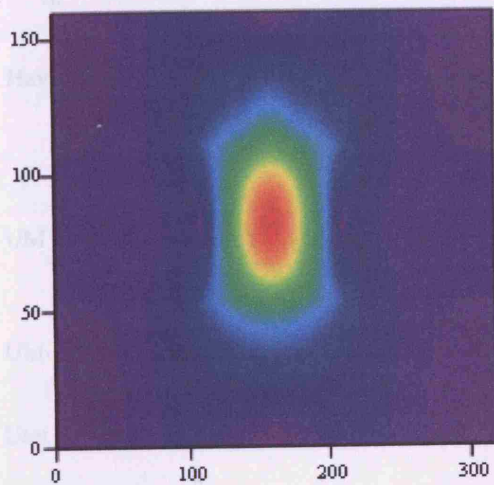
$$H_{m,n} := H_{tot,N-m,n}$$

$$E_{m,n} := E\phi_{N-m,n}$$

$$H_{m+N-1,n} := H_{tot,m,n}$$

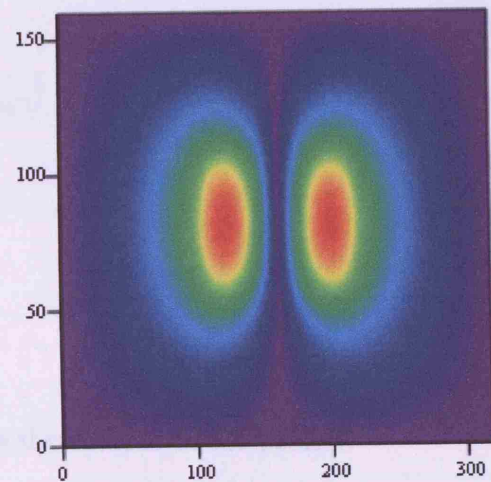
$$E_{m+N-1,n} := E\phi_{m,n}$$

Magnitude of H (axis in centre)



H

Magnitude of E (axis in centre)



E

Curved wall losses

$$m := 0..(N-1)$$

$$n := 0..(N-1)$$

$$\Delta Sc := 2 \cdot \pi \cdot R_c \cdot \Delta z$$

$$H_{av,n} := \frac{1}{2} \cdot (H_{z,N,n} + H_{z,N,n+1})$$

$$P_c := \sum_{n=0}^{N-1} \left[(H_{av,n})^2 \cdot \Delta Sc \cdot R_s \right]$$

End wall losses

$$m := 0..(N-1)$$

$$\Delta S_m := \pi \cdot [(m+1)^2 - m^2] \cdot \Delta r^2$$

$$n := 0..(N-1)$$

$$H_{av,t,m} := \frac{1}{2} \cdot (H_{r,m,N} + H_{r,m+1,N})$$

$$H_{av,b,m} := \frac{1}{2} \cdot (H_{r,m,0} + H_{r,m+1,0})$$

$$P_t := \sum_{m=0}^{130-1} \left[\left(H_{av_t_m} \right)^2 \cdot \Delta S_m \cdot R_s \right]$$

$$P_b := \sum_{m=0}^{130-1} \left[\left(H_{av_b_m} \right)^2 \cdot \Delta S_m \cdot R_s \right]$$

$$P_c = 1.11915 \times 10^{-7}$$

$$P_t = 9.66301 \times 10^{-8}$$

$$P_b = 7.19842 \times 10^{-8}$$

$$P_{tot} := P_c + P_t + P_b$$

$$P_{tot} = 2.80529 \times 10^{-7}$$

$$\Delta V_m := \Delta z \cdot \pi \cdot \left[(m+1)^2 - m^2 \right] \cdot \Delta r^2$$

$$H_{av_m,n} := \frac{1}{4} \cdot \left(H_{tot_m,n} + H_{tot_m,n+1} + H_{tot_m+1,n} + H_{tot_m+1,n+1} \right)$$

$$U_M := \frac{1}{2} \cdot \mu_0 \cdot \sum_{m=0}^{130-1} \left[\sum_{n=0}^{N-1} \left(H_{av_m,n} \right)^2 \cdot \Delta V_m \right]$$

$$U_M \cdot 10^{12} = 0.2082$$

$$U_{tot} := 2 \cdot U_M$$

Total energy stored in the volume of the cavity

$$Q_c := \omega \cdot \frac{U_{tot}}{P_{tot}}$$

Q value of conductor

$$Q_c = 9.51979 \times 10^4$$

$$\tan \delta := 1.4 \cdot 10^{-5}$$

$$\epsilon_r := 9.4$$

Loss tangent and dielectric constant of Sapphire puck

$$\tan \delta_l := 0.0001$$

$$\epsilon_{r1} := 2.06$$

Loss tangent and dielectric constant PTFE support

$$E_{av_m,n} := \frac{1}{4} \cdot \left(E_{\phi_m,n} + E_{\phi_m,n+1} + E_{\phi_m+1,n} + E_{\phi_m+1,n+1} \right)$$

$$N1 := 53$$

$$M1 := 130$$

$$N2 := 57$$

$$M2 := 85$$

$$N3 := 20$$

$$M3 := 115$$

$$N4 := 30$$

$$M4 := 80$$

$$M5 := 45$$

$$M7 := 35$$

$$M6 := 15$$

$$U_{E1} := \sum_{m=0}^{M1-1} \left[\sum_{n=0}^{N1-1} \left(E_{av_m,n} \right)^2 \cdot \Delta V_m \right]$$

$$U_{E1} = 0.05652$$

$$UE2 := \sum_{m=M5}^{M1} \left[\sum_{n=N1}^{N1+N2} (E_{av_{m,n}})^2 \cdot \Delta V_m \right] \quad UE2 = 0.27667$$

$$UE3 := \sum_{m=M6}^{M1} \left[\sum_{n=N1+N2}^{N1+N2+N3} (E_{av_{m,n}})^2 \cdot \Delta V_m \right] \quad UE3 = 0.04818$$

$$UE4 := \sum_{m=M7+M6}^{M1} \left[\sum_{n=N1+N2+N3}^{N1+N2+N3+N4-1} (E_{av_{m,n}})^2 \cdot \Delta V_m \right] \quad UE4 = 8.10344 \times 10^{-3}$$

$$UE5 := \sum_{m=0}^{M5-1} \left[\sum_{n=N1}^{N1+N2} (E_{av_{m,n}})^2 \cdot \Delta V_m \cdot \epsilon_r \right] \quad UE5 = 1.32528$$

$$UE6 := \sum_{m=0}^{M6-1} \left[\sum_{n=N1+N2}^{N1+N2+N3+N4-1} (E_{av_{m,n}})^2 \cdot \Delta V_m \cdot \epsilon_r \right] \quad UE6 = 3.23103 \times 10^{-3}$$

$$UE7 := \sum_{m=M6}^{M7} \left[\sum_{n=N1+N2+N3}^{N1+N2+N3+N4-1} (E_{av_{m,n}})^2 \cdot \Delta V_m \cdot \epsilon_r \right] \quad UE7 = 1.88212 \times 10^{-3}$$

$$UE_{tot} := UE1 + UE2 + UE3 + UE4 + UE5 + UE6 + UE7 \quad U_{tot} = 4.16396 \times 10^{-13}$$

$$W_s := \frac{UE_{tot} - UE5 - UE6}{UE5 + UE6} \quad W_s = 0.29458 \quad W \text{ for sapphire puck}$$

$$W_p := \frac{UE_{tot} - UE7}{UE7} \quad W_p = 912.78656 \quad W \text{ for PTFE support}$$

$$Qd1 := \frac{1 + W_s}{\tan \delta} \quad Qd1 = 9.24699 \times 10^4 \quad \text{Quality factor within the Sapphire puck}$$

$$Qd2 := \frac{1 + W_p}{\tan \delta_l} \quad Qd2 = 6.09191 \times 10^6 \quad \text{Quality factor within the PTFE support}$$

$$Q_{dtot} := \frac{Qd1 \cdot Qd2}{Qd1 + Qd2}$$

$$Q_u := \frac{Q_{dtot} \cdot Q_c}{Q_{dtot} + Q_c} \quad Q_u = 4.65486 \times 10^4 \quad \text{Final/ overall Unloaded Q from Superfish}$$

$$IL := -18.22 \quad \text{Insertion loss from VNA}$$

$$Q_{L_SF} := Q_u \cdot \left(1 - 10^{\frac{IL}{20}} \right) \quad Q_{L_SF} = 4.08351 \times 10^4 \quad \text{Loaded Q from Superfish}$$

$$Q_{L_VNA} := 37834 \quad \text{Loaded Q from the VNA}$$

$$\%error := \frac{Q_{L_SF} - Q_{L_VNA}}{Q_{L_VNA}} \cdot 100 \quad \%error = 7.93218 \quad \% \text{ error between the Superfish \& measurement}$$

Theoretical calculation of resonant frequency (f_{GHz})

$$\begin{aligned} a_{mm} &:= 4.5 & L_{\text{mm}} &:= 5.7 & f_{Pt} &:= 10.194 \\ f_{GHz} &:= \frac{34}{a_{mm} \sqrt{\epsilon_r}} \cdot \left(\frac{a_{mm}}{L} + 3.45 \right) & f_{Au} &:= 10.203 \\ & & f_{superfish} &:= 10.208 \\ & & f_{theory} &:= 10.448 \\ f_{GHz} &= 10.44755 & f_{HFSS} &:= 10.3 \end{aligned}$$

Error calculation of Resonant frequency obtained from VNA (or experiment)- ($\%error_{EXP_f0}$) and HFSS ($\%error_{HFSS_f0}$)

$$\%error_{EXP_f0} := \frac{f_{GHz} - 10.203}{10.203} \cdot 100 \quad \%error_{HFSS_f0} := \frac{f_{HFSS} - 10.194}{10.194} \cdot 100$$

$$\%error_{EXP_f0} = 2.39684 \quad \%error_{HFSS_f0} = 1.03983$$

Calculation of Loaded Quality factor (Q_{L_HFSS}) obtained from HFSS

$$\begin{aligned} Q_{U_HFSS} &:= 42891 \\ Q_{L_HFSS} &:= Q_{U_HFSS} \cdot \left(1 - 10^{\frac{IL}{20}} \right) \\ Q_{L_HFSS} &= 3.76264 \times 10^4 \end{aligned}$$

Error calculation of Loaded Quality factor ($\%HFSSerror_QL$) obtained from HFSS and VNA

$$\%HFSSerror_QL := \frac{Q_{L_VNA} - Q_{L_HFSS}}{Q_{L_VNA}} \cdot 100$$

$$\%HFSSerror_QL = 0.54874$$

APPENDIX Q: Limitation of RG-405, RG-402 and SMA Open Ended Coaxial Probes

All the results presented in this appendix are obtained from the same models (i.e. RG-405, RG-402 and SMA) developed in section 5.7.1 along with the parametric tool using the HFSS software. The general idea of this appendix is to map the complex admittance (Y_L) of the probe obtained from the 3D full wave OCP onto a complex permittivity (ϵ_1 and ϵ_2) plane. Such mappings provide a visual representation of how Y_L varies with ϵ_1 and ϵ_2 at a fixed frequency and give an indication of the sensitivity of the capacitances (i.e. C_0 and C_1) of the lumped capacitor model of the probes.

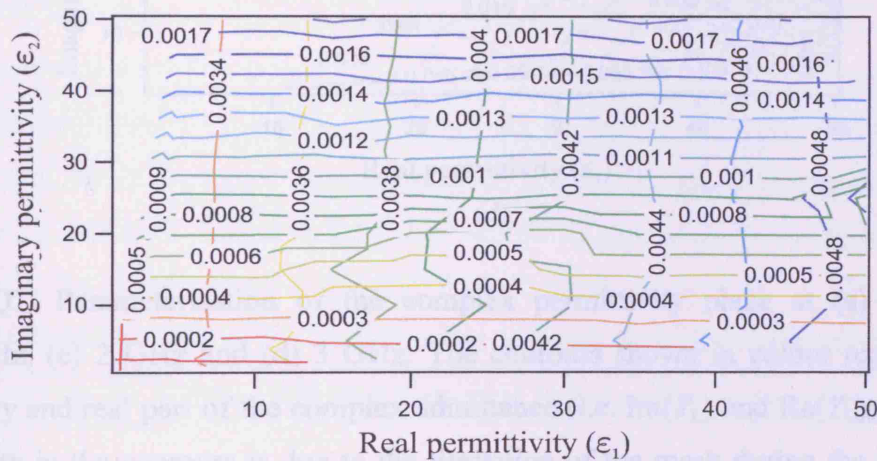
The complex permittivity is chosen to be the varying parameter, ranging from $5 \leq \epsilon_1 \leq 100$ and $5 \leq \epsilon_2 \leq 100$. For the different values of frequency (i.e. at 0.5 GHz, 1 GHz, 2 GHz and 3 GHz) the model generated sets of complex admittance (Y_L) as function of ϵ_1 and ϵ_2 . Simulations of all these OCPs took around 20-23 hours on a 3.4 GHz CPU and 2 GB RAM machine and the memory usage was around 1700-1950 MB. Finally, the generated complex admittances (Y_L) for the different OCPs were mapped onto a complex permittivity (ϵ_1 and ϵ_2) plane as shown below.

Q1: RG-405 OCP

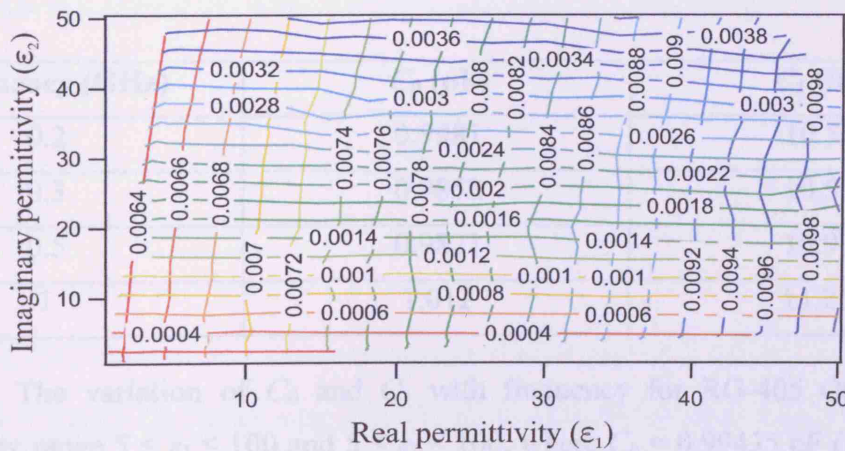
The generated complex admittance (Y_L) for the RG-405 OCP was mapped onto a complex permittivity (ϵ_1 and ϵ_2) plane as shown in fig. Q1. The vertical and horizontal lines of the contours correspond to $\text{Im}(Y_L)$ and $\text{Re}(Y_L)$, respectively. The departure from a square grid pattern is beginning to be visible at 2 GHz and it is manifest at 3 GHz. For any frequency (f) less than 2 GHz, we have a square grid characterised by $C_0(f)$ and $C_1(f)$. To check whether C_0 and C_1 vary with frequency for whole range of complex permittivity (i.e. $5 \leq \epsilon_1 \leq 100$ and $5 \leq \epsilon_2 \leq 100$), the calculations have been carried out on the square grids of the contour plot (i.e. fig. Q1) for $f = 0.2, 0.3, 0.5$ and 1 GHz. The results are shown in table Q1.

The results are shown in table Q1. It is apparent from the results that C_0 is practically constant compared to C_1 , whereas C_1 varies by a factor of ~ 1.1 over the given

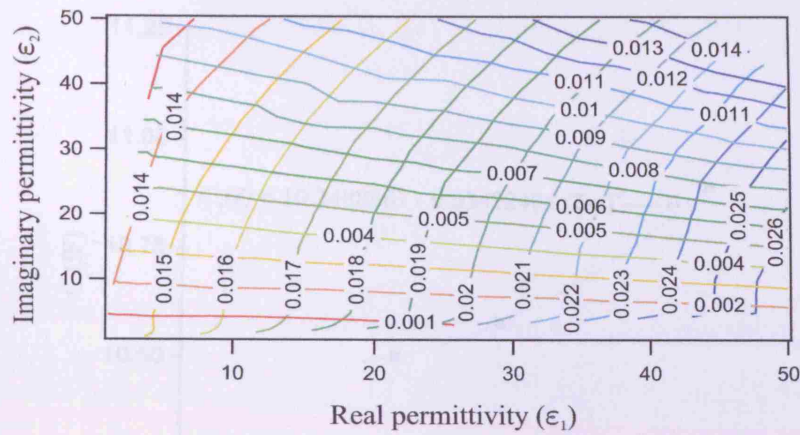
frequency range of 0.2 to 1 GHz. The variation of C_1 can be closely represented by a quadratic function of f : $C_1(f) = a_0 + a_1(2\pi f)^2$, with $a_0 = 10.3488667$ and $a_1 = 0.03422404$, where f and C_1 are in GHz and fF, respectively as shown in fig. Q2. The frequency independent term of $C_1(f)$ is 10.3488667 fF, which is close to the value found in chapter 5 from the HFSS simulation (i.e. 11.06 fF, see table 5.5) within the error of 6.4%. As mentioned section 5.9.1, instead of using the model $Y_L = j\omega(C_0 + C_1(\epsilon_1 - j\epsilon_2))$, where both C_0 and C_1 are independent of frequency, one should use: $Y_L = j\omega(C_0 + C_1(\epsilon_1 - j\epsilon_2))$, where $C_0 = 0.99435$ pF along with $C_1(f) = a_0 + a_1(2\pi f)^2$, to characterise the material properties below 2 GHz, where $a_0 = 10.3488667$ and $a_1 = 0.03422404$. In other words, this function can be treated as a *universal model* for the RG-405 OCP to characterise the properties of unknown materials up to 1 GHz with a maximal discrepancies of less than 4%.



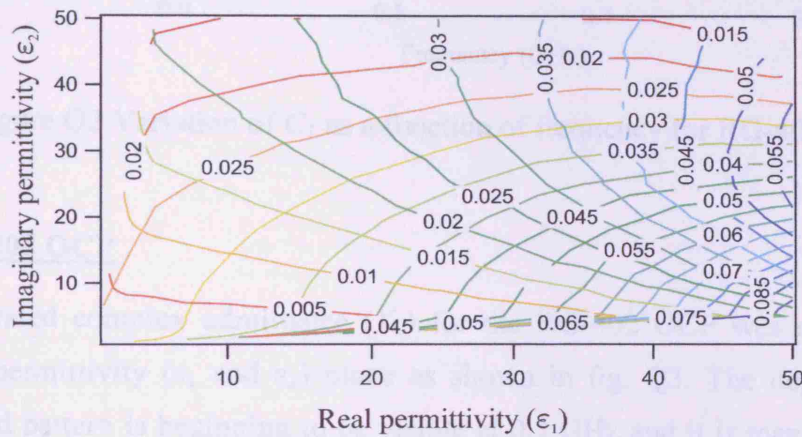
(a)



(b)



(c)



(d)

Figure Q1: Parameterisation of the complex permittivity plane at (a) 0.5 GHz, (b) 1 GHz, (c) 2 GHz and (d) 3 GHz. The contours shown in colour represent the imaginary and real part of the complex admittance (i.e. $\text{Im}(Y_L)$ and $\text{Re}(Y_L)$). The non-uniformity in the contours is due to the limitation of the mesh during the simulation process.

Frequency (GHz)	C_0 (pF)	C_1 (fF)
0.2	0.9981	10.51
0.3	0.9852	10.59
0.5	0.9821	10.91
1	1.012	11.25

Table Q1 The variation of C_0 and C_1 with frequency for RG-405 OCP for the permittivity range $5 \leq \epsilon_1 \leq 100$ and $5 \leq \epsilon_2 \leq 100$, where $C_0 = 0.99435$ pF (i.e. average value over the frequency range 0.2 – 1 GHz).

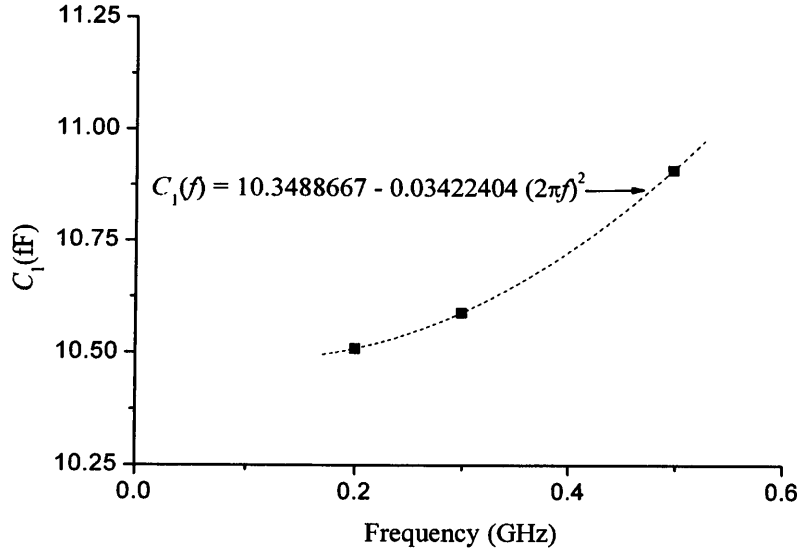


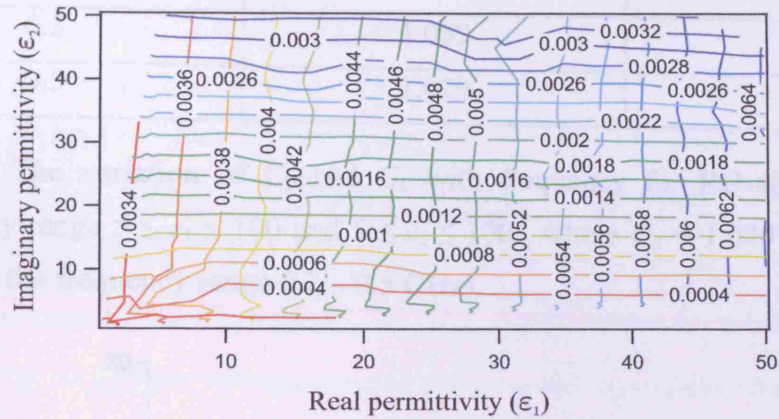
Figure Q2 Variation of C_1 as a function of frequency for RG-405 OCP.

Q2: RG-402 OCP

The generated complex admittance (Y_L) for the RG-402 OCP was mapped onto a complex permittivity (ϵ_1 and ϵ_2) plane as shown in fig. Q3. The departure from a square grid pattern is beginning to be visible at 0.5 GHz and it is manifest at 1 GHz. For any frequency (f) less than 0.5 GHz, we have a square grid characterised by $C_0(f)$ and $C_1(f)$. To check whether C_0 and C_1 vary with frequency for whole range of complex permittivity (i.e. $5 \leq \epsilon_1 \leq 100$ and $5 \leq \epsilon_2 \leq 100$), the calculations have been carried out on the square grids of the contour plot (i.e. fig. Q3) for $f = 0.2, 0.3$, and 0.5 GHz.

The results are shown in table Q2. It is apparent from these that C_0 is practically constant compared to C_1 , whereas C_1 varies by a factor of ~ 1.2 over the given frequency range of 0.2 to 0.5 GHz. The variation of C_1 can be closely represented by a quadratic function of f : $C_1(f) = a_0 + a_1(2\pi f)^2$, with $a_0 = 14.48175$ and $a_1 = 0.418267$, where f and C_1 are in GHz and fF, respectively as shown in fig. Q4. As mentioned section 5.9.1, instead of using the model $Y_L = j\omega(C_0 + C_1(\epsilon_1 - j\epsilon_2))$, where both the C_0 and C_1 are independent of frequency, one should use: $Y_L = j\omega(C_0 + C_1(\epsilon_1 - j\epsilon_2))$, where $C_0 = 1.049$ pF along with $C_1(f) = a_0 + a_1(2\pi f)^2$, to characterise the material properties below 0.5 GHz, where $a_0 = 14.48175$ and $a_1 = 0.418267$. In other words, this function can be treated as a *universal model* for the RG-402 OCP to characterise

the properties of unknown materials up to 0.5 GHz with a maximal discrepancy of less than 1%.



Frequency (GHz)	C_0 (pF)	C_1 (fF)
0.2	1.059	15.12
0.3	1.059	15.89
0.5	1.029	18.71

Table Q2 The variation of C_0 and C_1 with frequency for RG-402 OCP for the permittivity range $5 \leq \epsilon_1 \leq 100$ and $5 \leq \epsilon_2 \leq 100$, where $C_0 = 1.049$ pF (i.e. average value over the frequency range 0.2 – 0.5 GHz).

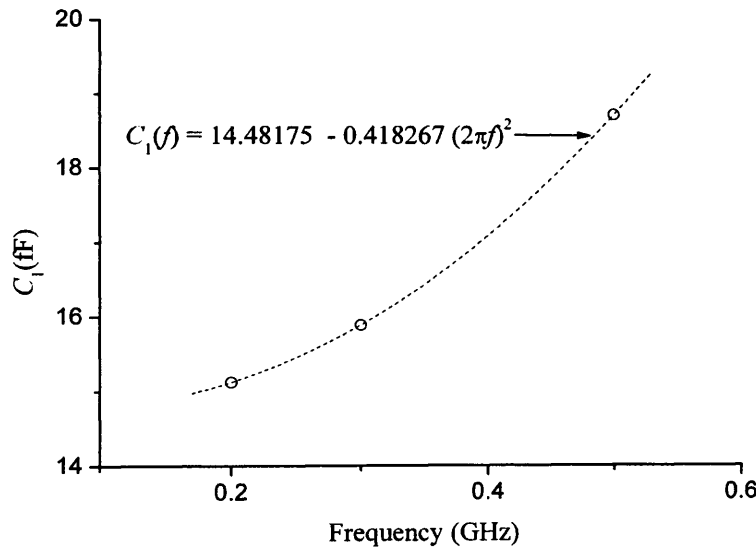


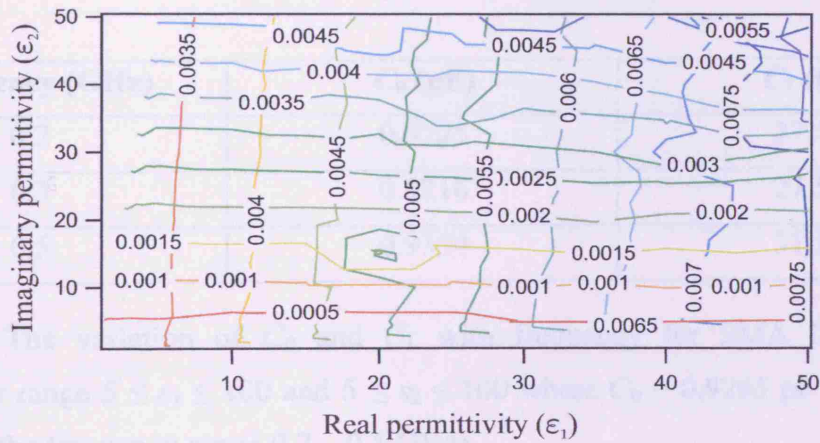
Figure Q4 Variation of C_1 as a function of frequency for RG-402 OCP.

Q3: SMA OCP

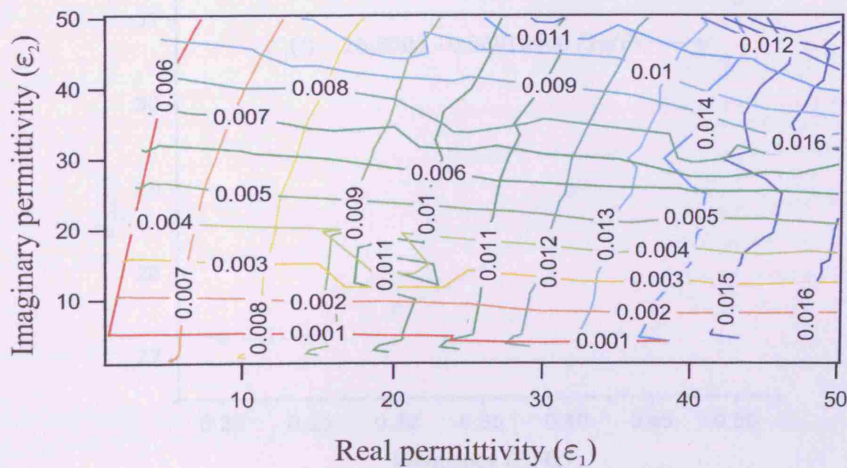
The generated complex admittance (Y_L) for the SMA OCP was mapped onto a complex permittivity (ϵ_1 and ϵ_2) plane as shown in fig. Q5. The departure from a square grid pattern is beginning to be visible at 0.5 GHz and it is manifest at 1 GHz. For any frequency (f) less than 0.5 GHz, we have a square grid characterised by $C_0(f)$ and $C_1(f)$. To check whether C_0 and C_1 vary with frequency for whole range of complex permittivity (i.e. $5 \leq \epsilon_1 \leq 100$ and $5 \leq \epsilon_2 \leq 100$), the calculations have been carried out on the square grids of the contour plot (i.e. fig. Q5) for $f = 0.2, 0.3$ and 0.5 GHz.

The results are shown in table Q3. It is apparent from the results that C_0 is practically constant compared to C_1 , whereas C_1 varies by a factor of ~ 1.2 over the given

frequency range of 0.2 to 0.5 GHz. The variation of C_1 can be closely represented by a quadratic function of f : $C_1(f) = a_0 + a_1(2\pi f)^2$, with $a_0 = 26.8005$ and $a_1 = 0.36918906$, where f and C_1 are in GHz and fF, respectively as shown in fig. Q6. The frequency independent term of $C_1(f)$ is 26.8005 fF which is very close to the value found in chapter 5 from the HFSS simulation (i.e. 27.5 fF, see table 5.5) within the error of 2.5 %. As mentioned section 5.9.1, instead of using the model $Y_L = j\omega(C_0 + C_1(\epsilon_1 - j\epsilon_2))$, where both C_0 and C_1 are independent of frequency, one should use: $Y_L = j\omega(C_0 + C_1(\epsilon_1 - j\epsilon_2))$, where $C_0 = 0.9265$ pF along with $C_1(f) = a_0 + a_1(2\pi f)^2$, to characterise the material properties below 0.5 GHz, where $a_0 = 26.8005$ and $a_1 = 0.36918906$. In other words, this function can be treated as a *universal model* for the SMA OCP to characterise the properties of unknown materials up to 0.5 GHz with a maximal discrepancy of less than 2.5%.



(a)



(b)

Figure Q6 Variation of C_1 as a function of frequency for SMA OCP.

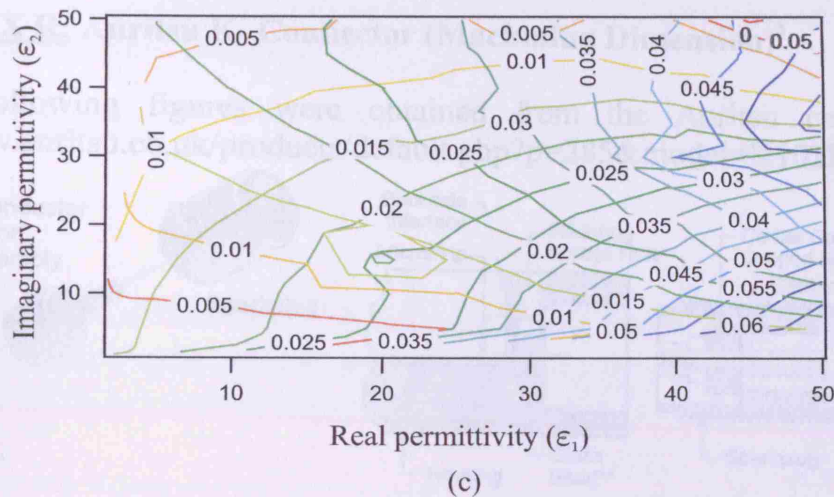


Figure Q5: Parameterisation of the complex permittivity plane at (a) 0.5 GHz, (b) 1 GHz and (c) 2 GHz. The contours shown in colour represent the imaginary and real part of the complex admittance (i.e. $\text{Im}(Y_L)$ and $\text{Re}(Y_L)$). The non-uniformity in the contours is due to the limitation of the mesh during the simulation process.

Frequency (GHz)	C_0 (pF)	C_1 (fF)
0.2	0.9225	27.22
0.3	0.9216	27.54
0.5	0.9354	31.18

Table Q3 The variation of C_0 and C_1 with frequency for SMA OCP for the permittivity range $5 \leq \epsilon_1 \leq 100$ and $5 \leq \epsilon_2 \leq 100$ where $C_0 = 0.9265$ pF (i.e. average value over the frequency range 0.2 – 0.5 GHz).

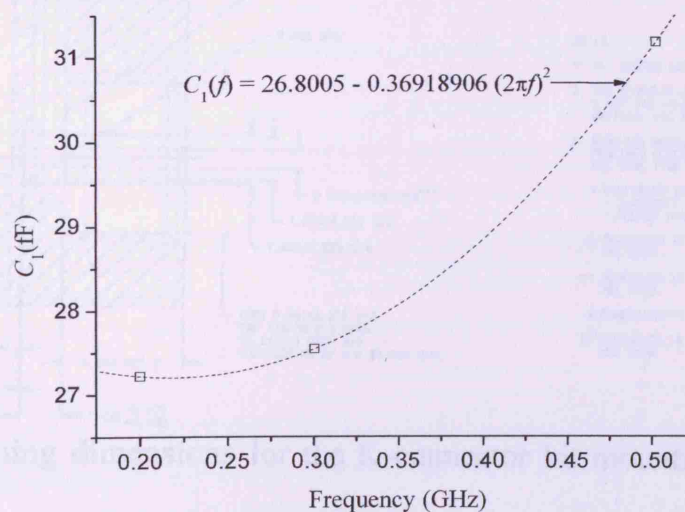


Figure Q6 Variation of C_1 as a function of frequency for SMA OCP.

APPENDIX R: Anritsu K- Connector (Machining Dimension)¹

All the following figures were obtained from the Anritsu company website (<http://www.anritsu.co.uk/products/default.php?p=285&model=K102F>)

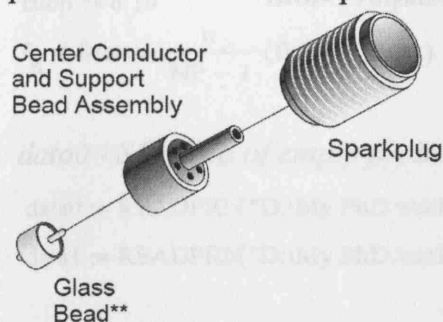


Figure R1 K-connector Kit.

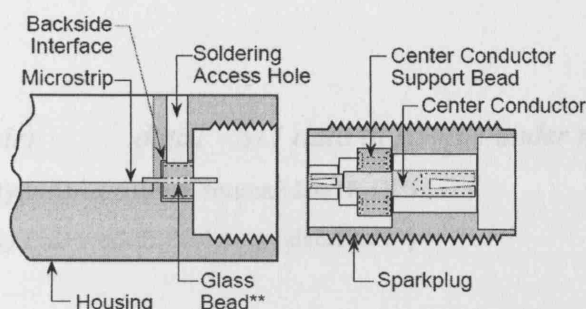


Figure R2 K-connector kit assembly.

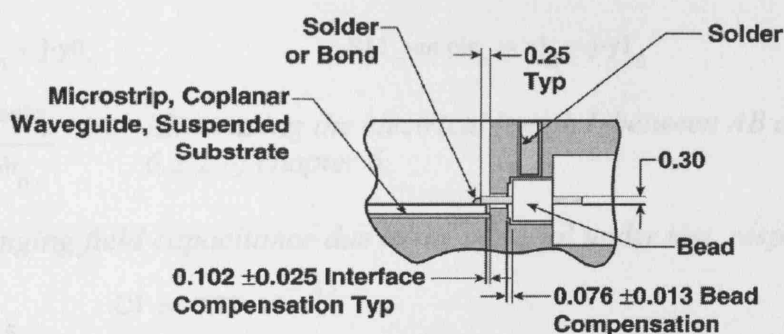
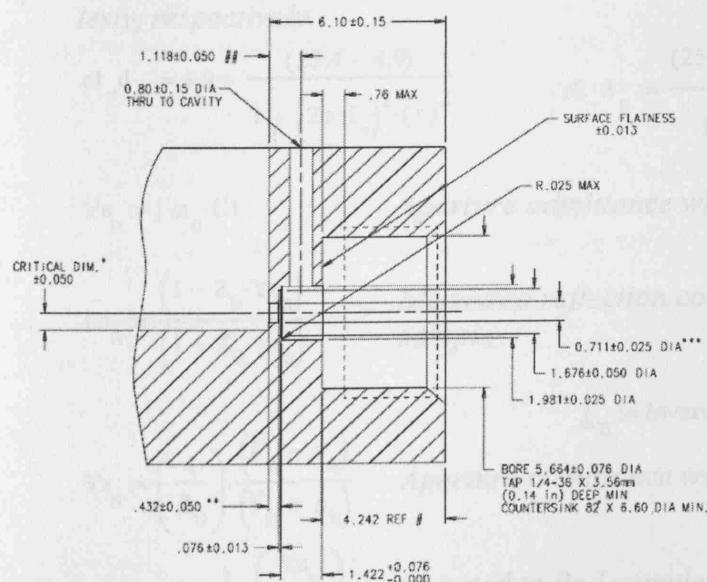


Figure R3 Installation of glass bead. In our case the glass bead was installed in the machined brass block (see fig. R4).



NOTES.

1. ALL DIMENSIONS ARE IN MILLIMETERS.
2. THE CONCENTRICITY OF THE 1.676, 1.981, AND 5.684 DIA HOLES TO THE 0.711 DIA HOLE IS CRITICAL AND MUST BE HELD WITHIN $\pm 0.038\text{mm}$.
3. WITH THE MODEL 01-104 DRILL KIT, ALL OF THE REQUIRED CONCENTRIC HOLES CAN BE MACHINED AT THE SAME TIME USING A SINGLE BIT.
 - * DIMENSION IS 0.152 (PIN RADIUS)
 - + SUBSTRATE
 - + SOLDER THICKNESS
- ** DIMENSION IS $0.889 \pm 0.050\text{mm}$ IF SLIDING CONTACTS ARE USED.
- *** DIMENSION IS $0.838 \pm 0.025\text{mm}$ IF SLIDING CONTACTS ARE USED.
- # DIMENSION IS 3.785mm IF SLIDING CONTACTS ARE USED.
- ## DIMENSION IS $1.575 \pm 0.050\text{mm}$ IF SLIDING CONTACTS ARE USED.

Figure R4 Machining dimensions for the K-connector kit mounting hole (i.e. on the brass block).

¹ Anritsu Company, "K Female Sparkplug Launcher Connector Model: K102F", <http://www.anritsu.co.uk/products/default.php?p=285&model=K102F> (accessed on 2nd April 2007).

APPENDIX S: Determination of Complex Permittivity of Unknown Materials Using Variational Model

$$\begin{aligned} f_{\text{start}} &:= 30 \cdot 10^3 & \text{Start Frequency} & & \text{NP} &:= 201 & \text{Number of points} \\ f_{\text{stop}} &:= 6 \cdot 10^9 & \text{Stop Frequency} & & n &:= 0..200 & j := \sqrt{-1} \\ f_n &:= f_{\text{start}} + \frac{n}{\text{NP} - 1} \cdot (f_{\text{stop}} - f_{\text{start}}) \end{aligned}$$

data0 - S11 data of empty probe (air) data1 - S11 data of sample under test

data0 := READPRN("D:\My PhD work\My PhD work\IEEE Journal\data18.d1")

data1 := READPRN("D:\My PhD work\My PhD work\IEEE Journal\data19.d1")

$$Z_0 := 50 \quad \omega := 2 \cdot \pi \cdot f$$

$$x0_n := \text{data0}_{n,0} \quad y0_n := \text{data0}_{n,1} \quad x1_n := \text{data1}_{n,0} \quad y1_n := \text{data1}_{n,1}$$

$$S11_air_n := x0_n + j \cdot y0_n \quad S11_sample_n := x1_n + j \cdot y1_n$$

$$\rho_n := \frac{S11_sample_n}{S11_air_n} \quad \text{Eliminating the electrical length } L \text{ between } AB \text{ and } AB'' - \text{ see section 6.2.2 of chapter 6.}$$

C1 is the fringing field capacitance due to the material under test, respectively.

$$C0 := 0 \quad C1 := 8.27 \cdot 10^{-15}$$

$$\tau := 14 \cdot 10^{-11} \quad \text{relaxation time of each dipole} \quad \text{freq} := \frac{1}{2 \cdot \pi \cdot \tau} \quad \text{freq} = 1.137 \times 10^9$$

ϵ_{1_d} and ϵ_{2_d} are the real and imaginary part of the Debye model of the material under test, respectively.

$$\epsilon_{1_d_n} := 4.9 + \frac{(25.4 - 4.9)}{1 + (2\pi f_n)^2 \cdot (\tau)^2} \quad \epsilon_{2_d_n} := \frac{(25.4 - 4.9) \cdot [2\pi f_n \cdot (\tau)]}{1 + (2\pi f_n)^2 \cdot (\tau)^2}$$

$$Y_{a_n} := j \cdot \omega_n \cdot C1 \quad \text{Aperture admittance without the sample (air)}$$

$$\Gamma_{a_n} := \frac{(1 - Z_0 \cdot Y_{a_n})}{(1 + Z_0 \cdot Y_{a_n})} \quad \text{Measured reflection coefficient at the reference plane } AB \text{ without the sample}$$

$$\Gamma_{\text{inv}_n} := \text{inverse_}\Gamma_{a_n} \quad \text{inverse_}\Gamma_{a_n} := \frac{(1 + Z_0 \cdot Y_{a_n})}{(1 - Z_0 \cdot Y_{a_n})}$$

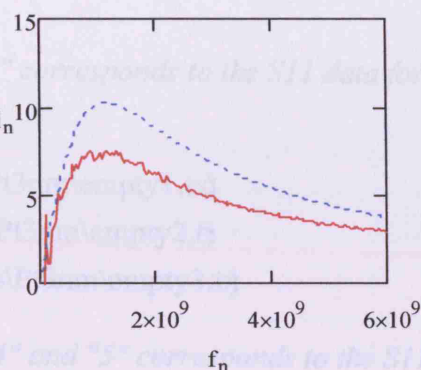
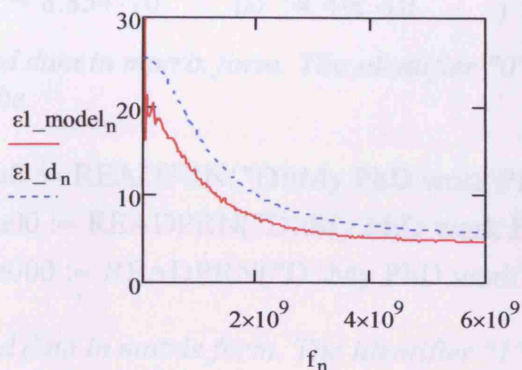
$$Y_{s_n} := \left(\frac{1}{Z_0} \right) \cdot \frac{(\Gamma_{\text{inv}_n} - \rho_n)}{(\Gamma_{\text{inv}_n} + \rho_n)} \quad \text{Aperture admittance with the sample}$$

$$\epsilon_{\text{model}_n} := \frac{1}{C1} \cdot \left(\frac{Y_{s_n}}{j \cdot \omega_n} \right) \quad \text{inverted to find complex permittivity of the sample}$$

ϵ_{1_model} and ϵ_{2_model} are the measured real and imaginary part of the complex permittivity of the material under test, respectively.

$$\epsilon_{1_model_n} := \text{Re}(\epsilon_{model_n})$$

$$\epsilon_{2_model_n} := -\text{Im}(\epsilon_{model_n})$$



Error Calculations

$$n := 4 \dots 200$$

$$\text{Number_of_points} := (200 - 4)$$

$$\text{Percent_}\epsilon_{1_model_n} := \frac{||\epsilon_{1_model_n}| - |\epsilon_{1_d_n}||}{|\epsilon_{1_d_n}|} \cdot 100$$

$$\text{Mean_}\epsilon_{1model_}\%_error_A := \frac{\sum_{n=3}^{200} \text{Percent_}\epsilon_{1_model_n}}{\text{Number_of_points}}$$

$$\text{Mean_}\epsilon_{1model_}\%_error_A = 23.112$$

$$\text{Percent_}\epsilon_{2_model_n} := \frac{||\epsilon_{2_model_n}| - |\epsilon_{2_d_n}||}{|\epsilon_{2_d_n}|} \cdot 100$$

$$\text{Mean_}\epsilon_{2model_}\%_error_A := \frac{\sum_{n=3}^{200} \text{Percent_}\epsilon_{2_model_n}}{\text{Number_of_points}}$$

$$\text{Mean_}\epsilon_{2model_}\%_error_A = 27.176$$

APPENDIX T: Coaxial Probe Analysis of Metal Oxide Nanoparticles

(All undefined symbols have their usual meanings, all units are S.I.)

$$\epsilon_0 := 8.854 \cdot 10^{-12} \quad \mu_0 := 4 \cdot \pi \cdot 10^{-7} \quad j := \sqrt{-1}$$

Read data in matrix form. The identifier "0", "00", "000" corresponds to the S11 data for the empty probe.

```
data0 := READPRN("D:\My PhD work\PhD_Thesis\Pt3nm\empty1.tx")
data00 := READPRN("D:\My PhD work\PhD_Thesis\Pt3nm\empty2.tx")
data000 := READPRN("D:\My PhD work\PhD_Thesis\Pt3nm\empty3.tx")
```

Read data in matrix form. The identifier "1", "2", "3", "4" and "5" corresponds to the S11 data for the 1, 2, 3, 4 & 5 drops of metal NPs, each drop form a thickness of 5um (after the complete evaporation of water).

```
data1 := READPRN("D:\My PhD work\PhD_Thesis\Pt3nm_1drop.tx")
data2 := READPRN("D:\My PhD work\PhD_Thesis\Pt3nm_2drop.tx")
data3 := READPRN("D:\My PhD work\PhD_Thesis\Pt3nm_3drop.tx")
data4 := READPRN("D:\My PhD work\PhD_Thesis\Pt3nm_4drop.tx")
data5 := READPRN("D:\My PhD work\PhD_Thesis\Pt3nm_5drop.tx")
```

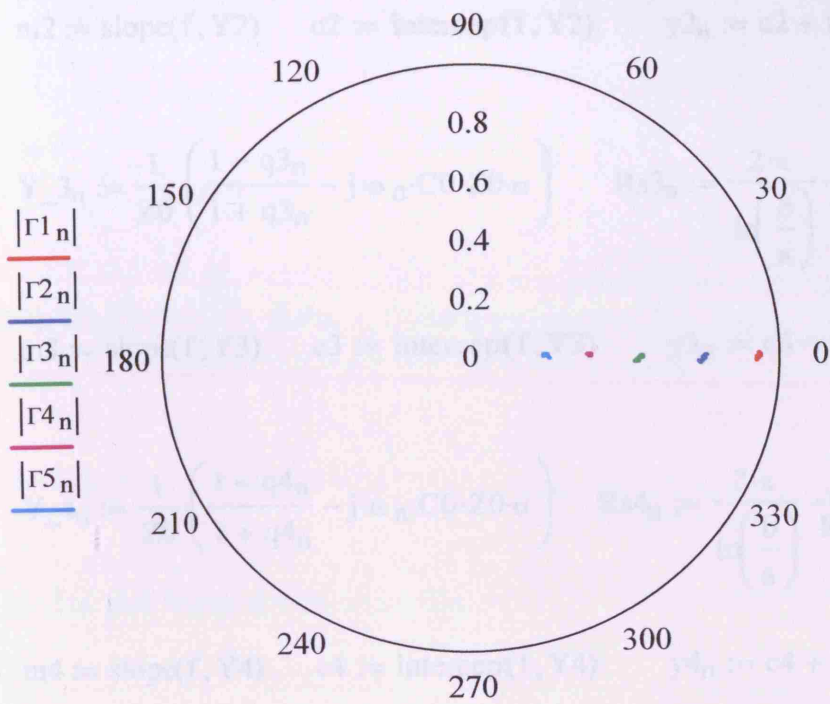
$$NP := 201 \quad f_{start} := data0_{0,0} \quad f_{stop} := data0_{0,1}$$

$$n := 0..NP - 1 \quad f_n := f_{start} + \frac{n}{NP - 1} \cdot (f_{stop} - f_{start})$$

$$\begin{aligned} \rho_{0n} &:= data0_{n+1,0} + j \cdot data0_{n+1,1} & \rho_{00n} &:= data00_{n+1,0} + j \cdot data00_{n+1,1} \\ \rho_{000n} &:= data000_{n+1,0} + j \cdot data000_{n+1,1} & \rho_{1n} &:= data1_{n+1,0} + j \cdot data1_{n+1,1} \\ \rho_{2n} &:= data2_{n+1,0} + j \cdot data2_{n+1,1} & \rho_{3n} &:= data3_{n+1,0} + j \cdot data3_{n+1,1} \\ \rho_{4n} &:= data4_{n+1,0} + j \cdot data4_{n+1,1} & \rho_{5n} &:= data5_{n+1,0} + j \cdot data5_{n+1,1} \end{aligned}$$

Eliminating the electrical length L between AB and AB'' - see section 6.3.1 of chapter 6.

$$\Gamma_{1n} := \frac{\rho_{1n}}{\rho_{000n}} \quad \Gamma_{2n} := \frac{\rho_{2n}}{\rho_{00n}} \quad \Gamma_{3n} := \frac{\rho_{3n}}{\rho_{000n}} \quad \Gamma_{4n} := \frac{\rho_{4n}}{\rho_{0n}} \quad \Gamma_{5n} := \frac{\rho_{5n}}{\rho_{000n}}$$



$$\arg(\Gamma_{1n}), \arg(\Gamma_{2n}), \arg(\Gamma_{3n}), \arg(\Gamma_{4n}), \arg(\Gamma_{5n})$$

$$C0 := 6.1 \cdot 10^{-15} \quad \omega_n := 2 \cdot \pi \cdot f_n \quad \begin{array}{ll} \text{outer radii of the probe} & \text{inner radii of the probe} \\ b := 0.863 \cdot 10^{-3} & a := 0.1525 \cdot 10^{-3} \end{array}$$

$$Z0 := 50 \quad \text{Characteristic impedance of the probe}$$

$$p_n := \frac{1 - j \cdot \omega_n \cdot C0 \cdot Z0}{1 + j \cdot \omega_n \cdot C0 \cdot Z0} \quad q_{1n} := p_n \cdot \Gamma_{1n} \quad q_{2n} := p_n \cdot \Gamma_{2n}$$

$$\alpha := 1 \quad q_{3n} := p_n \cdot \Gamma_{3n} \quad q_{4n} := p_n \cdot \Gamma_{4n} \quad q_{5n} := p_n \cdot \Gamma_{5n}$$

$$Y_{-1n} := \frac{1}{Z0} \cdot \left(\frac{1 - q_{1n}}{1 + q_{1n}} - j \cdot \omega_n \cdot C0 \cdot Z0 \cdot \alpha \right) \quad Rs_{1n} := \frac{2 \cdot \pi}{\ln\left(\frac{b}{a}\right)} \cdot \frac{1}{\text{Re}(Y_{-1n})} \quad Gs_{1n} := \frac{1}{Rs_{1n}}$$

$$Y_{1n} := \text{Im}(Y_{-1n})$$

$$m1 := \text{slope}(f, Y1) \quad c1 := \text{intercep}(f, Y1) \quad y1_n := c1 + m1 \cdot f_n \quad Cs0 := m1 \cdot \ln\left(\frac{b}{a}\right)$$

$$Y_{-2n} := \frac{1}{Z0} \cdot \left(\frac{1 - q_{2n}}{1 + q_{2n}} - j \cdot \omega_n \cdot C0 \cdot Z0 \cdot \alpha \right) \quad Rs_{2n} := \frac{2 \cdot \pi}{\ln\left(\frac{b}{a}\right)} \cdot \frac{1}{\text{Re}(Y_{-2n})} \quad Gs_{2n} := \frac{1}{Rs_{2n}}$$

$$Y_{2n} := \text{Im}(Y_{-2n})$$

$$m2 := \text{slope}(f, Y2) \quad c2 := \text{intercept}(f, Y2) \quad y2_n := c2 + m2 \cdot f_n \quad Cs1 := m2 \cdot \ln\left(\frac{b}{a}\right)$$

$$Y_{-3n} := \frac{1}{Z0} \cdot \left(\frac{1 - q3_n}{1 + q3_n} - j \cdot \omega_n \cdot C0 \cdot Z0 \cdot \alpha \right) \quad Rs3_n := \frac{2 \cdot \pi}{\ln\left(\frac{b}{a}\right)} \cdot \frac{1}{\text{Re}(Y_{-3n})} \quad Gs3_n := \frac{1}{Rs3_n}$$

$$Y3_n := \text{Im}(Y_{-3n})$$

$$m3 := \text{slope}(f, Y3) \quad c3 := \text{intercept}(f, Y3) \quad y3_n := c3 + m3 \cdot f_n \quad Cs2 := m3 \cdot \ln\left(\frac{b}{a}\right)$$

$$Y_{-4n} := \frac{1}{Z0} \cdot \left(\frac{1 - q4_n}{1 + q4_n} - j \cdot \omega_n \cdot C0 \cdot Z0 \cdot \alpha \right) \quad Rs4_n := \frac{2 \cdot \pi}{\ln\left(\frac{b}{a}\right)} \cdot \frac{1}{\text{Re}(Y_{-4n})} \quad Gs4_n := \frac{1}{Rs4_n}$$

$$Y4_n := \text{Im}(Y_{-4n})$$

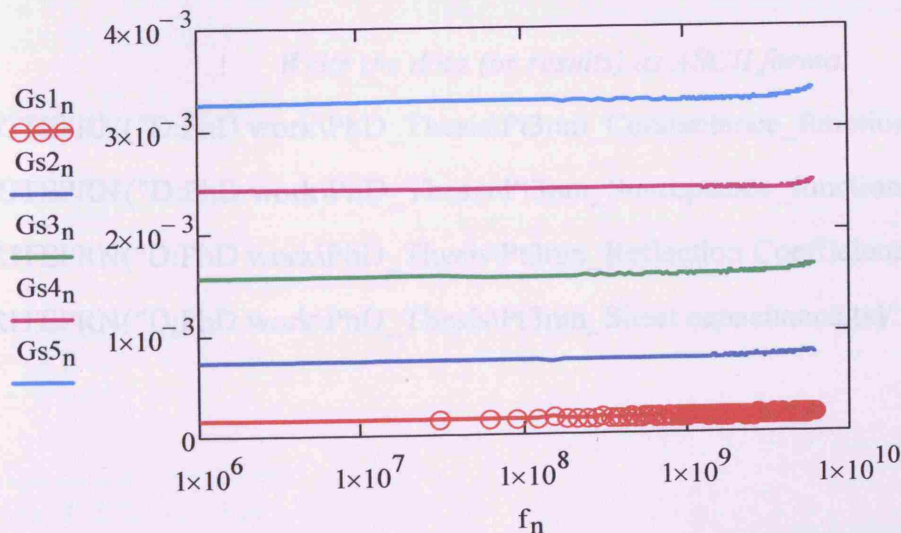
$$m4 := \text{slope}(f, Y4) \quad c4 := \text{intercept}(f, Y4) \quad y4_n := c4 + m4 \cdot f_n \quad Cs3 := m4 \cdot \ln\left(\frac{b}{a}\right)$$

$$Y_{-5n} := \frac{1}{Z0} \cdot \left(\frac{1 - q5_n}{1 + q5_n} - j \cdot \omega_n \cdot C0 \cdot Z0 \cdot \alpha \right) \quad Rs5_n := \frac{2 \cdot \pi}{\ln\left(\frac{b}{a}\right)} \cdot \frac{1}{\text{Re}(Y_{-5n})} \quad Gs5_n := \frac{1}{Rs5_n}$$

$$Y5_n := \text{Im}(Y_{-5n})$$

$$m5 := \text{slope}(f, Y5) \quad c5 := \text{intercept}(f, Y5) \quad y5_n := c5 + m5 \cdot f_n \quad Cs4 := m5 \cdot \ln\left(\frac{b}{a}\right)$$

Sheet conductance as a function of frequency



$$U := 15 \quad I_w := 4 \quad f_L = 1.200294 \times 10^8 \quad f_U = 4.5002775 \times 10^8$$

$$Rs0_0 := \frac{1}{U-L} \cdot \sum_{n=L}^U Rs1_n \quad Rs0_1 := \frac{1}{U-L} \cdot \sum_{n=L}^U Rs2_n \quad Rs0_2 := \frac{1}{U-L} \cdot \sum_{n=L}^U Rs3_n$$

$$Rs0_3 := \frac{1}{U-L} \cdot \sum_{n=L}^U Rs4_n \quad Rs0_4 := \frac{1}{U-L} \cdot \sum_{n=L}^U Rs5_n$$

$$Gs0_0 := \frac{1}{Rs0_0} \quad Gs0_1 := \frac{1}{Rs0_1} \quad Gs0_2 := \frac{1}{Rs0_2} \quad Gs0_3 := \frac{1}{Rs0_3} \quad Gs0_4 := \frac{1}{Rs0_4}$$

The last part writes the data to a file.

$$\begin{array}{llllll} GG_{n,0} := f_n & YY_{n,0} := f_n & yy_{n,0} := f_n & \Gamma_{n,0} := \text{Re}(\Gamma1_n) & \Gamma_{n,1} := \text{Im}(\Gamma1_n) & \\ GG_{n,1} := Gs1_n & YY_{n,1} := Y1_n & yy_{n,1} := y1_n & \Gamma_{n,2} := \text{Re}(\Gamma2_n) & \Gamma_{n,3} := \text{Im}(\Gamma2_n) & \\ GG_{n,2} := Gs2_n & YY_{n,2} := Y2_n & yy_{n,2} := y2_n & \Gamma_{n,4} := \text{Re}(\Gamma5_n) & \Gamma_{n,5} := \text{Im}(\Gamma5_n) & \\ GG_{n,3} := Gs3_n & YY_{n,3} := Y3_n & yy_{n,3} := y3_n & \Gamma_{n,6} := \text{Re}(\Gamma3_n) & \Gamma_{n,7} := \text{Im}(\Gamma3_n) & \\ GG_{n,4} := Gs4_n & YY_{n,4} := Y4_n & yy_{n,4} := y4_n & \Gamma_{n,8} := \text{Re}(\Gamma4_n) & \Gamma_{n,9} := \text{Im}(\Gamma4_n) & \\ GG_{n,5} := Gs5_n & YY_{n,5} := Y5_n & yy_{n,5} := y5_n & & & \end{array}$$

Write the data (or results) as ASCII format

```
WRITEPRN("D:PhD work\PhD_Thesis\Pt3nm_Conductance_function of frequency.txt"):= GG
WRITEPRN("D:PhD work\PhD_Thesis\Pt3nm_Susceptance_function of frequency.txt"):= YY
WRITEPRN("D:PhD work\PhD_Thesis\Pt3nm_Reflection Coefficient.txt"):= ΓΓ
WRITEPRN("D:PhD work\PhD_Thesis\Pt3nm_Sheet capacitance.txt"):= Cs
```

APPENDIX U: Input Text File for the Superfish Analysis of SDR

FISH Test: Sapphire DR with NO hole at the middle ; name of the file.
1 iteration, no resonance search
® kprob=1,icylin=1,dx=.01,dy=.01 ;kprob defines the problem (1:Superfish problem, 0: Poisson problem), icylin represents coordinate system (0: rectangular, 1: Cylindrical), dx and dy specify the x and y mesh size, relatively

nbsup=0, nbslo=0, nbsrt=0, nbslf=0, ;Describe the boundary conditions on the edges of the problem geometry

XDRI=0.81117,YDRI=0.31716,maxcy=10,freq=10448 & ;xdri and ydi designate x and y location for drive point, maxcy sets the maximum number of cycles to find resonant frequency, freq where the user set the approximate resonant frequency

&po x=0.0,y=0.0 &
&po x=0.0,y=1.30 &
&po x=1.60,y=1.30 & ;Assign the boundaries for the cavity
&po x=1.60,y=0.0 &
&po x=0.0,y=0.0 &

® mat=2 &
&po x=0.532,y=0.0 &
&po x=0.532,y=0.452 &
&po x=1.104,y=0.452 &
&po x=1.104,y=0.15 & ;Assign the boundaries for the sapphire puck
&po x=1.6,y=0.15 &
&po x=1.6,y=0.0 &
&po x=0.532,y=0.0 &

&mt mtid=2
epsilon=1, ; Assign the properties (i.e. μ and ϵ) of sapphire puck
mu=9.4 & ;(where $\mu \rightarrow \epsilon$ and $\epsilon \rightarrow \mu$)

® mat=3 &
&po x=1.3,y=0.15 &
&po x=1.3,y=0.50 &
&po x=1.60,y=0.50 & ;Assign the boundaries for the PTFE support
&po x=1.60,y=0.15 &
&po x=1.3,y=0.15 &

&mt mtid=3
epsilon=1, ; Assign the properties (i.e. μ and ϵ) of PTFE support
mu=2.06 &

APPENDIX V: Coaxial Probe Analysis of Pure Metal Nanoparticles

(All undefined symbols have their usual meanings, all units are S.I.)

$$\epsilon_0 := 8.854 \cdot 10^{-12} \quad \mu_0 := 4 \cdot \pi \cdot 10^{-7} \quad j := \sqrt{-1}$$

Read data in matrix form. The identifier "0", "00", "000" corresponds to the S11 data for the empty probe.

```
data0 := READPRN("D:\My PhD work\My PhD work\H2 adsorption\Pt3nm\empty1.txt" )
data00 := READPRN("D:\My PhD work\My PhD work\H2 adsorption\Pt3nm\empty2.txt")
data000 := READPRN("D:\My PhD work\PhD_Thesis\H2 adsorption\Pt3nm\empty3.txt" )
data0000 := READPRN("D:\My PhD work\PhD_Thesis\H2 adsorption\Pt3nm\empty4.txt")
```

Read data in matrix form. The identifier "1", "2", "3", "4" and "5" corresponds to the S11 data for the 1, 2, 3, 4 & 5 drops of metal NPs, each drop form a thickness of 5um (after the complete evaporation of water).

```
data1 := READPRN("D:\My PhD work\H2 adsorption\Pt3nm\Pt3nm_1drop_P3.txt" )
data2 := READPRN("D:\My PhD work\H2 adsorption\Pt3nm\Pt3nm_2drop_P1.txt" )
data3 := READPRN("D:\My PhD work\H2 adsorption\Pt3nm\Pt3nm_3drop_P1.txt" )
data4 := READPRN("D:\My PhD work\H2 adsorption\Pt3nm\Pt3nm_4drop_P4.txt" )
data5 := READPRN("D:\My PhD work\H2 adsorption\Pt3nm\Pt3nm_5drop_P3.txt" )
```

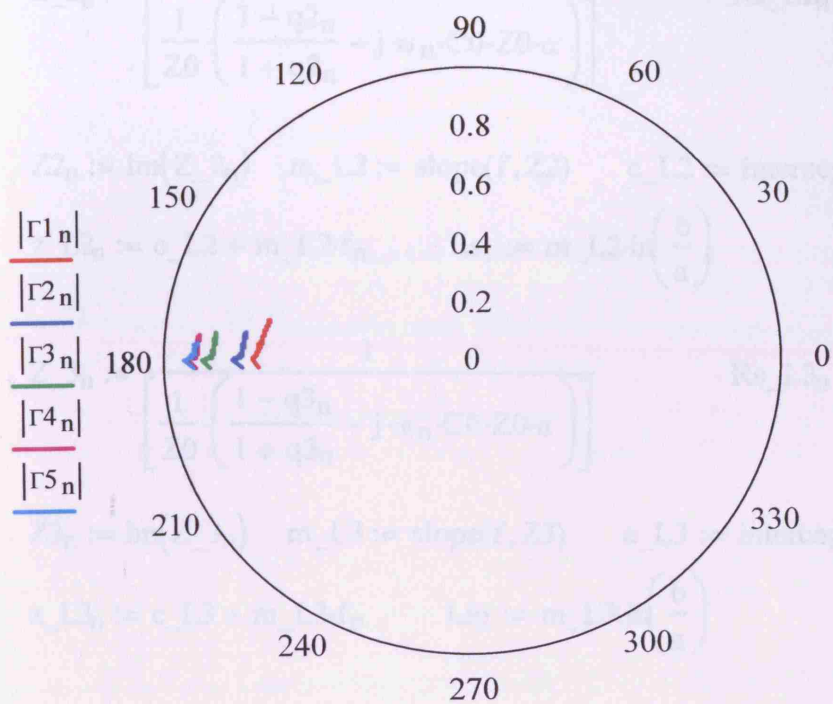
$$NP := 201 \quad f_{start} := data0_{0,0} \quad f_{stop} := data0_{0,1}$$

$$n := 0..NP - 1 \quad f_n := f_{start} + \frac{n}{NP - 1} \cdot (f_{stop} - f_{start})$$

$$\begin{aligned} \rho_{0n} &:= data0_{n+1,0} + j \cdot data0_{n+1,1} & \rho_{00n} &:= data00_{n+1,0} + j \cdot data00_{n+1,1} \\ \rho_{000n} &:= data000_{n+1,0} + j \cdot data000_{n+1,1} & \rho_{0000n} &:= data0000_{n+1,0} + j \cdot data0000_{n+1,1} \\ \rho_{1n} &:= data1_{n+1,0} + j \cdot data1_{n+1,1} & \rho_{2n} &:= data2_{n+1,0} + j \cdot data2_{n+1,1} \\ \rho_{3n} &:= data3_{n+1,0} + j \cdot data3_{n+1,1} & \rho_{4n} &:= data4_{n+1,0} + j \cdot data4_{n+1,1} \\ \rho_{5n} &:= data5_{n+1,0} + j \cdot data5_{n+1,1} \end{aligned}$$

Eliminating the electrical length L between AB and AB'' - see section 6.3.1 of chapter 6.

$$\Gamma_{1n} := \frac{\rho_{1n}}{\rho_{000n}} \quad \Gamma_{2n} := \frac{\rho_{2n}}{\rho_{0n}} \quad \Gamma_{3n} := \frac{\rho_{3n}}{\rho_{0n}} \quad \Gamma_{4n} := \frac{\rho_{4n}}{\rho_{0n}} \quad \Gamma_{5n} := \frac{\rho_{5n}}{\rho_{000n}}$$



$\arg(\Gamma_{1n}), \arg(\Gamma_{2n}), \arg(\Gamma_{3n}), \arg(\Gamma_{4n}), \arg(\Gamma_{5n})$

$$C0 := 6.1 \cdot 10^{-15} \quad \omega_n := 2 \cdot \pi \cdot f_n \quad \begin{array}{ll} \text{outer radii of the probe} & \text{inner radii of the probe} \\ b := 0.863 \cdot 10^{-3} & a := 0.1525 \cdot 10^{-3} \end{array}$$

$$Z0 := 50 \quad \text{Characteristic impedance of the probe}$$

$$p_n := \frac{1 - j \cdot \omega_n \cdot C0 \cdot Z0}{1 + j \cdot \omega_n \cdot C0 \cdot Z0} \quad q_{1n} := p_n \cdot \Gamma_{1n} \quad q_{2n} := p_n \cdot \Gamma_{2n}$$

$$\alpha := 1 \quad q_{3n} := p_n \cdot \Gamma_{3n} \quad q_{4n} := p_n \cdot \Gamma_{4n} \quad q_{5n} := p_n \cdot \Gamma_{5n}$$

$$Z_{_1n} := \frac{1}{\left[\frac{1}{Z0} \cdot \left(\frac{1 - q_{1n}}{1 + q_{1n}} - j \cdot \omega_n \cdot C0 \cdot Z0 \cdot \alpha \right) \right]} \quad R_{s_L1n} := \frac{2 \cdot \pi}{\ln\left(\frac{b}{a}\right)} \cdot \text{Re}(Z_{_1n})$$

$$Z_{1n} := \text{Im}(Z_{_1n}) \quad m_L1 := \text{slope}(f, Z1) \quad c_L1 := \text{intercep}(f, Z1) \quad G_{s_L1n} := \frac{1}{R_{s_L1n}}$$

$$z_L1n := c_L1 + m_L1 \cdot f_n \quad L_{s0} := m_L1 \cdot \ln\left(\frac{b}{a}\right)$$

$$Z_{2n} := \frac{1}{\left[\frac{1}{Z0} \cdot \left(\frac{1 - q_{2n}}{1 + q_{2n}} - j \cdot \omega_n \cdot C0 \cdot Z0 \cdot \alpha \right) \right]}$$

$$Rs_L2_n := \frac{2 \cdot \pi}{\ln\left(\frac{b}{a}\right)} \cdot \text{Re}(Z_{2n})$$

$$Z2_n := \text{Im}(Z_{2n}) \quad m_L2 := \text{slope}(f, Z2) \quad c_L2 := \text{intercept}(f, Z2) \quad Gs_L2_n := \frac{1}{Rs_L2_n}$$

$$z_L2_n := c_L2 + m_L2 \cdot f_n \quad Ls1 := m_L2 \cdot \ln\left(\frac{b}{a}\right)$$

$$Z_{3n} := \frac{1}{\left[\frac{1}{Z0} \cdot \left(\frac{1 - q_{3n}}{1 + q_{3n}} - j \cdot \omega_n \cdot C0 \cdot Z0 \cdot \alpha \right) \right]}$$

$$Rs_L3_n := \frac{2 \cdot \pi}{\ln\left(\frac{b}{a}\right)} \cdot \text{Re}(Z_{3n})$$

$$Z3_n := \text{Im}(Z_{3n}) \quad m_L3 := \text{slope}(f, Z3) \quad c_L3 := \text{intercept}(f, Z3) \quad Gs_L3_n := \frac{1}{(Rs_L3)_n}$$

$$z_L3_n := c_L3 + m_L3 \cdot f_n \quad Ls2 := m_L3 \cdot \ln\left(\frac{b}{a}\right)$$

$$Z_{4n} := \frac{1}{\left[\frac{1}{Z0} \cdot \left(\frac{1 - q_{4n}}{1 + q_{4n}} - j \cdot \omega_n \cdot C0 \cdot Z0 \cdot \alpha \right) \right]}$$

$$Rs_L4_n := \frac{2 \cdot \pi}{\ln\left(\frac{b}{a}\right)} \cdot \text{Re}(Z_{4n})$$

$$Z4_n := \text{Im}(Z_{4n}) \quad m_L4 := \text{slope}(f, Z4) \quad c_L4 := \text{intercept}(f, Z4) \quad Gs_L4_n := \frac{1}{Rs_L4_n}$$

$$z_L4_n := c_L4 + m_L4 \cdot f_n \quad Ls3 := m_L4 \cdot \ln\left(\frac{b}{a}\right)$$

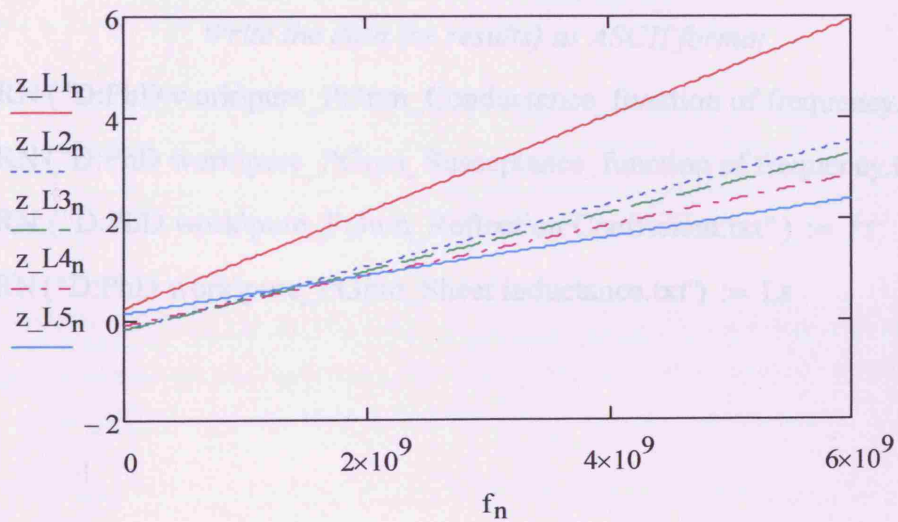
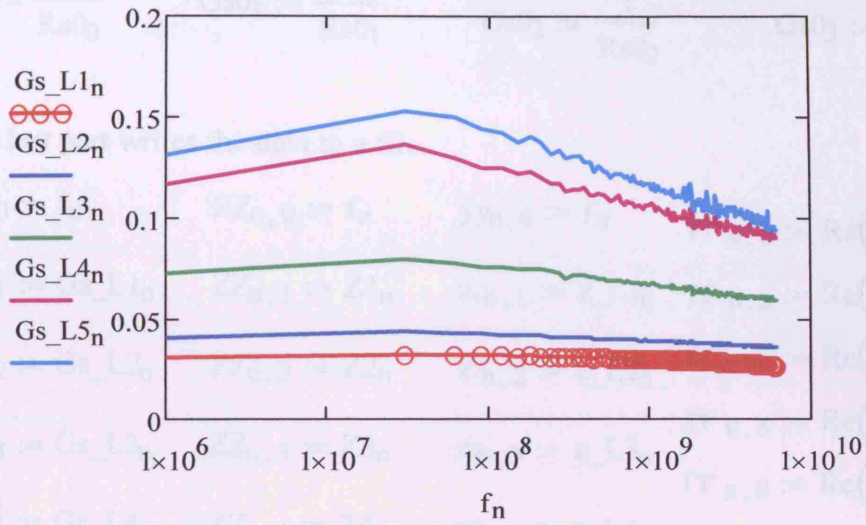
$$Z_{5n} := \frac{1}{\left[\frac{1}{Z0} \cdot \left(\frac{1 - q_{5n}}{1 + q_{5n}} - j \cdot \omega_n \cdot C0 \cdot Z0 \cdot \alpha \right) \right]}$$

$$Rs_L5_n := \frac{2 \cdot \pi}{\ln\left(\frac{b}{a}\right)} \cdot \text{Re}(Z_{5n})$$

$$Z5_n := \text{Im}(Z_{5n}) \quad m_L5 := \text{slope}(f, Z5) \quad c_L5 := \text{intercept}(f, Z5) \quad Gs_L5_n := \frac{1}{Rs_L5_n}$$

$$z_L5_n := c_L5 + m_L5 \cdot f_n \quad Ls4 := m_L5 \cdot \ln\left(\frac{b}{a}\right)$$

Sheet conductance as a function of frequency



$$U := 15 \quad L := 4 \quad f_L = 1.200294 \times 10^8 \quad f_U = 4.5002775 \times 10^8$$

$$Rs0_0 := \frac{1}{U-L} \cdot \sum_{n=L}^U Rs_L1_n \quad Rs0_1 := \frac{1}{U-L} \cdot \sum_{n=L}^U Rs_L2_n \quad Rs0_2 := \frac{1}{U-L} \cdot \sum_{n=L}^U Rs_L3_n$$

$$Rs0_3 := \frac{1}{U-L} \cdot \sum_{n=L}^U Rs_L4_n \quad Rs0_4 := \frac{1}{U-L} \cdot \sum_{n=L}^U Rs_L5_n$$

$$Gs0_0 := \frac{1}{Rs0_0} \quad Gs0_1 := \frac{1}{Rs0_1} \quad Gs0_2 := \frac{1}{Rs0_2} \quad Gs0_3 := \frac{1}{Rs0_3} \quad Gs0_4 := \frac{1}{Rs0_4}$$

The last part writes the data to a file.

$$\begin{array}{lllll} GG_{n,0} := f_n & ZZ_{n,0} := f_n & YY_{n,0} := f_n & \Gamma\Gamma_{n,0} := \text{Re}(\Gamma1_n) & \Gamma\Gamma_{n,1} := \text{Im}(\Gamma1_n) \\ GG_{n,1} := Gs_L1_n & ZZ_{n,1} := Z1_n & zz_{n,1} := z_L1_n & \Gamma\Gamma_{n,2} := \text{Re}(\Gamma2_n) & \Gamma\Gamma_{n,3} := \text{Im}(\Gamma2_n) \\ GG_{n,2} := Gs_L2_n & ZZ_{n,2} := Z2_n & zz_{n,2} := z_L2_n & \Gamma\Gamma_{n,4} := \text{Re}(\Gamma5_n) & \Gamma\Gamma_{n,5} := \text{Im}(\Gamma5_n) \\ GG_{n,3} := Gs_L3_n & ZZ_{n,3} := Z3_n & zz_{n,3} := z_L3_n & \Gamma\Gamma_{n,6} := \text{Re}(\Gamma3_n) & \Gamma\Gamma_{n,7} := \text{Im}(\Gamma3_n) \\ GG_{n,4} := Gs_L4_n & ZZ_{n,4} := Z4_n & zz_{n,4} := z_L4_n & \Gamma\Gamma_{n,8} := \text{Re}(\Gamma4_n) & \Gamma\Gamma_{n,9} := \text{Im}(\Gamma4_n) \\ GG_{n,5} := Gs_L5_n & ZZ_{n,5} := Z5_n & zz_{n,5} := z_L5_n & & \end{array}$$

Write the data (or results) as ASCII format

WRITEPRN ("D:PhD work\pure_Pt3nm_Conductance_function of frequency.txt") := GG

WRITEPRN ("D:PhD work\pure_Pt3nm_Susceptance_function of frequency.txt") := ZZ

WRITEPRN ("D:PhD work\pure_Pt3nm_Reflection Coefficient.txt") := $\Gamma\Gamma$

WRITEPRN ("D:PhD work\pure_Pt3nm_Sheet inductance.txt") := Ls

APPENDIX W: Detailed Derivation to Obtain the Internal Inductance of Porous Conducting Layer (assuming non-uniform current density, i.e. limit $t \gg \delta$)

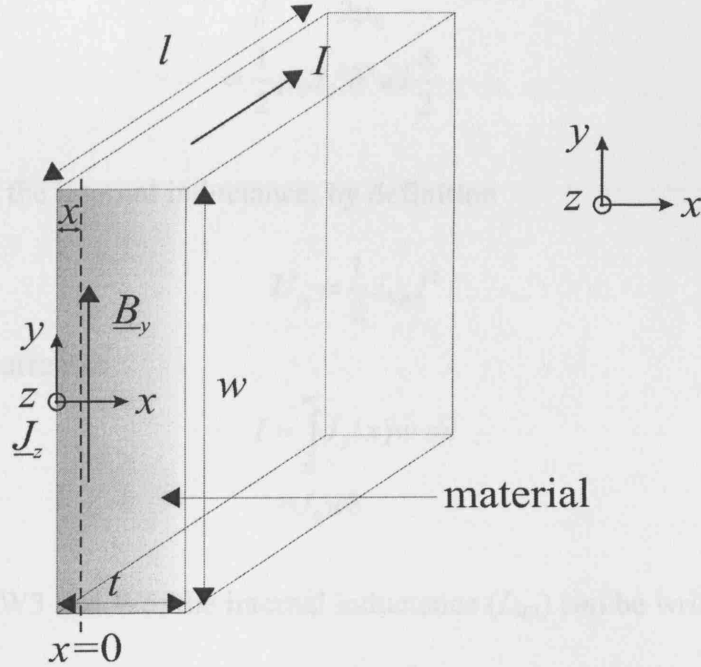


Figure W1 Shows the porous conducting sheet.

The current density ($J_z(x)$) at depth x shown, measured from the middle of the sheet, is

$$J_z(x) = J_0 e^{-x/\delta} \quad (W1)$$

where J_0 and δ are the current density magnitude and skin depth of the sheet, respectively.

We use Ampere's law to find $B_y(x)$ at depth x shown, measured from middle of sheet, as follows

$$\begin{aligned} \nabla \times B &= \mu_0 J \\ \frac{\partial B_y}{\partial x} &= \mu_0 J \rightarrow B_y = \mu_0 J_z \delta \end{aligned} \quad (W2)$$

The magnetic stored energy in a sliver of sheet, thickness dx is

$$\begin{aligned}
 U_m &= \int \frac{B^2}{2\mu_0} dV \\
 &\simeq \int_0^\infty \frac{\mu_0^2 J_0^2 \delta^2 e^{-2x/\delta}}{2\mu_0} w l dx \\
 &\simeq \frac{1}{2} \mu_0 J_0^2 \delta^2 w l \frac{\delta}{2}
 \end{aligned} \tag{W3}$$

Denoting L_{int} as the internal inductance, by definition

$$U_m = \frac{1}{2} L_{\text{int}} I^2 \tag{W4}$$

where the total current is

$$\begin{aligned}
 I &= \int_0^\infty J_z(x) w dx \\
 &= J_0 w \delta
 \end{aligned} \tag{W5}$$

Hence from Eq. W3 and W5, the internal inductance (L_{int}) can be written as

$$L_{\text{int}} \simeq \frac{1}{2} \frac{\mu_0 \delta}{w} l \tag{W5}$$

Therefore, the total internal inductance (L_{int}) of the sheet is

$$L_{\text{int}} \simeq \frac{\mu_0 \delta}{w} l \tag{W6}$$

(remembering that the sheet has two surfaces)

If the current density is uniform (i.e. limit $t \ll \delta$) then the equivalence formula is

$$L_{\text{int}} \simeq \frac{1}{24\pi} \mu_0 t \ln\left(\frac{b}{a}\right) \tag{W7}$$

where b and a are the outer and inner radii of the coaxial probe.

APPENDIX X: The Components (i.e. R, C and L) Values Chosen for the R-C and R-L Network Models

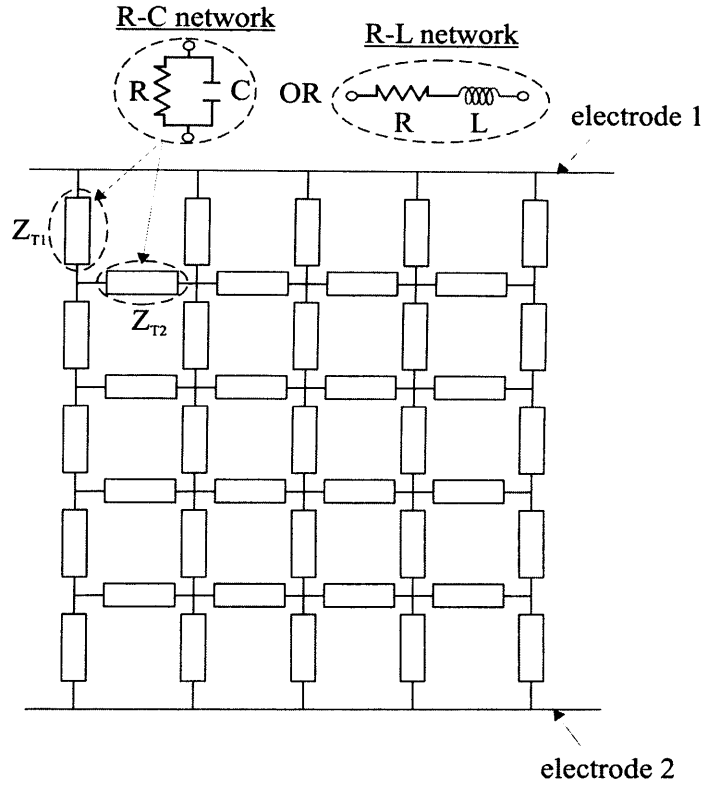


Figure X1 An example of 5×5 random R-C network and R-L network is shown, although the actual network used in this research is much larger (15×15).

In this research, the values of resistance (R), capacitance (C) and inductance (L) were the same values as obtained from the microwave experiments (see sections 6.3.2 and 6.5.2) as listed in table X1 below. As it is apparent from the TEM images (fig. 4.15) obtained for the Pt oxide NPs, the variations in the size distribution of the particles are very small, therefore the variations of resistance values are small, which leads to an assumption to make the variations of the resistance to be 10% of the actual values. For instance, for the 1 drop of 3 nm Pt oxide nanoparticle (NP) film, the individual vertical (e.g. Z_{T1}) and horizontal (e.g. Z_{T2}) components of the above circuit (see fig. X1) were replaced with the values of $R = 7000 \pm 10\% \Omega$ and $C = 1 \times 10^{-20} \text{ F}$. Similarly, the remaining 4 graphs of the fig. 6.57 were obtained separately by running the MATLAB script (i.e. using the MATLAB script to analyse the frequency response of this circuit) independently. In the similar manner the values listed in tables X2 and X3 were used in the same circuit independently to resemble the

microwave experimental results and has been found to predict the correct signature Pt oxide NP (tables X1 and X2 – see fig. 6.58) films, pure Pt and Au NP films (table X3 – see fig. 6.59), respectively.

No. of drops	Resistance (Ω)	Capacitance (F)
1 drop	$7000 \pm 10\%$	1×10^{-20}
2 drops	$1600 \pm 10\%$	1×10^{-20}
3 drops	$750 \pm 10\%$	1×10^{-20}
4 drops	$480 \pm 10\%$	1×10^{-20}
5 drops	$355 \pm 10\%$	1×10^{-20}

Table X1 shows the actual values used in the R-C network, which have been obtained from the microwave experiments (e.g. for 3.0 nm) Pt oxide NP films.

No. of drops	Resistance (k Ω)	Capacitance (fF)
1 drop	$71.4 \pm 10\%$	$25 \pm 5\%$
2 drops	$32.3 \pm 10\%$	$50 \pm 5\%$
3 drops	$18.0 \pm 10\%$	$100 \pm 5\%$
4 drops	$14.2 \pm 10\%$	$150 \pm 5\%$
5 drops	$10.2 \pm 10\%$	$200 \pm 5\%$

Table X2 shows the actual values used in the R-C network, which have been obtained from the microwave experiments (e.g. for 6.9 nm) Pt oxide NP films.

No. of drops	Resistance (Ω)	Inductance (nH)
1 drop	$70 \pm 10\%$	$0.6 \pm 10\%$
2 drops	$30 \pm 10\%$	$0.9 \pm 10\%$
3 drops	$20 \pm 10\%$	$1.2 \pm 10\%$
4 drops	$14 \pm 10\%$	$2.0 \pm 10\%$
5 drops	$12 \pm 10\%$	$3.0 \pm 10\%$

Table X3 shows the actual values used in the R-L network, which have been obtained from the microwave experiments (e.g. for 3.0 nm) pure Pt NP films (i.e. after the exposure of H₂ gas).

APPENDIX Y: MATLAB Script for Random Network Circuits

```
% *****
% Aslam Sulaimalebbe      Cardiff University
% Impedance algorithm of a 2D network with normal capacitive/inductive
%   distributions
% Based on method developed by Frank and Lobb 1988
% *****

clear
% Variables

for b = 1:1          %for loop with hold on to compare results (there is an
                    %end command associated with this at the bottom of the
                    %file)

n = 15;              % size of mesh
resistor = 1000;     % resistor value
%capacitor = 1e-9;    % capacitor value

capmean = 0.001e-12;
capdev = 0.1e-14;
indmean = 1e-4
inddev = 1e-11
prob = 0;            % probability of resistor
freq_start=0;
freq_stop=10e9;
number_of_points=100;

%f=[freq_start:freq_stop/(number_of_points-1):freq_stop];

% to create logarithmic frequency points
f=[0:number_of_points];
power=log10(freq_stop);
f=(10/number_of_points)*f;
f=10.^(f);
```

```

% Generate random impedance values
Radd=ones(n^2);      %address matrix (to locate resistors to be assigned)
Cadd=zeros(n^2);     %address matrix (to locate capacitors to be assigned an
admittance once frequency is allocated)

rand('twister',sum(100*clock));      % randomly initiate seed for twister
algorithm
    for row = 1:(n^2)
        for col = 1:(n^2)
            t=rand;
            if t>prob      %probability of resistor
                Radd(row,col)=0;
                Cadd(row,col)=1;
            end
        end
    end
    % normal distribution of capacitances

    randn('state',sum(100*clock));
    %paracap= capmean+capdev.*randn(n^2)+1e-70;
    serind= indmean+inddev.*randn(n^2)+1e-70;
    %parares= 350+0.*randn(n^2);
    serres= 65e3+0.*randn(n^2);
    %parares= (paracap./1e-9).*1000;

    for r = 1:number_of_points+1

        %capZ=1./(j*2*pi*f(r).*paracap);
        indZ=(j*2*pi*f(r).*serind);

        % in parallel with resistance
        %cell = (parares.*capZ)./(parares+capZ);
        % inductor in series with resistor
        cell = indZ+serres;

    Z=Radd*resistor+Cadd.*cell;

    % number of iteration based on centre node...
    % copy Z values into transformation algorithm

```



```

% starting point for diagonal (based on centre node)

% generate starting points
for start = (n+2):n^2

    row = ceil(start/n);
    % ( number of iterations for this diagonal will be lowest of either nodes to
    the right or downwards)
    if row*n-start<n-row
        number_of_iterations = row*n-start; % ( should be lowest of this or
n-row)
    else number_of_iterations = n-row;

end

% set initial Zdiag for this starting point

if (start+n-2)/round((start+n-2)/n)==n % if centre point is 2+(multiple of
n)
    Zdiag = Z(start-n-1,start-n);
else
    Zdiag = Z(start-n-1,start-n)+Z(start-n-1,start-1);
end

% for loop for each diagonal (starting at the above starting point).
for x = 0:number_of_iterations % (number of nodes in diagonal)

    m=start+(n+1)*x;

% clauses based on mesh position

% boundary position left          (is this necessary if starting points are
well programmed?)
if (m+n-1)/round((m+n-1)/n)~=n % if not 1+(multiple of n), then carry on.
(Otherwise end this cycle of for loop)

% boundary position right
if m/round(m/n)==n % if m is multiple of n (this will cover bottom
right node as well).
    Z(m-1,m) = (Zdiag*Z(m-1,m))/(Z(m-1,m)+Zdiag); % (diag and one below
it in parallel)
end
end
end

```

```

% boundary position bottom
else if m > n^2-n          % if m is in the bottom row
B1 = Zdiag;
B2 = Z(m-1,m);
B3 = Z(m-n,m);
B4 = Z(m,m+1);

% then the boundary transformation

% d-Y    1, 2, 3 go to 5,6,7
B5 = B1*B2*(1/(B1+B2+B3));
B6 = B1*B3*(1/(B1+B2+B3));
B7 = B2*B3*(1/(B1+B2+B3));
B8 = B7+B4;

% reassigns boundary transformation variables to matrix
Z(m-1,m) = B5;
Z(m-n,m) = B6;
Z(m,m+1) = B8;

    else

% transformation

% assigns transformation variables based on centre node

T1 = Zdiag;
T2 = Z(m-1,m);
T3 = Z(m-n,m);
T4 = Z(m,m+n);
T5 = Z(m,m+1);

% then the transformation
%firstly d-Y    1, 2, 3 go to 6, 7, 8
T6 = T2*T1*(1/(T1+T2+T3));
T7 = T1*T3*(1/(T1+T2+T3));
T8 = T2*T3*(1/(T1+T2+T3));

%secondly Y-d    4, 5, 8 go to 9, 10, 11

```

```

T9 = ((T4*T5)+(T5*T8)+(T4*T8))/T5;
T10 = ((T4*T5)+(T5*T8)+(T4*T8))/T4;
T11 = ((T4*T5)+(T5*T8)+(T4*T8))/T8;

% reassigns transformation variables to matrix
Zdiag = T11; % re-use diag which has simply moved
Z(m-1,m) = T6;
Z(m-n,m) = T7;
Z(m,m+n) = T9;
Z(m,m+1) = T10;

    end
end
end
end

Result = 0; %initialise result
    for i=1:n-1
        Result = Result + Z(n^2-i,n^2-i+1);
    end

fr(r,1) = f(r);
Zr(r,1) = Result;

y(r,1) = (1/Result); %*(1/j*2*pi*f(r)*8e-15);

end
loglog(fr,abs(1./Zr),'LineWidth',0.01)
hold on

end

```

